Universidad del País Vasco
Euskal Herriko Unibertsitatea

High temperature packed bed thermal energy storage systems based on low cost materials

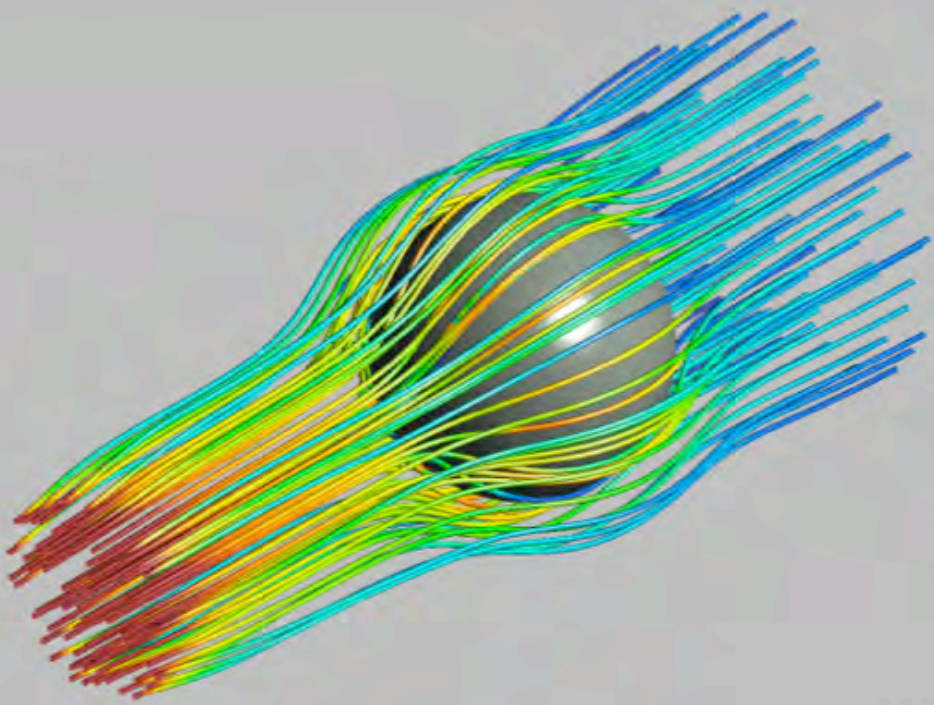

Iñigo Ortega Fernández

Bilbao, 21st July 2017

UNIVERSIDAD DEL PAÍS VASCO
EUSKAL HERRIKO UNIBERTSITATEA

ESCUELA DE INGENIERÍA DE BILBAO
BILBOKO INGENIARITZA ESKOLA

DEPARTAMENTO DE INGENIERÍA QUÍMICA Y EL MEDIO AMBIENTE
INGENIARITZA KIMIKOA SAILA ETA INGURUMENAREN INGENIARITZA

CIC ENERGIGUNE

High temperature packed bed thermal energy storage systems based on low cost materials

By

Iñigo Ortega Fernández

Thesis supervisors:

Dr. Javier Rodríguez Aseguinolaza

Dr. Abdessamad Faik

UPV/EHU supervisor:

Prof. Pedro Luis Arias Ergueta

A thesis submitted to apply for the degree of "DOCTOR IN ADVANCED MATERIALS ENGINEERING" with "INTERNATIONAL DOCTOR" mention

Bilbao, 21st July 2017

To my parents

A question that sometimes drives me hazy: am I or are the others crazy?

Albert Einstein

Index

Acknowledgements/agradecimientos

This thesis is the result of almost four years of very tough work that would not have been possible without the support and effort of many people. I will try not to forget any of you, just in case, I would like to thank in advance to all the people that has been direct or indirectly involved in this work.

En primer lugar, me gustaría dar las gracias a los dos co-directores de esta tesis. **Dr. Javier Rodríguez Aseguinolaza**, gracias por aportar a este trabajo tus grandes conocimientos e ideas, y sobre todo, por salir siempre al rescate en los momentos duros, que no han sido pocos. ¡¡¡Eres un grande!!! **Dr. Abdessamad Faik**, muchísimas gracias por tus aportes y horas de dedicación. No ha sido un camino de rosas llegar a este punto, pero gracias a ti, todo ha sido más fácil. Así mismo, me gustaría dar las gracias al departamento de *Ingeniería Química y el Medio Ambiente* de la *Universidad del País Vasco*, especialmente al **Prof. Pedro Luis Arias Ergueta** por su inestimable ayuda y consejos a lo largo de esta tesis, y por facilitarme la presentación de la misma.

Quiero dar las gracias al **CIC Energigune** y al grupo de personas que forman o han formado parte de este proyecto, por la gran oportunidad brindada al permitirme desarrollar esta tesis doctoral en un ámbito tan excepcional. En particular, quiero agradecer el apoyo recibido por todos los integrantes del grupo de almacenamiento térmico. I would not like to miss the opportunity to acknowledge **Dr. Bruno D'Aguanno** for the nice moments lived in Vitoria and the endless and motivating discussions that, undoubtedly, have had a relevant impact in the work described in this thesis.

I would also like to thank **Prof. Maurizio Barbato** and the members of the *Thermo-Fluid Dynamics laboratory* at *SUPSI*. Many thanks for sharing your knowledge with me; it was a very big pleasure to meet all of you in Switzerland.

The research activities performed in this thesis would not have been possible without the financial support of many research programmes and institutions. Among them, the *European Union Horizon 2020 Framework Programme* with the grant agreements *642067* (*RESLAG*) and *657690* (*ORC-Plus*), the *Spanish Ministry of Economy and Competitiveness* through the *7th European Union Framework Programme SOLAR-era.net* with the contract number *PCIN-2013-122-C03-01*

(*Slagstock*), and the *Department of Economic Development and Infrastructures of the Basque Country Government* through the projects *ETORTEK 2013* (*IE13-375*) and *ELKARTEK 2016* (*KK-2016/00037 – CICE2016*) are acknowledged. Of particular importance are the pre-doctoral contract *PRE_2014_1_130* from the *Department of Education, Linguistic Politics and Culture of the Basque Country Government* that allowed me to join *CIC Energigune* and the contract *EP_2016_1_0007* from the *EGONLABUR programme* to support the three-months-stay in Switzerland, both of them are specially acknowledged.

Una tesis no se consigue solo con un buen entorno científico y laboral sino también con unos grandes amigos que sepan darte el apoyo necesario en los buenos, y no tan buenos momentos. Dicho esto, me gustaría empezar dando las gracias a mi gran amigo **Pino** (Adrián) y a mis dos queridos "littles", **Eduardo** y **Rodrigo**. Por muchos más vinos, cervezas, días de esquí, surf, sidrerías y viajes locos!!! También quiero dar las gracias a mis grandes amigos de la infancia **Mayte**, **Vicky**, **Paola**, **Bea**, **Miguel** y **Andrés**, por que sigamos muchos años mas unidos compartiendo buenos momentos. **Asier**, **Marín** y compañeros "runners" **Fran** y **Jose Ángel** muchísimas gracias por estar siempre ahí y dar ánimos cuando más hacen falta. Quiero dar las gracias también a **Laura**, **Raquel**, **Elena**, **Dani (x2)**, **Saúl**, **Valle** y **Marta** por unirse a estas maravillosas personas y compartir grandes momentos con todos. Para terminar este párrafo, quiero dar las gracias a mi "cuñado" **Miguel**, por que sigas cuidando a mi hermanita y familia como hasta ahora y podamos seguir compartiendo grandes momentos juntos.

Si los amigos son importantes, todavía lo es más la **familia**. Muchas gracias a toda mi familia **asturiana** y **madrileña** por vuestro incondicional apoyo y cariño.

Para finalizar, he querido dejar a las cuatro personas mas importantes y que más quiero en este mundo: mis padres **Ángel** y **Conchi**, mi hermana **Carolina** y mi novia **Amaia**. No hay adjetivos positivos suficientes para describiros. Muchas gracias por estar siempre a mi lado, no dejarme caer en los momentos malos, darme lo mejor que tenéis, vuestro apoyo y cariño, y sobre todo, por aguantarme. Sin duda alguna, esta tesis no hubiera sido posible sin vosotros cuatro.

Thank you very much to everyone!!!
¡¡¡Muchas gracias a todos!!!
Eskerrik asko guztioi!!!

Abstract

Thermal energy storage (TES) is presented as a proven element to reach a sustainable and efficient management of any thermally driven process. The inherent thermodynamic limitations associated to a thermal system, such as the unavailability of an appropriate heat source, thermal losses or improvable cycle efficiencies, justify the implementation of a TES solution. In practice, numerous industrial processes present noticeable enhancement opportunities according to the mentioned gaps. In these terms, solar-thermal power production, intensive heat demanding heavy industries (steelmaking, glass, cement production, etc.) or compressed air energy storage are representative examples with such optimization potential.

However, even if the deployment of a TES can be conceptually a successful solution, its implementation on real application environments must satisfy very restrictive requirements, both, technical and economical. Considering these boundaries, the search of technically high performing and cost-effective TES solutions has become a priority of the industrial and scientific community. Among other TES concepts, the packed bed solution has been identified in the last years as a very promising technology. Its high operational flexibility, relative implementation simplicity, high thermal performance and cycle efficiency together with its highly techno-economic effective nature confer to this TES alternative a particular interest.

In this frame, this thesis aims at investigating the suitability of the packed bed storage alternative in order to provide a clear and concise proof-of-concept of this technology. For this purpose, a material and thermal performance analysis, able to demonstrate the large capabilities of this TES solution is presented. With these objectives, a complete study is carried out at different exploitation levels. First, new ceramic low-cost materials families are identified, the iron and steel slag and a natural ore, magnetite, with a clear suitability for high temperature TES systems. Their potential is demonstrated through a complete material analysis, including the characterization of the main structural, thermal and mechanical properties, which afterwards affect drastically to the packed bed thermal performance. Furthermore, considering that such solid materials operate in direct contact with

the heat transfer fluid, the stability and durability of the selected materials and the most usual heat transfer fluids is also addressed.

Second, a complete thermo-fluidic performance analysis is carried out over different packed bed designs implementing the mentioned selected materials. This study is accomplished by means of the development of an *ad hoc* physical model accounting for the most representative heat transfer and fluid flow mechanisms associated to the investigated storage configuration. After guaranteeing its accuracy with its exhaustive validation using experimental data, this model is used to obtain a complete design and optimization guideline of the main operational parameters governing the thermal performance of this type of TES systems.

Finally, the realistic deployment of a packed bed TES system based on the investigated materials in three different industrial environments is analysed. In particular, its integration in the heat recovery from the exhaust gases of a steelmaking furnace, in a compressed air energy storage plant and in a linear-Fresnel-type concentrated solar power plant is investigated following the previously obtained design and operation guideline.

Overall, the results obtained in this thesis demonstrate the viability of the packed bed TES solution in a wide range of operational conditions and implementation environments. The introduction of a new generation of low-cost materials for storage has revealed a new opportunity window able to provide a high temperature storage alternative with enhanced capabilities. The performed analysis has also shown the importance of a complete optimization design process in order to unlock the full potential of this TES concept. In this line, this work has clearly shown that an optimized balance among the storage material, operational conditions and design parameters of the packed bed can lead to an unprecedented performance, able to overcome the usual limitations of this sensible TES alternative.

Resumen

El almacenamiento de energía térmica se muestra como un elemento decisivo para lograr una gestión sostenible y eficiente de cualquier proceso térmico. Las limitaciones termodinámicas intrínsecas asociadas a cualquier sistema térmico, tales como la indisponibilidad de una fuente de calor apropiada, pérdidas térmicas o eficiencias cíclicas mejorables, justifican la utilización de sistemas de almacenamiento térmico. En la práctica, numerosos procesos industriales muestran oportunidades sustanciales de mejora de acuerdo con dichas limitaciones. En este sentido, la producción eléctrica termosolar, los procesos industriales con una demanda intensiva de calor (acerías, vidrieras, cementeras etc.) o el almacenamiento energético en aire comprimido son ejemplos representativos con un gran potencial de mejora.

Sin embargo, aunque la integración de soluciones de almacenamiento térmico puede ser una solución efectiva a nivel conceptual, su implantación en entornos industriales reales debe satisfacer requisitos muy restrictivos desde el punto de vista tecno-económico. Teniendo esto en cuenta, la búsqueda de tecnologías con un alto rendimiento y un bajo coste se ha convertido en una de las principales prioridades de las comunidades científica e industrial. De entre los diferentes conceptos de almacenamiento térmico, la solución de lecho fijo ha sido identificada como una tecnología muy prometedora. Su gran flexibilidad operacional, relativa simplicidad de implementación, alto rendimiento térmico e innata eficacia tecno-económica, le confieren un interés particular.

Teniendo en cuenta lo anterior, el objetivo de esta tesis es el estudio en profundidad de la solución de almacenamiento en lecho fijo para obtener una prueba de concepto de esta tecnología. Para tal fin, se presenta un análisis completo a diferentes niveles, imprescindibles para garantizar un desarrollo exitoso de esta alternativa de almacenamiento de calor. En primer lugar, se identifican nuevas familias de materiales cerámicos de bajo coste, como la escoria de acería o materiales naturales (magnetita), lo que asegura una solución económicamente competitiva y con un rendimiento mejorado a altas temperaturas de operación. De manera práctica, el potencial de este concepto de almacenamiento se demuestra a través de un análisis detallado de los materiales

propuestos, incluyendo la caracterización de sus principales propiedades estructurales, térmicas y mecánicas, las cuales afectarán drásticamente al comportamiento del lecho. Además, teniendo en cuenta que dichos materiales sólidos operan en contacto directo con el fluido caloportador, este trabajo también aborda la investigación de su estabilidad y durabilidad con los fluidos caloportadores más habituales. En segundo lugar, se presenta un análisis exhaustivo del comportamiento termo-fluídico sobre los diferentes diseños propuestos implementando los materiales investigados. Este estudio se lleva a cabo mediante el desarrollo de un modelo físico *ad hoc,* que contempla los mecanismos de transferencia de calor y dinámica de fluidos mas representativos asociados a la configuración de lecho fijo. Tras garantizar su precisión a través de una validación exhaustiva utilizando datos experimentales, el modelo se emplea para obtener una guía de diseño y operación de los principales parámetros que gobiernan el comportamiento térmico de los sistemas investigados.

Finalmente, este trabajo también analiza la integración de sistemas de almacenamiento en lecho fijo basada en los materiales estudiados en tres aplicaciones industriales, siguiendo la guía de diseño previamente obtenida. Estas aplicaciones contemplan la recuperación de calor de los gases de salida del horno una acería, en una planta de almacenamiento de energía en aire comprimido y en una central eléctrica termosolar con tecnología de espejos Fresnel.

Los resultados obtenidos en este trabajo de tesis demuestran la viabilidad del lecho fijo como solución para el almacenamiento térmico en un amplio rango de condiciones operacionales y entornos de implantación. La introducción de nuevos materiales de bajo coste ha revelado una oportunidad innovadora para proporcionar sistemas a alta temperatura con capacidades mejoradas. El análisis realizado también muestra la importancia de un proceso completo de optimización para extraer todo el potencial que el lecho fijo puede ofrecer. En esta línea, este trabajo indica claramente que un equilibrio optimizado entre el material de almacenamiento, las condiciones operacionales y los parámetros de diseño puede conducir a un rendimiento prometedor, capaz de superar las limitaciones habituales de esta alternativa de almacenamiento de calor sensible.

Laburpena

Prozesu termiko baten kudeaketa iraunkorra eta eraginkorra lortzeko bidean, energia termikoaren biltegiratzea elementu erabakigarri gisa aurkezten da. Edozein sistema termiko batek dituen berezko muga termodinamikoek, hala nola, bero iturri egoki baten eskuragarritasun ezak, bero galerak edo hobetu daitezkeen zikloen eraginkortasunak, bero biltegiratze sistemaren inplementazioa arrazoitzen dute. Praktikan, aipaturiko mugen aurrean funtsezko hobekuntza aukerak planteatzen dituzten prozesu industrial ugari aurki daitezke. Zentzu honetan, termo-eguzki ekoizpen elektrikoa, beroaren eskari intentsiboa duten prozesu industrialak (altzairutegiak, beirateak, zementu-fabrikak, eta abar.) edo aire konprimatu bidezko metatze energetikoa adibide adierazgarriak dira, oraindik hobekuntza ahalera handia dutelarik.

Hala ere, beroaren biltegiratze sistemen integrazioa, kontzeptu mailan, konponbide eraginkorra izan daitekeen arren, ikuspuntu tekno-ekonomikoari erreparatuz, baldintza oso murriztaileak bete behar ditu ingurune industrial erreal batean inplementatu ahal izateko. Hau kontutan hartuta, errendimendu altuko eta kostu baxuko teknologia bilaketa komunitate zientifiko eta industrialaren lehentasun nagusienetariko bat bihurtu da. Beroaren biltegiratze kontzeptu ezberdinen artetik, ohantze finkoa etorkizun handiko teknologia bezala identifikatu da. Bere eragiketa malgutasun handiak, inplementazio sinpletasun erlatiboak, errendimendu termiko altuak eta berezko eraginkortasun tekno-ekonomikoak, interes berezia ematen diote.

Aurrekoa kontutan hartuta, tesi honen helburua ohantze finkoko biltegiratze sistemaren ikaskuntza sakona egitean datza, teknologia honen proba kontzeptual bat lortzeko xedearekin. Horretarako, maila ezberdinetan egindako analisi sakon bat aurkezten da, biltegiratze sistema alternatibo honen garapen arrakastatsua bermatzeko. Lehenik, kostu baxuko material zeramikozko familia berriak identifikatu dira, altzairu-zepa edota material naturalak (magnetita) bezalakoak, ekonomikoki lehiakorra den soluzio bat eta operazio tenperatura altuetan errendimendu hobeak ziurtatzen dituena. Praktikan, biltegiratze kontzeptu honen ahalmena proposaturiko materialen analisi zehatz baten bidez frogatzen da, propietate mekaniko eta termiko baita egiturazko propietate nagusien

karakterizazioa barne, zeinak eragin garrantzitsua izango duten ohantze finkoaren portaeran. Gainera, aipaturiko material solidoak, bero-eramailea den fluidoarekin zuzeneko kontaktuan lan egiten duela kontuan hartuta, bi materialen arteko egonkortasuna eta iraunkortasunaren ikerketa egin da, ohikoenak diren fluido bero-eramaileak aztertuz. Bigarrenik, portaera termo-fluidikoaren analisi zehatza aurkezten da, proposatutako diseinu ezberdinetan eta ikertutako materialak erabiliz. Ikerketa hau *ad hoc* egindako eredu fisiko baten garapenaren bidez burutzen da, ohantze finko konfigurazio bati dagozkion bero transferentzia eta fluidodinamika mekanismo adierazgarrienak kontutan hartzen dituelarik. Datu esperimentalen bidezko balioztatze zehatz baten bidez doitasuna bermatu ondoren, eredua ikertutako sistemen portaera termikoa bideratzen duten parametro nagusien diseinu eta operazio gidaliburu bat lortzeko erabili da.

Azkenik, lan honek ere ohantze finkoan oinarritutako biltegiratze sistemen integrazioaren analisia egiten du, hiru aplikazio industrialetan, aurretik ikertutako materialetan oinarrituta eta lortutako diseinu gidaliburuari jarraituz. Aplikazio hauek altzairutegi bateko labearen irteerako gasen bero berreskurapena, aire konprimatu bidezko energia biltegiratzea eta Fresnel motako ispiluen termo-eguzki zentral bat ere jasotzen dute.

Tesi-lan honetan lortutako emaitzek ohantze finkoaren proposamenaren bideragarritasuna guztiz egiaztatzen dute, bero biltegiratze kontzeptu bezala, eragiketa-baldintza baita inplementazio ingurune zabal bat aintzat harturik. Kostu baxuko material berrien ahalerak, edukiera hobeak dituzten tenperatura altuko sistemen aukera berriztatzaileak erakutsi ditu. Egindako analisiak, erabateko optimizazio prozesua egitearen garrantzia erakusten du ere, ohantze finkoak eskaini dezakeen ahalera guztia ikus dadin. Bide honetan, lan honek argi eta garbi azaleratzen du biltegiratze materialaren, eragiketa-baldintzen eta diseinu parametroen arteko orekak errendimendu oparoa eskaintzen duela, ohikoak diren bero sentsible bidezko biltegiratze sistemek dituzten mugak gainditzeko gai izanik.

Nomenclature and symbols

Abbreviations

A-CAES	Adiabatic compressed air energy storage
BAT	Best available technology
BF	Blast furnace
BFS	Blast furnace slag
BOF	Basic oxygen furnace
BOFS	Basic oxygen furnace slag
BSE	Back-scattered electron
BSED	Back-scattered electron detector
CAES	Compressed air energy storage
CFD	Computational fluid dynamics
CSP	Concentrated solar power
D-CAES	Diabatic compressed air energy storage
DEM	Discrete Element Method
DSC	Differential scanning calorimetry
EAF	Electric arc furnace
EAFS	Electric arc furnace slag
EDX	Energy dispersive X-ray
EES	Electrical energy storage
FCC	Face centred cubic
FTIR	Fourier transform infrared
HCP	Hexagonal close packing
HTF	Heat transfer fluid
ICP	Inductively coupled plasma
IEA	International energy agency
LCOE	Levelized cost of electricity
LFA	Laser flash apparatus
LTE	Local thermal equilibrium
LTES	Latent thermal energy storage
MAE	Mean absolute error
MDSC	Modulated differential scanning calorimetry

NMR	Nuclear magnetic resonance
OES	Optical emission spectroscopy
OHF	Open hearth furnace
ORC	Organic Rankine cycle
PCM	Phase change material
PHES	Pumped hydroelectric energy storage
PISO	Pressure-implicit with splitting of operators
PRESTO	Pressure staggering option
PV	Photo-voltaic
RMSD	Root mean square deviation
SE	Secondary electron
SEM	Scanning electron microscopy
STA	Simultaneous thermal analysis
STES	Sensible thermal energy storage
TCS	Thermochemical energy storage
TES	Thermal energy storage
TGA	Thermo-gravimetric analysis
XRD	X-ray diffraction
XRPD	X-ray powder diffraction

Nomenclature

A	Area (m^2)
A_{fs}	Interfacial area density (m^{-1})
A_T	Modulation amplitude (K)
B	Exergy (J)
b	Interplanar distance (nm)
C_{ij}	Inertial resistance tensor (m^{-1})
C_2	Inertial resistance factor (m^{-1})
c_p	Specific heat at constant pressure ($J \cdot kg^{-1} \cdot K^{-1}$)
d	Diameter (m)
E	Energy (J)
e	Thickness (m)

F_{ij}	Permeability tensor (m^{-2})
$\vec{g}$	Gravitational acceleration (m/s^2)
Gr_L	Tank Grashof number ($g\cdot \rho^2\cdot \omega\cdot(T_{ext}-T_{amb})\cdot L^3\cdot \mu^{-2}$) (-)
H	Enthalpy ($J\cdot kg^{-1}$, J)
h_{fs}	Heat transfer coefficient between fluid and solid ($W\cdot m^{-2}\cdot K^{-1}$)
h_{loss}	Heat transfer coefficient of thermal losses ($W\cdot m^{-2}\cdot K^{-1}$)
h_{rs}	Radiation heat transfer coefficient between solid surfaces ($W\cdot m^{-2}\cdot K^{-1}$)
h_{rv}	Radiation heat transfer coefficient between voids ($W\cdot m^{-2}\cdot K^{-1}$)
h_w	Heat transfer coefficient between packed bed and tank wall ($W\cdot m^{-2}\cdot K^{-1}$)
K	Calibration constant
k	Thermal conductivity ($W\cdot m^{-1}\cdot K^{-1}$)
k_e^o	Stagnated effective thermal conductivity ($W\cdot m^{-1}\cdot K^{-1}$)
L	Tank length (m)
l	Sample thickness (m)
Ma	Mach number ($v\cdot v_{sound}{}^{-1}$) (-)
M	Molecular weight ($kg\cdot mol^{-1}$)
m	Mass (kg)
$\dot{m}$	Mass flow rate ($kg\cdot s^{-1}$)
n	Number of equivalent contact points for the semispherical surface of a particle
Pe	Peclet number (Re·Pr) (-)
Pr	Prandtl number ($c_p\cdot\mu^{-1}\cdot k^{-1}$) (-)
p	Pressure (Pa, bar)
Q	Heat (J)
R	Ideal gas constant ($J\cdot mol^{-1}\cdot K^{-}1$; $J\cdot kg^{-1}\cdot K^{-1}$)
r	Radio (m)
Ra_L	Tank Rayleigh number ($g\cdot \rho\cdot \omega\cdot(T_{ext}-T_{amb})\cdot L^3\cdot \mu^{-1}\cdot \alpha^{-1}$) (-)
Re_p	Particle Reynolds number ($v_\infty\cdot\rho\cdot d_p\cdot\mu^{-1}$) (-)
S_i	Momentum source term ($kg\cdot m^{-2}\cdot s^{-2}$)
S^H	Enthalpy source term ($W\cdot m^{-3}$)
S	Entropy ($J\cdot K^{-1}$)
T	Temperature (K)
t	Time (s)

U	Voltage (v)
V	Volume (m^3)
v	Velocity ($m \cdot s^{-1}$)
v_∞	Superficial velocity ($m \cdot s^{-1}$)

Greek letters

α	Thermal diffusivity ($m^2 \cdot s^{-1}$)
α_L	Linear thermal expansion (K^{-1})
β	Average inter-particle distance (m)
γ	Surface tension ($N \cdot m^{-1}$)
δ	Specific tolerance (%)
ε	Void fraction (-)
ε_s	Solid emissivity (-)
ζ	Ratio between the solid length affected by thermal conductivity and the particle diameter (-)
η	Efficiency (-)
θ	Angle (°)
κ	Ratio between solid and fluid thermal conductivities ($k_s \cdot k_f^{-1}$) (-)
λ	Wavelength (nm)
μ	Dynamic viscosity ($kg \cdot m^{-1} \cdot s^{-1}$)
ρ	Density ($kg \cdot m^{-3}$)
σ	Permeability factor (m^2)
σ_c	Compression strength (MPa)
$\bar{\bar{\tau}}$	Stress tensor (Pa)
ϕ	Angular frequency (s^{-1})
φ	Heating rate ($K \cdot s^{-1}$)
ψ	Effective fluid film thickness (m)
ω	Thermal expansion coefficient (K^{-1})

Subscripts

amb	Ambient
B	Exergy
c	Charge

d	Discharge
eff	Effective
ext	External
f	Fluid
fs	Fluid-solid
g	Gas
ins	Insulation
l	Liquid
max	Maximum
p	Particle
ref	Reference
s	Solid
t	Tank
tol	Tolerance
w	Wall
1	Top
2	Bottom
I	First thermodynamics law

List of Figures

List of Tables

Chapter 1:

Introduction

1 Introduction

Everything in the known universe, and maybe also in the not known one, is energy. It was there from the beginning of time, from the last 13.8 billion years, filling our empty universe with light, matter or heat. Even the fundamental interactions forces, such as electromagnetic, weak, strong and gravitation, are nothing more than different manifestations of energetic states fighting for equilibrium. Of course, the implications of simple principles like the energy conservation of a system can attain a huge and highly sophisticated physical formulation.

The relation of the different consequences and manifestations of energy operating in diverse systems, from the formation of a planet or the human biology to the tireless travel of a neutrino, with the energy conservation idea is one of the pillars of the understanding of whatever surrounding us. No matter the length or time scale, all is about energy and its evolution. As a result, it is not an easy task to describe in one paragraph the effort needed to understand this universal fact. Maybe it is enough to mention that few equations in physics are more famous than the Energy-Mass equivalence established by A. Einstein in 1905, and previously formulated as a paradox by H. Poincaré, $E=mc^2$. This simple expression contains the scientific and human knowledge legacy of thousands of years, from the electromagnetic field theory of J.C. Maxwell to the general gravitation laws announced by I. Newton.

But the story about energy is not only about its conservation and different appearances. Going through the human nature and its necessity of exploring the brand new acquired knowledge about energy, some basic sciences were rapidly developed. Thermodynamics and, after, statistical mechanics were the theories able to explain the concepts about energy and its implications, such as order/disorder, entropy, micro-scale interactions, energy exchanges etc. Thermodynamic equilibrium: this is another example of a simple idea underlying the universal dynamics. The search of this peaceful state is a continuous battle of all the known systems in the universe. In this path, with the final goal of attaining such a harmonious coexistence between all the existing things, some unexpected phenomena occur, such as the quantum Hall effect, the Seebeck effect, the Peltier effect and the Thomson effect. These effects can be interpreted as a reaction to a

perturbation causing a state to be separated from equilibrium. As usually happens, the most interesting things occur when the equilibrium is far. The most dramatic corollary of this idea is the death state of the universe predicted by Lord Kelvin. In this full universe at equilibrium state, no energy could flow to generate any useful work. As a consequence, no useful energy would be available with the corresponding terrible victory of entropy (chaos) over energy (order).

The rapid development of the mentioned concepts led to a new science for a new view of the universe. New technical developments such as heat engines, the steam cycle or the efficiency rules of thermally operated engines established by S. Carnot soon arose. The interpretation of the energy transfer in terms of heat and work cannot be separated from the mentioned scientific and technical frame. There is no need to mention the technical advances derived from Thermodynamics. Even if the societal changes are undeniable, we still are living in a society based on the industrial revolution of the XIX century reinvented to account for the information revolution. In this frame, the human evolution is, and will be, bounded to the story of energy. Faster, better, stronger. How to survive in this cold and empty universe taking the opposite direction, at least locally, to the entropy? The answer was clear from the beginning: consuming an increasing amount of energy, available close to our habitat. One can search on the first existing documentary records and will obtain a clear view of the human story of energy. The management and storage of the energy, mainly coming from the solar source, was the key. First, photosynthesis was enough. The plants are really good on this, so, while they did the capturing and storing work, we could take advantage of this with a vegetarian diet. However, if the human society presents and increasing work demand, looking for the improvement of its survival conditions, the need of energy is also equivalent. Following this logic, the search of more concentrated energetic sources soon started. A change on the diet from vegetarian to include meat is only one example of this energetic demand. What come after is well known. Energy became a priority for almost everything, from heating to the creation of complex societies full of services making the life of people easier.

Thousands of years after the energy competition started, today, we still remain searching more concentrated energetic sources able to provide the energetic

demand of modern societies. Regardless of whether this model is sustainable or not, the complexity on this search has lead to the development of highly sophisticated energetic sources, such as nuclear, or even nuclear fusion sources which are currently under development. Everything corresponds to the same necessities and to the same logic: how to extract the energy stored on different materials, sources or processes. This is the cost of our battle against entropy and all the solutions are welcome. New energetic solutions, energy capture and storage alternatives help to enhance our life quality in a sustainable manner. The success on overcoming this challenge will not only be the success of our society, but also the one of the generations to come.

1.1. Energetic and storage contexts overview

Energy is intrinsically associated to the development of human societies. The enhancement of our life quality towards the availability of better services, life comfort, transportation, industrial activities or the demand of a larger population requires a continuous search of new solutions able to supply a massive amount of energy, according to the demand. As a consequence, its production, management and distribution are one of the most concerning problems at global scale. In this line, the worldwide increasing electric power demand has become in an unprecedented challenge that requires appropriate solutions from different involved agents, from the scientific and technologic level up to the change and adaptation of new common energetic policies. According to the *International Energy Outlook 2016* [1], in 2012 around 549 quadrillion BTU (161 PWh) were consumed worldwide. In addition, it is estimated a considerable growth of this demand by 2040 when, 814 quadrillion BTU (239 PWh) are calculated to be consumed. This supposes an increment of around 48% in the energetic demand. The evolution of the energy consumption from 1990 to 2012 and the predictions from this date to 2040 are presented in Figure 1.1.

The traditional approach to solve this energy demand has been, historically, the deployment of fossil sources such as coal, gas or oil. Although the access to fossil energy sources represented one of the major revolutions in our history, the continuous increasing energetic dependence of advanced societies are currently

reaching a non-sustainable scenario where the drawbacks of this massive exploitation are manifesting severe environmental hazards. Quantitatively, attending to how this energy is produced, according to the *International Energy Agency* (IEA) [2] in 2014 the production from fossil fuels (oil, coal and natural gas) accounted for 81.2%. In addition, nuclear supposed a 4.7%. A comparison of the sources used in the energy production between 1971 and 2014 is presented in Figure 1.2.

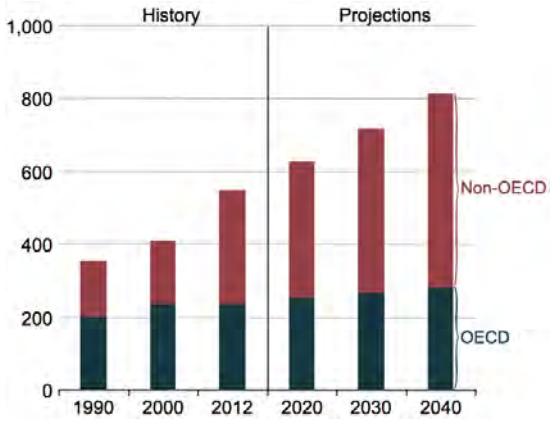

Figure 1.1. World energy consumption, 1990-2040 (quadrillion BTU) [1].

The progressive depletion of the conventionally exploited fossil resources [3,4], together with the associated pollution or greenhouse gas emission problems [5], are leading to an increasing interest in the development of alternative energy production methods. In this line, the increasing emission of CO_2 represents one of the major challenges that our societies must solve. Several examples can be found at a global scale, where the emission of massive amounts of hazardous greenhouse gases derived from heavy industrial activities or transportation, are causing a severe environmental impact. One example of this undesirable human action is super-populated and super-polluted cities, where the presence of NO_x and other contaminant agents are reaching dramatic levels. Another clear impact of the greenhouse emissions derived from the action of advanced societies is the climate change. The increasing acceptance of this global effect as a consequence of the exploitation of fossil resources is currently a worldwide fact, which needs to be urgently addressed. The inclusion of this topic as a priority in the main international agenda of the most representative forums is also a good example of

the paramount importance of this issue. Derived from the international policymaking and from global agreements, some important actions have been taken in order to palliate and control the impact of fossil source energy exploitation. One of the most important approaches to this problem has been the establishment of a common actuation protocol with the goal of reducing and controlling the greenhouse gas emission by the advanced industrial and societal activities, known as *Kyoto protocol* [6]. Even if the application of this protocol has derived on immediate actions such as the search of sustainable energetic sources or the drastic limitation on the emission of hazardous contaminants, the successful solution to the energy scenario and its negative environmental impact is still far.

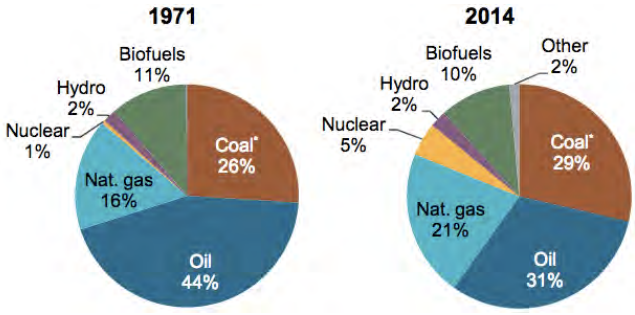

Figure 1.2. Total energy supply by fuel [2].

In agreement with this reinforced effort to search a sustainable and green solution to the energetic scenario, renewable energies and the optimization of intensive energy demanding processes, such as heavy industries or power generation plants play a capital role. The interest on these topics from the international scientific community has suffered a drastic increase in the last years. As a direct consequence of this huge research effort, new solutions have been successfully proposed and implemented covering the complete value chain of the energetic problem: generation, storage, management and final distribution.

As mentioned above, one of the most promising solutions to reach a satisfactory energy supply through sustainable and green procedures, maintaining a limited and small environmental impact, are the renewable energy sources.

Many clean production alternatives have been proposed, and some of them extensively exploited in the last years. The most representative ones are hydroelectric, wind and solar power production (see Figure 1.3). Although the

exploitation of these sources has been very limited in comparison to fossil alternatives, in the last decade renewable sources have experimented a noticeable increase, reaching to around 40% of the total power production in some countries such as Spain [7]. Worldwide, wind power is one of the most exploited renewable energies with a total installed power of 433 GW [8]. Solar source has also been identified as a key energy to contribute in a decisive manner to the overall energy production scheme. In this line, photovoltaic electric generation has been of particular importance, opening new power generation alternatives and markets suited for self-generation and also for a wider industrial deployment.

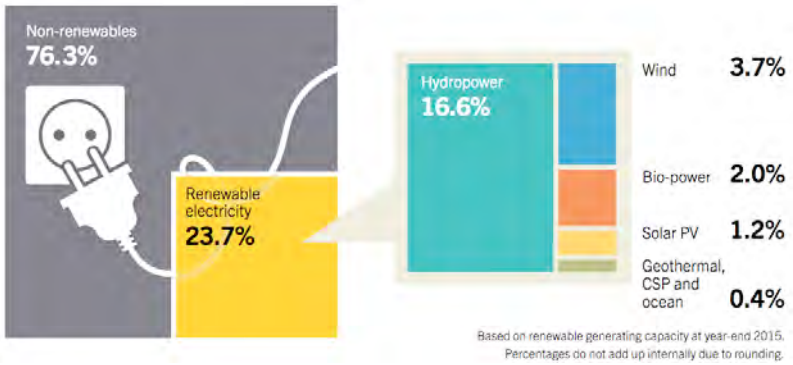

Figure 1.3. Estimated energy share of global electricity production (end 2015) [8].

Solar thermal power production has also demonstrated a very appropriate capacity to contribute in the global energy generation frame. This production technology is currently at a very active development stage and it has shown a clear interest in areas where the solar irradiation levels are high enough. Its implementation has been extensive in countries such as Spain, where the total installed generation power was around 2.5 MW in 2013 [7].

However, renewables still need to overcome many challenges on their path to become fully competitive with fossil source energies. The main ones are their associated high cost, and the management of the energetic source intermittency [9], i.e. sun, wind, etc. One possible solution to deal with intermittences of the primary energetic input is the energy storage. This concept represents a direct strategy to eliminate the fluctuations of the renewable source. The underlying idea is to capture the available excess of energy when it is possible, and to use it when the primary input does not permit full power production. This concept represents

a successful solution, which permits to provide stable power on demand even with low values of the primary renewable source or even null input.

Table 1.1. Energy storage concepts and costs [10-13].

	Energy storage concept	Capacity cost ($/kWh)	Efficiency (%)
Electrical	Sealed lead acid battery	333	80
	Lithium ion battery	600	85
	Supercapacitor	10000	95
	High-speed flywheel	1600	95
	Pumped hydroelectric	75	85
	Compressed air	55	60-80
Thermal	Double-tank indirect	89	97
	Double-tank direct	50	97
	Packed bed thermocline	34	97

Different energy storage alternatives have been proposed and implemented in this frame. Considering that the usual final objective of the renewable production is the electricity generation, one possible direct alternative is the electrical energy storage (EES). Such systems enable electricity to be produced at low demand or low generation cost periods, or from intermittent energy sources. Consequently, EES is presented as a strategic and necessary component to decoupling such power sources with the time-requirements of the energy production.

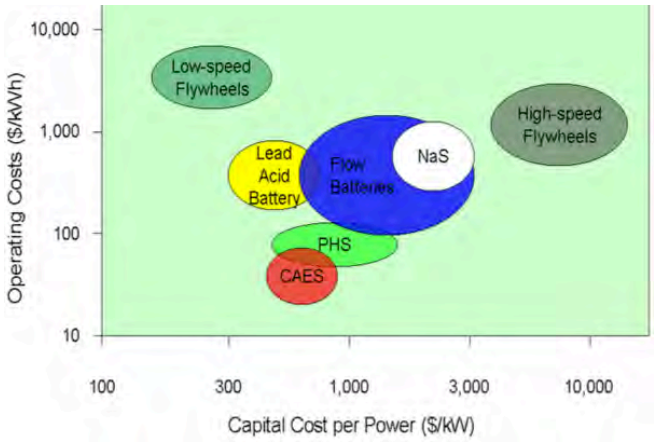

Figure 1.4. Comparison of various EES technologies in capital investment and operating cost [10].

Currently, different EES concepts are available. Some of the most representative ones are included in Table 1.1 together with their cost per kWh [14]. In addition, the capital versus the operation costs is included in Figure 1.4. Finally, the tendency of the efficiency achieved in these storage concepts with the advances of each technology is presented in Figure 1.5.

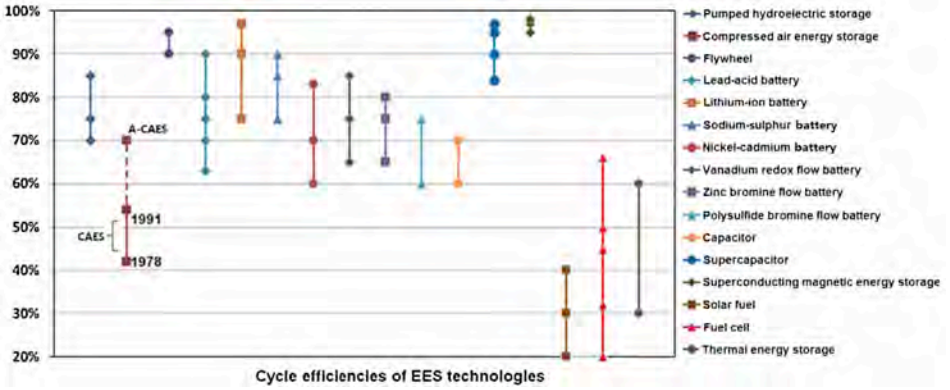

Figure 1.5. Comparison of various EES technologies in cycle efficiency [15].

Even if many EES alternatives have been introduced, only two are, nowadays, applicable for energy storage at large scale (above 100 MW in one single unit): pumped hydroelectric energy storage (PHES) and compressed air energy storage (CAES) [10]. Currently, the worldwide installed EES capacity is dominated by PHES. With an installed capacity at the end of 2015 of up to 145 GW, PHES represents about 97% of the global EES capacity [8]. The power ratings of the existing PHES plants are in the range of 1 MW up to 3 GW with a round efficiency up to 85% [15]. A schematic view of how the EES capacity is shared between the different available technologies is presented in Figure 1.6. The included data corresponds to the year 2011.

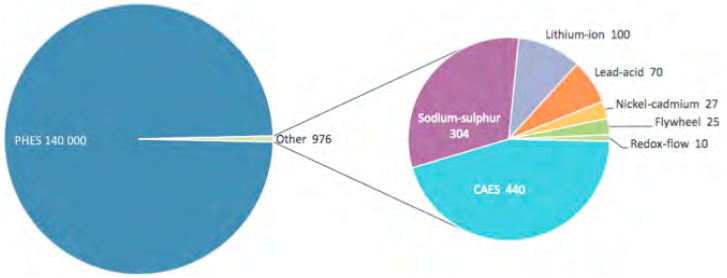

Figure 1.6. Global installed grid-connected electricity storage capacity (MW) [16].

Despite PHES is a well-known mature and efficient solution it also presents some limitations. Among them, the relatively low energy density, the scarcity of available sites for two large reservoirs and one or two dams, a long commissioning time (typically ~10 years) and high environmental impact (i.e. removing trees prior to the reservoir being flooded). These drawbacks have introduced CAES as an attractive option in the last years (see section 1.4.3).

Attending to the maturity of most common EES technologies, in Figure 1.7 their status versus the capital requirements and the technological risks is shown. As already mentioned at the large-scale, PHES is the most commercialized concept. As it is introduced in section 1.4.3, CAES is still at a demonstration status and new configurations such as adiabatic-CAES at a research stage.

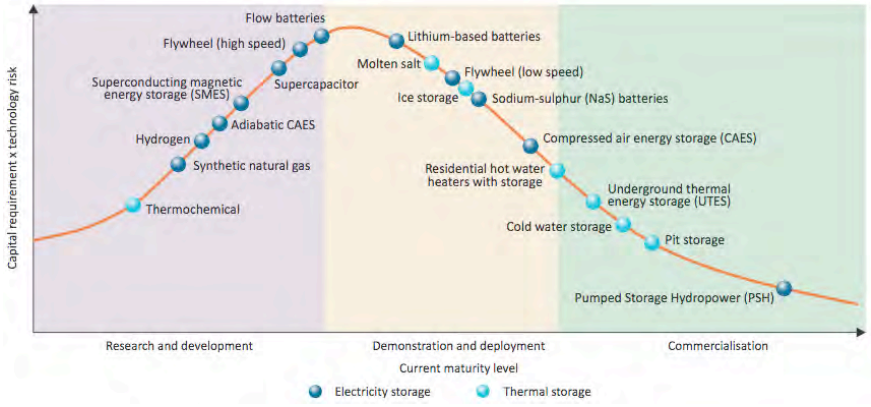

Figure 1.7. Maturity of energy storage technologies [17-19].

Although the EES is the most mature and extensively implemented energy storage alternative, it is not the only solution. Considering that most of the power production applications are based on implementation of thermal engines such as steam turbines, Rankine cycles, etc. the storage of energy in form of heat results of paramount importance. Taking into account that the main subject of this thesis corresponds to thermal energy storage (TES), the state-of-the-art of this technology is described in detail in the next section.

1.2. Thermal energy storage (TES)

Heat is, together with work, one of the basic forms of energy. The First Law of Thermodynamics establishes that the change of the internal energy of an isolated

system can only be generated by heat dissipation/absorption and by work. As a consequence, any useful work extracted from a thermal process involves necessarily the absorption of a certain amount of heat that is partially converted into work, as established by the Second Law of Thermodynamics, depending on the overall work efficiency of the system. Based on the fundamental nature of heat as energetic source, many thermally powered systems are widely exploited in the energy and power production frame. As an example, thermal engines such as steam, gas turbines, combustion or diesel engines and Rankine, Otto or Diesel cycles are the basis of the current power production.

In this frame, considering the importance of heat as a primary energy, the optimization of any thermal energy driven process becomes of great importance in order to increase the overall efficiency of any thermal system. Consequently, heat must be identified as a valuable resource able to give a determinant added value to any thermal process. Based on this premise, as mentioned in the previous section, this thesis work is focused on thermal energy storage and its implications on relevant application areas such as solar-thermal renewable power generation, industrial waste heat recovery or adiabatic compressed air energy storage. In all cases, the vision of heat as a valuable asset leads to the basic concept proposed and developed in this work, thermal energy storage.

With the objective of storing heat, different physical principles can be used. Among the most extended ones, due to their practical implementation, three general methodologies have been introduced: sensible, latent or thermochemical heat storages. In the following each of them is described in detail.

1.2.1. Sensible thermal energy storage (STES)

The underlying physical mechanism of sensible heat storage is the variation of the temperature of a selected storage medium, a solid, liquid or gaseous material. In other words, the stored energy is sensible through a temperature change. Considering that STES, and any other heat storage alternatives, are based on a storage material selection, the corresponding thermophysical properties of such material, govern the main storage characteristics in agreement with equation:

$$E = V \cdot \rho \cdot c_p \cdot \Delta T; \tag{1.1}$$

where, V, ρ and c_p are the storage material volume, density and specific heat respectively, and ΔT is the temperature variation suffered by the material.

According to eq. (1.1), the maximization of the sensible storage capacity depends directly on the density and specific heat of the selected storage material. As a consequence, large values of the mentioned magnitudes are promoted on the search of suitable storage materials. In addition, the capacity is proportional to the temperature change, which is usually maximized based on the operational temperature range of the storage material and the particular application deployed. Considering all the mentioned boundaries, and operational considerations, STES is the lead concept implemented in the vast majority of industrial and commercial applications. Its relative simplicity and effectiveness are found to be determinant on the industrial deployment of this storage technology, which otherwise, have been the key factors on the growth and development of STES. A good example of the maturity degree and expansion of this storage alternative is the concentrated solar power (CSP) production industry, which has identified STES as a core strategic approach to the definitive boost of this technology.

Although, in principle, any state of aggregation of matter can be exploited for STES, solids and liquids are the most commonly implemented materials. Liquid fluids are, by far, the most implemented STES solutions, such as water [20], mixtures of molten nitrate salts [21] and organic/synthetic thermal oils [22].

As mentioned above, even if CSP is one of the most important opportunity windows for STES [23-25], industrial process heat recovery is also an attracting application field with an increasing interest [26-28]. In all these cases the most implemented storage technology involves molten nitrate salts in a double-tank configuration [13]. Regarding the storage material, the leading candidate is the commercially called *Solar salt*, a binary salt with a chemical formulation of 60 wt% of $NaNO_3$ and 40 wt% of KNO_3. According to the main optimization boundaries established above, in addition to the mentioned large density and specific heat, these salt mixtures must meet severe quality, safety and operational standards in terms of low viscosity, low vapour pressure, low chemical reactivity and low cost.

Many examples of large-scale industrial exploitation of nitrate molten salts as STES material can be found in the CSP environment. Among them, Andasol I

(Granada, Spain) with 7.5 hours of storage (1.01 GWh), Gemasolar (Sevilla, Spain) with 15 hours of storage, Noor 1 (Ouarzazate, Morocco) with 3 hours of storage or Crescent Dunes (Tonopah, EEUU) with up to 10 hours of storage (1.1 GWh) are examples of this technology. A picture of the TES unit based on molten salt double-tank solution of Andasol I is shown in Figure 1.8.

Figure 1.8. Double-tank TES system in the CSP plant of Andasol I [29].

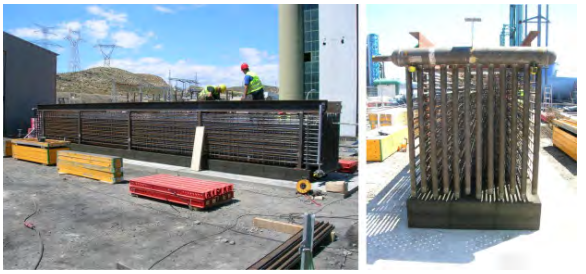

(a)

(b)

Figure 1.9. STES based on concrete as storage medium: a) facility at DLR [30,31] and b) prototype at Masdar Institute [32].

Attending to the exploitation of solid STES materials, the most investigated solutions consist in concrete blocks. In this field, two main experiences are reported in literature. The first one corresponds to the facility designed by DLR in 2006 [30,31] and shown in Figure 1.9a. The second, and more recent, is the one

constructed and tested by EnergyNest in Masdar Institute (Figure 1.9b) [32]. Both STES devices consist in a concrete block with internal steel piping enclosing a thermal oil flow, used as heat carrier, to supply/extract the heat from the storage unit. These two facilities have permitted the experimental demonstration of this storage technology as a modular and easily scalable STES concept.

As a summary, Table 1.2 compiles the energy density, thermal conductivity and operating temperature range of the most widely proposed STES solid and liquid materials.

Table 1.2. Materials used in STES applications.

Material	Energy density ($kWh \cdot m^{-3} \cdot K^{-1}$)	Thermal conductivity ($W \cdot m^{-1} \cdot K^{-1}$)	Operating temperature (°C)	Ref.
High temperature concrete	0.7	1.0	up to 350	[30]
Reinforced concrete	0.5	1.5	200-400	[33,34]
Heatcrete®	0.5-1	1.7-2.5	20 - 450	[32]
NaCl	0.5	7.0	200-500	[33,34]
Cast iron	1.1	37.0	200-400	[33,34]
Silica fire bricks	0.5	1.5	200-700	[33,34]
Solar salt	0.75	0.5	260-565	[35]
HITEC	0.78	0.6	142-454	[36]
HitecXL	0.85	0.5	133-500	[37]
Therminol VP1	0.52	0.1	12-400	[38]
Syltherm 800	0.40	0.1	R.T.-400	[39]
Delcoterm Solar E15	0.50	0.12	R.T.-320	[40]
Liquid sodium	0.31	71.0	270-530	[41]

Although sensible heat storage technologies show an important degree of maturity and are commercially available, they clearly demand a noticeable enhancement. In this line, the mentioned STES technologies present several shortcomings that should be overcome in the short term, according to the operational requirements of a new and enhanced energetic exploitation roadmap. Considering that most of the commercial sensible TES applications are based on

liquid materials, some limitations are derived from the narrow operation temperature range offered by usual liquids such as water or molten salts. The former needs the implementation of high-pressure systems, with the consequent technological difficulties. The second only permits its operation between 290-565 °C (*Solar salt*), which implies a huge effort avoiding the salt solidification, and limits the maximum operation temperature range. However, many research works have been presented in the last years aiming at finding new salt mixtures with enhanced thermal properties such as lower melting temperatures [42-44] and higher specific heat or thermal conductivity values [45,46]. In addition, the cost of the molten salts is highly expensive (around 625 €/t in the case of the *Solar salt* [47]), which drastically affects to the final cost and techno-economic efficiency of the overall energy management process.

In order to overcome the mentioned limitations of current STES technologies, different STES concepts have been proposed in the last years. The introduced innovations not only include the storage material or heat transfer fluids, but also the storage concept itself. Aligned with this idea, high temperature and cost effective materials have been identified as potential solutions for the new generation storage alternatives. As an example, the exploitation of air as heat transfer fluid [48-50] if introduced together with STES materials able to operate at temperatures above 600 °C can represent a breakthrough concept to overcome the current technological limitations. Together with the material enhancement, some authors have also introduced the solid packed bed storage concept [51-55]. This technology proposes the use of a packing of small solid particles forming a bed that performs as heat storage medium in a single-tank configuration. A hot/cold heat transfer fluid (liquid or gas) is interstitially circulated through the solid packing to exchange its heat content to/from the solid material. This STES concept is the core subject of the present work and the conceptual description as well as its state-of-the-art is discussed in section 1.3.

1.2.2. Latent thermal energy storage (LTES)

In addition to the sensible variation of the internal energy of a material associated to a temperature change (STES), isothermal or quasi-isothermal

internal energy involving mechanisms can also be exploited to store heat. In this frame, heat can be exchanged with a thermal system maintaining constant any of the thermodynamic variable magnitudes such as temperature, pressure or volume. The underlying exploited physical mechanism leading to the exchange of the internal energy of a material under isothermal conditions is based on its phase changes. In such processes, the internal energy of a thermodynamic system is not used to promote a temperature variation, but to rearrange its internal structure at a molecular or atomic level. This change is the result of the search of the equilibrium phase of the heat exchanging material, according to the minimization of the Gibbs energy. As a consequence, the thermal energy is used to generate a different molecular or atomic arrangement by means of the latent heat involved in the corresponding phase change. Based on this definition, only first order phase transitions can be exploited since a latent heat is involved in the transformation process. Other phase change mechanisms such as higher order transitions cannot be considered for thermal storage, because no latent heat is involved. As an example, second order transitions such as paramagnetic-ferromagnetic phase transitions are not suited for TES. Examples of transitions with an associated latent heat able to exchange thermal energy, and exploited in TES applications are:

- Melting – Solidification ($Solid \leftrightarrow Liquid$): this phase change usually occur in a temperature range between 10 and 1500 °C, depending on the material. The volume change between the solid and liquid phases presents a controllable and predictable behaviour. The associated operation pressures also show controllable values, suitable for the practical implementation.
- Evaporation – Condensation ($Liquid \leftrightarrow Gas$): even if these phase changes show higher latent enthalpies when compared to solid-liquid transformations, the huge volume change between liquid and gaseous phase involves the implementation of very complex practical devices. As a consequence, this transition mechanism does not show a strong attractive for LTES applications.
- Vaporisation – Liquefaction ($Solid \leftrightarrow Gas$): solid-gas transitions show the same shortcomings of the liquid-gas ones with the additional disadvantage that most of these transformations are violent and very complex to control.

- Structural transition ($Solid \leftrightarrow Solid$): usually presents a limited latent heat value if compared to the rest of phase change mechanisms.

In all the mentioned phase change mechanisms, the exchanged energy with the transitional thermodynamic system can be described as follows:

$$E = m \cdot \Delta H_{latent}; \tag{1.2}$$

where, m is the mass of the material suffering the phase change and ΔH_{latent} the transition latent heat per unit mass.

The materials used in these applications are commonly called phase change materials, PCM. Considering eq. (1.2), the right selection of a PCM must include a large transition latent heat value. However, this is not the only requirement to perform a satisfactory PCM choice. In addition to the standard requirements applicable to any storage material, a PCM shall be selected based on the following criteria:

- The reversibility of the phase transition must be guaranteed in order to obtain a successful cyclic operation of the storage.
- The transformation temperatures, both on the heating and cooling processes, must meet the requirements of the selected storage application.
- As a consequence of the last requirement, the thermal hysteresis, subcooling or superheating effects suffered in the transition must be limited, controlled and reproducible.

Regarding the PCM selection, many materials have been proposed in the last years. In the low temperature range (melting points below 100 °C) different paraffin [56,57], fatty acids [58] or hydrated salts [59] with latent heats between 130 and 260 $J \cdot g^{-1}$ have been reported. In the same temperature range, recent investigations have proposed the use of sugar alcohols [60,61] such as erythritol or xylitol due to their high latent heats around 300-350 $J \cdot g^{-1}$. However, these materials present some shortcomings as large sub-cooling processes, which avoid reproducible melting/solidification performance of the PCM. Another associated problem of all the mentioned organic PCM materials is their intrinsic low thermal conductivity value [62], which leads to noticeable difficulties in their practical deployment. Many authors have presented different alternatives to overcome

these limitations such as their encapsulation [56, 63-65] or their insertion in carbon matrixes with the objectives of enhancing the thermal conductivity of the obtained composite material [66]. Above these temperatures (>100 °C), the available alternatives are limited. Some inorganic salts [67-69] and metal alloys [70,71] have been reported above this temperature. However, the main difficulty associated to these two PCM families, which has limited its deployment in real applications, is their high corrosiveness.

Even if LTES technology has been extensively investigated, there is a lack of experiences at industrial scale. Only a few number of facilities have permitted the demonstration of this concept at lab-scale. For example, Bayón et al. [72] presented experimental results of a 100 kW_{th} LTES system using an eutectic mixture of KNO_3 and $NaNO_3$ as PCM with expanded graphite fins for improving the thermal conductivity of the salt. The performed experiments of such facility were carried out under real operating conditions with steam produced by a parabolic-trough collector in the Plataforma Solar de Almería (PSA). Rozenfeld et al. [73], presented experimental measurements of a novel double-pipe unit with a helical fin attached in the internal pipe, throughout the heat transfer fluid flows. The PCM, commercial grade eicosane ($C_{20}H_{42}$), an organic compound with melting temperature of 36.7 °C, was located in the external part of the pipe. Blanco-Rodriguez et al. [74] published experimental results of an eutectic Mg and Zn alloy with a melting temperature around 340 °C. The used set up consisted of a shell and tube heat exchanger with the PCM on the shell side and a thermal oil in the internal axial tube, circulated at temperatures of 381 and 306 °C during the charge and discharge operations respectively.

Comparing STES and LTES principles the latter present two main advantages. On one hand, LTES systems show higher energetic density than STES, based on the usually large latent heat values. On the other hand, considering the isothermal nature of the mentioned phase transitions, PCM materials are able to supply or absorb thermal energy at constant temperature.

However, although the technologic advantages of LTES show a clear improvement in comparison with STES, some drawbacks limit the implementation of this storage technology. The first one is the higher cost of a PCM if compared to

current sensible materials such as molten salts, concretes or ceramic materials. The second one is associated to the flexibility in the operating temperature. Phase transitions occur at a fixed temperature, which implies a unique operation temperature. Even if this limitation can be overcome following a cascade LTES concept introduced by several authors [75,76], the complexity of this solution presents more restrictions than STES systems, which allow the operation in a wider temperature range.

1.2.3. Thermochemical heat storage (TCHS)

So far, STES and LTES have been defined as heat storage alternatives based on the variation of the internal energy of a single material. In the first one, the energy is associated to the temperature variation, whereas the second TES mechanism underlies on a first order phase change process undergone at isothermal conditions with an associated latent heat. In both mentioned cases, the thermal energy is absorbed or released without changing the storage material chemical nature. Removing this constant composition boundary, a third route to store heat can be opened by means of the exploitation of chemical reactions between different materials. In certain reaction processes a large amount of heat is exchanged when the reactant materials are combined to generate different product materials. These particular cases are known as thermochemical reactions, and the involved reaction heat can be exploited in the TES frame establishing a third TES alternative so-called thermochemical heat storage (TCHS).

Starting from the mentioned conceptual approach, TCHS makes use of reversible chemical reactions or sorption processes. In TCHS reactions, heat is used to dissociate a compound (AB) into two reaction products (A and B). These products can be stored separately and, when heat is required, can be combined again to activate the exothermic reaction where, the previously consumed heat is released. On the other hand, in reversible sorption processes heat is consumed and released through desorption and adsorption (physical bonding) or desorption and absorption (uptake/dissolution of a material) processes respectively.

Comparing the TCHS with STES or LTES, the former presents the highest energetic density since, reaction enthalpies are usually much higher that latent

ones [22,77]. As a consequence, the storage density is noticeably increased with large storage capacities on small TES volumes. In addition, the separated treatment of the product components of the thermochemical reaction after the primary heat is absorbed, represents one of the most important advantages of TCHS. This makes possible the uncoupling of the thermal storage with temperature boundaries, since no reverse reaction will be promoted up to the recombination of the product materials, regardless of the temperature [78]. An important consequence of this behaviour is the avoiding of sophisticated and expensive thermal insulation strategies, usual in STES and LTES.

However, some limiting factors affect to the complete deployment of this technology at industrial scale. Among them, the complexity of the reactors and heat exchangers required for reaching high reaction yields, or the need of finding low-cost reactions with good cyclability and long lifetime.

Following the description used in STES and LTES, the exchanged energy in a thermochemical reaction can be defined as follows:

$$E = m \cdot \Delta H_{reaction}; \tag{1.3}$$

where m is the mass of the material of the limiting reactant and $\Delta H_{reaction}$ the reaction enthalpy per unit mass.

Among the potential chemical reactions with clear implementation potential in the thermal energy storage frame, gas-solid reactions have been demonstrated as the most suitable ones [79]. These reactions take place at constant temperature for a given pressure, what allows the selection of reactants and reaction conditions adapted to a specific application. In addition, the pressure presents a very important effect on the reaction temperature, which can be exploited to control this last parameter. As a consequence, different charge or discharge temperatures can be obtained by adjusting appropriately the pressure of the system. This phenomenon is known as “thermal upgrade” [80].

Different gas-solid reactions have been reported in the literature as successful candidates for TCHS [79]. These reactions can be grouped in four main families:

- Hydration/dehydration: in these reactions, water is removed/taken from/by a hydrated molecule. Investigated reactions of this family are

$SrBr_2 \cdot 6H_2O$ / $SrBr_2 \cdot H_2O$ [81], $MgSO_4 \cdot 7H_2O$ / $MgSO_4$ [82], $MgCl_2 \cdot 6H_2O$ / $MgCl_2 \cdot H_2O$ [83], $CaCl_2 \cdot 2H_2O$ / $CaCl_2 \cdot H_2O$ [84], $NaS_2 \cdot 5H_2O$ / $NaS_2 \cdot 2H_2O$ [85] or $Ca(OH)_2$ / CaO [86].

- Reduction/oxidation (Redox): in these reactions, oxygen is removed/taken from/by a molecule. Examples of these reactions are Co_3O_4 / CoO [87], Mn_2O_3 / Mn_3O_4 [88], BaO_2 / BaO [79] or CuO / Cu_2O [79].
- Hydrogenation/dehydrogenation: in these reactions, hydrogen is removed/taken from/by a molecule. Proposed reactions of this typology are MgH_2 / Mg [89], $NaMgH_3$ / NaH+Mg [90] or Mg_2FeH_6 / Mg+Fe [91].
- Carbonation/decarbonation: in these reactions, carbon dioxide is removed/taken from/by a molecule. Some examples of this reaction typology are $CaCO_3$ / CaO [92] or $SrCO_3$ / SrO [93].

Even if TCHS has extensively been studied in the last years as a promising TES alternative, this technology is still at a fundamental laboratory stage, far from any proven design able to work at a commercial scale [94]. Even if the material and reaction selection for TCHS presents an increasing interest from the community, the implementation of the proposed materials and reactions in customized TES solutions is only supported by a limited number of publications. An example of an experimental facility was reported by Schmidt et al. [86] testing an indirectly operated fixed bed reactor the system $CaO/Ca(OH)_2$. The investigation consisted in the study of this reaction at low water vapour pressures under different heating and cooling loads. The experiments revealed that the handling of the reaction gas not only affects to the operating range of the storage but also has a significant influence on its thermal performance. Another example is the work reported by Singh et al. [95] where experiments on a 74 kWh_{th} prototype reactor installed at the Solar Tower Jülich in Germany implementing the redox reaction Co_3O_4/CoO are presented. In this work the obtained experimental results were validated with a theoretical model used for the determination of the effect in the storage of different boundaries such as inlet temperatures or inlet mass flow rate.

From the point of view of the technological development of TCHS, both, material and TES deployment concepts are equally important and must be addressed in parallel in order to obtain a satisfactory TES concept, suited for real

scale applications. Aligned with this idea, no universal solution can be found for TCHS implementing any reaction under specific TES conceptual solutions. The success of the TCHS necessarily implies the customization of the selected materials, reactions and the particular deployment TES solution.

1.2.4. Storage concepts

The implementation of the aforementioned heat storage principles requires the development of suitable storage concepts for its deployment in real applications. As detailed in the STES, LTES and TCHS sections, each heat storage alternative presents a particular problematic which makes necessary a customized design. Leading apart the detailed requirements of each TES alternative, in this section, a general heat storage conceptual implementation survey is provided. Based on the current TES deployment frame, in the following, the most widely storage deployment strategies are detailed, also depicted in Figure 1.10.

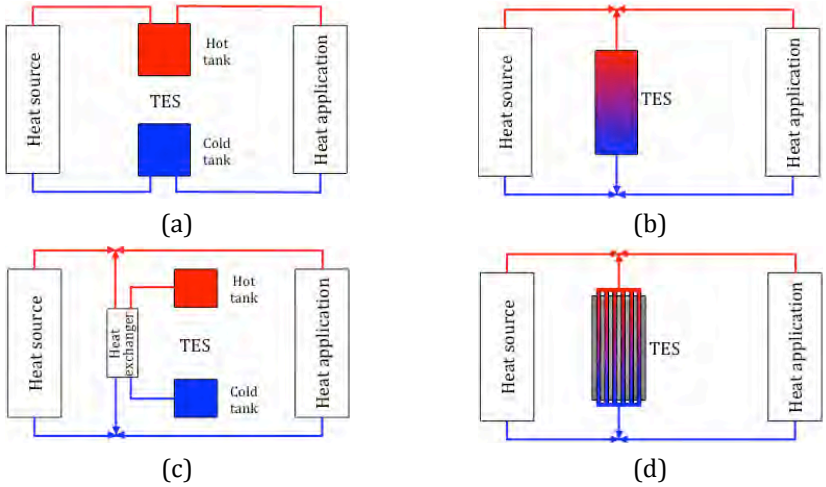

Figure 1.10. TES configurations: a) active direct storage; b) active storage with thermocline; c) active indirect storage and d) passive storage with concrete.

- Active storage: the storage medium moves through the TES unit. As an example of the application of this TES concept, in the CSP environment these systems typically use a double-tank solution (one for the hot fluid and other for the cold fluid) or a single-tank (thermocline concept without filler material, see section 1.3) to contain the storage medium. Currently two different configurations can be found in commercial systems:

- Direct storage: the heat transfer fluid and storage medium are the same. This TES deployment strategy is shown in Figure 1.10a, where a single fluid is used as HTF and storage medium. As it can be observed, in this configuration, the hot fluid coming from the heat source, i.e. industrial process, solar field, etc. is directly fed to the hot tank. From this tank is sent to the particular heat demanding application, i.e. power block, industrial process, etc. and once cooled down, it is introduced back into the cold tank. When the heat source is again available, the fluid is circulated through the heat source starting the cyclic thermal operation again. A second example of active storage with a single fluid solution is provided in Figure 1.10b, showing a thermocline TES concept. Under this configuration, when there is heat surplus, hot fluid from the heat source is introduced through the upper part of the tank and released cold from bottom. Inside the storage tank coexists both, cold and hot, fluids separated by a temperature stratification region called thermocline. When it is necessary to take heat from the storage tank, the cold fluid is inserted in the storage through the bottom part and obtained hot from the top.
- Indirect storage: two materials are used, one as heat transfer fluid and other as storage medium. In this configuration, a heat exchanger is required (Figure 1.10c). In this case, the hot fluid coming from the heat source can be either used to feed a heat exchanger to heat up the secondary fluid used as storage medium or directly consumed in the heat demanding application. When no heat source is available, the fluid from the hot tank is feed in the heat exchanger to heat up the HTF.

- Passive storage: the heat transfer fluid is circulated through a storage medium. In this case, the storage medium is static and does not move through the TES unit. This is the case of thermocline systems when using solid fillers as storage material (see section 1.3), or systems such as the one presented in Figure 1.9. Figure 1.10d shows a passive storage configuration where a solid material is used as storage medium. Under this configuration, the implemented heat transfer fluid is circulated through the storage

medium releasing/receiving heat. Depending on the design of the TES unit, the heat transfer fluid can be in direct contact (see section 1.3) or not (see Figure 1.9) with the storage medium.

1.3. Packed bed TES systems

The choice of a TES deployment strategy is never an easy task. A large number of system boundaries need to be balanced in order to optimize the overall system performance including technical and economical considerations. From the TES deployment strategies mentioned in the previous section no winning alternative can be identified without including a detailed analysis of the heat source, demand or other system implementation limitations.

However, in the search of a new generation of TES alternatives, which could provide a cost effective, high temperature and efficient performance, the indirect storage alternatives have been suggested in the last years as an appropriate solution. The decoupling of the heat transfer fluid and the storage medium presents very attracting advantages, such as the drastic reduction of the amount of fluid needed. Usually, the used fluids are very expensive and demand continuous technical attention to avoid undesired malfunction such as freezing, decomposing, overpressure and other issues. Considering this phenomenology, the substitution of a large amount of fluid by a solid material with appropriate thermal and chemical properties could open a new generation of TES alternatives with enhanced thermal performance, operation temperature range and cycle efficiency.

Aligned with these ideas, the packed bed storage concept has been introduced by different authors [54,55,96]. Packed bed TES systems are a single-tank solution where the hot and cold fluid zones coexist in the same volume without any physical separation. It consists in the ordered or random packing of solid individual particles, with regular or irregular shape, conforming a fixed solid bed arrangement. Through the empty volume fraction between the solid pebbles, a fluid (gas or liquid) is interstitially circulated. This fluid is used as a heat transfer fluid introducing/extracting the heat to/from the packed bed. In this configuration, the heat exchange between the fluid and the solid leads to a natural temperature stratification phenomenon in the solid bed, known as thermocline.

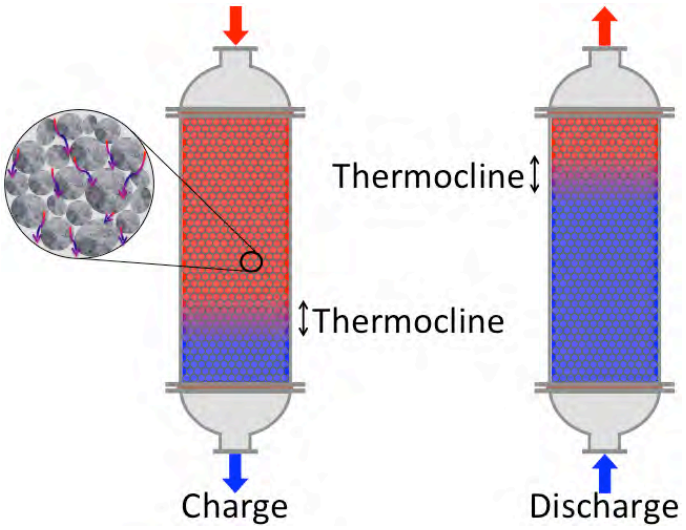

Figure 1.11. Schematic view of a packed bed TES system.

A schematic view of this TES concept is presented in Figure 1.11. In the left-hand-side a TES tank during the charge operation is presented, where the hot heat transfer fluid is introduced through the upper part, whereas the cold fluid is extracted from the bottom. The discharge operation is schematized in the right-hand-side where the cold heat transfer fluid is fed through the lower part of the tank and released hot from the top. This operation strategy is selected in order to maintain a high thermodynamic quality of the stored energy by exploiting buoyancy-driven effects to establish a thermocline zone. As a consequence, the hot and cold system regions are separated naturally, avoiding any convective mixing phenomenon.

In addition, in Figure 1.11 the local configuration of the solid particles is also shown together with a representation of the interstitial fluid flow. The random nature of the solid packing also implies a random interstitial fluid flow. Consequently, highly complex local heat transport mechanisms between the fluid and the solid particles can be expected (see section 4.1.3.2). Such heat transport mechanisms govern the performance of the packed bed TES unit affecting directly to the size and shape of the thermocline. In order to understand the general performance of this type of TES systems, in Figure 1.12 different scenarios of the thermocline inside the packed bed are presented.

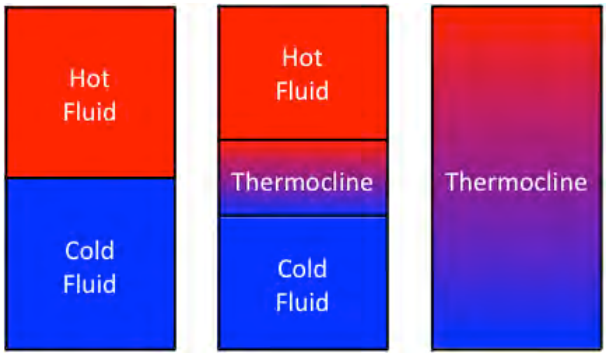

Figure 1.12. Schematic view of the temperature stratification phenomenon.

In the left-hand-side the ideal situation, where no thermocline is formed, is presented. In this case, cold and hot regions are perfectly separated and no storage volume is wasted in containing the thermocline. The positive consequence of this scenario is that all the charged material is at the fluid maximum temperature. This ideal step transition between the hot and cold storage zones cannot be obtained in real application since the heat transport between both zones cannot be avoided.

The opposite performance is the scenario presented in the right-hand-side, where the thermocline region occupies all the storage volume. The direct consequence of this undesired TES system behaviour is the impossibility of storing heat at the maximum fluid temperature and hence, the minimization of the storage capacity.

The scenario shown in the middle (Figure 1.12) is the most realistic one. Under this performance, the thermocline is contained in a small and controlled volume. The optimization of the temperature stratification process must be aligned with the objective of the target behaviour depicted in the left-hand-side of the Figure 1.12. This goal can be reached by means of an exhaustive optimization and balance of the main design parameters of this TES system such as the fluid flow, container geometry and solid particle size and shape according to the density, specific heat and thermal diffusivity of the storage material.

In addition to the aforementioned conceptual advantages, this TES solution presents several techno-economical benefits in comparison to current solutions such as the molten salt double-tank technology presented in section 1.2. Among them, the following ones can be highlighted:

- The possibility of releasing hot fluid at constant temperature during the discharge process being a single-tank solution. Depending on the final application of the heat, this performance is of paramount importance as is the case of power production via a steam turbine.
- The use of solid materials, typically ceramic, as TES medium allows the extension of the system operating temperature range from ambient to temperatures above 1000 °C when, for example, air is used as heat transfer fluid.
- Since it consists in a single-tank solution, and it allows the use of low cost TES materials, the required investment of this technology is lower than the molten salt double-tank solution. In addition, in the case of using molten salts as heat transfer fluid, the substitution of a noticeable amount of this material, around 65-70%, by a solid medium, considerably reduces the amount of required salt. Taking into account the high cost of this material, the impact on the required investment is very relevant. In the case of using air as heat transfer fluid, the substitution of the molten salt would be complete, which leads to an even higher cost reduction (see Table 1.1).

The material choice for a packed bed storage arrangement is not something trivial. In order to make a successful selection, the following requirements are expected:

- High energetic density: as presented in section 1.2.1, this property is determinant in STES applications. With the objective of increasing the storage capacity, large values of this magnitude are desired in order to minimize the size of the storage maintaining similar storage capacities.
- Moderate thermal conductivity: this transport property plays an important role in the heat transfer between the TES material and the heat transfer fluid, in the thermocline generation and in the heat transfer inside the solid particles. Very large values of this property promote the thermocline spreading in the axial direction reducing the storage capacity of the system. On the other hand, low values may cause important thermal gradients inside the particles leading to considerable waste of the storage capacity of the TES medium.

- High mechanical resistance: in real systems, the packed configuration of the solid medium, with lengths of several meters, and the large temperature variations generate high stresses in the solid material. In this regard high mechanical resistance, mainly under compression strength, is necessary.
- Similar thermal expansion than container materials: different thermal expansion between the TES medium and the container material may cause strong stresses in both materials causing mechanical failures such as the well-known ratcheting effect [98,99].
- Stable in the operating temperature range: the selected TES material should not suffer degradation or irreversible transformations in the selected operation temperature range.
- Durability: the solid material and the heat transfer fluid operate in direct contact. In this regard, the complete compatibility between both materials must be guaranteed during the expected life cycle of the system (estimated in 25-30 years in the case of CSP plants).
- Reduced cost and wide availability: in order to compete with other storage concepts, the material must have the lowest cost as possible, and be widely available, preferentially close to the TES deployment place.

Taking all these requirements into account, the effort of the scientific community searching for materials that meet all these requirements has been enormous in the last years. The investigated materials range from natural rocks to low cost ceramics, industrial by-products, etc. In this field, Allen et al. [100] analysed the suitability of different natural rocks (dolerite, granite, gneiss etc.) from South Africa for packed bed systems operated with air. Jemmal et al. [101] investigated the suitability of gneiss rock as filler material in packed bed TES at temperatures up to 1000 °C showing the potential of this type of rock in terms of high thermal capacities, high density and good thermal stability. Grirate et al. [102] studied different rocks from Morocco (quartzite, basalt, granite, hornfels and marble) concluding the high potential of the quartzite as an economic and efficient filler material in thermocline systems using thermal oil as heat transfer fluid. Regarding industrial by-products, Gutierrez et al. [103] presented a review article including different industrial wastes that can be valorised in the field of TES.

Among them, asbestos containing wastes, fly ashes, by-products from the salt industry and from the metal industry, wastes from steel process and from copper refining process and dross from the aluminium industry, and municipal wastes (glass and nylon) were studied. This review shows that the valorisation of these materials in the TES field is possible, and that more studies are needed to achieve their industrial deployment. Furthermore, different research articles have been published investigating any possible corrosion phenomena between filler materials and different heat transfer fluids such as thermal oils or molten nitrate salts [96,104-107].

In addition to the material requirements, an optimized design of the storage container and an adequate thermal management of the packed bed are also important in order to maximize the storage capacity of the system. In this line, most of the related research effort is oriented to the development of numerical models whereas only few include experimental results [51,52,96,108,109]. Regarding the literature available studies, extensive work can be found addressing the thermal behaviour of such systems. Some experimental and numerical descriptions of particular packed bed devices are also found, with pre-selected operational parameters [110-113]. Finally, an important effort is also being carried out in the description of generic packed bed storage behaviour through dimensionless analysis [65,114-116].

Even if the packed bed storage concept has been widely introduced, its full implementation at commercial scale is still unclear. One of the issues that needs to be addressed is the detailed analysis of the thermocline stability over multiple charge/discharge cycles. In this regard, only a reduced number of publications can be found dealing with this subject. For example, Bruch et al. [117] performed experimental and numerical investigations in a pilot scale oil/rock thermocline TES system. Geissbühler et al. [118] published experimental results of three charge/discharge cycles performed in a combined sensible/latent bed operated with air, together with its numerical validation. Odenthal et al. [119] presented different operational strategies for a rocks packed bed operated with molten salt as heat transfer fluid. Regarding the system efficiency, Bayón et al. [120] studied the influence of the percentage of the thermocline to be extracted in the cycling

operation in a quartzite rock/sand and molten salt system. Yang et al. [121] studied the influence of Reynolds number and the tank height in a molten salt and quartzite rock thermocline tank operating under stationary state conditions.

Another issue that has arisen concerning the thermal performance of packed bed TES systems is the temperature drop observed in the released fluid during the discharge operation when the thermocline region is partially extracted. A direct consequence of this behaviour is the possible time-reduction of supplying heat at the required temperature and hence, the lost of efficiency in the final application of the heat. In order to overcome this limitation, in the last years some authors have published theoretical and experimental results including a layer of a PCM material [122,123] or a thermochemical system [124] in the upper part of the tank to stabilize the output fluid temperature.

Although the interest of the industrial and scientific community on this type of storage is increasing in the last years, there is still a lack of technology viability demonstration, which could open a real deployment of packed bed TES systems. Currently, only a few real storage units are in use from the first packed bed heat storage system implemented by using a mineral oil, Caloria HT-43®, as heat transfer fluid and a sand/rock mixture as storage material (Solar One Project, Barstow; USA) [96]. This plant was in operation from 1982 to 1986 and had a total capacity of 170 MWh_{th}. A second industrial experience was constructed in the Ait Baha desert (Morocco) in 2014 [125]. This unit uses natural rocks as storage medium and air as heat transfer fluid. In this plant, the stored heat coming from a solar field is used as input energy in a cement production plant. Some pictures of this facility are included in Figure 1.13.

Figure 1.13. Thermocline TES unit constructed by Airlight Energy [125].

1.4. Thermal energy storage applications

As established in the sections above, TES can be exploited by means of different technologies, concepts and final solutions. Many TES alternatives have been introduced such as STES, LTES or TCHS. Furthermore, the underlying physical mechanisms, storage materials, heat transfer fluids and the TES deployment system open a wide application window for heat storage. A good example of this implementation potential is based on the suitability of TES to the complete temperature range, from low to high temperatures.

Conceptually, the application of a TES solution can be suited for any thermodynamic system involving the production or demand of heat. In practical terms, TES implies important added value to any thermally activated process:

- Noticeable increase of the thermal efficiency: the storage of heat, that in principle is a lost, implies a better management of the available energetic resources, minimizing the thermal losses and leading to an optimum energy deployment framework.
- Dispatchability of the energy: TES allows decoupling the production of the thermal energy to its consumption. As a consequence, an energy-on-demand scheme is promoted.
- On the power production frame, the last mentioned point presents particular relevance since the matching of the energy supply with the demand peaks allows the maximization of the production revenues with the associated optimization of the resources.

Based on these premises, the implementation of a TES solution can be the key to obtain a better exploitation of the energetic sources and to give a determinant boost to the related renewable or heavy industrial sector, in the search of a green and efficient energy deployment scenario. With this goal, in the following sections, the main TES exploitation applications are explained.

1.4.1. Concentrated solar power

Solar radiation is one of the most available renewable sources in the earth. The large magnitude of solar energy available makes it a highly appealing source for

electricity production. It is estimated that enough solar radiation reaches the Earth's surface to fuel the production of electrical energy for all of its habitants [126]. Although solar-thermal methodology is not the only manner to produce electricity from solar source, it is of particular interest based on its large capacity and its potential to be stored. In essence, the solar-thermal power production consists in the concentration of the solar radiation by means of mirrors in a small area. This power production technology is commonly known as concentrated solar power (CSP). A heat transfer fluid (HTF) absorbs the heat transported by the concentrated radiation, which is afterwards used to run a power block and produce electricity. Taking this into account, five are the main components in a CSP plant: the solar field, the receiver, the power block, the HTF and, in many plants, the TES unit. In Figure 1.14 a schematic view of a generic CSP plant is presented.

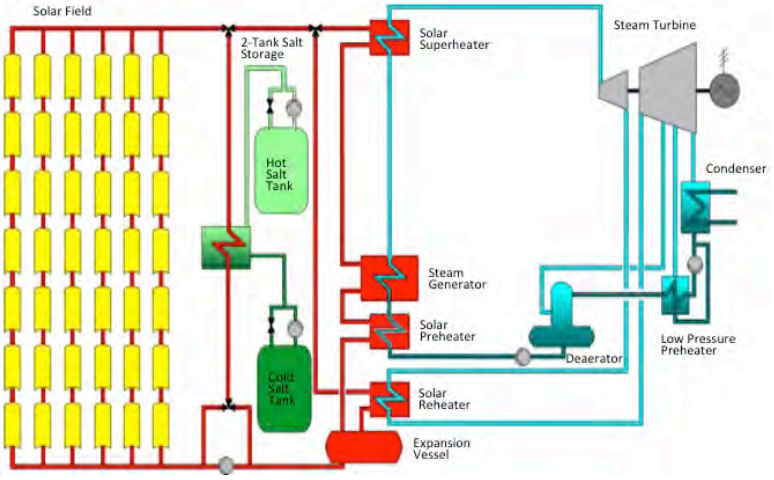

Figure 1.14. Schematic view of a parabolic through CSP plant equipped with a molten salt double-tank TES system [41].

Depending on the principle used for concentrating the solar radiation, CSP plants can be classified as [24,127-129]:

- Central receiver/tower: in this configuration an oval solar field formed by thousand of mirrors, called heliostats, focus the solar radiation in a receiver located in the upper part of a tower. In this point, the HTF is exposed to the concentrated solar radiation, and as a consequence, it is heat at temperatures up to 700 °C [130], depending on the used fluid. In Figure 1.15a an example of this configuration is presented. The image corresponds

to the *Gemasolar* plant [131], located in Sevilla (Spain). This was the first commercial CSP plant of this typology with a molten salt heat storage system constructed in the world.

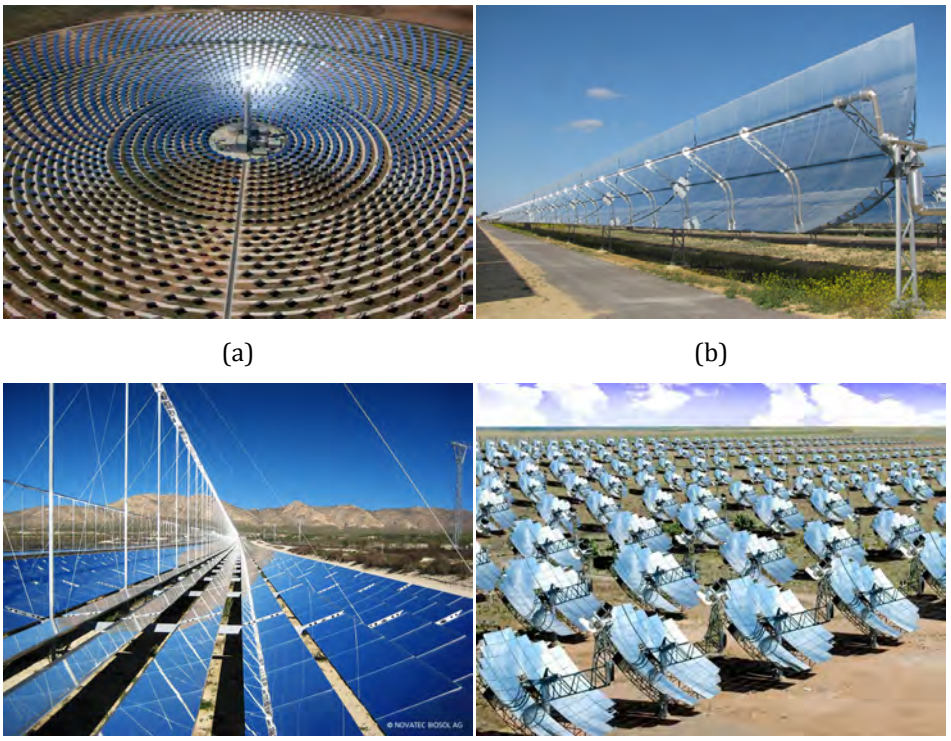

(a) (b)

(c) (d)

Figure 1.15. CSP plant technologies. a) Central tower (Gemasolar [131]); b) Parabolic through (Valle 1 and Valle 2 [132]); c) Linear Fresnel (Puerto Errado 2 [133]) and d) Stirling parabolic dish (California [134]).

- Parabolic through: in this configuration, parabolic mirrors are used for concentrating the solar radiation. The receiver consists in a pipe located in the focal point of the parabola. Such collectors are oriented in direction North-South to maximize the concentration. With this technology, it is possible to concentrate the solar radiation up to 100 times reaching temperatures up to 550 °C [130]. An example of this configuration is included in Figure 1.15b. The presented picture corresponds to *Valle 1 and Valle 2* plants located in Cádiz (Spain) [132].
- Linear Fresnel: in this configuration, series of long, parallel and planar mirrors concentrate the radiation in a single receiver located over them. In

this type of collectors, it is possible to heat the HTF up to 320 °C [130]. In Figure 1.15c an example of this technology is presented. The particular image corresponds to the CSP plant *Puerto Errado 2* located in Murcia (Spain) [133].

- Stirling parabolic dish: in this technology a parabolic dish is used to concentrate the solar radiation on its focal point, together with a Stirling thermal engine for power production. Temperatures around 750 °C can be achievable in the receptor. Many single units ranging from 5 to 100 kW constitute a CSP plant of this typology. A picture of this technology is presented in Figure 1.15d. This figure corresponds to the plant of *CondiSys Solar Technology* located in California [134].

According to ESTELA, Greenpeace International and SolarPACES, the worldwide installed solar thermal energy in 2006 was 0.5 GW. Meanwhile, it increased by a factor of 10 to almost 5 GW in 2015 [135]. This growth is an indicator of the increasing interest on this technology, which shows the clear potential of this renewable energy.

Nowadays, the most implemented CSP technology is the parabolic trough one and reaches an 82% of the total installed capacity. Central tower plants accounts for a 13% of the total capacity, however, this technology has been the most developed in the last years. Less implanted technologies are the linear Fresnel and the parabolic dish ones with a share of 4% and <1%, respectively [136].

Regarding the heat transfer fluid used in CSP plants, the most common ones are thermal oils or molten nitrate salts. The former are suitable for solar fields where temperatures up to 400 °C are reached. One of the most extended thermal oils in CSP plants is Therminol® VP-1. Molten nitrate salts are used in plants where the temperature in the solar field is higher, typically in central tower plants. The most implemented salt mixture is the *Solar salt*. This salt permits the plant operation up to 565 °C, limited by the nitrates decomposition. In addition to these two families of HTF, gases such as air have been reported by many researchers as promising HTF for extending the temperature operation of new generation central tower CSP plants up to 700-800 °C [48,137].

Table 1.3. CSP plants in operation equipped with TES [136].

Name	Location	Power (MW)	CSP technology	TES technology	Capacity (h)
Andasol I	Spain	50	P.T.	2-T.I.	7.5
Andasol II	Spain	50	P.T.	2-T.I.	7.5
Andasol III	Spain	50	P.T.	2-T.I.	7.5
Arenales	Spain	50	P.T.	2-T.I.	7
Aste 1A	Spain	50	P.T.	2-T.I.	8
Aste 1B	Spain	50	P.T.	2-T.I.	8
Astesol II	Spain	50	P.T.	2-T.I.	7.5
Caceres	Spain	50	P.T.	2-T.I.	7.5
Casablanca	Spain	50	P.T.	2-T.I.	7.5
Crescent Dunes	USA	110	C.T.	2-T.D.	10
Extresol 1	Spain	50	P.T.	2-T.I.	7.5
Extresol 2	Spain	50	P.T.	2-T.I.	7.5
Extresol 3	Spain	50	P.T.	2-T.I.	7.5
Gemasolar	Spain	20	C.T.	2-T.D.	15
La Africana	Spain	50	P.T.	2-T.I.	7.5
La Dehesa	Spain	50	P.T.	2-T.I.	7.5
La Florida	Spain	50	P.T.	2-T.I.	7.5
Manchasol 1	Spain	50	P.T.	2-T.I.	7.5
Manchasol 2	Spain	50	P.T.	2-T.I.	7.5
PS 10	Spain	11	C.T.	S.S.	1
PS 20	Spain	20	C.T.	S.S.	1
Solana	USA	280	P.T.	2-T.I.	6
Valle I	Spain	50	P.T.	2-T.I.	7.5
Valle II	Spain	50	P.T.	2-T.I.	7.5
Termosol I	Spain	50	P.T.	2-T.I.	9
Termosol II	Spain	50	P.T.	2-T.I.	9

P.T.: Parabolic trough; C.T.: Central tower/receiver; LF: Linear Fresnel; 2-T.I.: Double-tank indirect molten salt; 2-T.D.: Double-tank direct molten salt; S.S.: Saturated steam.

Together with the mentioned plant components, a TES solution is presented as a key element in many CSP plants. The integration of a TES system in a CSP plant improves its performance in terms of: i) palliation of fluctuations when weather conditions are variable; ii) extending the number of hours of power generation in low radiation periods or at night; and iii) aligning the electricity production with the demand [117]. All these benefits confer a determinant operation flexibility, dispatchability and overall efficiency increase to the CSP generation. In this frame, this technology can reduce noticeably the levelized cost of the electricity (LCOE) in order to attain competitive values.

As already mentioned in section 1.2, most common TES technology used in CSP plants consists in molten salts double-tank solution. In Table 1.3 a summary of worldwide operating CSP plants implementing TES systems and their typology are presented.

1.4.2. Waste heat recovery

According to the *IEA*, 30% of the global energy consumption corresponds to industrial applications [139]. However, the efficiency in the energy consumption in the industrial sector is, nowadays, far from a green and sustainable deployment scenario. According to Fernández et al. [140], if the best available technologies (BAT) were implemented in the heavy industrial activity, around 18% of the consumed energy could be saved. In addition, it is estimated that, in some industrial processes, approximately between 20 and 50% of the input energy is lost as waste heat in the form of hot exhaust gases, chemical combustion processes, water cooling, and heat losses from hot equipment surfaces and heated products [140]. Taking this into account, if properly recovered and stored, it may represent a huge reduction of primary energy supply together with the associated reduction of the pollutant and greenhouse gas emissions. The *U.S. Department of Energy* reported a summary of industrial applications with potential sources of waste heat [141]. In Table 1.4 medium and high temperature processes are collected. In addition, in Figure 1.16 the energy consumption, waste heat losses, and work potential from process with and without heat recovery systems in the U.S. industry are presented.

Table 1.4. Temperature classification of waste heat sources [140].

Range	Source	Temperature (°C)
High (>650 °C)	Nickel refining furnace	1370-1650
	Steel electric arc furnace	1370-1650
	Basic oxygen furnace	1200
	Aluminium reverberatory furnace	1100-1200
	Copper refining furnace	760-820
	Steel heating furnace	930-1040
	Copper reverberatory furnace	900-1090
	Hydrogen plants	650-980
	Fume incinerators	650-1430
	Glass melting furnace	1300-1540
	Coke oven	650-1000
	Iron cupola	820-980
Medium (230-650 °C)	Steam boiler exhaust	230-480
	Gas turbine exhaust	370-540
	Reciprocating engine exhaust	320-590
	Heat treating furnace	430-650
	Drying & baking ovens	230-590
	Cement kiln	450-620

Even if the benefits of a better exploitation of the thermal energy in heavy industries is clear, the practical implementation of enhanced efficiency solutions, such as TES or waste heat recovery, is often facing difficulties of different natures. As a consequence, the largest amount of industrial waste heat remains underutilized [27]. According to Pehnt et al. [142] the most relevant barriers that avoid the full industrial deployment of heat recovery technologies are:

- Technological barriers:
  - No nearby heat sink.
  - No information about heat sinks nearby.
- Production process barriers:
  - Disturbance of the operation.
- Financial and administrative barriers:

- Too high rate of return expectations.
- Uncertainty of the economic future for the investing company.

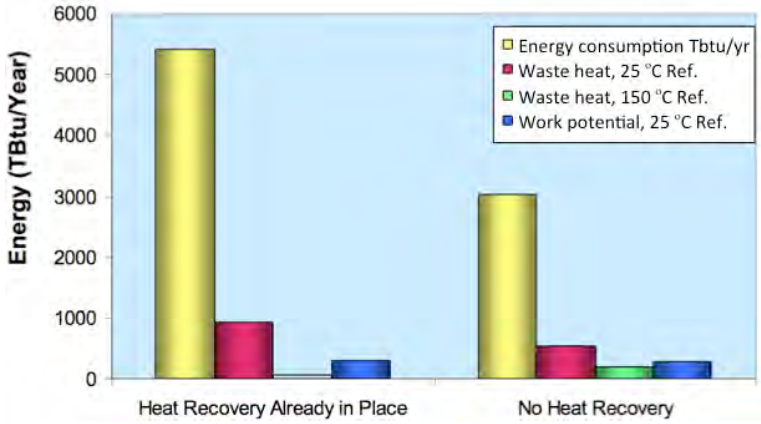

Figure 1.16. Waste heat losses and work potential from processes with and without heat recovery in the U.S. industry [140].

Related to the technological barriers, the integration of a TES in a heat recovery system allows solving the problem of mismatching between intermittences in the heat source and, the eventual required continuous supply in the heat demanding application. Furthermore, in 2014, the *IEA* highlighted the use of TES in this sector as a key application to achieve a low-carbon future due to the temporal and geographic decoupling of heat supply and demand [143]. Overall, the implementation of a TES system in cogeneration systems, power production cycles and industries with an intensive primary energy demand is receiving an increasing attention in terms of energy saving and CO_2 emission reduction [144,145]. Particular industrial processes that have received attention from the scientific community for heat recovery including a TES system are foundries [146,147], steelmakers [148-150], pulp and paper [151,152] or cement and concrete [153] among others.

1.4.3. Compressed air energy storage

As introduced in section 1.1, in the field of large-scale EES, a valid alternative to PHES is represented by compressed-air energy storage (CAES). CAES plants operate on a "decoupled" Brayton cycle in which, depending on the grid availability/request of electric energy, the air compression and expansion stages

occur at different times. During periods of energy surplus, the compression phase occurs and electricity is absorbed from the grid to activate a motor-compressor unit compressing air. The thermal energy produced during compression is removed by means of intercoolers and aftercoolers and the high-pressure low-temperature air is then stored in a large air reservoir. During peak periods of electricity demand from the grid, the air expansion stage takes place. The stored compressed air is fed through a combustion chamber, aiming at increasing its enthalpy, before being expanded in a gas turbine-generator unit for electricity production. In a conventional CAES plant there are four main components:

- The motor/generator: provide for alternate engagement to the compressor or turbine block.
- The compressors block: it may require two or more stages, intercoolers and aftercoolers, to achieve economic air compression and to reduce the moisture content of the compressed air.
- The turbine block: consist of a high- and low- pressure turbines.
- The air storage cavity: element used for the storage of the compressed air. Typically is located in a natural cavern under-ground, i.e. salt caverns.

A scheme of the configuration of a conventional CAES plant together with its main described-components is presented in Figure 1.17.

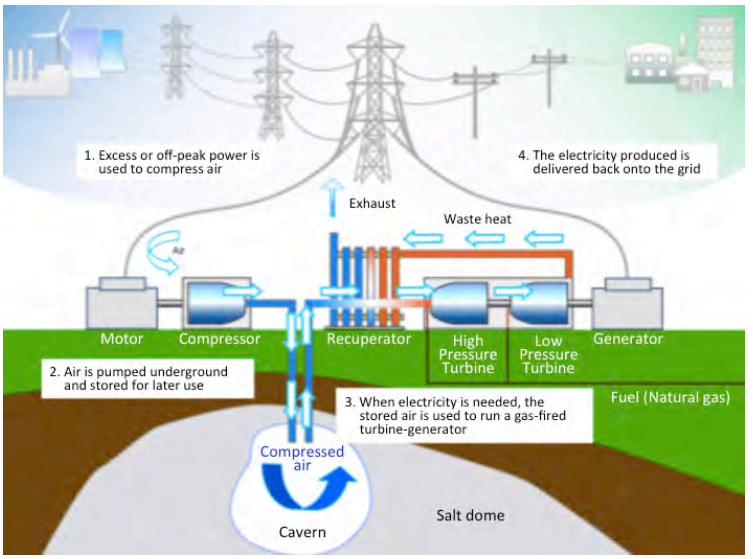

Figure 1.17. CAES plant scheme and components [154].

As of today, only two industrial-scale CAES plants are successfully in operation: the 321 MW *Huntorf* plant (Germany), and the 110 MW *McIntosh* plant (Alabama, U.S.). Commissioned at the end of 1978, *Huntorf* plant is the world's first CAES plant. On the other hand, McIntosh CAES plant, commissioned in 1991, can be considered as second-generation CAES in which a recuperator is exploited to pre-heat the compressed air before entering the combustion chamber. The round-trip efficiencies are 42% and 54% for the *Huntorf* and the *McIntosh* CAES plants respectively [155].

Up to now, the detailed CAES process deals only with the air compression/expansion stages, without implementing any strategy to recover the heat involved on both processes. Considering the relevance of this thermal energy, and the impact it could have on the optimization of the overall CAES process, different modifications to the standard concept have been proposed and developed. In the following, a general classification based on the thermal energy management during the air compression/expansion stages is given [155]:

- If thermal energy is wasted during compression and heat from a different source, usually burning natural gas in a combustion chamber, is supplied prior to expansion, the CAES concept is known as diabatic (D-CAES).
- Conversely, if thermal energy produced during compression is stored to be then exploited before expansion, the associated CAES concept is known as adiabatic (A-CAES) [156].

Considering the particular attractive of exploiting the thermal energy generated and demanded in the CAES process, the A-CAES methodology is attracting an increasing attention. As an example, the development of the A-CAES concept was the subject of the research project "ADELE" (2010-2013) [157] with the construction of the world's first 260 MW prototype expected as outcome of the "ADELE-ING" project (2013-present) [158]. Since in the A-CAES concept there is no need of burning fuel for the air heating process, the expected round-trip efficiency is in the order of 70% [157], which implies a clear enhancement of around 25% when compared with the standard CAES. As a consequence, the TES system is a key component for a successful implementation of the A-CAES.

Many authors have addressed this topic in the last years. Most research works available in the literature deal with the dynamic analysis of the complete A-CAES process by means of modelling tools [129,156,159-163] and few with experimental data [164]. Packed bed TES systems are nowadays presented as a satisfactory solution for heat management in A-CAES plants. The implementation of this type of systems allows the direct heat recovery from the compressed air avoiding the use of sophisticated heat exchangers. Some works have been published in the last years addressing this solution. Barbour et al. [129] developed a numerical model of an A-CAES system incorporating a packed bed TES, including its validation compared to analytical solutions. Their results suggest that efficiencies above 70% could be achievable, which is higher than many of the previous estimations for A-CAES systems using indirect-contact heat exchangers. Sciacovelli et al. [165] developed for the first time a plant model that blends together algebraic and differential sub-models detailing the transient features of the thermal storage, the cavern, and the compression/expansion stages. Their results show that a 60-70% of round efficiency is achievable when the TES unit efficiency is kept above 90%. Peng et al. [166] presented a parametric analysis of a packed bed system based on PCM pebbles. They found that increasing particle diameter results in a decrease in the charge efficiency, and the charge efficiency increases with an increase in inlet pressure of the compressed air. However, up to our knowledge, there is a lack of investigation about the temperature stratification phenomenon inside the packed bed TES coupled to an A-CAES process and the cyclic performance when operating under pressurized conditions.

Overall, the mentioned drastic increase of the cycle efficiency makes very interesting the deployment of a packed bed TES solution in the A-CAES frame, which makes this energy consumption/production process highly attractive.

1.5. Material selection for packed bed TES solutions

Towards an effective packed bed exploitation scenario, the selection of the storage material is one of the key points, together with the design optimization, to reach a successful techno-economical deployment of this storage technology. Aligned with this idea, the search of a low cost material and high thermal performance is the basis of the mentioned TES appropriate exploitation.

In addition to the conventional requirements of a STES material established in section 1.2.1, the packed bed solution added thermal and mechanical requirements to the storage material (section 1.3). With the objective of obtaining a successful balance between the thermal performance and the economical investment associated to the TES, different low cost material materials have been introduced based on industrial solid by-products. In this line, the valorisation of low cost industrial waste materials can represent a satisfactory solution, which balances a correct economical feasibility maintaining a high thermal performance.

1.5.1. By-products from the iron and steel production

Steel is indispensable to our modern way of life. The intrinsic benefits of steel make it the most adequate choice in a significant number of applications. Almost everything that we use is either made from, or manufactured with steel. Annually, around 1,620 million tonnes of steel (2015) are produced worldwide [167].

Steel is manufactured via three main routes: blast furnace-basic oxygen furnace (BF-BOF), that accounts for the 70% of the worldwide steel production; electric arc furnace (EAF), with a share of around 29%; and the open hearth furnace (OHF) which makes up about 1% of the total produced steel [168]. These three routes are shown in Figure 1.18.

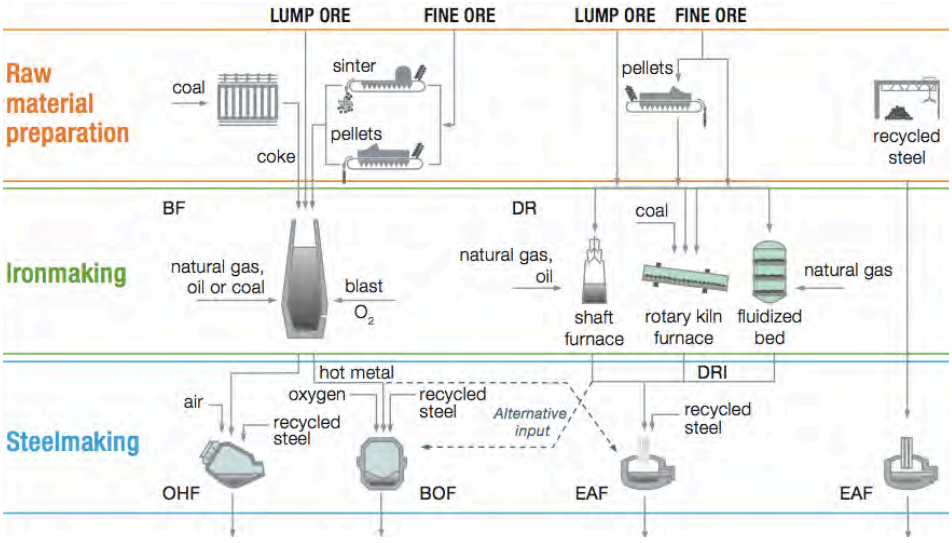

Figure 1.18. Steel production routes [57,168].

The BF-BOF route uses raw materials such as iron ore, coal, lime and recycled steel. First, iron-rich ores are reduced to iron in the BF with coal, also called pig iron. In subsequent processes, the iron is transformed to steel in the BOF. In the latter, oxygen is injected into the furnace to remove the impurities in the charge consisting of carbon, silicon, manganese, phosphorus and iron oxides.

On the other hand, the EAF route makes use of electricity and steel scrap for the production of steel. Depending on the plant configuration and availability of steel scrap, other sources of metallic iron can also be used. Once iron is charged in the furnace, an electric arc is used to molten the scrap. Slagging agents such as lime or magnesite are added to the molten ferrous scrap in order to capture the existing impurities and to protect the bath from excessive heat losses and oxidation.

Finally, the OHF is a very energy intensive route, and nowadays, only four furnaces of this type are known to be in operation in the world. Its use is in decline mainly because of its many environmental and economic disadvantages.

Three solid by-products are generated during the iron and steel production: the slag, which represents 90% of the produced waste material, dust and sludge. On average, each produced tonne of steel results in 200 kg (EAF) to 400 kg (BF-BOF) of by-products. Overall, more than 400 million tonnes of iron and steel slag are yearly produced in the world. As an example, in Europe, the steel industry generated around 15 million tonnes of slag in 2004 [169] while in 2010, the slag production raised up to 21.8 million tonnes [170].

Since the slag has lower density than the molten iron/steel, it floats and can be easily removed once the smelting process is finished. Depending on the furnace and the cooling procedure, different slag types are produced, summarized in the following.

The BF slag (BFS) is mainly composed by silica (33–38%) and calcium oxide (35–42%), with lower concentrations of magnesium oxide (7–12%) and alumina (10–15%). Taking into account that the BF process is reductive, the content of iron oxide is considerably low (<1%) [171]. Typically, BFS is classified by its cooling method. In these terms, three commercial types of BFS can be found: air-cooled, granulated and pelletized or expanded. The former is hard and dense, and is especially suitable for its use as construction aggregate. Granulate slag is rapidly

solidified with water to form sand-sized particles of glass and is mainly used to make cementitious material. Finally, pelletized slag, cooled down with a mixture of water and air processes, has a vesicular texture (like volcanic rock) and is most commonly used as a lightweight aggregate.

On the other hand, the main components of steel slag (BOF and EAF) are calcium oxide (35-45%), silica (11-17%) and iron oxides (16-26%). Lower concentrations of alumina (1-6%), manganese oxide (2-6%) and magnesium oxide (2-9%) are also found. In this case, the high content of iron oxides are related to the oxidation processes in these furnaces [171]. Steel slag is typically cooled like air-cooled BF slag and is mainly used for the same purposes. As the production process varies at this stage, depending on the type of steel being manufactured, the resulting slag also presents diverse chemical properties difficulting a clear valorisation of this material compared to iron slag. Some of the generated slag is used internally in the steelmaking furnace or sinter plant, while approximately 50% of the slag is used externally in construction applications.

The worldwide slag valorisation rate varies from over 80% for steel slag to nearly 100% for iron slag. However, the remaining slag is landfilled or stored at site in the iron or steelmaker locations waiting for a final application. Taking this into account, there is still a clear potential of this by-product to find a complete valorisation scheme. According to EUROSLAG [170], in Europe, although a relevant amount of slag is reused for several applications, around 13% is landfilled. Considering the large production amount of this material, a huge potential for new valorisation applications is foreseen.

1.5.2. Natural material: magnetite ore

Magnetite ore (Fe_3O_4) is a material usually found in the exploitation of iron mining. Even if its extraction is a collateral consequence of the iron mining activity, there are several applications for this material itself.

The magnetic properties of this mineral have attracted the attention for many applications since the 8th century [172]. Today, its applications range from drug delivery, magnetic resonance imaging [173,174] to cancer therapy [175], nanocomposites, ferrofluids [176,177] and more [178]. On the other hand,

magnetite ore has many advantages such as availability, low cost (0.19 €/kg), ecological friendliness and non-flammability. In addition, magnetite ore could be considered as an iron feedstock for the pig iron production in the blast furnace. However, its high density and lack of permeability have been often identified as severe limitations for its implementation in practical terms [179]. Consequently, a large reserve of magnetite ore has been lying unutilized over the years. For instance, in the Indian context, out of 28.52 billion tonnes of total iron ore, 17.88 billion tonnes are hematite ore and the rest are magnetite ore [179].

Based on the mentioned material properties, usually representing a technical limitation for the exploitation of magnetite ore, its implementation in the TES frame is found to be of particular interest. In this case, its large density and low permeability represent an important advantage, as both properties are conferring an unique ability to magnetite ore to store heat.

1.6. Thesis objectives and scope

The main objective of the presented research is **the study of the suitability of two families of low cost ceramic materials, the iron and steel slag and the magnetite ore, for their application in high temperature packed bed thermal energy storage systems**. In order to achieve such general and ambitious objective, different partial goals have been established:

- The characterization of the main structural, mechanical and thermal properties of the slag and magnetite ore that governs the performance of the material in packed bed thermal energy storage arrangements.
- The determination of the durability and compatibility of the selected ceramic materials to operate in direct contact with commonly used heat transfer fluids.
- The development of an *ad hoc* theoretical model for the description of all the heat transfer and fluid flow mechanisms associated to packed bed thermal energy storage solutions.
- The determination of the main design and operational parameters of packed bed thermal energy storage units.

- The deployment of the proposed thermal energy storage solution in three different industrial environments: concentrated solar power, industrial waste heat recovery and compressed air energy storage.

Taking into account the presented general and partial objectives this thesis work is divided in seven chapters together with an annex section.

In **chapter 1**, the most relevant topics affecting the activities carried out in this thesis work are introduced. This chapter starts with a short overview of the current energetic context and continues with a detailed description of the most relevant aspects and typologies of thermal energy storage systems. In addition, a detailed description of the state-of-the-art of packed bed systems is presented together with the most common applications where such systems can be applied. Finally, a brief description of the two materials families investigated in this thesis work is also included.

In **chapter 2** the characterization of the main structural, mechanical and thermal properties of the investigated materials is reported. Before presenting the obtained results, the origin and particularities of the different slag samples and the magnetite ore considered in this study are presented. Furthermore, a description of the experimental techniques and protocols followed in the measurement of the different properties is also included. Finally, a comparison analysis between the results obtained for the investigated materials and other materials reported in the literature for the packed bed thermal energy storage applications is also addressed.

In **chapter 3**, the stability of the selected materials in chapter 2 is investigated up to 1100 °C under air atmosphere. In addition, the compatibility between these materials and two different heat transfer fluids (a molten nitrate salt and a thermal oil) is also addressed. As a conclusion of this chapter, the suitability of these materials to work in direct contact with the mentioned heat transfer fluids at their maximum operation temperatures is extracted.

Chapter 4 is devoted to the presentation of the theoretical model developed in this thesis work for the description of all the heat transfer and fluid flow mechanisms present in packed bed thermal energy storage systems. In order to confirm its high quality and accuracy, the model is validated with experimental

results from literature. In addition, this section contains the implemented methods for solving the mass, energy and momentum conservation equations and the definition of the formula used in the description of the energetic, entropic and exergetic performances.

In **chapter 5** the developed model is implemented for understanding the thermal performance of the investigated materials in a packed bed configuration. Overall, in this chapter a complete guideline and optimization analysis of the main design and operational parameters is presented.

Chapter 6 is devoted to the analysis of the deployment of a packed bed thermal energy storage system based on the materials studied in this thesis work in three different industrial environments. As first application, the coupling of a thermal energy storage unit with the particular operation of an electric arc furnace for heat recovery from the exhaust gases is considered. Second, the study of the integration of a slag-based packed bed in a compressed air energy storage plant according to the operation parameters of the Huntorf plant is addressed. Finally, the design and operation strategy of a magnetite ore packed bed for a linear-Fresnel-type concentrated solar power plant is presented.

Finally, in **chapter 7** the general conclusions extracted from the activities carried out in this thesis work are presented. Furthermore, a summary of possible future activities associated to the developed work is also included.

In the **annex** section, the thermo-physical properties of all the heat transfer fluids and insulating materials considered in the design of the storage tanks in chapters 5 and 6 are included, as well as the list of the publications released from work carried out in this thesis.

1.7. References

[1] U.S. Energy Information Administration, "International energy outlook," 2016.

[2] International Energy Agency (IEA), "Key world energy trends: World energy balances," Statistics 2016.

[3] J. Speirs, C. McGlade, and R. Slade, "Uncertainty in the availability of natural resources: Fossil fuels, critical metals and biomass," *Energy Policy*, vol. 87, pp. 654-664, 2015.

[4] British Petroleum (BP), "BP Statistical Review of World Energy," 2016.

[5] U.S. Environmental Protection Agency, "Inventory of U.S. Greenhouse Gas Emissions and Sinks: 1990 - 2014," 2016.

[6] Kyoto protocol [Online]: http://www.kyotoprotocol.com/

[7] SolarPACES Country information [Online]: http://www.solarpaces.org/country-information/spain

[8] REN21, "Renewables 2016 - Global status report," 2016.

[9] P. W. Parfomak, "Energy storage for power grids and electric transportation: A technology assessment," *Congresional Reseach Service*, 2012.

[10] H. Chen, X. Zhang, J. Liu, and C. Tan, "Compressed Air Energy Storage," in *Energy Storage - Technologies and Applications*.: InTech, 2013.

[11] S. Schoenung, "Energy storage systems cost update," SANDIA, 2011.

[12] Electric Power Research Institute (EPRI), "Solar thermocline storage systems: a preliminary design study," 2010.

[13] M. Medrano, A. Gil, I. Martorell, X. Potau, and L.F. Cabeza, "State of the art on high-temperature thermal energy storage for power generation. Part 2 - Case studies," *Renewable and Sustainable Energy Reviews*, vol. 14, no. 1, pp. 56-72, 2010.

[14] M.N. Strasser and R.P. Selvam, "A cost and performance comparison of packed bed and structured thermocline thermal energy storage systems," *Solar Energy*, vol. 108, pp. 390-402, 2014.

[15] X. Luo, J. Wang, M. Dooner, and J. Clarke, "Overview of current development in electrical energy storage technologies and application potential in power system operation," *Applied Energy*, vol. 137, pp. 511-536, 2015.

[16] Electric Power Research Institute (EPRI), "Electrical energy storage technology options," 2010.

[17] B. Decourt and R. Debarre, "Electricity storage," Factbook 2013.

[18] H. Paksoy, "Thermal energy storage today," in *IEA Energy Storage Technology Roadmap Stakeholder Engagement Workshop*, Paris, 2013.

[19] International Energy Agency (IEA), "Technology roadmap - Energy storage," , 2014.

[20] L. Valenzuela, "12 - Thermal energy storage concepts for direct steam generation (DSG) solar plants," *Advances in Concentrating Solar Thermal Research and Technology*, pp. 269-289, 2017.

[21] S. Ushak, A. G. Fernández, and M. Grageda, "3- Using molten salts and other liquid sensible storage media in thermal energy storage (TES) systems," *Advances in Thermal Energy Storage Systems*, pp. 49-63, 2015.

[22] A. Gil et al., "State of the art on high temperature thermal energy storage for power generation. Part 1 - Concepts, materials and modellization," *Renewable and Suistainable Energy Reviews*, vol. 14, pp. 31-55, 2010.

[23] C. Prieto, R. Osuna, A.I. Fernández, and L.F. Cabeza, "Thermal storage in a MW scale. Molten salt solar thermal pilot facility: Plant description and commissioning experiences," *Renewable Energy*, vol. 99, pp. 852-866, 2016.

[24] M. Liu et al., "Review on concentrating solar power plants and new

developments in high temperature thermal energy storage technologies," *Renewable and Sustainable Energy Reviews*, vol. 53, pp. 1411-1432, 2016.

[25] T. Bauer et al., "Material aspects of Solar salt for sensible heat storage," *Applied Energy*, vol. 111, pp. 1114-1119, 2013.

[26] K. Merlin, J. Soto, D. Delaunay, and L. Traonvouez, "Industrial waste heat recovery using an enhanced conductivity latent heat thermal energy storage," *Applied Energy*, vol. 183, pp. 491-503, 2016.

[27] L. Miró, J. Gasia, and L.F. Cabeza, "Thermal energy storage (TES) for industrial waste heat (IWH) recovery: A review," *Applied Energy*, vol. 179, pp. 284-301, 2016.

[28] R. Hackl and S. Harvey, "From heat integration targets toward implementation - A TSA (total site analysis)-based design approach for heat recovery systems in industrial clusters," *Energy*, vol. 90, pp. 163-172, 2015.

[29] SENER [Online]: http://www.ingenieriayconstruccion.sener/

[30] D. Laing, W.D. Steinmann, R. Tamme, and C. Richter, "Solid media thermal storage for parabolic trough power plants," *Solar Energy*, vol. 80, pp. 1283-1289, 2006.

[31] D. Laing, C. Bahl, T. Bauer, D. Lehmann, and W.-D. Steinmann, "Thermal energy storage for direct steam generation," *Solar Energy*, vol. 85, pp. 627-633, 2011.

[32] N. Hoivik et al., "Demonstration of EnergyNest thermal energy storage (TES) technology," in *SolarPACES Conference*, Abu Dhabi (UAE), 2016.

[33] M.A. Geyer, "Thermal storage for solar power plants," in *Solar power plants*.: Springer-Verlag, 1991, pp. 199-214.

[34] Pilkington Solar International GmbH, "Survey of thermal storage for parabolic trough power plants," National Renewable Energy Laboratory, 2000.

[35] SQM, "SQM's Thermo-Solar salts," Datasheet.

[36] Coastal Chemical Co., L.L.C., "HITEC Heat transfer salt," Datasheet.

[37] Coastal Chemical Co., L.L.C., "HITEC XL Heat transfer salt," Datasheet.

[38] Therminol, "Therminol VP-1," Datasheet.

[39] Dow, "Syltherm 800: silicone heat transfer fluid," Datasheet.

[40] DELCO, "DelcoTerm Solar E15," Datasheet.

[41] U. Herrmann, M. Geyer, and D. Kearney, "Overview on thermal storage systems," in *Workshop on Thermal Storage for Trough Power Systems*, 2002.

[42] V.M.B. Nunes, C.S. Queriós, M.J.V. Lourenço, F.J.V. Santos, and C.A. Nieto de Castro, "Molten salts as engineering fluids – A review Part I. Molten alkali nitrates," *Applied Energy*, vol. 183, pp. 603-611, 2016.

[43] R. Serrano-López, J. Fradera, and S. Cuesta-López, "Molten salts database for energy applications," *Chemical Engineering and Processing: Process Intensification*, vol. 73, pp. 87-102, 2013.

[44] A.G. Fernández, S. Ushak, H. Galleguillos, and F.J. Pérez, "Development of new molten salts with LiNO3 and Ca(NO3)2 for energy storage in CSP

plants," *Applied Energy*, vol. 119, pp. 131-140, 2014.

[45] H. Tiznobaik and D. Shin, "Enhanced specific heat capacity of high-temperature molten salt-based nanofluids," *International Journal of Heat and Mass Transfer*, vol. 57, pp. 542-548, 2013.

[46] R. Hentschke, "On the specific heat capacity enhancement in nanofluids," *Nanoscale Research Letters*, vol. 11:88, 2016.

[47] N. Calvet et al., "Matériau de stockage thermique par chaleur sensible pour centrales électro-solaires testé sous flux solaire concentré," in *Proceedings in Congres Francais de Thermique*, 2010.

[48] P. Good et al., "Towards a commercial parabolic trough CSP system using air as heat transfer fluid," *Energy Procedia*, vol. 49, pp. 381-385, 2014.

[49] P. Good, G. Ambrosetti, A. Pedretti, and A. Steinfeld, "A 1.2 MWth solar parabolic trough system based on air as heat transfer fluid at 500 °C — Engineering design, modelling, construction, and testing," *Solar Energy*, vol. 139, pp. 398-411, 2016.

[50] L. Heller, "Literature review on heat transfer fluids and thermal energy storage systems in CSP plants," Solar Thermal Energy Research Group (STERG), 2013.

[51] M. Cascetta, G. Cau, P. Puddu, and F. Serra, "A comparison between CFD simulation and experimental investigation of a packed-bed thermal energy storage system," *Applied thermal engineering*, vol. 98, pp. 1263-1272, 2016.

[52] G. Zanganeh, A. Pedretti, S. Zavattoni, M. Barbato, and A. Steinfeld, "Packed-bed thermal storage for concentrated solar power - Pilot-scale demonstration and industrial-scale design," *Solar Energy*, vol. 86, pp. 3084-3098, 2012.

[53] G. Zanganeh, A. Pedretti, A. Haselbacher, and A. Steinfeld, "Design of packed bed thermal energy storage systems for high-temperature industrial process heat," *Applied Energy*, vol. 137, pp. 812-822, 2015.

[54] A. Meier, C. Winkler, and D. Wuillemin, "Experiment for modelling high temperature rock bed storage," *Solar Energy Materials*, vol. 24, no. 1-4, pp. 255-264, 1991.

[55] K.A.R. Ismail and R. Stuginsky, "A parametric study on possible fixed bed models for pcm and sensible heat storage," *Applied Thermal Engineering*, vol. 19, pp. 757-788, 1999.

[56] P. Bose and V.A. Amirtham, "A review on thermal conductivity enhancement of paraffinwax as latent heat energy storage material," *Renewable and Sustainable Energy Reviews*, vol. 65, pp. 81-100, 2016.

[57] F. Agyenim, N. Hewitt, P. Eames, and M. Smyth, "A review of materials, heat transfer and phase change problem formulation for latent heat thermal energy storage systems (LHTESS)," *Renewable and Sustainable Energy Reviews*, vol. 14, pp. 615-628, 2010.

[58] X. Meng et al., "Preparation and thermal properties of fatty acids/CNTs composite as shape-stabilized phase change materials," *Journal of Thermal Analysis and Calorimetry*, vol. 111, pp. 377-384, 2013.

[59] S.A. Mohamed et al., "A review on current status and challenges of inorganic

phase change materials for thermal energy storage systems," *Renewable and Sustainable Energy Reviews*, vol. 70, pp. 1072-1089, 2017.

[60] E. Palomo del Barrio, R. Cadoret, J. Daranlot, and F. Achchaq, "New sugar alcohols mixtures for long-term thermal energy storage applications at temperatures between 70 °C and 100 °C," *Solar Energy Materials and Solar Cells*, vol. 155, pp. 454-468, 2016.

[61] E. Palomo del Barrio et al., "Characterization of different sugar alcohols as phase change materials for thermal energy storage applications," *Solar Energy Materials and Solar Cells*, vol. 159, pp. 560-569, 2017.

[62] B. Cárdenas and N. León, "High temperature latent heat thermal energy storage: Phase change materials, design considerations and performance enhancement techniques," *Renewable and Sustainable Energy Reviews*, vol. 27, pp. 724-737, 2013.

[63] A. Jamekhorshid, S.M. Sadrameli, and M. Farid, "A review of microencapsulation methods of phase change materials (PCMs) as a thermal energy storage (TES) medium," *Renewable and Sustainable Energy Reviews*, vol. 31, pp. 531-542, 2014.

[64] Y.E. Milián, A. Gutierrez, M. Grágeda, and S. Ushak, "A review on encapsulation techniques for inorganic phase change materials and the influence on their thermophysical properties," *Renewable and Sustainable Energy Reviews*, vol. 73, pp. 983-999, 2017.

[65] R. Bayón and E. Rojas, "Analytical function describing the behaviour of a thermocline storage tank: A requirement for annual simulations of solar thermal power plants," *International Journal of Heat and Mass Transfer*, vol. 68, pp. 641-648, 2014.

[66] M. Karthik, A. Faik, P. Blanco-Rodríguez, J. Rodriguez-Aseguinolaza, and B. D'Aguanno, "Preparation of erythritol–graphite foam phase change composite with enhanced thermal conductivity for thermal energy storage applications," *Carbon*, vol. 94, pp. 266-276, 2015.

[67] M. Kenisarin and K. Mahkamov, "Salt hydrates as latent heat storage materials: Thermophysical properties and costs," *Solar Energy Materials & Solar Cells*, vol. 145, pp. 255-286, 2016.

[68] B. Zalba, J.M. Marín, L.F. Cabeza, and H. Mehling, "Review on thermal energy storage with phase change: materials, heat transfer analysis and applications," *Applied Thermal Engineering*, vol. 23, pp. 251-257, 2003.

[69] M. Liu, W. Saman, and F. Bruno, "Review on storage materials and thermal performance enhancement techniques for high temperature phase change thermal storage systems," *Renewable and Sustainable Energy Reviews*, vol. 16, pp. 2118-2132, 2012.

[70] E. Risueño et al., "Experimental investigation of Mg-Zn-Al metal alloys for latent heat storage application," *Journal of Alloys and Compounds*, vol. 685, pp. 724-732, 2016.

[71] E. Risueño et al., "Zinc-rich eutectic alloys for high energy density latent heat storage applications," *Journal of Alloys and Compounds*, vol. 705, pp. 714-721, 2017.

[72] R. Bayón, E. Rojas, L. Valenzuela, E. Zarza, and J. León, "Analysis of the experimental behaviour of a 100 kWth latent heat storage system for direct steam generation in solar thermal power plants," *Applied Thermal Engineering*, vol. 30, pp. 2643-2651, 2010.

[73] A. Rozenfeld, Y. Kozak, T. Rozenfeld, and G. Ziskind, "Experimental demonstration, modeling and analysis of a novel latent-heat thermal energy storage unit with a helical fin," *International Journal of Heat and Mass Transfer*, vol. 110, pp. 692-709, 2017.

[74] P. Blanco-Rodriguez et al., "Experiments on a lab scale TES unit using eutectic metal alloy as PCM," *Energy Procedia*, vol. 69, pp. 769-778, 2015.

[75] H.J. Xu and C.Y. Zhao, "Thermodynamic analysis and optimization of cascaded latent heat storage system for energy efficient utilization," *Energy*, vol. 90, pp. 1662-1673, 2015.

[76] H. Shabgard, C.W. Robak, T.L. Bergman, and A. Faghri, "Heat transfer and exergy analysis of cascaded latent heat storage with gravity-assisted heat pipes for concentrating solar power applications," *Solar Energy*, vol. 86, pp. 816-830, 2012.

[77] A. Alovisio, R. Chacartegui, C. Ortiz, J.M. Valverde, and V. Verda, "Optimizing the CSP-calcium Looping integration for thermochemical energy storage," *Energy Conversion and Management*, vol. 136, pp. 85-98, 2017.

[78] C. Agrafiotis, M. Roeb, M. Schmücke, and C. Sattler, "Exploitation of thermochemical cycles based on solid oxide redox systems for thermochemical storage of solar heat. Part 1: Testing of cobalt oxide-based powders," *Solar Energy*, vol. 102, pp. 189-211, 2014.

[79] L. André, S. Abanades, and G. Flamant, "Screening of thermochemical systems based on solid-gas reversible reactions for high temperature solar thermal energy storage," *Renewable and Sustainable Energy Reviews*, vol. 64, pp. 703-705, 2016.

[80] L. Jiang et al., "Experimental investigation on an innovative resorption system for energy storage and upgrade," *Energy Conversion and Management*, vol. 138, pp. 651-658, 2017.

[81] F. Marias, P. Neveu, G. Tanguy, and P. Papillon, "Thermodynamic analysis and experimental study of solid/gas reactor operating in open mode," *Energy*, vol. 66, pp. 757-765, 2014.

[82] S. Hongois, F. Kuznik, P. Stevens, and J.-J. Roux, "Development and characterisation of a new MgSO4–zeolite composite for long-term thermal energy storage," *Solar Energy Materials and Solar Cells*, vol. 95, pp. 1831–1837, 2011.

[83] C. Ferchaud, H. Zondag, R. de Boer, and C.C.M. Rindt, "Characterization of the sorption process in thermochemical materials for seasonal solar heat storage applications," in *12th International Conference on Energy Storage*, Lleida (Spain), 2012.

[84] E. Courbon, A. Skrylnyk, S. Hennaut, P. Andre, and M. Frere, "Single procedure to evaluate thermal energy storage densities of solid-gas systems: Application to solar energy storage in buildings," in *Récents*

Progrès en Génie des Procédés.: Ed. SFGP, 2011.

[85] R. de Boer, W.G. Haije, J.B.J. Veldhuis, and S.F. Smeding, "Solid-sorption cooling with integrated thermal storage: the sweat prototype," in *International Conference on Heat Powered Cycles*, Larnaca (Cyprus), 2004.

[86] M. Schmidt, A. Gutierrez, and M. Linder, "Thermochemical energy storage with CaO/Ca(OH)2 – Experimental investigation of the thermal capability at low vapor pressures in a lab scale reactor," *Applied Energy*, vol. 188, pp. 672-681, 2017.

[87] C. Agrafiotis, M. Roeb, M. Schmücker, and C. Sattler, "Exploitation of thermochemical cycles based on solid oxide redox systems for thermochemical storage of solar heat. Part 2: Redox oxide-coated porous ceramic structures as integrated thermochemical reactors/heat exchangers," *Solar Energy*, vol. 114, pp. 440–458, 2015.

[88] A.J. Carrillo, D.P. Serrano, P. Pizarro, and J.M. Coronado, "Thermochemical heat storage at high temperatures using Mn2O3/Mn3O4 system: narrowing the Redox hysteresis by metal Co-doping," *Energy Procedia*, vol. 73, pp. 263-271, 2015.

[89] M. Paskevicius, D.A. Sheppard, K. Williamson, and C.E. Buckley, "Metal hydride thermal heat storage prototype for concentrating solar thermal power," *Energy*, vol. 88, pp. 469-477, 2015.

[90] D.A. Sheppard, M. Paskevicius, and E. Craig, "Thermodynamics of hydrogen desorption from NaMgH3 and its application as a solar heat storage medium," *Chemistry of Materials*, vol. 23, no. 19, pp. 4298–4300, 2011.

[91] M. Felderhoff and B. Bogdanović, "High temperature metal hydrides as heat storage materials for solar and related applications," *International Journal of Molecular Sciences*, vol. 10, pp. 325-344, 2009.

[92] K.G. Sakellariou, G. Karagiannakis, Y.A. Criado, and A.G. Konstandopoulos, "Calcium oxide based materials for thermochemical heat storage in concentrated solar power plants," *Solar Energy*, vol. 122, pp. 215-230, 2015.

[93] N.R. Rhodes et al., "Solar thermochemical energy storage through carbonation cycles of SrCO3/SrO supported on SrZrO3," *Chemsuschem*, vol. 8, pp. 3793–3798, 2015.

[94] C. Prieto, P. Cooper, A.I. Fernández, and L.F. Cabeza, "Review of technology: Thermochemical energy storage for concentrated solar power plants," *Renewable and Sustainable Energy Reviews*, vol. 60, pp. 909-929, 2016.

[95] A. Singh et al., "Solar thermochemical heat storage via the Co3O4/CoO looping cycle: Storage reactor modelling and experimental validation," *Solar Energy*, vol. 144, pp. 453-465, 2017.

[96] J.E. Pacheco, S.K. Showalter, and W.J. Kolb, "Development of a molten-salt thermocline thermal storage system for parabolic trough plants," *Journal of Solar Energy Engineering*, vol. 124, pp. 152-159, 2002.

[97] S. Yagi and D. Kunii, "Studies on effective thermal conductivities in packed beds," *AIChE Journal*, vol. 3, no. 3, pp. 373-381, 1957.

[98] I. González, C.D. Pérez-Segarra, O. Lehmkuhl, S. Torras, and A. Oliva, "Thermo-mechanical parametric analysis of packed-bed thermocline

energy storage tanks," *Applied Energy*, vol. 179, pp. 1106-1122, 2016.

[99] R.M. Olsen, "Thermal Ratchet Stopping Shovel Wall," US20150184950 A1, January 2, 2014.

[100] K.G. Allen, T.W. von Backstrom, D. G. Kroger, and A.F.M. Kisters, "Rock bed storage for solar thermal power: Rock characteristics, suitability and availability," *Solar Energy Materials & Solar Cells*, vol. 126, pp. 170-183, 2014.

[101] Y. Jemmal, N. Zari, and M. Maaroufi, "Thermophysical and chemical analysis of gneiss rock as low cost candidate material for thermal energy storage in concentrated solar power plants," *Solar Energy Materials and Solar Cells*, vol. 157, pp. 377–382, 2016.

[102] H. Grirate et al., "Characterization of several Moroccan rocks used as filler material for thermal energy storage in CSP power plants," *Energy Procedia*, vol. 49, pp. 810-819, 2014.

[103] A. Gutierrez et al., "Advances in the valorization of waste and by-product materials as thermal energy storage (TES) materials," *Renewable and Sustainable Energy Reviews*, vol. 59, pp. 763-783, 2016.

[104] F. Motte, Q. Falcoz, E. Veron, and X. Py, "Compatibility tests between Solar Salt and thermal storage ceramics from inorganic industrial wastes," *Applied Energy*, vol. 155, pp. 14–22, 2015.

[105] A. Kere, N. Sadiki, X. Py, and V. Goetz, "Applicability of thermal energy storage recycled ceramics to high temperature and compressed air operating conditions," *Energy Conversion and Management*, vol. 88, pp. 113-119, 2014.

[106] S. Guillot et al., "Corrosion effects between molten salts and thermal storage material for concentrated solar power plants," *Applied Energy*, vol. 94, pp. 174–181, 2012.

[107] N. Calvet et al., "Compatibility of a post-industrial ceramic with nitrate molten salts for use as filler material in a thermocline storage system," *Applied Energy*, vol. 109, pp. 387–393, 2013.

[108] P. Klein, T.H. Roos, and T.J. Sheer, "Experimental investigation into a packed bed thermal storage solution for solar gas turbine systems," *Energy procedia*, vol. 49, pp. 840-849, 2014.

[109] J.-F. Hoffmann, T. Fasquelle, V. Goetz, and X. Py, "A thermocline thermal energy storage system with filler materials for concentrated solar power plants: Experimental data and numerical model sensitibity to different experimental tank scales," *Applied Thermal Engineering*, vol. 100, pp. 753-761, 2016.

[110] Z. Yang and S. V. Garimella, "Thermal analysis of solar thermal energy storage in a molten-salt thermocline," *Solar Energy*, vol. 84, pp. 974-985, 2010.

[111] A. Mawire, M. McPherson, R.R.J. van den Heetkamp, and S.J.P. Mlatho, "Simulated performance of storage materials for pebble bed thermal energy storage (TES) systems," *Applied Energy*, vol. 86, pp. 1246-1252, 2009.

[112] M.M. Valmiki et al., "Experimental investigation of thermal storage

processes in a thermocline tank," *Journal of Solar Energy Engineering*, vol. 134, pp. 1-9, 2012.

[113] C. Xu, Z. Wang, Y. He, X. Li, and F. Bai, "Sensitivity analysis of the numerical study on the thermal performance of a packed-bed molten salt thermocline thermal storage system ," *Applied Energy*, vol. 92, pp. 65-75, 2012.

[114] M. Y. Haller et al., "A method to determine stratification efficiency of thermal energy storage processes independently from storage heat losses," *Solar Energy*, vol. 84, pp. 997-1007, 2010.

[115] W. van Antwerpen, C.G. du Toit, and P.G. Rousseau, "A review of correlations to model the packing structure and effective thermal conductivity in packed beds of mono-sized spherical particles," *Nuclear Engineering and Design*, vol. 240, pp. 1803–1818, 2010.

[116] R. Bayón and E. Rojas, "Simulation of thermocline storage for solar thermal power plants: From dimensionless results to prototypes and real-size tanks," *International Journal of Heat and Mass Transfer*, vol. 60, pp. 713-721, 2013.

[117] A. Bruch, J.F. Fourmergué, and R. Couturier, "Experimental and numerical investigation of a pilot-scale thermal oil packed bed thermal storage system for CSP power plant," *Solar Energy*, vol. 105, pp. 116-125, 2014.

[118] L. Geissbühler, M. Kolman, G. Zanganeh, A. Haselbacher, and A. Steinfeld, "Analysis of industrial-scale high-temperature combined sensible/latent thermal energy storage," *Applied Thermal Engineering*, vol. 101, pp. 657-558, 2016.

[119] C. Odenthal, N. Breidenbach, and T. Bauer, "Modelling and operation strategies of DLR's large scale thermocline test facility (TESIS)," in *SolarPACES Conference*, Abu Dhabi (UAE), 2016.

[120] R. Bayón, E. Ricas, and E. Rojas, "Study of thermocline tank performance in dynamic processes stand-by periods with an analytical function," *Energy Procedia*, vol. 49, pp. 725-734, 2014.

[121] Z. Yang and S.V. Garimella, "Cyclic operation of molten-salt thermal energy storage in thermoclines for solar power plants," *Applied Energy*, vol. 103, pp. 256-265, 2013.

[122] G. Zanganeh et al., "Experimental and numerical investigation of combined sensible–latent heat for thermal energy storage at 575 °C and above," *Solar Energy*, vol. 114, pp. 77-90, 2015.

[123] G. Zanganeh, M. Commerford, A. Haselbacher, A. Pedretti, and A. Steinfeld, "Stabilization of the outflow temperature of a packed-bed thermal energy storage by combining rocks with phase change materials," *Applied Thermal Engineering*, vol. 70, pp. 316-320, 2015.

[124] S. Ströhle, A. Haselbacher, Z.R. Jovanovic, and A. Steinfeld, "Upgrading sensible-heat storage with a thermochemical storage section operated at variable pressure: An effective way toward active control of the heat-transfer fluid outflow temperature," *Applied Energy*, 2017.

[125] Airlight Energy [Online]: http://www.airlightenergy.com/ait-baha-csp-pilot-plant/

[126] D.Y. Goswamin, F. Kreith, and J.F. Kreider, *Principles of Solar Engineering*. New York: Taylor & Francis, 2000.

[127] D.A. Baharoon, H.A. Rahman, W.Z.W. Omar, and S.O. Fadhl, "Historical development of concentrating solar power technologies to generate clean electricity efficiently – A review," *Renewable and Sustainable Energy Reviews*, vol. 41, pp. 996-1027, 2015.

[128] T.M. Pavlovíc, I.S. Radonji´c, D.D. Milosavljevi´c, and L.S. Panti´c, "A review of concentrating solar power plants in the world and their potential use in Serbia," *Dragana D. Milosavljevi´ c, Lana S. Panti´ c*, vol. 16, pp. 3891-3902, 2012.

[129] E. Barbour, D. Mignard, Y. Ding, and Y. Li, "Adiabatic compressed air energy storage with packed bed thermal energy storage," *Applied Energy*, vol. 155, pp. 804-815, 2015.

[130] W.-D Steinmann, "Thermal energy storage systems for concentrating solar power (CSP) technology," *Advances in Thermal Energy Storage Systems*, pp. 511-531, 2015.

[131] Torresol, Gemasolar [Online]: http://www.torresolenergy.com/TORRESOL/planta-gemasolar/es

[132] Torresol, Valle 1 and Valle 2 [Online]: http://www.torresolenergy.com/TORRESOL/valle1-valle2-plants/en

[133] Tubosol, Puerto Errado 2 [Online]: http://www.puertoerrado2.com/home/

[134] CondiSys Solar Technology [Online]: http://www.heag.cn/file/20111129833641364.pdf

[135] STELA, Greenpeace International and SolarPACES, "Solar thermal electricity - Global outlook," 2016.

[136] X. Xu, K. Vignarooban, B. Xu, K. Hsu, and A.M. Kannan, "Prospects and problems of concentrating solar power technologies for power generation in the desert regions," *Renewable and Sustainable Energy Reviews*, vol. 53, pp. 1106-1131, 2016.

[137] A. Tiddens, M. Röger, H. Stadler, and B. Hoffschmidt, "Air return ratio measurements at the solar tower Jülich using a tracer gas method," *Solar Energy*, vol. 146, pp. 351-358, 2017.

[138] CSP World [Online]: http://cspworld.org/cspworldmap

[139] IEA, Key World Energy Statistics 2016, [Online]: https://www.iea.org/publications/freepublications/publication/KeyWorld2016.pdf

[140] A. I. Fernández, C. Barreneche, L. Miró, S. Brückner, and L. F. Cabeza, "19-Thermal energy storage (TES) systems using heat from waste," in *Advances in Thermal Energy Storage Systems*.: Elsevier, 2015, pp. 479-492.

[141] U.S. Department of Energy, "Waste heat recovery: technology and opportunities in the U.S. industry," Industrial Technologies Program, 2008.

[142] M. Pehnt, J. Boedekery, M. Arens, E. Jochem, and F. Idrissora, "Die Nutzung industrieller Abwärme–technisch-wirtschaftliche Potenziale und

energiepolitische Umsetzung," Heidelberg (Germany), 2010.

[143] International Energy Agency [Online]: www.iea.org

[144] P. Arce, M. Medrano, A. Gil, E. Oró, and L.F. Cabeza, "Overview of thermal energy storage (TES) potential energy savings and climate change mitigation in Spain and Europe," *Applied Energy*, vol. 88, pp. 2764-2774, 2011.

[145] G. Li and X. Zheng, "Thermal energy storage system integration forms for a sustainable future," *Renewable and Sustainable Energy Reviews*, vol. 62, pp. 736-757, 2016.

[146] J. Selvaraj, M. Thenarasu, S. Aravind, and P. Ashok, "Waste heat recovery from castings and scrap preheating by recovered heat using an intermediate heat transfer medium," *Applied Mechanics and Materials*, vol. 813-814, pp. 776-781, 2015.

[147] O. Andersson, L. Rydell, and T. Algotsson, "Efficient usage of waste heat by applying a seasonal energy storage (BTES)," in *ITT Water & Wastewater AB*, Emmaboda (Sweden), 2009.

[148] L.B. Katter and D.J. Peterson, "Application of thermal energy storage to process and waste heat recovery in the iron and steel industry," U.S. Department of Energy, Rocket Research Company, 1978.

[149] N. Maruoka and T. Akiyama, "Exergy recovery from steelmaking off-gas by latent heat storage for methanol production," *Energy*, vol. 31, no. 10-11, pp. 1632-1642, 2006.

[150] T. Steinparzer et al., "Heat exchangers and thermal energy storage concepts for the off-gas heat of steelmaking devices," *Journal of Physics: Conference Series*, vol. 395, p. 012158, 2012.

[151] W.D. Beverly, M. Rubeck, G.L. Vieth, and P.J. Hurley, "Applications of thermal energy storage in the paper and pulp industry," *Journal of Energy*, vol. 2, no. 6, pp. 375-380, 1978.

[152] J.H. Carr, P.J. Hurley, and P.J. Martin, "Applications of thermal energy storage to process heat storage and recovery in the paper and pulp industry," U.S. Department of Energy, Boeing Engineering and Construction Company, 1978.

[153] F.A. Jaeger, D.G. Beshore, F.M. Miller, and Ellis M. Gartner, "Thermal energy storage/waste heat recovery applications in the cement industry," in *Proceedings from the First Industrial Energy Technology Conference*, Houston (U.S.), 1978.

[154] Ridge Energy Storage & Grid Services L.P., "The Economic Impact of CAES on wind in TX, OK, and NM," 2005.

[155] M. Budt, D. Wolf, R. Span, and J. Yan, "A review on compressed air energy storage: Basic principles, past milestones and recent developments," *Applied Energy*, vol. 170, pp. 250-268, 2016.

[156] N. Hartmann, O. Vöhringer, C. Kruck, and L. Eltrop, "Simulation and analysis of different adiabatic compressed air energy storage plant configurations," *Applied Energy*, vol. 93, pp. 541-548, 2012.

[157] RWE Power AG., 2010, ADELE - adiabatic compressed-air energy storage

for electricity supply [Online]: https://www.rwe.com/web/cms/mediablob/en/391748/data/364260/1/rwe-power-ag/innovations/Brochure-ADELE.pdf

[158] S. Zunft, "Adiabatic CAES: The ADELE-ING project," in *SCCER Heat & Electricity Storage Symposium*, Villigen (CH), 2015.

[159] Y. Mazloum, H. Sayah, and M. Nemer, "Dynamic modeling and simulation of an isobaric adiabatic compressed air energy storage (IA-CAES) system," *Journal of Energy Storage*, vol. 11, pp. 178-190, 2017.

[160] L. Nielsen and R. Leithner, "Dynamic simulation of an innovative compressed air energy storage plant – detailed modeling of the storage cavern," *WSEAS Transactions on Power Systems*, vol. 8, no. 4, pp. 253-263, 2009.

[161] D. Wolf and M. Budt, "LTA-CAES – A low-temperature approach to adiabatic compressed air energy storage," *Applied Energy*, vol. 125, pp. 158-164, 2014.

[162] X. Luo et al., "Modelling study, efficiency analysis and optimisation of large-scale adiabatic compressed air energy storage systems with low-temperature thermal storage," *Applied Energy*, vol. 162, pp. 589-600, 2016.

[163] J.-L. Liu and J.-H. Wang, "A comparative research of two adiabatic compressed air energy storage systems," *Energy Conversion and Management*, vol. 108, pp. 566–578, 2016.

[164] S. Wang, X. Zhang, L. Yang, Y. Zhou, and J. Wang, "Experimental study of compressed air energy storage system with thermal energy storage," *Energy*, vol. 103, pp. 182-191, 2016.

[165] A. Sciacovelli et al., "Dynamic simulation of adiabatic compressed air energy storage (A-CAES) plant with integrated thermal storage – Link between components performance and plant performance," *Applied Energy*, vol. 185, pp. 16-28, 2017.

[166] H. Peng, R. Li, X. Ling, and H. Dong, "Modeling on heat storage performance of compressed air in a packed bed system," *Applied Energy*, vol. 160, pp. 1-9, 2015.

[167] Worldsteel Association. (2016) Fact sheet on steel and raw materials.

[168] Worldsteel Association. (2016) Fact sheet on energy use in the steel industry.

[169] EUROSLAG, "Legal status of slags: position paper," Technical report 2006.

[170] EUROSLAG and EUROFER, "Position paper on the status of ferrous slag," Technical report 2012.

[171] EUROSLAG [Online]: http://www.euroslag.com/products/properties/

[172] A. Mills, "The lodestone: History, physics, and formation," *Annals of Science*, vol. 61, no. 3, pp. 272-319, 2004.

[173] J. Roger, J.N. Pons, R. Massart, A. Halbreich, and J.C. Bacri, "Some biomedical applications of ferrofluids," *The European Physical Journal Applied Physics*, vol. 5, pp. 321-325, 1999.

[174] S. Oswald, W. Kinzelbach, A. Greiner, and G. Brix, "Observation of flow and

transport processes in artificial porous media via magnetic resonance imaging in three dimensions," *Geoderma*, vol. 80, no. 3, pp. 417-429, 1997.

[175] A. Jordan, R. Scholz, P. Wust, H. Fähling, and R. Felix, "Magnetic fluid hyperthermia (MFH): Cancer treatment with AC magnetic field induced excitation of biocompatible superparamagnetic nanoparticles," *Journal of Magnetism and Magnetic Materials*, vol. 2011, no. 1-3, pp. 413-419, 1999.

[176] A. Navrotsky, L. Mazeina, and J. Majzlan, "Size-driven structural and thermodynamic complexity in iron oxides," *Science*, vol. 319, no. 5870, pp. 1635-1638, 2008.

[177] R.R. Hong, T.T. Pan, and H.Z. Li, "Microwave synthesis of magnetic Fe3O4 nanoparticles used as a precursor of nanocomposites and ferrofluids," *Journal of Magnetism and Magnetic Materials*, vol. 303, no. 1, pp. 60-68, 2006.

[178] L. Blaney, "Magnetite (Fe3O4): properties, synthesis, and applications," *Lehigh Preserve*, vol. 15, 2007.

[179] S.K. Kuila, R. Chatterjee, and D. Ghosh, "Kinetics of hydrogen reduction of magnetite ore fines," *International Journal of Hydrogen Energy*, vol. 41, pp. 9256-9266, 2016.

Chapter 2:

Materials characterization and selection

2 Materials characterization and selection

In the introduction chapter two families of candidate materials, iron and steel slag and magnetite ore, have been presented. In order to demonstrate their suitability for high temperature heat storage solutions, in this chapter their main structural, thermal and mechanical properties are characterized. Furthermore, the obtained results are compared with materials reported in the literature for similar thermal energy storage purposes. Finally, among the studied materials families, a selection of the most promising ones according to the specific requirements for a packed bed TES material presented in section 1.3 is carried out. The chosen materials are used in further investigation activities within this thesis.

2.1. Proposed thermal energy storage materials

A total of seven materials are considered for analysis, six slag samples with different origin and a natural ore, magnetite. In the following, the source and characteristics of each of these candidate materials are described in detail.

2.1.1. Blast furnace slag

An air-cooled blast furnace slag (BFS) is selected for analysis. After the slag treatment in the plant, it is presented as porous irregular particles with an average diameter below 3 cm. Before its characterization, the material is sieved and only the fraction above 1 cm is considered. In Figure 2.1 the general aspect of the BFS used in this thesis is depicted.

Figure 2.1. Investigated BFS sample.

2.1.2. Basic oxygen furnace slag

Two basic oxygen furnace slag (BOFS) samples are also studied in this work. One of them comes from the unique steelmaker in Spain using this technology and,

the second one, from a Chinese steelwork. In this thesis, the former is referred as *BOF Slag 1* and the latter as *BOF Slag 2*.

A mixed cooling process using air in a first step, and water in a second one was implemented in the obtainment of *BOF Slag 1* at the steelworks. Meanwhile, *BOF Slag 2*, was cooled down in open air. Regarding *BOF Slag 1*, it is found in two fractions: one below 2 cm and another from 2 to 5 cm. Due to the requirements for the different characterization techniques applied in this work, the latter is selected. On the other hand, the supplied *BOF Slag 2* has an average particle size between 5 and 10 cm. Both selected BOFS fractions are shown in Figure 2.2.

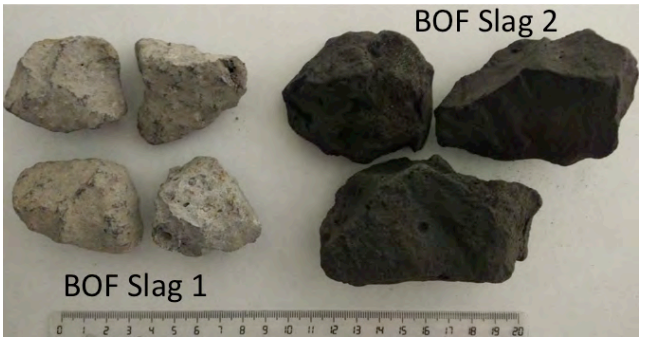

Figure 2.2. Investigated BOFS samples.

2.1.3. Electric arc furnace slag

Additionally, three electric arc furnace slag (EAFS) samples coming from different steelmakers are considered. The main difference between them, apart from their slight variation in the chemical composition (see Table 2.3), is the cooling procedure while obtaining them in the steelworks. The slag referred as *EAF Slag 1*, was directly chilled using water in a process that takes around 4-5 hours, whereas the one called *EAF Slag 2* in this work was cooled down by a mixed process that takes around 4-6 hours (2-3 hours in open air and another 2-3 hours with water) and, the one as *EAF Slag 3* was solidified under open air in a process that takes around 3-5 days.

Even if *EAF Slag 1* and *2* are provided by different companies, both of them are managed in the steelworks by an external waste treatment agent, which prepares the material for the valorisation as an aggregate for construction applications. In both plants, the solidified slag is crushed into three fractions: <0.5 cm, 0.5-1.2 cm

and 1.2-2.5 cm. Taking into account the requirements in the preparation of the samples for the different characterizations techniques (see section 2.2) used in this work, large samples were supplied for its use in this thesis (see Figure 2.3 for its general aspect). Finally, *EAF Slag 3* comes from a small steel producer and the slag is obtained as big blocks. In order to obtain samples for characterization, the received blocks were crushed, up to the size shown in Figure 2.3.

Figure 2.3. Investigated EAFS samples.

2.1.4. Magnetite ore

In addition to the aforementioned six slag samples, a natural material, magnetite ore, is also considered. In particular, natural magnetite supplied by LKAB minerals (Sweden) is selected for investigation, henceforth denoted as *Magnetite ore*. This material is presented as pebbles of approximately 1 cm as it is shown in Figure 2.4. Big samples were also received in order to perform the machining of the specimens required for the different characterization techniques.

Figure 2.4. Investigated magnetite ore.

2.2. Characterization techniques

2.2.1. Inductively coupled plasma – optical emission spectroscopy

Elemental analysis of the studied materials is performed by means of the inductively coupled plasma – optical emission spectroscopy (ICP-OES) technique, with a Perkin Elmer Optima 2000 OV experimental equipment.

ICP-OES is one of the most usual techniques used for elemental analysis due to its good detection limits, applicability to multi-elemental samples and high specificity. In this experimental methodology, a liquid sample is nebulized in a special spray-chamber and a plasma source is used to dissociate the generated droplets into its constituent atoms or ions, exciting them to a higher energy level. With this operation, photons of a characteristic wavelength are emitted depending on the analysed element. The obtained light is recorded by means of an optical spectrometer and, by comparison of the obtained signal intensity with calibrated standards, the measurement provides the quantitative composition of the sample.

For the measurements carried out in this chapter, fine powders of the considered materials are prepared and digested in an ETHOS 1 Advanced Microwave Digestion System in a two-step process as described by Fiore et al. in [1]. Firstly, samples are digested with a 1:1 solution of phosphoric (85%) and sulphuric (96%) acid. After cooling, hydrofluoric acid (48%) is added to the mixture and a new digestion is performed. The final digested samples are filled up with ultrapure water and filtrated to 0.45 μm. This elemental analysis is performed for the expected major components in the samples (Al, Ca, Cr, Fe, Mg, Mn and Si).

2.2.2. Scanning electron microscopy

Scanning electron microscopy (SEM) is a technique that allows microstructural and morphology investigations of a given sample. It produces high-resolution images of a sample by a focused beam of accelerated electrons. When the electron beam interacts with the sample, it results in the emission of electrons or photons. These particles, collected with an adequate detector provide information about the microstructure, topography and chemical composition of the sample.

Among the resulting particles, secondary electrons (SE) are electrons removed from the sample surface due to an ionization process generated by the electron beam. They are produced when an electron passes close to the nucleus of an atom supplying it enough energy to jump out of the structure. This type of electrons are very close to the surface and hence, they can provide topographical information of the sample at very high resolution (less than 1 nm).

Characteristic X-rays are produced when a SE is removed and a deeper electron can jump to fill the left gap. The excess of energy of the migrating electron is emitted as X-ray. This X-ray, characteristic of each element, can be used to obtain information on the sample composition, for example, by means of an energy dispersive X-ray spectrometer (EDS or EDX).

Back-scattered electrons (BSE) are electrons reflected from the sample by elastic scattering produced by the collision of the electron beam with the atom nucleus. Since the intensity of the BSE is proportional to the atomic number, they provide information about the distribution of different elements in the sample. These electrons are removed from deeper locations than SE and, consequently, the quality of the obtained images ranges from 5 to 10 nm.

In this thesis, polished samples of the studied materials are imaged by means of a Quanta 200 FEG SEM, operated in high vacuum mode at 30 kV, selected after an optimization process, and with a BSE detector (BSED). In addition, EDX analyses are carried out in order to obtain chemical compositional maps of the different observed sample zones.

2.2.3. X-ray powder diffraction

X-ray diffraction is a widely used technique for the determination and characterization of crystalline material structures. A crystalline solid consists of ordered three-dimensional periodic arrangements of atoms. The unit cell is the basic repeating unit that defines a crystal. When electromagnetic radiation (i.e X-ray) impact on the crystalline material, the different planes can scatter and reflect the incident radiation so diffraction patterns are generated. The diffracted X-ray beam is composed by a large number of scattered rays of different parallel planes that accomplish the following conditions:

1. The normal plane must be parallel to the diffraction vector;
2. The angle of incidence θ on a plane atom is equal to the scattering angle (θ);
3. The angle of diffraction (2θ) is the sum of the incidence and scattered angles;
4. The Bragg law [2] is satisfied:

$$n \cdot \lambda = 2 \cdot b \cdot sin\theta; \tag{2.1}$$

where n is a positive integer determined by the diffraction order, λ is the incident beam wavelength, b the interplanar distance and θ the incidence angle. In an X-ray diffractometer the wavelength is known and, the sample is rotated to generate a family of planes when a specific angle (θ) is reached.

A crystalline powder sample consists of a large number of randomly orientated crystals. For any given lattice plane, there are crystals in the sample orientated with appropriate Bragg angle θ as to produce diffraction. These crystals take up any possible angular positions and therefore the diffracted beams are emitted as cones of radiation, also named Debye cones.

A diffraction pattern shows the angle position (2 θ) and the intensity of the generated peaks. Each of these peaks corresponds to a set of crystal planes, where the distance between the planes determines the peaks positions and the intensity, the amount of atoms in such plane. By analysing the obtained diffractograms, qualitative and quantitative information of the sample crystals might be obtained among other parameters.

In this thesis, the X-ray powder diffraction (XRPD) technique is used for the crystal phase identification analysis of the studied materials. Measurements are performed by means of a BRUKER D-8 Advance Diffractometer in Bragg-Brentano geometry (θ-θ) using CuK$\alpha_{1,2}$ radiation. Data is collected between 20° and 110° in 2θ with a step size of 0.02° and counting time of 8 seconds per step.

Additionally, the Fullprof software [3] is used to refine the obtained diffractograms in order to get the right phase compositions and the positions of the Bragg peaks.

2.2.4. Gas pycnometry

Gas pycnometry is an extensively used technique for measuring skeletal density and volume of solid materials. This technique relies on the Boyle's law [4] and the displacement method to perform accurate measurements of solid volumes. An inert gas, usually helium or nitrogen, is used as displacement medium.

The sample is introduced in a chamber of known volume and properly sealed. During the measurement, the inert gas is admitted and then expanded into another internal volume. The pressures observed upon filling the measurement sample chamber and then discharging it into the secondary one allow the calculation of the solid sample volume following the relation:

$$p_1 \cdot V_1 = p_2 \cdot V_2; \tag{2.2}$$

where p_1 and p_2 correspond to the pressure in the measurement and secondary chambers respectively; V_1 to the gas volume in the chamber containing the sample and, V_2 the secondary chamber volume. The difference between V_1 and the total volume of the chamber corresponds to the sample volume. Dividing this value by the sample weight, the skeletal density of the material is obtained.

A helium pycnometer AccuPyc II 1340 is used to determine skeletal densities, which provides an experimental error below 0.01% of the cell chamber volume. In the measurements, a 10 cm^3 cell and samples of around 3.5 cm^3 are used.

2.2.5. Hg porosimetry

Porosimetry is a technique that permits measurements of pore size, volume and distribution among other porosity-related properties of a material. This technique involves the intrusion of a non-wetting liquid at high pressure into a material. By this procedure, the pore size can be determined based on the external pressure needed to force the liquid into a pore against the opposing force of the surface tension of the liquid using the Washburn equation [5]:

$$p_l - p_g = -\frac{4 \cdot \gamma \cdot cos\theta}{d_{pore}}; \tag{2.3}$$

where p_l and p_g are the pressure of the intruded liquid and the gas respectively; γ the liquid surface tension; θ the liquid contact angle and d_{pore}, the pore diameter.

Since mercury does not wet most substances and spontaneously do not penetrate pores by capillary action, is one of the most usual liquids used in porosimetry. Taking this into account, the pore size distribution is determined by means of the mercury porosimetry technique with a Pore Master 60 from Quantachrome Instruments, which provides an experimental error below 0.1%. For the measurements small samples of around 1 gram are used.

2.2.6. Dilatometry

Dilatometry is a thermo-analytical technique for the measurement of expansion or shrinkage of a material when subjected to a controlled temperature change. To determine the thermal expansion coefficient, two physical quantities must be measured on a sample: displacement and temperature.

In this thesis, a push-rod dilatometer Model 402C from Netzsch (Figure 2.5) is used. In this type of devices, the measured sample is heated in a furnace and horizontal displacements are transmitted to a sensor by means of push rods. This method is a widely used technique for the determination of the thermal expansion coefficient [6] in isotropic materials with an experimental error below 1%.

Since the measuring system (connecting rod) is exposed to the same temperature as the sample, it also expands. Consequently, the obtained expansion value is a relative measurement. This value is converted afterwards by using a previous measurement of a known/reference rod material.

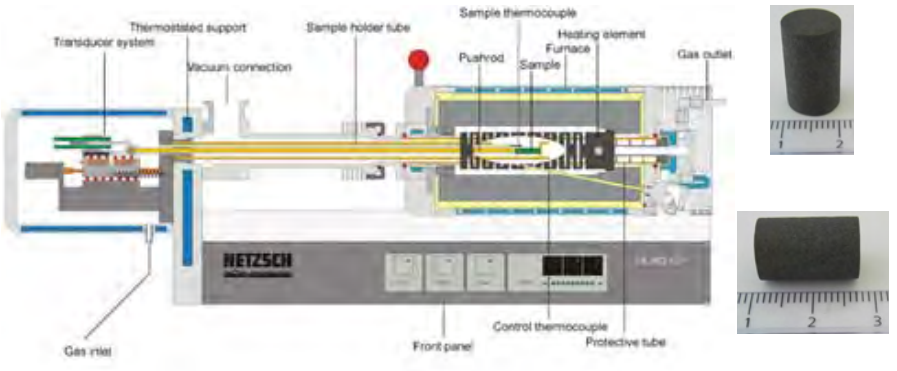

Figure 2.5. Dilatometer and samples used for thermal expansion measurements.

The dilatometer used for this work is equipped with an alumina sample holder and push rod. The temperature measurement is performed by means of a calibrated S-type thermocouple. Measurements are carried out from ambient temperature (~20 °C) up to 1000 °C at a heating rate of 10 °C/min using as reference/calibration material an alumina rod of 0.6 cm diameter and 2 cm length. For the linear thermal expansion measurements, cylindrical rods of ~1 cm of diameter and length between 2.5 and 3.0 cm are machined (see Figure 2.5).

2.2.7. Compression tests

The maximum strength a material can stand under compression forces before mechanical failure is a critical material property in many applications. A universal compression machine INSTRON 4206 operated at room temperature is used in this thesis. For these measurements, cubical samples of around 1 cm x 1 cm x 1 cm are prepared, and a test speed of 0.3 cm/min and a load cell of 100 KN applied. Figure 2.6 contains an image of the device used for the performed measurements together with an example of the machined samples.

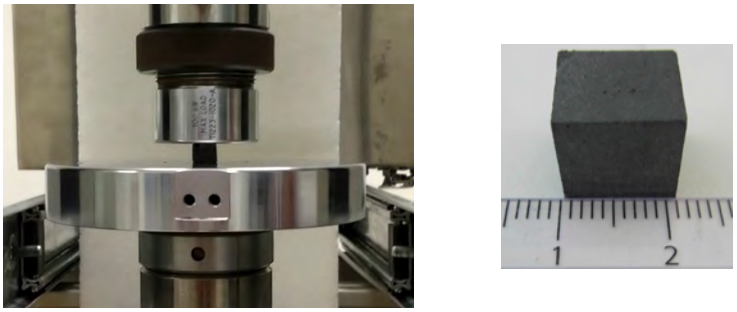

Figure 2.6. Device and sample used for compression strength measurements.

2.2.8. Modulated differential scanning calorimetry

The modulated differential scanning calorimetry (MDSC) method developed by Reading et al. [7] is implemented in this work for the determination of the specific heat [8]. This method consists in performing a standard differential scanning calorimetry (DSC) measurement, adding a sinusoidal periodic temperature oscillation experiment comprising constant heating rate and temperature segments:

$$\frac{dT}{dt} = \varphi + A_T \cdot \phi \cdot \cos(\phi \cdot t); \quad (2.4)$$

where dT/dt is the instantaneous heating rate, φ the underlying heating rate, A_T the amplitude of the modulation, ϕ the angular frequency and t the time.

Applying this heating rate, the resultant heat flow can be described as follows:

$$\frac{dQ}{dt} = c_p \cdot \varphi + f(T,t); \quad (2.5)$$

where dQ/dt is the total heat flow and $f(T,t)$ a heat flow from kinetic processes (temperature and time dependent). The first term on the right-hand-side is commonly known as "specific heat component."

The specific heat of the sample is continuously determined by dividing the modulated heat flow amplitude by the modulated heating rate amplitude:

$$c_p = c_p K \cdot \frac{Heat\ flow\ (Sample) - Heat\ flow\ (blank)}{Heating\ rate}; \quad (2.6)$$

where $c_p K$ is a calibration constant.

For the performed specific heat measurements a MDSC Q2000 from TA Instruments is used, which provides an experimental error in this property below 3%. The modulation amplitude and period are fixed to ±1 K and 120 s respectively. The selected continuous heating rate is 2 K·min^{-1}. These experimental conditions are fixed after an optimization analysis. The instrument is calibrated before each measurement using sapphire as standard reference material. A solid planar piece of around 20 mg is placed in highly conductive aluminium hermetic pans ensuring a good thermal contact between the sample surface and the base of the pan.

2.2.9. Laser flash method

The laser flash method consists in the determination of the superficial temperature change as a function of time of a planar solid sample heated up from the opposite parallel surface by a high intensity and short duration laser pulse. Laser flash measurements are performed in a laser flash apparatus (LFA). The mathematical analysis of the temperature/time function allows the determination of the thermal diffusivity (α). Under adiabatic conditions, thermal diffusivity can be calculated as:

$$\alpha = 0.1388 \cdot \frac{l^2}{t_{0.5}}; \tag{2.7}$$

where l is the thickness of the sample and $t_{0.5}$ is the time at 50% of the temperature increase measured at the rear of tested sample.

Even if the laser flash method is mainly used for measuring thermal diffusivity, the specific heat (c_p) can also be determined with this technique following the equation given by Parker et al. [9]:

$$c_p = \frac{Q}{\rho \cdot l \cdot A} \cdot \frac{1}{\Delta T_{max}}; \tag{2.8}$$

where Q is the energy absorbed by the sample, l and A are the sample thickness and area respectively, and ΔT_{max} is the maximum temperature detected in the rear surface. However, this equation is only valid for adiabatic cases neglecting radiative heat losses from the sample surfaces. In order to include these heat losses different mathematical models are available [10-12]. In this thesis, a heat loss correction according to Cowan [10] is used. This model assumes that heat losses follow an exponential decay.

In order to evaluate the specific heat, the maximum temperature reached in the rear face of the sample is needed. However, the detector of the LFA, a thin gold strip, gives a voltage signal (U). Taking into account that:

$$\Delta U \propto \Delta T; \tag{2.9}$$

a reference specific heat measurement of a known material is needed in order to find the proportional constant. Taking this into account, the specific heat of the sample can be calculated according to the following expression:

$$c_p = \frac{T^{Ref}}{T} \cdot \frac{(\rho \cdot l)^{Ref}}{\rho \cdot l} \cdot {c_p}^{Ref}. \tag{2.10}$$

Finally, the thermal conductivity of the sample (k) can be obtained from the thermal diffusivity and specific heat values measured with this technique, and the density according to the following equation:

$$k = \alpha \cdot \rho \cdot c_p. \tag{2.11}$$

For all the measurements carried out with the LFA, square samples with a side length of 1 cm and a thickness of 0.2 cm are used. The sample machining

guarantees parallel faces and smooth surfaces. In order to minimize the experimental error, a graphite film prime is added over the sample surfaces. These measurements are performed with a LFA 457 MicroFlash apparatus from Netzsch, which provides an experimental error below 5%.

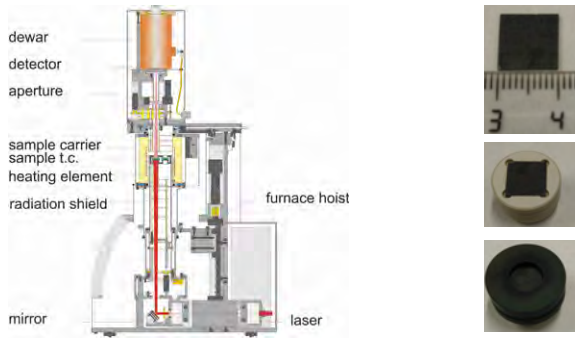

Figure 2.7. Laser flash apparatus, sample holder and sample.

2.3. Thermo-physical properties of the studied materials

This section is devoted to present the main structural, mechanical and thermal properties of the seven investigated TES materials. In these terms, the above-mentioned techniques are applied to determine their chemical composition, crystallographic structure, density, porosity, thermal expansion, maximum compression strength, specific heat, thermal diffusivity and thermal conductivity.

2.3.1. Chemical composition and structural analysis

In order to determine the elemental composition of the seven investigated materials, the ICP-OES technique is applied. Additionally, to analyse their crystallographic phases and superficial structures, XRPD and SEM techniques are used respectively. Finally, their density, porosity and pore size distribution are measured by gas pycnometry and Hg porosimetry techniques.

2.3.1.1. Chemical composition

The obtained ICP-OES elemental compositions are presented as a function of the measured material typology: BFS, BOFS, EAFS and *Magnetite ore,* in Table 2.1, Table 2.2, Table 2.3 and Table 2.4 respectively. In order to discuss the

representativeness of the proposed TES candidates, chemical compositions of similar materials, reported in literature, are also included in each table.

Table 2.1. Elemental analysis of *BF slag* together with literature-reported data.

	Al (%w)	Ca (%w)	Cr (%w)	Fe (%w)	Mg (%w)	Mn (%w)	Si (%w)
BF Slag	9.7	29.3	-	0.2	4.0	1.3	14.1
[13]	2.9	34.3	-	0.7	4.0	2.4	14.4
[14]	2.3	27.6	-	0.8	4.6	-	14.0
[15]	5.9	29.4	-	1.9	5.0	-	16.0
[16]	6.7	29.5	-	0.3	3.6	-	16.1

Attending to the *BF Slag* chemical composition (Table 2.1), it is mainly composed by calcium, silicon and aluminium. It can be observed that, even if *BF Slag* is a by-product from the iron production, its content in this metal is negligible. When comparing the obtained chemical composition with other BFS samples from literature, it can be seen that most of the elements are in a similar concentration range with a slightly higher concentration of aluminium. The obtained results permit to consider the investigated *BF Slag* as representative sample of other BFS produced worldwide.

Table 2.2. Elemental composition of the investigated and literature-reported BOFS samples.

	Al (%w)	Ca (%w)	Cr (%w)	Fe (%w)	Mg (%w)	Mn (%w)	Si (%w)
BOF Slag 1	6.8	19.2	-	0.4	3.4	2.0	15.5
BOF Slag 2	1.2	26.6	0.1	20.9	3.7	3.6	8.3
[17]	0.6	33.1	-	16.2	5.0	2.1	5.2
[18]	1.7	31.0	-	20.0	3.5	-	6.3
[19]	0.9	35.1	-	17.1	2.9	1.1	6.2
[19]	1.7	30.5	-	17.2	3.1	1.4	9.0
[19]	1.0	32.8	-	10.8	3.5	1.5	5.8

Regarding the chemical composition of the two investigated BOFS samples (Table 2.2), considerable differences are found. *BOF Slag 2* has an important content in iron, meanwhile this metal can be considered as a trace (0.4%) in *BOF*

Slag 1. On the other hand, in both BOFS samples the major components are calcium and silicium while, aluminium, magnesium and manganese are present at considerably lower concentrations.

Comparing the obtained compositions with those reported in literature, similar concentrations are found for *BOF Slag 2*. These results allow concluding that *BOF Slag 2* is representative of other BOFS generated worldwide whereas, *BOF Slag 1* should be considered as a special slag.

Going through the obtained results from the elemental characterization of the three investigated EAFS samples (Table 2.3), calcium and iron are obtained as predominant elements. Elements such as aluminium, silicium, magnesium, manganese or chromium are present at much lower concentrations. On the other hand, comparing the obtained chemical compositions with those from EAFS samples reported in literature, similar values are found. Only small differences (slightly higher values) are observed for calcium in *EAF Slag 1* and *3*, and for iron in *EAF Slag 2*. In addition, silicium concentrations in *EAF Slag 1* and *2* are lower than those reported in the literature. This compositional similarity makes the studied EAFS samples representative of other worldwide-produced.

Table 2.3. Elemental composition of the investigated and literature-reported EAFS samples.

	Al (%w)	Ca (%w)	Cr (%w)	Fe (%w)	Mg (%w)	Mn (%w)	Si (%w)
EAF Slag 1	2.4	23.5	0.7	25.9	6.7	2.1	5.2
EAF Slag 2	2.1	16.3	1.7	35.4	3.6	4.8	3.5
EAF Slag 3	4.1	22.1	1.2	25.6	0.6	1.4	10.1
[20]	4.5	18.6	1.7	22.8	4.6	4.3	7.0
[21]	3.9	17.1	-	29.7	3.1	3.5	7.1
[22]	1.5	18.3	-	24.6	4.5	0.2	8.7
[23]	4.5	14.7	-	22.8	2.2	-	10.6

Finally, from the chemical composition obtained for the *Magnetite ore* (Table 2.4), it can be observed that the considered material is mainly composed by iron. Additionally, some traces of aluminium, calcium, silicon, magnesium and manganese are also present.

Table 2.4. Elemental analysis of *Magnetite ore*.

	Al	Ca	Cr	Fe	Mg	Mn	Si
$\%_w$	0.2	2.1	-	57.5	0.2	0.1	1.0

2.3.1.2. Superficial and crystallographic analysis

In order to understand how the detected elements are distributed in the structure of each material, SEM and XRPD techniques are applied. In Figure 2.8, Figure 2.10, Figure 2.12 and Figure 2.14, the SEM images of *BF Slag*, BOFS, EAFS and *Magnetite ore,* are presented respectively. In addition, their corresponding compositional EDX maps are also included in each image. In a similar way, Figure 2.9, Figure 2.11, Figure 2.13 and Figure 2.15 contain the XRPD patterns obtained for the seven investigated materials. For each material, a pattern in red dots, and another one in continuous black line are presented corresponding to the measured and calculated with the Fullprof program ones. Additionally, the vertical bars on each pattern correspond to the Bragg reflections of the different crystallographic phases identified in the material.

Attending to the surface image and EDX maps obtained for *BF Slag* (Figure 2.8), two main compositional zones can be distinguished: one rich in calcium and aluminium and, another one in calcium, silicium and manganese. Regarding the size of the crystalline aggregates forming the slag, they are in the order of hundred of micrometres. This large size is caused by the slow cooling method applied to this material in the steelworks.

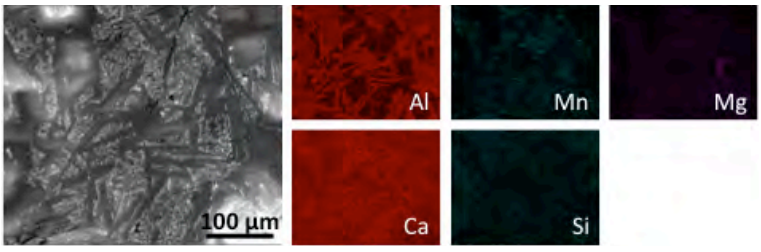

Figure 2.8. *BF Slag* SEM image and EDX maps.

On the other hand, from the measured XRPD pattern and its refinement analysis using the Fullprof program (Figure 2.9), three crystallographic phases are identified in the *BF Slag*. These phases are calcium manganese oxide ($CaMnO_{2.8}$), magnesium aluminium silicate ($MgAlSi_{1.5}O_8$) and Akermanite

($Ca_2(Al_{0.46}Mg_{0.54})((Al_{0.23}Si_{0.77})_2O_7)$). The first one can be associated to the light grey zone in Figure 2.8, the second one to the medium grey area and the third one to the darkest zone.

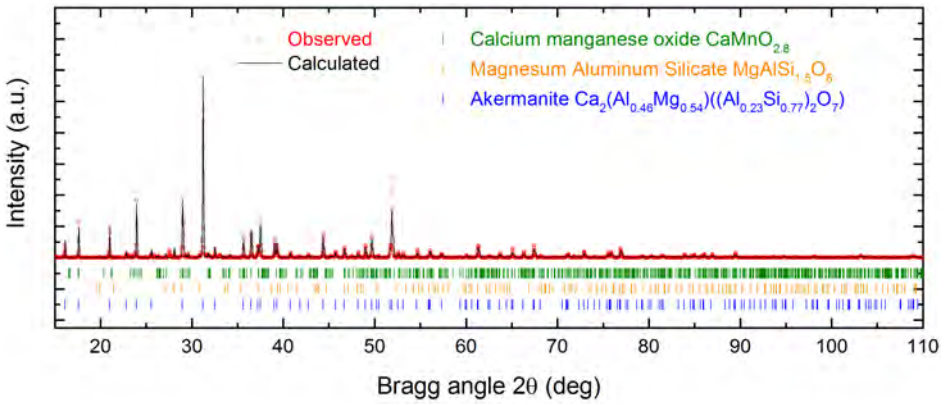

Figure 2.9. *BF Slag* XRPD pattern and Bragg reflections of the identified crystallographic phases.

Regarding the two investigated BOFS samples, their surface images and the corresponding EDX maps are presented in Figure 2.10a and b, for *BOF Slag 1* and *2* respectively. Attending to the results of *BOF Slag 1*, calcium and silicium are present in the entire sample. Additionally, an aluminium and magnesium rich region is also distinguished (dark grey zone). On the other hand, two regions can be differentiated in *BOF Slag 2*: one rich in iron and manganese (white zone), and a second one rich in calcium, silicium and aluminium (dark grey zone).

Additionally, the formed crystals in both BOFS samples are in the order of 100 μm. Even if a faster cooling rate was applied in the obtainment of *BOF Slag 1*, it presents slightly higher crystal sizes than *BOF Slag 2*.

From the XRPD patterns obtained for *BOF Slag 1* (Figure 2.11), three phases are found: Akermanite ($Ca_2(Al_{0.46}Mg_{0.54})((Al_{0.23}Si_{0.77})_2O_7)$), calcio-olivine ($Ca_2SiO_4$) and soda-melilite ($CaNaAlSi_2O_4$). Comparing between the EDX maps (Figure 2.10a) and the identified crystallographic phases, the Akermanite corresponds to the aluminium and magnesium rich region (dark grey zones), and the two additional phases to the calcium and silicium rich regions (clear grey zones).

On the other hand, from the patterns of *BOF Slag 2* (Figure 2.11), five crystallographic phases are identified: Larnite (Ca_2SiO_4), Brownmillerite

($Ca_2Fe_2O_5$), Sillimanite (Al_2SiO_5), Magnetite ($Fe_{2.964}O_4$) and Wustite ($Fe_{0.925}O$). From these five phases, the former three correspond to the darkest region in the SEM image in Figure 2.10b. Meanwhile, the other two match with the iron rich areas (white zone in SEM image in Figure 2.10b).

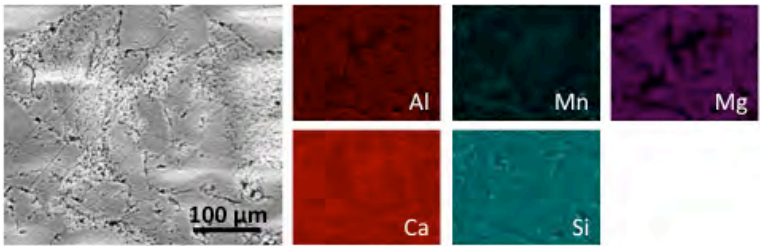

(a)

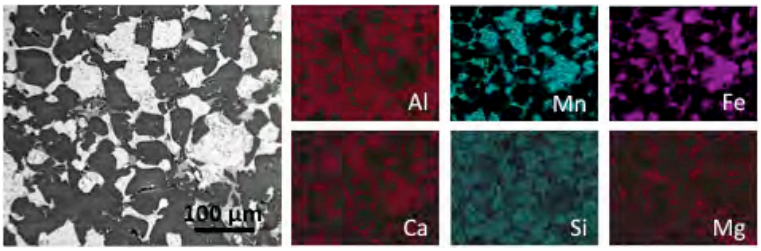

(b)

Figure 2.10. SEM images and EDX maps of: (a) *BOF Slag 1* and (b) *BOF Slag 2*.

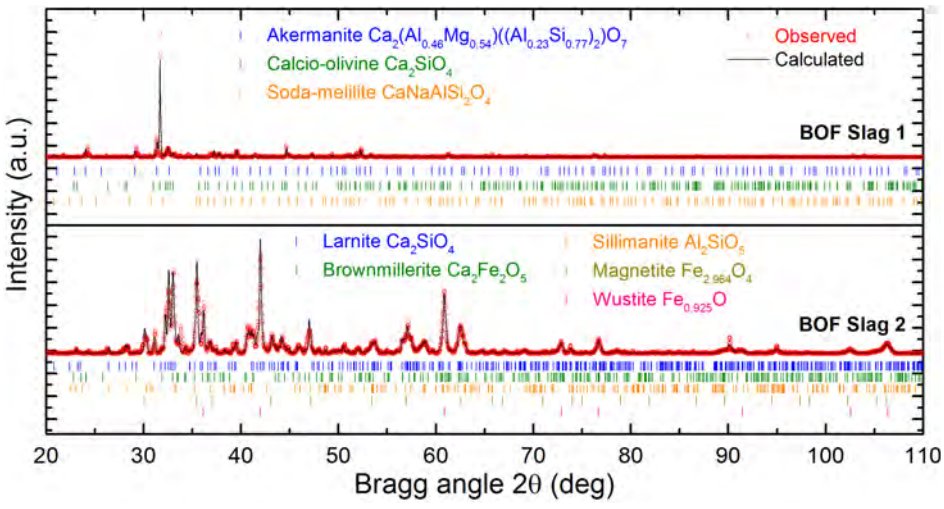

Figure 2.11. XRPD patterns of the BOFS samples and Bragg reflections of the identified crystallographic phases.

Concerning EAFS samples, from the obtained SEM images and EDX maps (Figure 2.12), three different compositional regions are observed in each one. Additionally, for each of these regions, a crystallographic phase is identified from the XRPD and the refinement analysis using the Fullprof software (Figure 2.13).

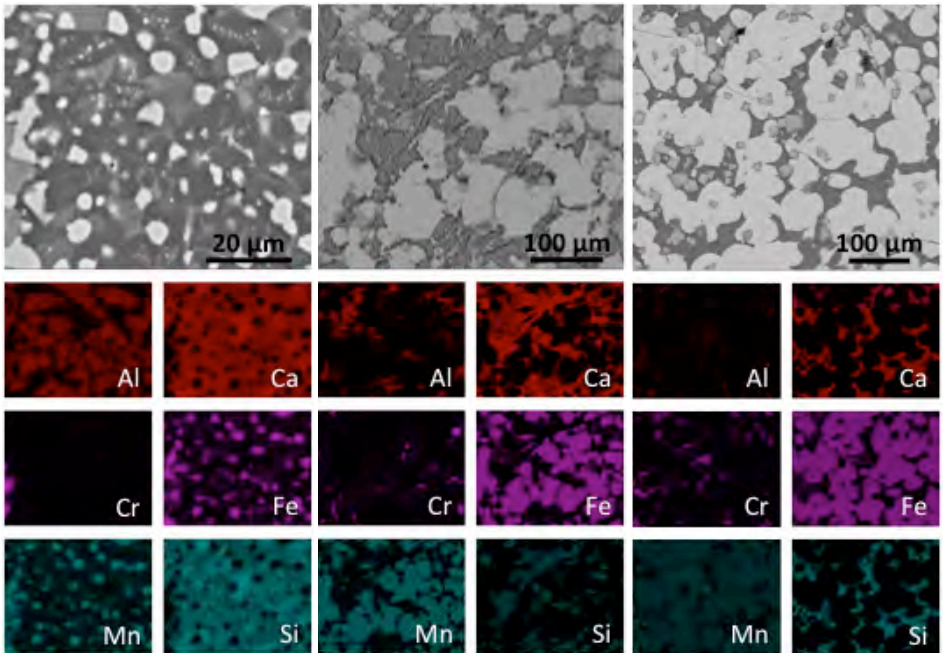

(a) (b) (c)

Figure 2.12. SEM images and EDX maps of: (a) *EAF Slag 1*; (b) *EAF Slag 2*; (c) *EAF Slag 3*.

In *EAF Slag 1*, these three regions are rich in iron (white zones), calcium, silicium and aluminium (dark grey areas) and in silicium and calcium (light grey regions) respectively. Considering the results obtained with XRPD and the consequent Fullprof refinement, these three zones correspond to Wustite ($Fe_{0.925}O$), Gehlenite ($Ca_2Mg_{0.25}Al_{1.5}Si_{1.25}O_7$), and Bredigite ($Ca_{14}Mg_2(SiO_4)_8$) respectively. In *EAF Slag 2* a white region, rich in iron, is found as in *EAF Slag 1*. In addition, two grey zones, one rich in calcium and silicium, and another one in calcium and aluminium are detected. The identified crystallographic phases for these three zones are Wustite (associated to the white zones) and, Mayenite ($Ca_{12}Al_{14}O_{33}$) and Larnite (Ca_2SiO_4) for the two grey areas. In *EAF Slag 3* similar superficial and crystallographic information is obtained as for *EAF Slag 1*.

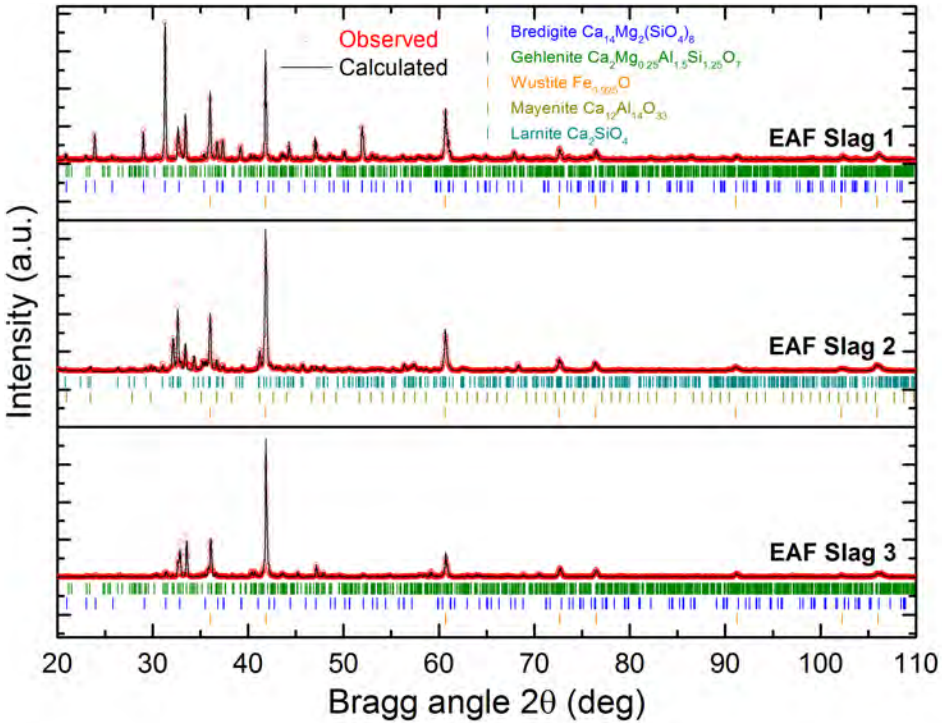

Figure 2.13. XRPD patterns of the EAFS samples and Bragg reflections of the identified crystallographic phases.

Additionally, from the SEM images in Figure 2.12 it is also observed that the sizes of the crystals forming *EAF Slag 1* are smaller than the ones of the *EAF Slag 2* and *3*. This is related to the faster cooling rate applied to *EAF Slag 1,* when obtained in the steelworks, in comparison to the slower ones of *EAF Slag 2* and *3*.

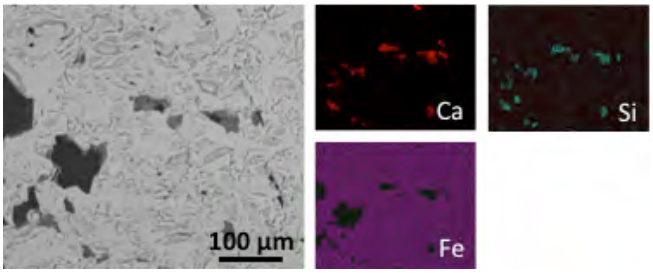

Figure 2.14. *Magnetite ore* SEM image and EDX maps.

Finally, from the SEM image obtained for *Magnetite ore* (Figure 2.14), a predominant white region, rich in iron, is observed. Additionally, smaller darker areas rich in calcium and silicon are also identified.

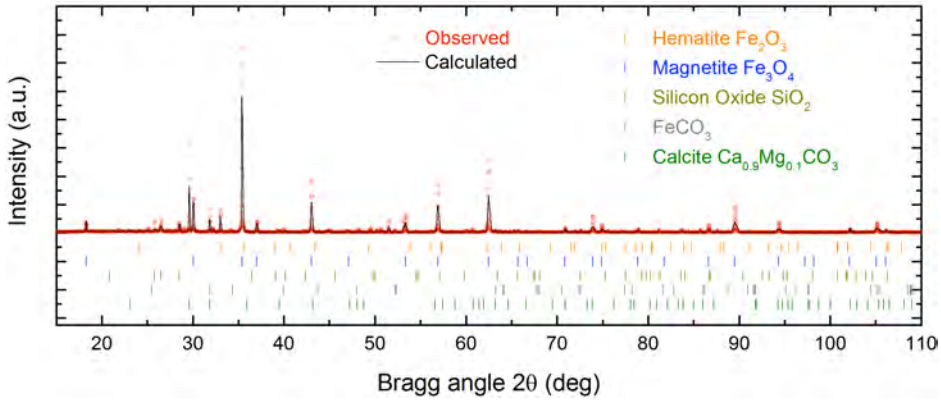

Figure 2.15. *Magnetite ore* XRPD pattern and Bragg reflections of the identified crystallographic phases.

Attending to the phases identified with the XRPD pattern and the refinement analysis using the Fullprof software, two iron oxides are obtained associated to the white area on Figure 2.14, Hematite (Fe_2O_3) and Magnetite (Fe_3O_4), together with an iron carbonate ($FeCO_3$). In addition, the darker areas correspond to Calcite ($Ca_{0.9}Mg_{0.1}CO_3$) and silica (SiO_2).

2.3.1.3. Density and porosity

Skeletal density values measured with the helium pycnometry technique of the seven investigated materials are reported in Table 2.5. In this table, the apparent densities, measured with a high precision microbalance (error below 0.1 μg) and a calibre in cubical samples are also included.

Table 2.5. Density and porosity of the investigated materials.

	Skeletal density ($kg \cdot m^{-3}$)	Apparent density ($kg \cdot m^{-3}$)	Total porosity (%)	Hg porosity (%)
BF Slag	2980	2487	16.5	14.9
BOF Slag 1	3236	3130	3.4	2.9
BOF Slag 2	3878	3732	3.9	3.7
EAF Slag 1	3880	3650	5.9	3.6
EAF Slag 2	4111	3924	4.5	4.5
EAF Slag 3	4260	4110	3.5	2.7
Magnetite ore	5011	4920	1.8	0.7

The obtained apparent densities are in good agreement with those reported in the literature for each material typology [24-27], exception made for *BOF Slag 1* that presents a slightly lower value. Comparing between the different materials, the lowest density is obtained for *BF Slag* whereas, the highest for *Magnetite ore*. Intermediate density values between *BF Slag* and *Magnetite ore* are obtained for the two steel slag types, BOFS and EAFS.

In addition to the density values, in Table 2.5 the total porosity of the seven investigated materials is also included. This total porosity is calculated from the skeletal and apparent densities as:

$$Total\ porosity\ (\%) = \left(1 - \frac{Apparent\ density}{Skeletal\ density}\right) \cdot 100. \quad (2.12)$$

Attending to the obtained values, porosities between 3 and 6% are obtained for both steel slag types. Meanwhile, a very large value is obtained for *BF Slag* and a slightly lower for *Magnetite ore*. It can be noted that high apparent density and low porosity are desired in a TES material to minimize the size of the system (see section 1.2.1.). In this regard, any of the steel slag samples or the *Magnetite ore*, present more promising properties than, for example, the studied *BF Slag*.

Finally, in order to study the distribution of the mentioned porosity in each material, the mercury porosimetry technique is used. The obtained pore size distributions are presented in Figure 2.16, where Figure 2.16a contains *BF Slag*; Figure 2.16b, *BOF Slag 1* and *2*; Figure 2.16c, *EAF Slag 1*, *2* and *3*; and Figure 2.16d, *Magnetite ore*. In all the plots, the pore size distribution is represented between 200 μm and 3 nm, covering the macro and mesopore ranges [28].

In the results presented in the four graphs of Figure 2.16, the majority of the pores are concentrated in the order of tens of micrometres, exception made for the *Magnetite ore*. In a detailed analysis of the distribution in *BF Slag* (Figure 2.16a), some pores with mean diameter between 4 μm and 20 nm are also present. A relevant peak is obtained in the detection limit region of the measurement (around 3-4 nm), which indicates the presence of micropores. Regarding the two considered BOFS samples (Figure 2.16b), wide peaks around 1 μm and 13 nm appear in *BOF Slag 1* and *2* respectively. As in *BF Slag*, at very low pore diameters a relevant peak is also present in *BOF Slag 1*. In the measurements of the three

investigated EAFS samples, similar results are obtained between them. Porosity peaks are obtained in the region of tens of micrometres and, as in previous cases, a peak below 3-4 nm indicating the presence of some micropores. Finally, a negligible porosity is detected in the analysed range for *Magnetite ore*. The presence of various peaks below 10 nm reveals that the majority of the pores in this material have a mean diameter in the range of micropores.

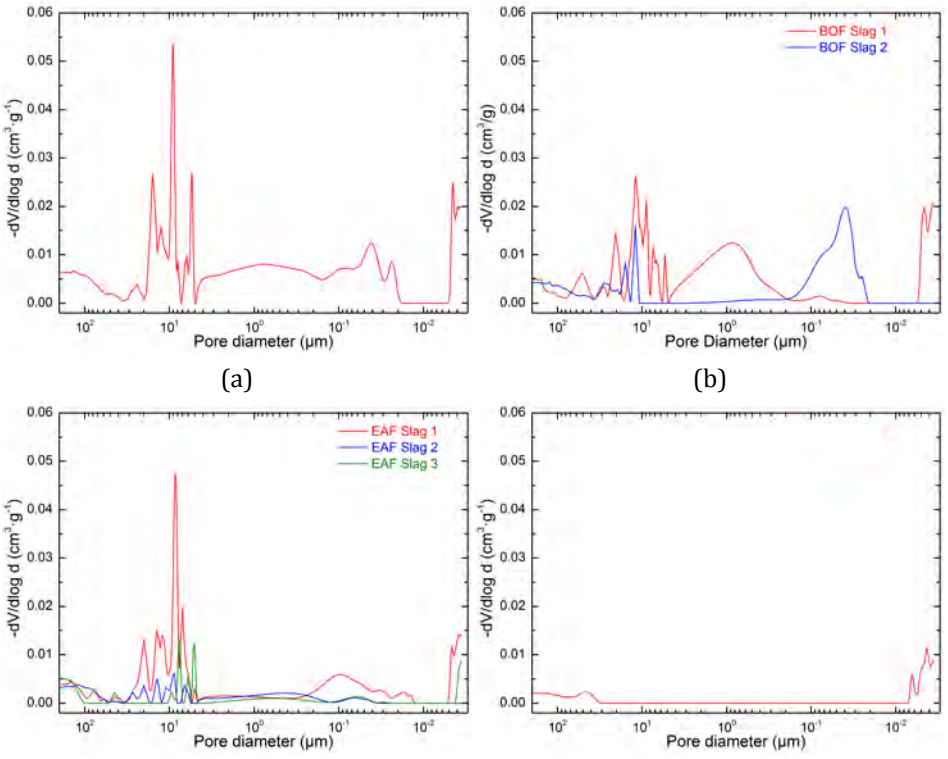

Figure 2.16. Pore size distribution measured with the Hg porosimetry technique. (a) *BF Slag*; (b) BOFS samples; (c) EAFS samples; (d) *Magnetite ore*.

Additionally, the total porosity information can also be extracted from the Hg porosimetry measurements. The obtained results are also included in Table 2.5. As it can be observed, in all the cases (exception made of *EAF Slag 2*) the values obtained with this technique are lower than the obtained with the He pycnometer. These results can be expected since Hg atoms are much larger than He ones and cannot penetrate in the smaller pores. In this regard, with the Hg porosimetry technique is not possible to reach micrometric scales.

2.3.2. Mechanical properties

This section is devoted to the analysis of the main mechanical properties of the seven investigated materials. As indicated in section 1.3, two of these main properties are the thermal expansion and the maximum compressive strength before failure.

2.3.2.1. Thermal expansion

The linear thermal expansion of the seven investigated materials is determined by dilatometry. In particular, the push-rod technique is used from 30 to 1000 °C. The obtained results are presented in Figure 2.17.

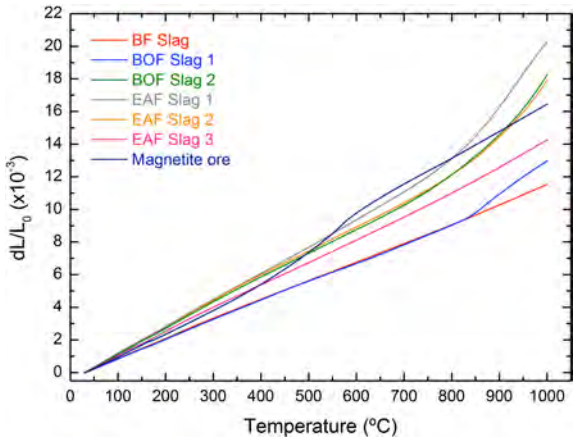

Figure 2.17. Thermal expansion of the investigated materials.

Attending to the experimental results depicted in Figure 2.17, it is observed that *BF Slag* and *EAF Slag 3* present a linear trend with temperature. However, in the rest of the analysed materials an inflexion point is found at different temperatures. These changes on the lineal thermal expansion slope can be associated to an eventual physico-chemical transformation in the material. In *BOF Slag 1*, this inflexion point appears at 850 °C. In the case of *BOF Slag 2*, *EAF Slag 1* and *EAF Slag 2*, very similar curves are observed with a change in the curve around 750 – 800 °C. Finally, *Magnetite ore* shows different performance in comparison to the six slag samples. In this case, a transformation occurs around 550 °C.

From the curves presented in Figure 2.17, the coefficient of linear thermal expansion (α_L) can be calculated with the following expression:

$$\alpha_L = \frac{dL}{L_0} \cdot \frac{1}{\Delta T}. \quad (2.13)$$

The α_L values of the seven investigated materials calculated using eq. (2.13) are presented in Table 2.6 for five temperature ranges.

Table 2.6. Linear thermal expansion coefficient of the investigated materials.

	Temperature range (°C)				
	30 – 200	200 – 400	400 – 600	600 – 800	800 – 1000
	Linear thermal expansion, $\alpha_L \cdot 10^{-5}$ (K^{-1})				
BF Slag	1.23	1.20	1.14	1.15	1.24
BOF Slag 1	1.20	1.21	1.11	1.18	1.97
BOF Slag 2	1.59	1.58	1.45	1.69	3.06
EAF Slag 1	1.65	1.63	1.65	1.88	3.56
EAF Slag 2	1.60	1.63	1.46	1.61	2.89
EAF Slag 3	1.49	1.42	1.37	1.44	1.63
Magnetite ore	1.38	1.53	2.18	1.68	1.66

2.3.2.2. Compressive strength

The maximum strength before mechanical failure of the solid under compressive forces is determined by performing compressive tests over cubical samples (around 1 cm x 1 cm x 1 cm). Up to five specimens are tested for each material. A representative measurement for each of the seven investigated materials is included in Figure 2.18, where the obtained strain-stress curve is presented.

As it can be observed in Figure 2.18, the maximum compressive resistance is obtained for *BOF Slag 2* and *EAF Slag 2* with values around 400 MPa. The rest of the steel slags (*BOF Slag 1* and *EAF Slag 1* and *3*) show slightly lower values, around 300 MPa. On the other hand, *BF Slag* and *Magnetite ore* present very low and average maximum compressive values when compared to the rest of the investigated materials respectively. Values around 100 MPa are attained for *BF Slag* and 200 MPa for *Magnetite ore*.

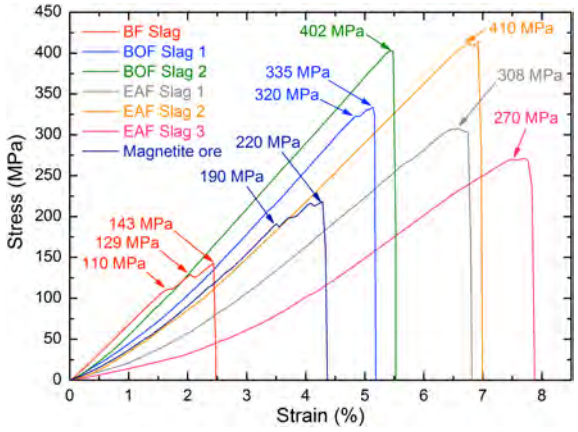

Figure 2.18. Compression strength of the investigated materials.

2.3.3. Thermal properties

This section is devoted to the determination of the main thermal properties of the materials governing the energy storage capacity and thermal performance in packed bed TES systems: specific heat, thermal diffusivity and thermal conductivity.

2.3.3.1. Specific heat

The specific heat is measured from 50 to 1000 ℃ by using two complementary experimental methods. On one hand, MDSC technique is applied between 50 and 450 ℃ and, on the other hand, the LFA technique between 500 and 1000 ℃. These two techniques are applied since the MDSC gives a lower experimental error than the LFA one (<3% and <5% respectively), and because of the temperature limitation of the MDSC device used in this work to 500 ℃.

The specific heat values obtained for the seven investigated materials by the two mentioned complementary techniques are presented in Figure 2.19. The values obtained values with the MDSC technique are plotted in continuous lines, whereas the experimental values measured with the LFA correspond to the dots connected with dashed lines.

As observed in Figure 2.19, the obtained values with the MDSC and LFA are in good agreement following a continuous trend (450 – 500 ℃). In all the materials, the specific heat shows a monotonous increase up to an almost constant value at

high temperatures. However, in the case of the *Magnetite ore*, a calorimetric peak is detected around 550 ℃. This behaviour can be associated to an eventual phase transition, chemical or any other physical evolution of the material. This phenomenon is studied in detail in chapter 3.

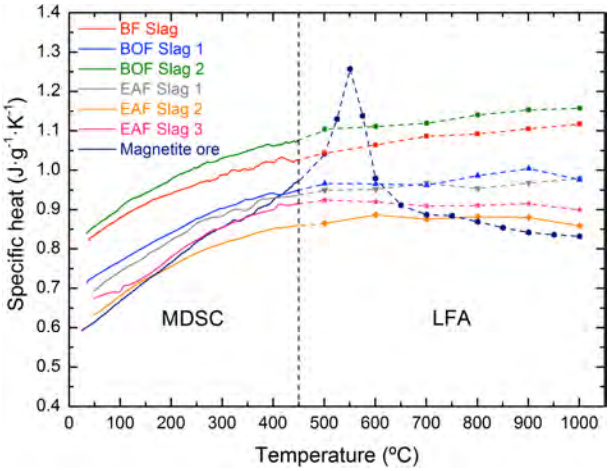

Figure 2.19. Specific heat of the investigated materials.

BF Slag and *BOF Slag 2* show slightly higher specific heat values than the other materials. In these two cases, they range from 0.8 $J \cdot g^{-1} \cdot K^{-1}$ at room temperature to 1.15 $J \cdot g^{-1} \cdot K^{-1}$ at 1000 ℃. On the other hand, for the three EAFS samples and *BOF Slag 1*, the specific heat varies from 0.65 to 0.9 $J \cdot g^{-1} \cdot K^{-1}$ in the investigated temperature range. Finally, *Magnetite ore* ranges from 0.6 $J \cdot g^{-1} \cdot K^{-1}$ at room temperature to 0.8 $J \cdot g^{-1} \cdot K^{-1}$ at high temperature.

2.3.3.2. Thermal diffusivity

The thermal diffusivity values of the seven investigated materials measured with the laser flash technique are presented in Figure 2.20.

A decrease of this property from room temperature to 1000 ℃ is obtained in all the materials exception made of *BF Slag* and *Magnetite ore*. In the case of *BF Slag* a change on the trend of this property with temperature is obtained at 600 ℃. This behaviour can be related to some transformation in the material that is not clearly observed in other properties (thermal expansion or specific heat) analysed up to now. Attending to the *Magnetite ore*, a trend change is also observed.

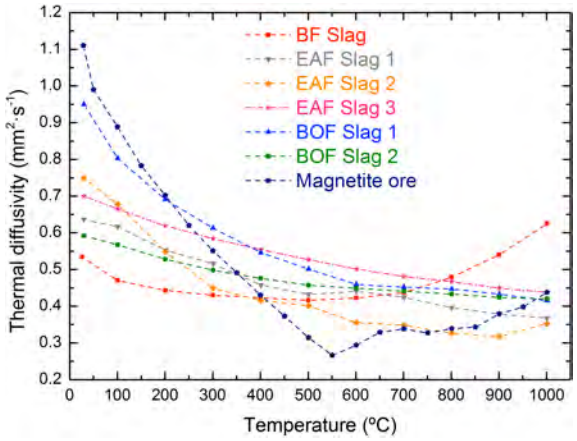

Figure 2.20. Thermal diffusivity of the investigated materials.

2.3.3.3. Thermal conductivity

Finally, the thermal conductivity of the investigated materials calculated from the specific heat, thermal diffusivity, apparent density and linear thermal expansion following eq. (2.11) is included in Figure 2.21.

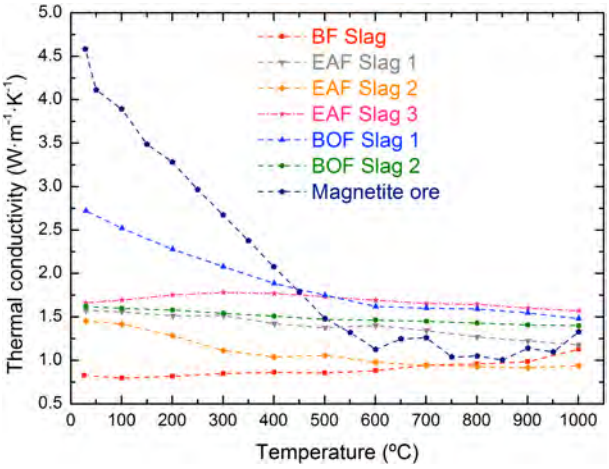

Figure 2.21. Thermal conductivity of the investigated materials

Thermal conductivity presents an almost flat performance in all the cases with the exception of *Magnetite ore*, *BOF Slag 2* an *EAF Slag 2,* where a decrease of this property is observed. Attending to the obtained values, a considerable difference between *Magnetite ore* and the slag materials at temperatures below 500 °C is found.

2.4. Results discussion and comparison

In section 2.3 the main compositional, structural, mechanical and thermal properties of the seven investigated materials within this thesis work have been presented. In order to analyse their suitability for the considered configuration (packed bed), they are compared with other materials reported in the literature for similar applications. Eight additional materials are considered for comparison: four natural rocks (Quartzite, Granite, Marble and Basalt), a by-product obtained from the treatment of asbestos-containing waste, Cofalit®, a high temperature concrete and two pure oxide materials (alumina and zirconia). For the sake of clarity, in Table 2.7 and Table 2.8 the main properties of the seven investigated and literature-reported materials are summarized respectively.

As explained in section 1.3, four parameters are critical in the selection of an appropriate material for packed bed TES applications: storage density, thermal expansion, resistance under compression strength and thermal conductivity.

The storage density of the material can be calculated following the expression:

$$Storage\ density = \rho \cdot c_p \cdot \Delta T. \tag{2.14}$$

As it can be observed in eq. (2.14), the storage density depends directly on the material density and specific heat. Taking this into account, larger values of the mentioned thermal properties promote higher storage densities. Consequently, a noticeable reduction on the required amount of TES material and tank size for storing the same energy can be obtained.

In Table 2.7 and Table 2.8, for the calculation of the storage densities, the temperature range currently exploited in TES systems based on *Solar salt*, 290 – 565 °C, is taken into account as reference for the analysis. In this regard, the specific heat and apparent densities are evaluated at the average temperature (427.5 °C). The obtained values are presented in the last column of the mentioned tables.

Table 2.7. Investigated materials properties summary from 290 to 565 °C

Material	ρ	Porosity	α_L	Max. σ_C[a]	c_p	λ	Storage density[b]
	$kg \cdot m^{-3}$	%	K^{-1}	MPa	$J \cdot g^{-1} \cdot K^{-1}$	$W \cdot m^{-1} \cdot K^{-1}$	$kWh_{th} \cdot m^{-3}$
BF Slag	2487	16.5	$1.15 \cdot 10^{-5}$	130	0.98 - 1.05	0.84 – 0.87	196
BOF Slag 1	3236	3.4	$1.15 \cdot 10^{-5}$	320	1.03 – 1.11	1.55 – 1.46	265
BOF Slag 2	3878	3.9	$1.49 \cdot 10^{-5}$	400	0.90 – 0.96	2.09 – 1.65	279
EAF Slag 1	3650	5.9	$1.62 \cdot 10^{-5}$	310	0.82 – 0.95	1.51 – 1.39	260
EAF Slag 2	3924	4.5	$1.51 \cdot 10^{-5}$	410	0.81 – 0.88	1.13 – 1.01	258
EAF Slag 3	4110	3.5	$1.37 \cdot 10^{-5}$	270	0.78 – 0.92	1.77 – 1.70	286
Magnetite ore	5011	1.8	$1.91 \cdot 10^{-5}$	200	0.84 – 1.11	2.71 – 1.27	364

[a] Measured at room temperature.
[b] For the calculation of the storage density, the c_p values are taken at 427.5 °C.

Table 2.8. Properties of sensible thermal energy storage materials reported in literature.

Material	ρ	Porosity	α_L	Max. σ_C	c_p	λ	Storage density	Ref.
	$kg \cdot m^{-3}$	%	K^{-1}	MPa	$J \cdot g^{-1} \cdot K^{-1}$	$W \cdot m^{-1} \cdot K^{-1}$	$kWh_{th} \cdot m^{-3}$	
Quartzite	2685	0.525	$3.35 \cdot 10^{-5}$	46 – 141	850	7.7	174	[29-31]
Granite	2610	0.5	$8.04 \cdot 10^{-6}$	230	900	2.2	179	[29,32,33]
Marble	2640	0.73	$1.08 \cdot 10^{-5}$	70.1	1470	2.9	296	[29,33,34]
Basalt	2490	11.16	$5.4 \cdot 10^{-6}$	262	850	2.0	162	[29,35,36]
Cofalit	3120	-	$8.8 \cdot 10^{-6}$		860	2.7	205	[37,38]
HT concrete	2750	-	$9.3 \cdot 10^{-6}$	Medium	916	1.0	192	[39]
Alumina	3953	-	$7.53 \cdot 10^{-6}$	>2000	1157	11.98	349	[40,41]
Zirconia	5999	-	$1.08 \cdot 10^{-5}$		597	2.68	274	[40]

Attending to the storage density of the seven investigated materials, the highest value is obtained for the *Magnetite ore*, while the lowest one is found for *BF Slag*. Similar values are attained for BOFS and EAFS samples. *BF Slag* shows similar values than materials such as HT Concrete, Granite or Quartzite, whereas EAFS and BOFS samples properties like the Marble or Zirconia ones. The *Magnetite ore* presents higher storage density than the rest of the investigated materials similar to Alumina.

The second parameter to be taken into account when selecting a suitable material for packed bed TES applications is its thermal expansion in the application temperature range. Different thermal expansion coefficients between the container and TES materials may cause mechanical failures of the system such as the so-called ratcheting [42,43]. In addition, from the point of view of the TES material, different thermal expansion coefficients of the phases/crystals may also cause internal stresses upon heating/cooling, ending in the formation of internal cracks in the material. In order to analyse the suitability of the investigated materials as a function of this property, the linear thermal expansion coefficients of some materials typically used in the container construction are presented in Table 2.9. This table includes two usual stainless steels (AISI 304 and 316), a carbon steel, a special nickel alloy suitable for high temperature and a concrete.

Table 2.9. Candidate container materials.

		α_L (K^{-1})	Ref.
Stainless steel	AISI 304	$1.73 \cdot 10^{-5}$	[44]
	AISI 316	$1.62 \cdot 10^{-5}$	[45]
Carbon steel	ASTM A516	$1.2 \cdot 10^{-5}$	[46]
Special alloy	INCONEL 600	$1.44 \cdot 10^{-5}$	[47]
Concrete	High Temperature	$9.6 \cdot 10^{-6}$	[39]

Comparing the linear thermal expansion coefficients measured for the seven investigated materials (Table 2.7) with those of container materials (Table 2.9), it can be observed that for *BF Slag* and *BOF Slag 1*, similar values to carbon steel are obtained. *BOF Slag 2*, and the three EAFS samples show similar or slightly lower thermal expansion coefficients than both stainless steels. Finally, *Magnetite ore*

presents a slightly larger thermal expansion coefficient compared to the rest of the container construction materials included in Table 2.9.

This good matching in the thermal expansion coefficients between the investigated and tank-construction materials, allows concluding that typical mechanical problems are not expected when using them together, in the right combination.

Regarding the maximum compression strength, it has to be pointed out that, the higher is this property, the better. In these terms, comparing the obtained values for the investigated materials with those literature-reported, similar or higher values are attained. This is an indication of their suitability for packed bed solutions.

Finally, comparing the thermal conductivity of the investigated and literature-reported materials, *BF Slag* presents much lower values while the rest are in the same range than most of the natural rocks (exception made for Quartzite) and Cofalit®. It has to be pointed out that this property has a strong impact on the thermal performance of the packed bed unit. Overall, the obtained thermal conductivities for the seven investigated materials, present average values, which are very promising for packed bed applications.

2.5. Conclusions

In this chapter the main compositional, structural, mechanical and thermal properties of seven low cost materials have been analysed for consideration as potential candidates for sensible TES applications in packed bed arrangements. These materials are six by-products of the iron and steel industry (one BFS, two BOFS and three EAFS) and a natural material, magnetite ore.

The compositional analysis showed that the six analysed slag samples are multiphase materials while *Magnetite ore* is almost pure.

Overall, *BF Slag* presents low density, with high porosity, and similar specific heat than the rest of the materials. This results in a low storage density. From the two analysed BOFS types, *BOF Slag 1* was concluded not to be representative of other BOFS generated worldwide because of its chemical composition. On the other hand, *BOF Slag 2* presents similar composition to those BOFS reported in

literature. The three investigated EAFS samples were found representative from other EAFS generated worldwide. All the thermo-physical properties of both steel slag types, BOFS and EAFS, are very similar. They show good mechanical resistance, intermediate thermal conductivity and appropriate storage densities. Finally, *Magnetite ore* presents very high density together with low porosity. This results in a very high storage density.

Considering these general conclusions from the characterization carried out in this chapter, *BF Slag* is discarded for further analysis due to its poor mechanical and thermal properties compared to other slag types. *Magnetite ore* is selected because of its promising thermal properties and homogenous composition that can lead to a better mechanical performance upon cycling, avoiding internal cracks caused by different thermal expansion coefficients in the phases forming the material. From the steel slags, both typologies presented very similar promising properties. Taking this into account, the three EAFS samples are chosen for further analyses within this thesis since EAF is the most spreading steel production technology in Europe, and in the Basque country.

2.6. References

[1] S. Fiore, M.C. Zanetti, and B. Ruffino, "Waste characterization in steel casting and recycling opportunities in Europe," *American Journal of Applied Sciences*, vol. 5 (5), pp. 512-518, 2008.

[2] W.H. Bragg and W.L. Bragg, "The reflection of X-rays by crystals," *Proceedings of the Royal Society of London A*, vol. 88, pp. 428-438, 1913.

[3] J. Rodriguez-Carvajal, "Recent advances in magnetic structure determination by neutron powder diffraction," *Physica B: Condensed Matter*, vol. 192 (1-2), pp. 55-59, 1993.

[4] J.B. West, "Robert Boyle's landmark book of 1660 with the first experiments on rarified air," *Journal of Applied Physiology*, vol. 98, pp. 31-39, 2005.

[5] E.W. Washburn, "The dynamics of capillary flow," *Physical Review*, vol. 17 (3), no. 3, pp. 273-283, 1921.

[6] "Standard test method for linear thermal expansion of solid materials with a push-rod dilatometer," ASTM International, ASTM E228 - 11, 2016.

[7] M. Reading, D. Elliott, and V. Hill, "Some aspects of the theory and practice of modulated differential scanning calorimetry," in *21st North American Analysis Society Conference*, 2003, pp. 145-150.

[8] R.L. Danley, "New modulated DSC measurement technique," *Thermochimica Acta*, vol. 402, no. 1-2, pp. 91-98, 2003.

[9] W.J. Parker, R.J. Jenkins, C.P. Butler, and G.L. Abbott, "Flash method of determining thermal diffusivity, heat capacity, and thermal conductivity," *Journal of Applied Physics*, vol. 32, pp. 1679-1684, 1961.

[10] R.D. Cowan, "Pulse method of measuring thermal diffusivity at high temperatures," *Journal of Applied Physics*, vol. 34, pp. 926-927, 1963.

[11] J.A. Cape and G.W. Lehman, "Temperature and finite pulse-time effects in the Flash method for measuring thermal diffusivity," *Journal of Applied Physics*, vol. 34, pp. 1909-1913, 1963.

[12] B.K. Larson and K. Koyama, "Correction for finite-pulse-time effects in very thin samples using the flash method of measuring thermal diffusivity," *Journal of Applied Physics*, vol. 38 (2), pp. 465-474, 1967.

[13] A. Bouaziz et al., "Efficiency of high energy over conventional milling of granulated blast furnace slag powder to improve mechanical performance of slag cement paste," *Powder Technology*, vol. 308, pp. 37-46, 2017.

[14] H. Xuquan, J. Mingming, Z. Xiaorong, and T. Cilai, "Mechanical properties and hydration mechanisms of high-strength fluorogypsum-blast furnace slag-based hydraulic cementitious binder," *Construction and Building Materials*, vol. 127, pp. 137-143, 2016.

[15] W. Duan, Q. Yu, T. Wu, F. Yang, and Q. Qin, "The steam gasification of coal with molten blast furnace slag as heat carrier and catalyst: Kinetic study," *International Journal of Hydrogen Energy*, vol. 41, pp. 18995-19004, 2016.

[16] S. Hyun-Oh, J.-M. Yang, Y.-S. Yoon, and D. Mitchell, "Mix design of concrete for prestressed concrete sleepers using blast furnace slag and steel fibers," *Cement and Concrete Composites*, vol. 74, pp. 39-53, 2016.

[17] Q. Li, H. Ding, A. Rahman, and D. He, "Evaluation of Basic Oxygen Furnace (BOF) material into slag-based asphalt concrete to be used in railway substructure," *Construction and Building Materials*, vol. 115, pp. 593-601, 2016.

[18] W. Yang, Y. Xue, S. Wu, Y. Xiao, and M. Zhou, "Performance investigation and environmental application of basic oxygen furnace slag – Rice husk ash based composite cementitious materials," *Construction and Building Materials*, vol. 123, pp. 493-500, 2016.

[19] J. Xie, S. Wu, L. Zhang, Y. Xiao, and W. Ding, "Evaluation the deleterious potential and heating characteristics of basic oxygen furnace slag based on laboratory and in-place investigation during large-scale reutilization," *Journal of Cleaner Production*, vol. 133, pp. 78-87, 2016.

[20] L. Yurramendi, S. Caballero, and C. del Rio, "Los residuos industriales como reactivos para el secuestro de CO2," *AFINIDAD LXVIII*, no. 551, pp. 6-14, 2011.

[21] J.M. Manso, J.A. Polanco, M. Losañez, and J.J. González, "Durability of concrete made with EAF slag as aggregate," *Cement & Concrete Composites*, vol. 28, pp. 528-534, 2006.

[22] M. Ameri, S. Hesami, and H. Goli, "Laboratory evaluation of warm mix asphalt mixtures containing electric arc furnace (EAF) steel slag," *Construction and Building Materials*, vol. 49, pp. 611-617, 2013.

[23] E. Anastasiou, K. Georgiadis Filikas, and M. Stefanidou, "Utilization of fine

recycled aggregates in concrete with fly ash and steel slag," *Construction and Building Materials*, vol. 50, pp. 154-161, 2014.

[24] EUROSLAG [Online]: http://www.euroslag.com/products/properties/

[25] T. Sofilić, A. Mladenovič, and U. Sofilić, "Characterization of the EAF steel slag as aggregate for use in road construction," in *4th International Conference on Safety & Environment in Process Industry*, Florence, Italy, 2010.

[26] Australian (Iron & Steel) Slag Association, "Quick reference guide 4: electric arc furnace slag ," 2015.

[27] G.R. Woolley, J.M. Goumans, and P.J. Wainwright, *Waste materials in construction: Science and engineering for recycling for environmental protection*.: Pergamon, 2000.

[28] J. Rouquerol et al., "Recommendations for the characterization of porous solids," *Pure and Applied Chemistry*, vol. 66, no. 8, pp. 1739-1758, 1994.

[29] H. Grirate et al., "Experimental and numerical investigation of potential filler materials for thermal oil thermocline storage," *Solar Energy*, vol. 131, pp. 260-274, 2016.

[30] J. Liu, X. Han, X. Jiang, H. Wang, and Z. Cui, "Thermal expansion characteristics of quartzite particles up to 1600 ºC," *Chemical Engineering and Processing*, vol. 48, pp. 885-891, 2009.

[31] V. Gupta and R. Sharma, "Relationship between textural, petrophysical and mechanical properties of quartzites: A case study from northwestern Himalaya," *Engineering Geology*, vol. 135-136, pp. 1-9, 2012.

[32] M. Hokka et al., "Effects of strain rate and confining pressure on the compressive behavior of Kuru granite," *International Journal of Impact Engineering*, vol. 91, pp. 183-193, 2016.

[33] V. Gräf, M. Jamek, A. Rohatsch, and E. Tschegg, "Effects of thermal-heating cycle treatment on thermal expansion behavior of different building stones," *International Journal of Rock Mechanics & Mining Sciences*, vol. 64, pp. 228-235, 213.

[34] J. Peng, G. Rong, M. Cai, M.-D. Yao, and C.-B. Zhou, "Physical and mechanical behaviors of a thermal-damaged coarse marble under uniaxial compression," *Engineering Geology*, vol. 200, pp. 88-93, 2016.

[35] R.A. Schultz, "Brittle strength of basaltic rock masses with applications to venus," *Journal of Geophysical Research*, vol. 98, pp. 10883-10895, 1993.

[36] E.B. Dane Jr., "Density at high temperature: thermal expansion," in *Handbook of Physical Constants*., 1942, vol. 36, pp. 27-37.

[37] N. Calvet et al., "Matériau de stockage thermique par chaleur sensible pour centrales électro-solaires testé sous flux solaire concentré," in *Proceedings in Congres Francais de Thermique*, 2010.

[38] X. Py et al., "Low-cost recycled material for thermal energy storage applied to solar power plants," in *SolarPACES Conference*, Berlin, 2009.

[39] D. Laing, W.D. Steinmann, R. Tamme, and C. Richter, "Solid media thermal storage for parabolic trough power plants," *Solar Energy*, vol. 80, pp. 1283-1289, 2006.

[40] Z.P. Zhang, S.W. Zhou, Q. Li, W. Li, and M. Swain, "Residual stresses in frabrication of core-veneered ceramic prostheses," *Advanced Materials Research*, vol. 97, pp. 2241-2244, 2010.

[41] P. Auerkari, *Mechanical and physical properties of engineering alumina ceramics*.

[42] R.M. Olsen, "Thermal Ratchet Stopping Shovel Wall," US20150184950 A1, January 2, 2014.

[43] I. González, C.D. Pérez-Segarra, O. Lehmkuhl, S. Torras, and A. Oliva, "Thermo-mechanical parametric analysis of packed-bed thermocline energy storage tanks," *Applied Energy*, vol. 179, pp. 1106-1122, 2016.

[44] AK Steel, "304/304L Stainless steel data sheet," 2007.

[45] AK Steel, "316/316L Stainless steel data sheet," 2007.

[46] Matweb [Online]: www.matweb.com

[47] S. Raju et al., "Thermal expansion studies on Inconel-600 by high temperature X-ray diffraction," *Journal of Nuclear Materials*, vol. 325, pp. 18-25, 2004.

Chapter 3:

Compatibility of the selected materials with heat transfer fluids

3 Compatibility of the selected materials with heat transfer fluids

In the previous chapter four materials have been selected due to their promising thermo-physical properties for thermal energy storage applications in packed bed arrangements, three electric arc furnace slags (EAFS) and the *Magnetite ore*. Taking into account that the packed bed configuration leads to a direct contact between the heat transfer fluid and the storage medium, in this chapter any transformation, corrosion or degradation phenomenon that may occur in/between both materials is addressed. In this regard, compatibility analysis between the investigated EAFS samples and the *Magnetite ore* with some of the most usual heat transfer fluids implemented in industrial applications (air, molten nitrate salt and thermal oils) are performed in this chapter. In order to guarantee a safe technological deployment, such tests are performed at the maximum operation temperature of the investigated heat transfer fluids.

3.1. Materials

In addition to the three EAFS samples and the *Magnetite ore,* in this chapter a molten nitrate salt and a thermal oil are also investigated.

First, the most extended molten nitrate salt in CSP plants, the so-called *Solar salt* is used for the compatibility analysis. As already indicated, this salt consists in a mixture of 60%$_w$ of sodium nitrate ($NaNO_3$) and a 40%$_w$ of potassium nitrate (KNO_3) with a purity around 99.5%$_w$ [1]. In order to avoid the possible impurity-related interferences on the corrosion phenomena, the *Solar salt* tested in this thesis is prepared by using trace metal grade (99.999%$_w$) nitrates from Sigma-Aldrich. In the salt preparation, both nitrate powders are mixed, melted under argon atmosphere and, once solidified, crushed into powder. Finally, the composition of the prepared salt and its thermal properties are analysed by means of ICP-OES, XRPD and DSC techniques to guarantee its right preparation.

Second, the commercial *Delcoterm Solar E15* thermal oil from *Delco* company is considered. This oil is a complex mixture of hydrocarbons obtained by treating a petroleum fraction with hydrogen in presence of a catalyst. The average size of these hydrocarbons is in the range of C15-C30. Due to its thermal properties, high distillation point (2%) and flash point, low vapour pressure and inertness against steels, this oil is suitable for oleo-thermal plants [2].

3.2. Characterization techniques

In addition to the characterization techniques presented in section 2.2, in the investigation of the materials resulted from the mentioned compatibility tests, the following techniques are also considered.

3.1.1. Thermogravimetry

In thermogravimetric analysis (TGA), the evolution of the mass of a sample is monitored as a function of a controlled temperature change. During the measurement, different gases can be used as purging medium such as dry air, argon, nitrogen or CO_2 among others. This technique is useful for the investigation of a variety of physical phenomena, such as decomposition, oxidation/reduction, loss of water, etc.

Thermogravimetric measurements presented in this chapter are performed from ambient temperature to 1100 °C, under dry air atmosphere with a STA 449 F3 from Netzsch coupled to a mass spectrometer. This equipment offers a high resolution, up to 0.1 μg.

3.1.2. Differential scanning calorimetry

Differential scanning calorimetry (DSC) technique is used for the phase change enthalpy and transition temperature determination. In this differential experimental technique the amount of heat required to increase the temperature of a reference pan, and a pan containing a sample is measured. The underlying physical measurement principle is based on the controlled heat supply to both, reference and sample pans. In the absence of a heat producing or absorbing phenomena associated, for example, to a phase transition or a chemical reaction process of the sample, a zero difference is obtained between them. When the mentioned physical mechanisms occur, a neat heat supply imbalance is suffered by the sample, which is automatically compensated by the calorimeter to maintain a similar temperature in both, reference and sample pans. As a consequence, a heat supply peak is observed, which allows the characterization of phase transitions. In these terms, both, the transition temperature and latent heat values can be accurately measured.

For these measurements, around 25 mg of powdered samples are placed in highly conductive aluminium hermetic pans, ensuring a good thermal contact with the measuring capsule. After an optimization analysis of the measurement conditions, a 10 $K \cdot min^{-1}$ heating and cooling ramps are applied from 25 to 530 °C. In total, three heating/cooling cycles are performed to each sample. The DSC used for these measurements is a Q2000 from TA Instruments, which provides a calorimetric and temperature precision up to a 0.05% and 0.01 °C respectively.

3.1.3. Inductively coupled plasma – optical emission spectroscopy

This technique has already been presented in section 2.2.1. In addition to the compositional analysis of the ceramic materials, in this chapter this characterization technique is used in the investigation of the nitrate salts. For the performed measurements, salt powders are directly dissolved in a 2% nitric acid (HNO_3) solution prepared with ultrapure water (milliQ), and its composition determined via a Perkin Elmer Optima 2000 OV.

3.1.4. Ion chromatography

The ion chromatography technique is used in the determination of the nitrite (NO_2^-) and nitrate (NO_3^-) concentrations. In this technique, a chromatography column is used to separate molecules depending on their respective charged group. This separation is based on the ionic interactions of the molecules in the sample with the column fixed matrix. Essentially, molecules undergo electrostatic interactions with opposite charges in the column matrix. The ionisable molecules present in the sample compete for binding to the immobilized charges on the stationary phase. These ionisable molecules are retained or eluted based on their charge. Molecules that do not bind or bind weakly to the stationary phase are first to be released from the column. Taking this into account, a molecule can be identified and quantified based on its retention time inside the chromatographic column. For such determination, a previous measurement of a reference sample with known concentrations on the investigated molecules is necessary.

A Dionex ICS-3000 ion chromatographer coupled with a conductivity detector is used in this work. For the measurements, salt samples are dissolved in ultrapure

water (milliQ) and analysed in an isocratic regimen with sodium hydroxide 100 mM as eluent.

3.1.5. Fourier transform infrared spectroscopy

Infrared spectroscopy is a powerful technique to observe the vibrations of molecular bonds based on electromagnetic radiation absorption. In the obtained spectrum, the intensity of a peak is related to the change in the dipolar moment from ground to an excited state. During measurements, the frequency of the radiation is moved and the radiation absorbed (or transmitted) by the sample is monitored.

In this thesis work, Fourier transform infrared spectroscopy (FTIR) technique is used to identify any degradation of the chemical structure of the investigated heat transfer fluids. In particular, a Bruker FTIR Vertex 70 spectrometer is applied at wavenumbers from 500 to 4000 cm^{-1}.

3.1.6. Raman spectroscopy

Raman spectroscopy is a complementary technique to FTIR. In this case, the intensity of the peaks in the resulting spectrum is related to the polarity of the bonds. In this technique, the sample is irradiated with a monochromatic light of a known frequency causing two different types of dispersion: Rayleigh dispersion, which is generated with the same wavelength than the incident beam; and Raman dispersion, at different wavelengths, which results in the Raman spectrum.

In this thesis work, Raman spectroscopy measurements are conducted in the range 200 – 4000 cm^{-1} with a resolution of 4 cm^{-1} using a Ranishaw InVia spectrometer equipped with a 532 nm green laser operated at a power of 0.5 mW. The laser spot size is approximately 1 mm in diameter.

3.1.7. Liquid-state nuclear magnetic resonance

Nuclear magnetic resonance (NMR) is a spectroscopic technique used to obtain microscopic chemical and physical information on molecules in a static magnetic field. In this thesis, this technique is applied to identify a possible corrosion mechanism in the investigated thermal oil.

This technique is based on the degrees of freedom of electronic and nuclear spins. The spin of charged particles has a magnetic dipole moment associated with it; if such particles are placed in a magnetic field, the energy of these magnetic dipoles depends on their orientation with respect to the field. The magnetic energy levels split into two groups when a magnetic field is applied depending on the how the nuclear spins are aligned: parallel or antiparallel. The energy difference between these two states is associated with the frequency of absorption, which at the same time depends on the particular element and also on its chemical environment.

In liquid-state NMR the obtained spectrum has high resolution since dipolar interactions and anisotropic effects are averaged out by the nuclear spin transitions.

In the characterization of the thermal oils, two types of nuclei are measured ^{1}H and ^{13}C. NMR spectra are recorded on a Bruker AVANCE 400 using Chloroform-D as solvent. 32 scans are acquired using a direct excitation sequence for the ^{1}H spectra while 4096 scans are used for recording the ^{13}C one with Waltz-16 decoupling during acquisition.

3.3. Stability with air

In this section, the stability of the four selected materials, three EAFS samples and the *Magnetite ore* is analysed under air atmosphere up to 1100 °C. The main objective is to determine the suitability of implementing these materials when air is used as heat transfer fluid.

3.3.1. Thermogravimetric analysis

The thermogravimetric technique is used to determine the thermal stability of the selected materials. In this regard, around 60 mg of powder are introduced in small alumina pans and measured from room temperature to 1100 °C using dry air in the measurement chamber. A total of three cycles are performed in each material. The obtained mass evolution with temperature is presented in Figure 3.1. In this figure, plots from a) to c) correspond to *EAF Slag 1*, *2* and *3* respectively, and Figure 3.1d to the *Magnetite ore*.

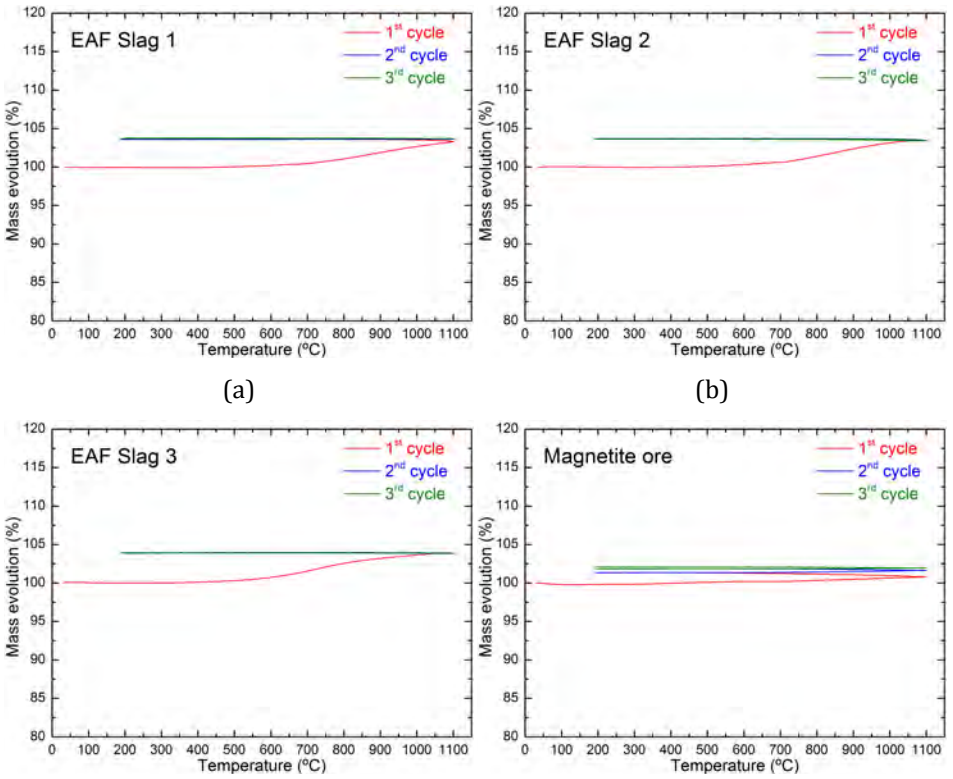

Figure 3.1. Thermogravimetric analysis of: (a) *EAF Slag 1*; (b) *EAF Slag 2*; (c) *EAF Slag 3* and (d) *Magnetite ore*.

Attending to the TGA results, a small mass variation is observed during the first heating run in the four materials. This variation is more pronounced in the case of the EAFS samples than in the *Magnetite ore*. In the three EAFS samples, after the third heating/cooling run, a mass variation around 3.5 - 4% is attained. Meanwhile, values around 2.5% are observed in the *Magnetite ore*. It has to be pointed out that in the case of the EAFS samples, this mass variation occurs in the first heating run. However, in the case of the *Magnetite ore*, up to two complete cycles are required to stabilize the material.

In order to get more information about the observed transformations, in the following, different characterization techniques are applied to determine the transformations in the crystallographic structure of the materials, and an eventual modification of their thermo-physical properties.

3.3.2. X-ray powder diffraction

X-ray powder diffraction (XRPD) technique is used to determine the crystallographic information of the investigated materials, after the thermal cycling performed in the TGA.

The obtained results for the three EAFS samples are presented in Figure 3.2 where, from bottom to top, *EAF Slag 1*, *EAF Slag 2* and *EAF Slag 3,* are included respectively. For each measurement, two patterns are shown corresponding to the observed and calculated ones using the Fullprof program. In addition, below each pattern vertical bars are included with the Bragg reflections of the identified crystallographic phases.

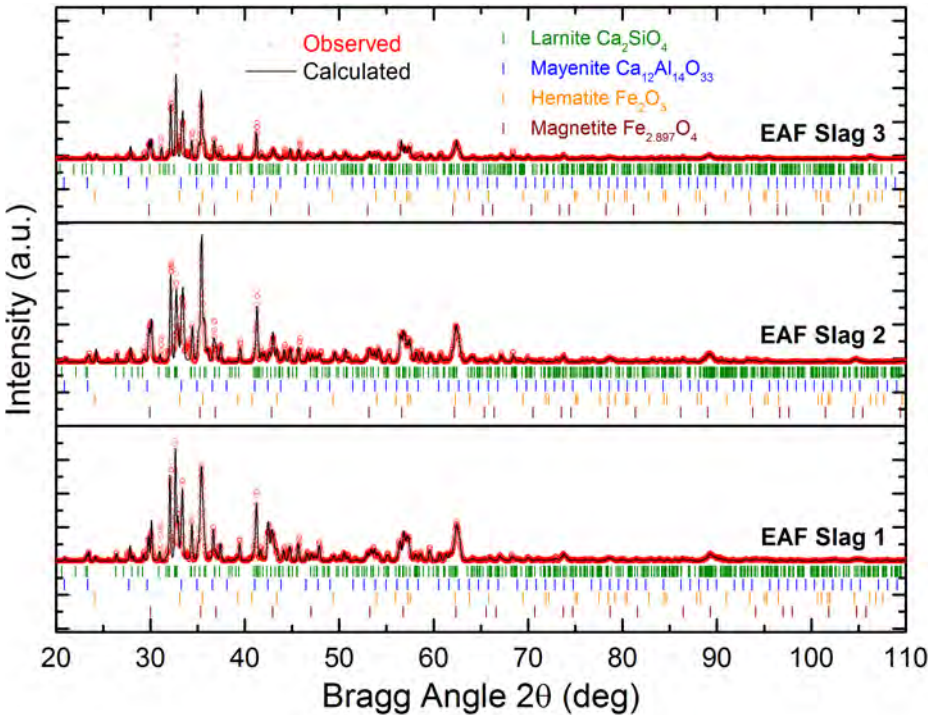

Figure 3.2. XRPD patterns of the thermal treated EAFS samples.

It can be observed that in the three EAFS samples the same four crystallographic phases are identified: Larnite (Ca_2SiO_4), Mayenite ($Ca_{12}Al_{14}O_{33}$), Hematite (Fe_2O_3) and Magnetite ($Fe_{2.897}O_4$). Comparing these results with the obtained ones for the pristine materials (Figure 2.13), the main modification is observed in the oxidation of the Wustite ($Fe_{0.925}O$) to form Hematite and

Magnetite. A possible mechanism of this oxidative process is summarized as follows:

$$6FeO + O_2 \rightarrow 2Fe_3O_4 \quad (3.1)$$

$$4FeO + O_2 \rightarrow 2Fe_2O_3 \quad (3.2)$$

$$4Fe_3O_4 + O_2 \leftrightarrow 6Fe_2O_3 \quad (3.3)$$

According to the obtained results, it is concluded that the mass gain observed in the three EAFS samples, is mainly related to an oxidation process that starts at temperatures around 500 - 600 °C. Once Hematite and Magnetite phases are formed, the material does not show any further mass change.

Attending to the *Magnetite ore*, the measured XRPD pattern and the calculated one with Fullprof software are presented in Figure 3.3.

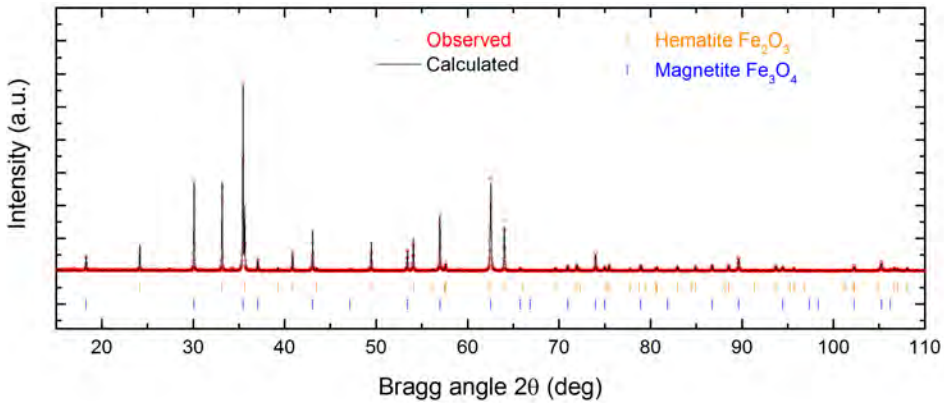

Figure 3.3. XRPD patterns of the thermal treated *Magnetite ore*.

In this case, only two crystallographic phases are detected: Hematite and Magnetite. Comparing this result with the pristine *Magnetite ore* in Figure 2.15, it is observed that SiO_2, $FeCO_3$ and $Ca_{0.9}Mg_{0.1}CO_3$ phases are not present in the measured sample. As already mentioned in chapter 2, SiO_2 is an impurity in the *Magnetite ore*. Taking this into account, the absence of this impurity in the sample used for the TGA measurement should be the reason why it is not experimentally found in the XRPD pattern of the treated material. On the other hand, the absence of $FeCO_3$ and $Ca_{0.9}Mg_{0.1}CO_3$ in the thermal treated *Magnetite ore* can be associated to their decomposition. This process could be the underlying reason of the slight

mass reduction observed in the TGA measurement at temperatures around 100 - 200 °C (Figure 3.1d).

In addition, the transformation of some Magnetite to Hematite following the reaction mechanism indicated in eq. (3.3) is the reason of the mass gain observed at temperatures above 300 °C in the TGA measurement (Figure 3.1d) in the first heating run. In order to confirm this observation, small pieces of around 10 grams are introduced in alumina crucibles and then placed in a muffle furnace at 1100 °C for 500 hours (see Figure 3.4). After 50 and 175 hours one sample is removed from the furnace and characterized with XRPD.

Figure 3.4. Long-term experiments under air atmosphere at 1000 °C.

From the obtained patterns, the ratio between both crystallographic phases, Magnetite and Hematite, is calculated considering the intensities of the main peaks. These ratios are collected in Table 3.1.

Table 3.1. Degree of Magnetite to Hematite transformation as a function of time.

Time (h)	Magnetite ($\%_w$)	Hematite ($\%_w$)
0	99	1
50	73	27
175	59	41
500	60	40

From these results, a progressive oxidation of the Magnetite leading to Hematite formation is observed. In the equilibrium, the investigated material consists mainly in a 60$\%_w$ of Magnetite and 40$\%_w$ of Hematite. As observed in Table 3.1, this equilibrium is reached approximately after one week under the experimental conditions.

These results agree with the obtained ones in the TGA (Figure 3.1d). In this case, considering the powdered nature of the tested samples, this oxidation happens faster than in solid pieces, as it is the case in the performed long-term experiments. In the latter, small pieces are used and, taking into account the low porosity of the *Magnetite ore*, the penetration of air becomes more difficult, making this process slower.

3.3.3. Thermo-physical properties

The oxidation mechanisms suffered in the four investigated materials may have a direct impact in their main thermo-physical properties. In order to determine any relevant modification in such properties, in this section the most representative ones, affecting to the performance in packed bed arrangements, are investigated.

3.3.3.1. Density and porosity

The skeletal and apparent densities are collected in Table 3.2. Additionally, the density variation in comparison to the pristine materials (Table 2.5) is included between brackets.

Table 3.2. Density of thermal treated materials.

	Skeletal density ($kg \cdot m^{-3}$)	Apparent density ($kg \cdot m^{-3}$)	Total porosity (%)
EAF Slag 1	3680 (-5.2%)	3430 (-6.0%)	6.8
EAF Slag 2	4031 (-1.9%)	3814 (-2.8%)	5.4
EAF Slag 3	4030 (-5.4%)	3770 (-8.3%)	6.5
Magnetite ore	5003 (-0.2%)	4909 (-0.2%)	1.9

From the obtained density values, in all the cases both densities, skeletal and apparent, are lower than in the pristine materials. The reason of this behaviour is that Magnetite or Hematite crystals densities are lower than the Wustite one. Attending to the results obtained for the *Magnetite ore,* an almost negligible density variation is observed in comparison to the pristine material. Such variation is associated to the low difference between the densities of Magnetite and Hematite crystals [3].

Additionally, in Table 3.2 the total porosity calculated from the skeletal and apparent density values according to eq. (2.12) is also included. Comparing these results with those obtained for the pristine materials, a slight increase in the porosity values of the three EAFS samples is observed. Meanwhile, in the case of the *Magnetite ore*, it remains almost invariable.

3.3.3.2. Linear thermal expansion

Thermal expansion of the four selected materials is determined by dilatometry. The measured samples correspond to the same specimens used in section 2.3.2.1 after being treated isothermally at 1000 °C during 500 hours. This long thermal treatment ensures the complete oxidation of the material. The obtained linear thermal expansion curves are collected in Figure 3.5.

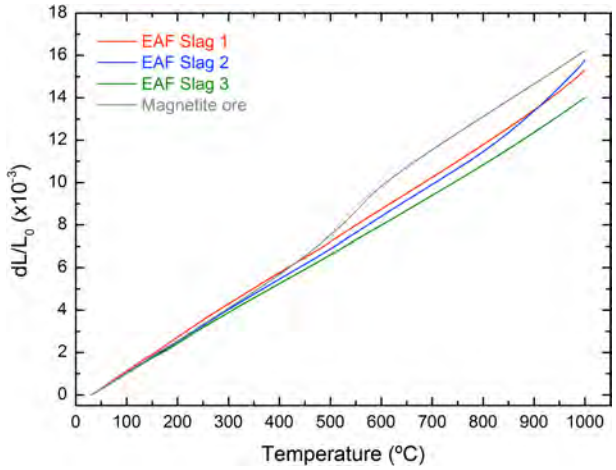

Figure 3.5. Linear thermal expansion of thermal treated materials.

Attending to the results plotted in Figure 3.5, *EAF Slag 1* and 3 present a linear trend with temperature. However, the curve associated to *EAF Slag 2* shows an inflexion point around 800-850 °C, as observed in the pristine material (see Figure 2.17). Finally, in the *Magnetite ore*, a change in the thermal expansion curve is obtained between 500 and 575 °C, which corresponds to the reversible solid-solid transition between Magnetite and Hematite [4].

Additionally, the coefficients of thermal linear expansion calculated according to eq. (2.13) for five temperature ranges from 30 to 1000 °C are presented in Table 3.3.

Table 3.3. Linear thermal expansion coefficient of the thermal treated materials.

	Temperature range (°C)				
	20 – 200	200 – 400	400 – 600	600 – 800	800 – 1000
	Linear thermal expansion, $\alpha_L \cdot 10^{-5}$ (K^{-1})				
EAF Slag 1	1.60	1.52	1.49	1.52	1.76
EAF Slag 2	1.48	1.47	1.47	1.52	2.16
EAF Slag 3	1.43	1.41	1.37	1.42	1.59
Magnetite ore	1.50	1.57	2.07	1.65	1.56

Comparing the results obtained for the pristine EAFS samples (Table 2.6) with those from the oxidized ones, lower values are obtained for the former. This is in good agreement with ref. [5] where, a lower thermal expansion is obtained for FeO than for Fe_2O_3 and Fe_3O_4. On the other hand, *Magnetite ore* presents almost similar values before and after the thermal treatment.

3.3.3.3. Specific heat

Specific heat of the four selected materials, measured from room temperature to 450 °C with the MDSC, and from this temperature to 1000 °C with LFA is presented in Figure 3.6.

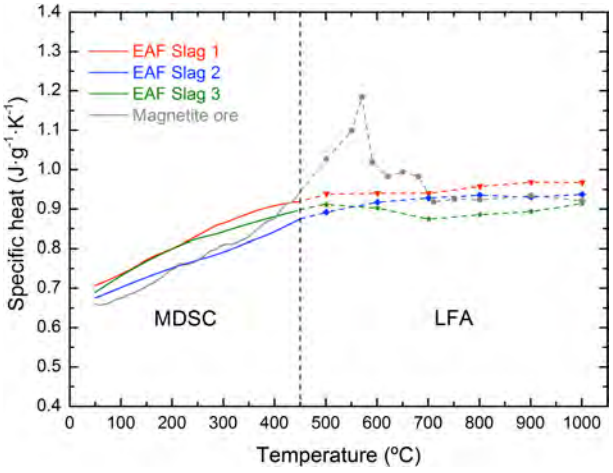

Figure 3.6. Specific heat of thermal treated materials.

Attending to the EAFS samples specific heat curves, a monotonous increase from 0.70 $J \cdot g^{-1} \cdot K^{-1}$ at room temperature to an almost saturated value around 0.95 $J \cdot g^{-1} \cdot K^{-1}$ at 600 °C is observed. On the other hand, *Magnetite ore* presents similar

specific heat behaviour than EAFS samples up to 450-500 °C where, a calorimetric peak is observed. As discussed in ref. [4], this peak corresponds to the reversible solid-solid transition between Magnetite and Hematite iron oxides. Once this transition is finished, around 700 °C, a saturated value of 0.95 $J \cdot g^{-1} \cdot K^{-1}$ is attained.

Comparing these values with the obtained for the pristine materials (Figure 2.19) no relevant differences are found. In the case of the EAFS samples, a similar trend is observed in the three samples, with slight differences in the obtained absolute values. On the other hand, in *Magnetite ore* slightly higher values are obtained in the saturation region (temperature above 600 °C).

3.3.3.4. Thermal diffusivity and conductivity

Finally, in Figure 3.7a the thermal diffusivity of the three EAFS samples and of the *Magnetite ore* measured with the LFA technique is presented. In addition, in this figure, the thermal conductivity of these four materials calculated from the density, specific heat and thermal diffusivity measurements according to eq. (2.11) is also included (Figure 3.7b).

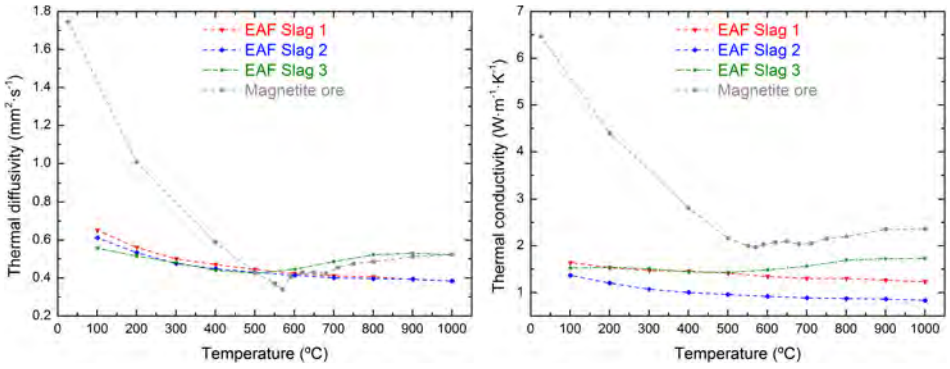

(a) (b)

Figure 3.7. a) Thermal diffusivity and b) thermal conductivity of the thermal treated materials.

The three EAFS samples present almost similar thermal diffusivity and conductivity values. The thermal diffusivity ranges from 0.6 $mm^2 \cdot s^{-1}$ at room temperature to 0.5 $mm^2 \cdot s^{-1}$ at 1000 °C. With a similar behaviour, the thermal conductivity ranges from 1.5 $W \cdot m^{-1} \cdot K^{-1}$ at ambient temperature to 0.9 - 1.6 $W \cdot m^{-1} \cdot K^{-1}$ depending on the sample. On the other hand, *Magnetite ore* presents larger thermal diffusivity and conductivity values at low temperatures (below 500 °C)

than EAFS samples. At ambient temperature, this material present values around 1.75 $mm^2 \cdot s^{-1}$ and 6.5 $W \cdot m^{-1} \cdot K^{-1}$ for the thermal diffusivity and conductivity respectively. On the other hand, at temperatures higher than 600 °C the values of these two properties are very close to the ones of the EAFS. It has to be pointed out the trend change observed in both properties at temperatures around 550 °C corresponds to the already-mentioned solid-solid transition.

Comparing the obtained values with those measured for the pristine materials (Figure 2.20 and Figure 2.21) no major differences are observed for the three EAFS samples in both properties. However, in the case of the *Magnetite ore*, higher thermal diffusivity and conductivity values are obtained for the oxidized material.

3.4. Corrosion study with *Solar salt*

In this section, the compatibility between the three EAFS samples and the laboratory-prepared *Solar salt* is investigated in detail. The main objective of this section is the investigation of any incompatibility/corrosion mechanism that may happen between both materials when operating in direct contact at the maximum working temperature of the latter, 565 °C.

3.4.1. Protocol of the compatibility tests

In Figure 3.8 a summary of the protocol followed in the preparation of the compatibility tests is presented. A total of seven assemblies are arranged. In three of them, two sheets of 2 mm thickness are tested in direct contact with approximately 20 grams of salt. This amount of salt ensures a total cover-up of the sheets. In each of these three assemblies a different EAFS type is introduced. In other three reactors, two additional sheets of each EAFS type are placed without salt, to be used in the subsequent characterisation as reference materials. Finally, an assembly filled only with salt to be used as reference is prepared.

As it can be observed in Figure 3.8, the alumina crucibles are covered with lids, then place into stainless steel reactors, and finally hermetically closed. All this process is carried out inside a glove box to avoid oxygen, humidity or any other impurity inside the reactors. Finally, all the assemblies are introduced in a furnace at 565 °C during 1000 hours.

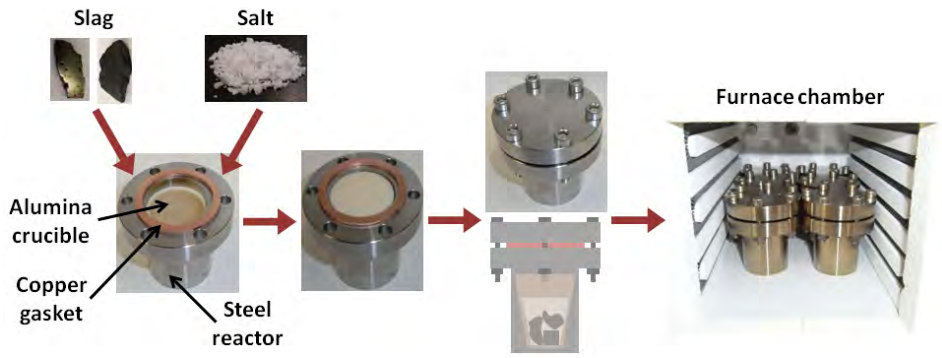

Figure 3.8. Protocol followed in the preparation of the compatibility tests.

Once the experiments are finished, the stainless steel reactors are removed from the furnace and cooled down to room temperature to ensure the total solidification of the salt. Then, the reactors are opened and the tested materials removed from the crucible.

The two slag sheets are manually separated from the solidified salt. One of them, with salt attached, is broken to analyse the internal interface cross section between both materials (see Figure 3.9). In order to analyse the salt resulting from the compatibility experiment, a small amount is carefully removed from the slag surface. The second sample is introduced into warm distilled water (60 °C) to ensure the complete removal of the attached salt. Finally, the slag pieces are dried during 24 hours at 110 °C. These cleaned slag sheets are used for the rest of the characterization.

Figure 3.9. Schematic procedure for the salt-slag interface analysis.

3.4.2. Results

3.4.2.1. Interface study

In Figure 3.10 the SEM images of the interface formed between the EAFS samples and the salt, once the compatibility tests are finished, are presented. In all

these images, the slag is on the left-hand-side, while the salt is on the right-hand-side.

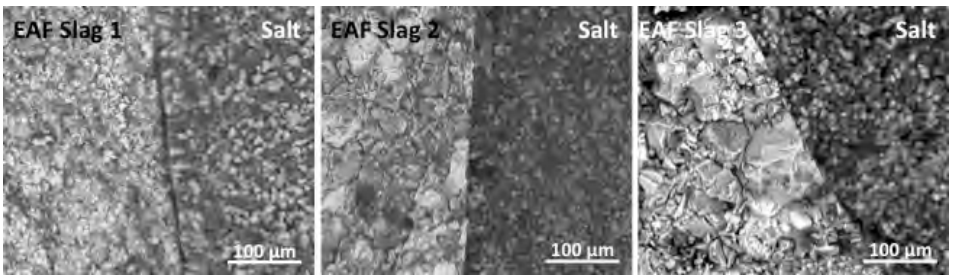

Figure 3.10. SEM images of the interface between the EAFS samples and the *Solar salt*.

As it can be observed in the three SEM pictures, there is no formation of corrosion layers at the interface between both materials in any of the systems. In addition, no modifications on the crystals aspect, size or distribution in the EAFS samples and salt surfaces are observed. Consequently, it can be concluded that the SEM analysis does not provide any evidence of corrosion mechanisms at the interface between both materials. Taking into account these results, both separate materials are deeply characterized in order to confirm this conclusion or to identify any non-visual corrosion phenomenon.

3.4.2.2. Crystallographic analysis

In order to analyse a possible transformation in the crystalline structure of the salt and EAFS samples, their structural characterization by means of XRPD and SEM techniques is presented in the following.

3.4.2.2.1. Molten nitrate salt

In Figure 3.11, the XRPD patterns obtained in the analysis of the powdered salt after the performed compatibility tests are presented. This figure contains, starting from the bottom, the pattern corresponding to the reference salt, followed by the ones tested with the *EAF Slag 1*, *EAF Slag 2* and *EAF Slag 3* respectively. For each sample, two patterns are included: one in red circles corresponding to the experimental data, and another one in continuous black line, which corresponds to the calculated pattern, obtained by Fullprof refinement software. In addition, three

vertical bars are presented in green, blue and brown corresponding to the obtained Bragg reflections for the $NaNO_3$, α-KNO_3 and γ-KNO_3 phases respectively.

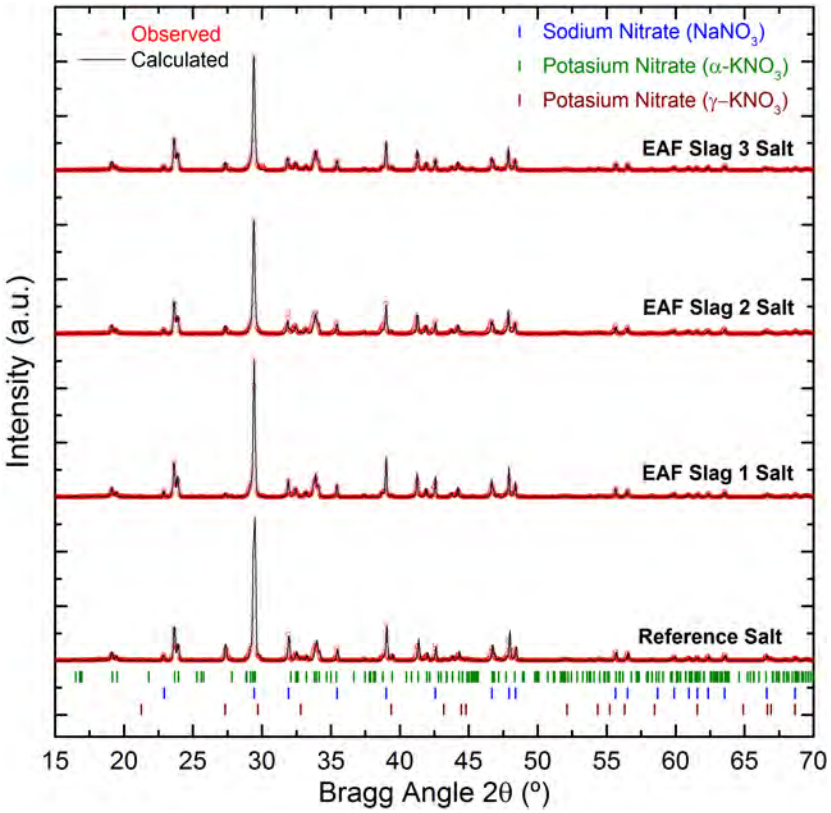

Figure 3.11. XRPD patterns *Solar salt* samples after the corrosion tests.

KNO_3 can crystallize into several phases, α-KNO_3, γ-KNO_3 and β-KNO_3 when it is heated from room temperature to high temperature as reported in [6]. The first solid phase transition from α-KNO_3 to γ-KNO_3 occurs at 100 °C while the second one, from γ-KNO_3 to β-KNO_3 at 124 °C. As it can be observed in Figure 3.11, a small amount of γ-KNO_3 phase is obtained in all diffractograms. The presence of this phase (γ-KNO_3) is associatd to the cooling rate of the system after the compatibility tests.

On the other hand, the good agreement between the measured patterns and the ones obtained in the refinement with Fullprof for the four salt samples can be observed in Figure 3.11 Taking into account these results, it can be concluded that no significant transformation occurs in the crystallographic structure or in the

components of the salt ($NaNO_3$ and KNO_3) after being in direct contact with the EAFS at 565 °C during 1000 hours.

3.4.2.2.2. Electric arc furnace slag

This subsection is devoted to the structural study of the three tested EAFS samples. In this regard, in Figure 3.12 the XRPD patterns of the three EAFS samples are presented. Starting from the top, Figure 3.12a contains the diffractograms of the *EAF Slag 1*, the one in the middle, Figure 3.12b, corresponds to the *EAF Slag 2* and, on the bottom, Figure 3.12c, the one of the *EAF Slag 3* is included. In each of these figures, two patterns are presented: on the lower part, the one corresponding to the slag sample used as reference material (tested without salt), and on the upper part, the one corresponding to the slag that was in contact with the salt. As it was indicated for Figure 3.11, for each measurement two different curves are presented corresponding to the experimental (red dots) and to the one calculated (continuous black line) with Fullprof. The vertical bars correspond to the Bragg reflection of the detected phases.

As it can be observed in the three pictures of Figure 3.12, the same four crystallographic phases (Larnite, Mayenite, Hematite and Magnetite) are found in the three references and tested EAFS samples. On the other hand, comparing each of the XRPD patterns obtained for the reference and tested materials, no significant modification in the peaks positions or intensities are observed. Attending to these results, it can also be concluded that the crystalline structure of the three EAFS samples does not suffer any significant transformation or corrosion issue after being in direct contact with the analysed salt at 565 °C during 1000 hours.

In order to obtain more information regarding the structure of the studied EAFS samples, their surfaces are imaged by means of a SEM. A total of six pieces are measured, three corresponding to the reference materials and three to the ones tested with salt (Figure 3.13).

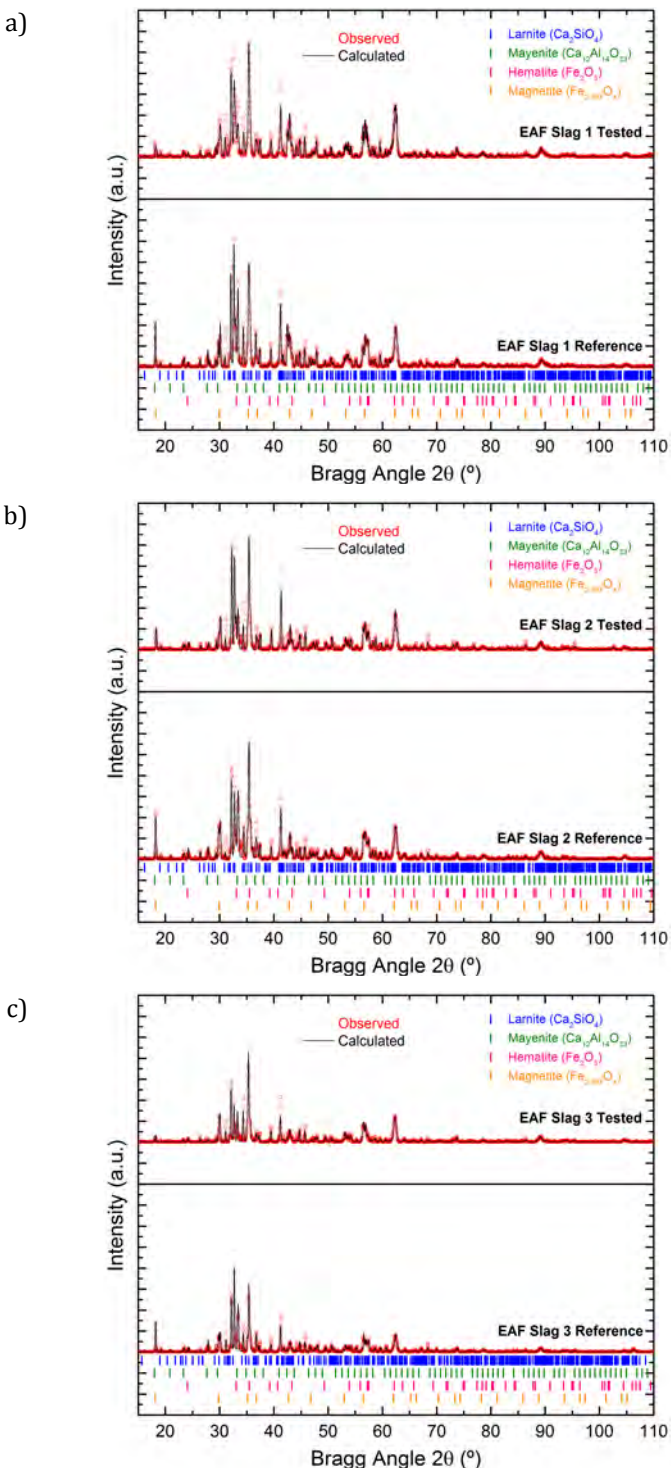

Figure 3.12. XRPD patterns of: a) *EAF Slag 1*, b) *EAF Slag 2* and c) *EAF Slag 3*.

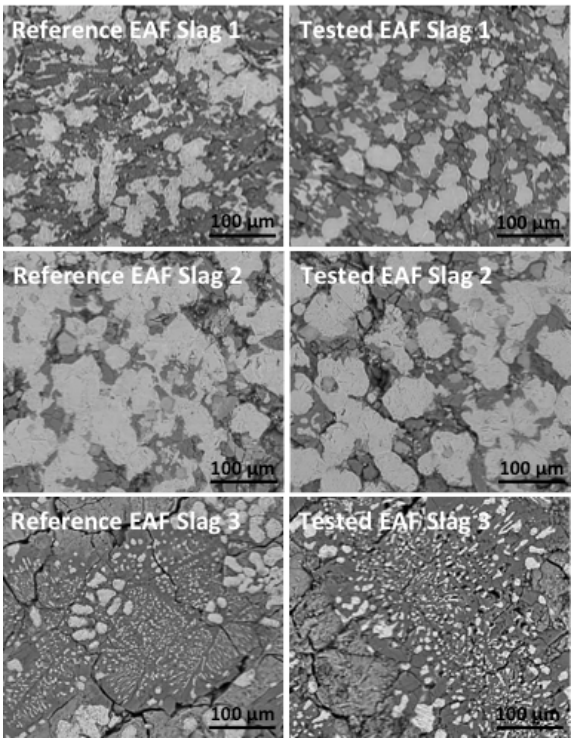

Figure 3.13. SEM images of the tested EAFS samples.

Comparing each image on the left with its corresponding one on the right, it can be observed that there is no morphological modification or transformation in the general aspect of the crystallographic domain in the EAFS samples. Additionally, attending to their size, no reduction or growth can be observed as a consequence of the direct contact with the molten salt. Overall, these results confirm the ones obtained by XRPD, where no crystallographic transformation is observed in the EAFS samples after a direct contact with the molten nitrate salt during 1000 h at 565 °C.

3.4.2.3. Thermal analysis of the molten nitrate salt

In order to study in more detail any corrosion phenomenon that could occur on the *Solar salt* during the compatibility test, its melting/solidification temperatures and enthalpies are analysed via DSC technique. A total of five salt samples are measured, corresponding to the pristine salt, the one used as reference (tested without being in contact with any EAFS type), and the three samples tested with the different EAFS materials considered within this thesis.

In each calorimetric measurement, three thermal cycles between 30-530 °C are performed. Figure 3.14 contains the obtained five DSC curves corresponding to the third cycle. In addition, in Table 3.4 the obtained melting and solidification temperatures together with the calculated phase change enthalpies are presented.

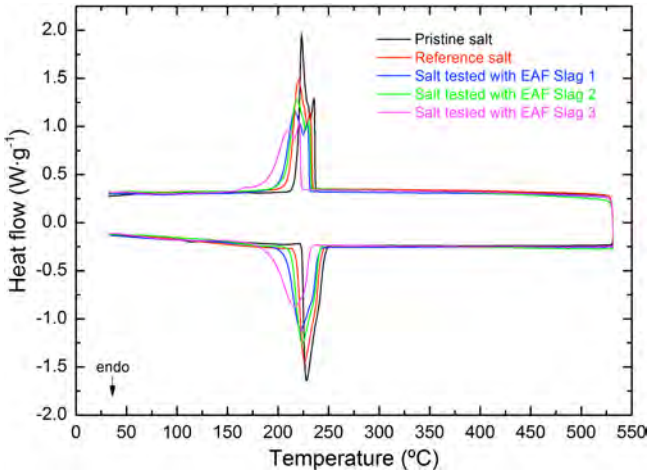

Figure 3.14. DSC curves of the different *Solar salt* samples.

Comparing the DSC curves (Figure 3.14) obtained for the pristine salt (black) with the ones for the tested salt samples (reference, *EAF Slag 1*, *EAF Slag 2* and *EAF Slag 3*), major differences between them can be observed. Looking at the pattern of the reference salt (red), and comparing it with the pristine one (black), a noticeable (8 °C) decrease on the melting and solidification temperatures is observed, as well as a widening on the phase transition peak. This observation can be related with the degradation of some nitrates to nitrites that typically reduce the melting point of the salt. The effect of adding nitrites and, its impact on the melting temperature has extensively been studied [7-9] with the general conclusion that even low concentrations of nitrites (below sensitivity of XRPD analysis), considerably reduce the salt melting temperature. In order to confirm this phenomenon, in section 3.4.2.5, the concentration of nitrates and nitrites in each salt is investigated.

On the other hand, comparing the pristine and reference DSC curves, to the ones of the EAFS tested salt samples, a considerable reduction on the melting temperatures together with a widening of the calorimetric peaks is observed.

This modification of the salt thermal behaviour may not be only justified due to the formation of nitrites but also because of some cation exchange between the EAFS and the salt affecting to the salt structure/composition. Aiming at analysing this hypothesis, in section 3.4.2.4 the elemental composition of all the involved materials is analysed in detail by means of ICP-OES technique.

As it can be appreciated in Table 3.4, the melting temperatures are more affected by the degradation phenomenon than those of the solidification. The phase change enthalpy values also show an important reduction when compared to the one of the pristine salt. As observed for the melting/solidification temperatures, this variation is also stronger for the case of the salt tested with EAFS than in the case of the reference salt.

Table 3.4. Melting and solidification temperatures and phase change enthalpies.

Salt sample	T_{melt} (°C)	T_{sol} (°C)	ΔH_f ($J \cdot g^{-1}$)
Pristine	221	238	123
Reference	212	235	120
EAF Slag 1	197	232	114
EAF Slag 2	207	234	114
EAF Slag 3	176	224	108

Overall, the results presented in this section show an important transformation on the thermal properties of the nitrate salt after being in direct contact with the different EAFS samples. These results reveal a possible corrosion or incompatibility phenomenon between both materials that is not observed by crystallographic techniques like XRPD or SEM. So as to get a better understanding of the processes occurring between both materials, the chemical composition of all the involved materials as well as the concentration of nitrates and nitrites in the salt samples are presented in the following sections.

3.4.2.4. Chemical composition of the involved materials

With the objective of analysing the possible cation migration from EAFS samples to the salt or vice versa, the chemical composition of the involved materials is measured by means of the ICP-OES technique.

Salt samples are analysed to determine the content of the most abundant elements in the EAFS (Al, Ca, Cr, Fe, Mg, Mn and Si). The insertion of low concentrations of some of these elements in the salt structure can strongly affect to its thermal properties. For example, the addition of calcium nitrate ($Ca(NO_3)_2$) to the sodium and potassium nitrate system can lead to an important reduction on the melting temperature as is the case of the well-known salt mixture "*HITEC XL*" with a melting temperature of 120 °C [10].

The chemical composition of the three salts tested in contact with EAFS samples is presented in Table 3.5. The values associated to the pristine and reference salts are not included in Table 3.5 since none of the mentioned elements are over the detection limits (d.l.) of the measurement, 20 ppm.

Table 3.5. Elemental composition of the tested *Solar salt* samples.

Element	Salt tested with		
	EAF Slag 1	*EAF Slag 2*	*EAF Slag 3*
Al (ppm)	< d.l.	< d.l.	< d.l.
Ca (ppm)	185	138	216
Cr (ppm)	< d.l.	< d.l.	< d.l.
Fe (ppm)	95	77	149
Mg (ppm)	24	< d.l.	< d.l.
Mn (ppm)	< d.l.	< d.l.	< d.l.
Si (ppm)	509	80	381

The results presented in Table 3.5 confirm the hypothesis that some cations from the EAFS migrate to the salt during the corrosion tests. The main elements moving to the salt from the EAFS are silicon, calcium and iron. Comparing the concentrations of these elements with the decrease on the melting/solidification temperatures and phase change enthalpies presented on Table 3.4, a clear trend is evidenced between them. The stronger the migration, the more pronounced the modification of the salt thermal properties. The major transformation in Figure 3.14 is observed for the salt tested with the *EAF Slag 3*, which corresponds to the salt with a higher concentration of Si, Ca and Fe (Table 3.5). On the other hand, the softer transformation on thermal properties is observed for the salt tested with

EAF Slag 2, which also corresponds to the salt with the lowest concentrations of the mentioned elements.

Additionally, the elemental composition of the three analysed EAFS samples is presented in Table 3.6. In this case, the concentrations of Na and K are also measured to analyse whether these elements move from the salt to the EAFS samples. For each EAFS type, two measurements are presented corresponding to the reference and the salt-tested EAFS samples respectively.

Table 3.6. Elemental composition of the EAFS samples.

Element	*EAF Slag 1*		*EAF Slag 2*		*EAF Slag 3*	
	Ref.	Tested	Ref.	Tested	Ref.	Tested
Al ($\%_w$)	2.1	1.8	2.1	2.0	3.5	3.0
Ca ($\%_w$)	22.3	21.7	16.3	15.8	21.9	19.9
Cr ($\%_w$)	0.7	0.7	1.7	1.5	< d.l.	< d.l.
Fe ($\%_w$)	25.9	25.6	35.4	33.1	25.9	25.6
Mg ($\%_w$)	6.7	6.7	3.6	3.3	0.6	0.6
Mn ($\%_w$)	2.1	2.1	4.8	4.6	1.4	1.4
Si ($\%_w$)	4.9	5.0	3.6	3.5	9.8	9.8
Na ($\%_w$)	0.2	0.2	0.1	0.2	0.2	0.4
K ($\%_w$)	0.1	0.1	< d.l.	< d.l.	0.1	0.1

No significant variations in the concentration of the main EAFS elements (Al, Ca, Cr, Fe, Mg, Mn and Si) are found. The small variations observed between the reference and tested materials are related to the heterogeneous nature of the EAFS. On the other hand, sodium and potassium concentrations slightly vary on the *EAF Slag 2* and *EAF Slag 3*. However, they do not vary on *EAF Slag 1* probably, because of the very small-migrated amount (ppm level).

As a consequence, the presented results confirm that one of the reasons of the salt thermal properties modification is the migration (i.e. ion exchange) of elements from the EAFS to the salt.

3.4.2.5. Nitrate/nitrites concentration

Another phenomenon that also affects to the variation on the thermal properties, the nitrite formation, is investigated in this section. Aiming at studying

the possible contribution of the nitrites on the salt melting/solidification temperatures reduction, the ion chromatography technique is selected. The obtained results for the pristine and reference salts together with the three tested salts with the considered EAFS samples are presented on Table 3.7. The results are given as the ratio between nitrites and nitrates on each sample.

Table 3.7. Mass ratio between nitrites and nitrates in the *Solar salt* samples.

Sample	$[NO_2^-]/[NO_3^-]$
Pristine	0
Reference	0.007
EAF Slag 1	0.022
EAF Slag 2	0.012
EAF Slag 3	0.055

Attending to the results in Table 3.7, it can be observed that there is no presence of nitrites in the pristine salt. However, in the other four salt samples some nitrites are formed during the compatibility experiment. In the case of the reference salt, the small amount of nitrites justifies the differences observed in the DSC curve. As presented by Lomonaco et al. [7], even very low concentrations of nitrites can considerably reduce the melting point when compared to the pure nitrate salt. On the other hand, as explained by Bauer et al. [11], the formation of nitrites in nitrate salts is a very well known reverse decomposition reaction on which oxygen is released. The formation of small amounts of nitrites in the arrangement used in the compatibility test of this study can be justified due to absence of oxygen inside the reactors.

In the case of the salt samples tested with EAFS, the concentrations of nitrites are much larger than in the case of the reference salt. This phenomenon can be justified due to the fact that the EAFS, in presence of oxygen, tends to be oxidized to form more stable phases (see section 3.3). During this process, the EAFS takes oxygen from the salt because of the absence of oxygen inside the used reactors. A proof of this mechanism is the small decrease of intensity observed in the slag XRPD patterns (Figure 3.12) at angles around 18°, when comparing the tested samples to the reference ones. The peak obtained at this angle corresponds to Magnetite (Fe_3O_4), which at high temperature can be oxidized to Hematite (Fe_2O_3).

This oxidation may occur in the EAFS in contact with the salt when nitrates are decomposed to nitrites following the next reaction mechanism:

$$2(K/Na)NO_3 \rightarrow 2(K/Na)NO_2 + O_2 \quad (3.4)$$

$$4Fe_3O_4 + O_2 \rightarrow 6Fe_2O_3 \quad (3.5)$$

In addition, in Figure 3.15 the experimental correlation between the nitrites formation and the decrease on the melting/solidification temperature is presented. The obtained results show a linear relation that suggests that the presence of nitrites in the salt is the stronger contributor to the transformation of the salt thermal properties.

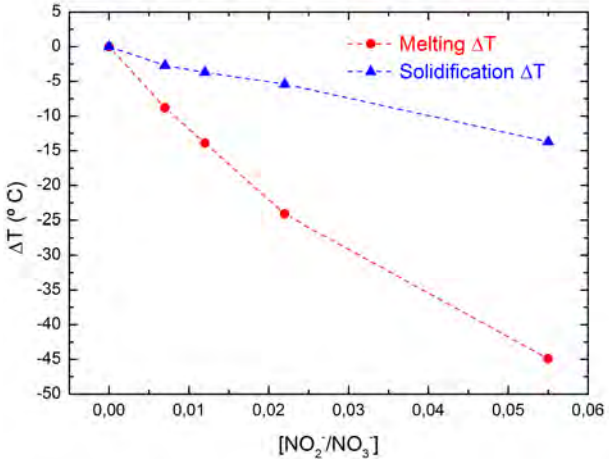

Figure 3.15. Variation on the melting and solidification temperatures of the *Solar salt* as a function of the nitrites concentration.

Overall, the presence of nitrites in the tested salt samples, together with the migration of some of the major elements present on the EAFS confirm the results observed in the DSC and, that corrosion/degradation phenomena occur in the salt when working in direct contact with EAFS at 565 °C.

3.5. Corrosion study with thermal oil

This section is devoted to the analysis of the compatibility between the *Magnetite ore* and the *Delcoterm Solar E15* oil. The main objective is to determine the suitability of this TES material and HTF to operate in direct contact at the maximum operational temperature of the latter, 310 °C.

3.6.1. Protocol

The protocol followed in the preparation of the corrosion tests is similar to the one used in the case of the *Solar salt* experiments (see section 3.4.1 and Figure 3.8). In this case, two sheets of *Magnetite ore* of around 2 mm thickness are tested in direct contact with enough oil to ensure their coverage. A total of four assemblies are prepared. In three of them, *Magnetite ore* is put in contact with oil, meanwhile in the fourth one, *Magnetite ore* sheets are introduced without oil. These assemblies are prepared and hermetically closed in a glove box, before being introduced in the furnace, in order to avoid the presence of oxygen and humidity.

The corrosion test is performed isothermally at 310 °C during 1500 hours. From the three assemblies with oil, two are removed at intermediate times, one after 500 hours and another one after 1000 hours. These two samples, removed during the thermal treatment, are used to investigate how the *Magnetite ore* or the oil evolve under eventual corrosion phenomena.

Once the experiments are finished, the steel reactors are opened and the *Magnetite ore* sheets removed from the oil. The remaining oil is kept in bottles for its characterization. In order to remove the oil impregnated in the *Magnetite ore*, the tested sheets are cleaned with ethanol and distilled water.

3.6.2. Results

In order to discuss any possible corrosion/degradation mechanism that may occur during the compatibility experiments, in this section the detailed characterization of the *Magnetite ore* samples and the tested thermal oils are presented. With this purpose the crystallographic structure of the *Magnetite ore* is analysed before and after the tests by SEM and XRPD. On the other hand, a possible transformation or degradation in the chemical structure of the thermal oil is analysed by means of FTIR, Raman spectroscopy and liquid-state NMR.

3.6.2.1. Magnetite ore crystallographic analysis

In order to study the interface of the *Magnetite ore* that was in contact with the thermal oil during the corrosion study, the SEM technique is used. For this

purpose, samples are imaged following the protocol presented in Figure 3.9. The obtained pictures of the *Magnetite ore* after 500, 1000 and 1500 hours of experiment are included in Figure 3.16.

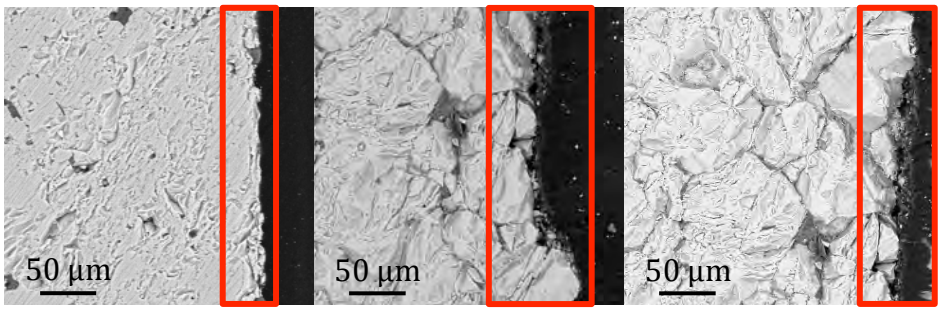

(a) (b) (c)

Figure 3.16. SEM cross-section images of the *Magnetite ore* after: a) 500; b) 1000; and c) 1500 hours of direct contact with *Delcoterm Solar E15*.

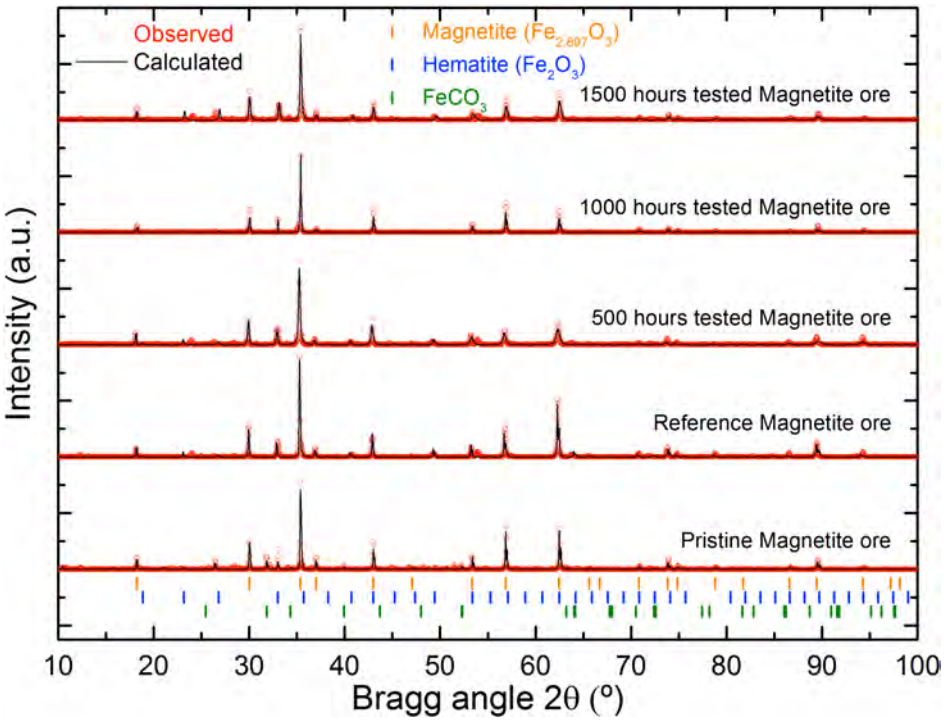

Figure 3.17. XRPD patterns of the different *Magnetite ore* samples.

In the three SEM pictures shown in Figure 3.16 no corrosion layer formation in the interface that was in contact with the thermal oil is observed. The differences

appreciated in the surface rugosity and crystals shape and size are associated to the inhomogeneity of the natural material, on one hand, and to the fracture process performed in the sample obtainment. It has to be noted that after the sample fracture, the material is not polished in order to avoid the modification of the surface.

So as to verify that the *Magnetite ore* does not suffer structural modifications, XRPD technique is used. The obtained patterns together with the Fullprof calculated ones are included in Figure 3.17. Vertical bars correspond to the Bragg reflections of the identified crystallographic phases. From bottom to top, pristine, reference, 500, 1000 and 1500 hours tested *Magnetite ore* patterns are presented.

Attending to the pattern associated to the pristine ore, similar structure than the sample characterized in chapter 2 (Figure 2.15) is found. The main crystallographic phases forming the material are the Magnetite and Hematite, as iron oxides, and some carbonates. Comparing this pattern with the obtained for the *Magnetite ore* tested without oil and the ones corresponding to the oil-tested after 500, 1000 and 1500 hours, no transformation in the Magnetite and Hematite phases is observed. However, the lack of the most representative peaks of the carbonates, 32° and 52° is observed in all the thermal treated materials. This transformation happens according to the reactions shown in the following [12,13]:

$$3FeCO_3 \rightarrow Fe_3O_4 + 2CO_2 + CO \quad (3.6)$$

$$FeCO_3 + Fe_2O_3 \rightarrow Fe_3O_4 + CO_2 \quad (3.7)$$

$$3Fe_2O_3 + CO \rightarrow 2Fe_3O_4 + CO_2 \quad (3.8)$$

Concerning reaction (3.7), as discussed in ref. [14], the juxtaposition of Hematite and ferrous iron like Siderite is found to favour the Magnetite production. This was estimated to occur at 220–280 °C and 1–2 bar [15] and shown experimentally at ~370 °C and 2 bar [16]. Nonetheless, it is most probably that the second step of the transformation occurs according to eq. (3.8), which takes place only at low CO concentrations [17]. Taking into account the low concentration of carbonates in the *Magnetite ore*, this should be the environment for the reaction since low amount of CO is released according to eq. (3.6).

XRPD measurements suggest that, apart from the transformation of $FeCO_3$ to Fe_3O_4, no further decomposition or transformation on the *Magnetite ore* happened during the compatibility experiments. These results confirm the suitability, from the point of view of the *Magnetite ore*, to operate at temperatures up to 310 °C in direct contact with *Delcoterm Solar E15* oil. These results are in agreement with the work published by Fasquelle et al. in ref. [18] where the compatibility between the thermal oil, Jarytherm® DBT, and three TES materials is investigated. In this work the compatibility is considered acceptable even if some oil penetration is observed in the material, which might become an issue under the conditions of thermal cycling.

3.6.2.2. Delcoterm Solar E15 oil structural analysis

In order to confirm the full compatibility between the *Magnetite ore* and the *Delcoterm Solar E15* oil, FTIR, Raman spectroscopy and liquid-state NMR techniques are applied to detect a possible transformation or degradation in the oil.

Figure 3.18 contains the FTIR spectra obtained in the analysis of the pristine and 1500 hours tested oil. In this figure, no modification in the intensity or shape of the most representative bands (720, 1375, 1460, 2850, 2920 and 2955 cm^{-1}) can be observed in the oil after being in contact with the *Magnetite ore*. This result suggests that the oil remains unmodified after the carried out corrosion test.

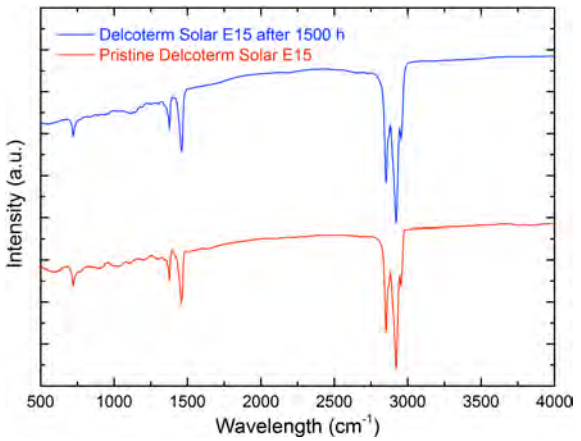

Figure 3.18. FTIR spectra of the pristine and 1500 hours-tested *Delcoterm Solar E15* oil.

In order to obtain a further confirmation regarding the stability of the thermal oil, in Figure 3.19 the spectra obtained with this technique are presented. In the lower and upper part of the plot, the spectra associated to the pristine and 1500 hours tested oils are shown.

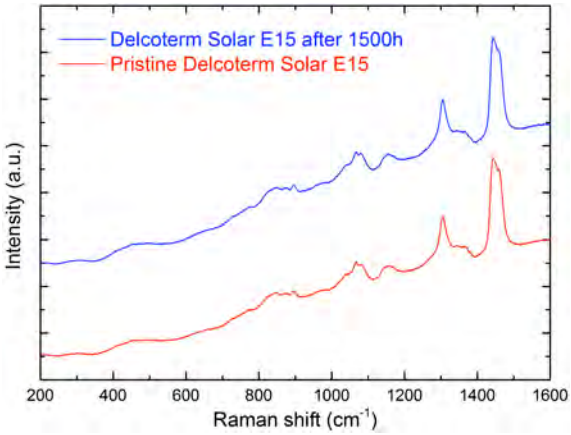

Figure 3.19. Raman spectra of the pristine and 1500 hours-tested *Delcoterm Solar E15* oil.

Attending to the results obtained with the Raman spectroscopy, similar results than those obtained with the FTIR are attained. In this case, no transformation in the shape or intensity in the representative bands (848, 876, 896, 1037, 1068, 1080, 1156, 1306, 1367, 1444 and 1460) is observed after the thermal treatment.

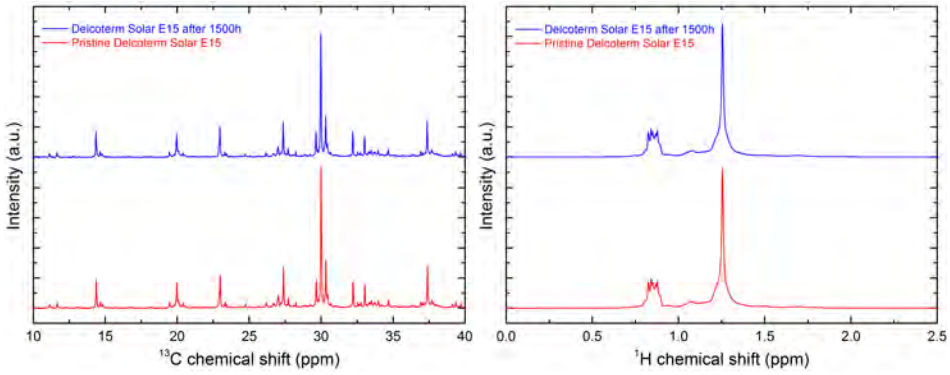

(a) (b)

Figure 3.20. (a) ^{13}C and (b) ^{1}H liquid-state NMR spectra of the pristine and 1500 hours-tested *Delcoterm Solar E15* oil.

The obtained results with both characterization techniques, FTIR and Raman spectroscopy, permit to confirm that no transformation occurs in the thermal oil

when operating in direct contact with the *Magnetite ore*. In order to obtain an additional confirmation of these results, liquid-state NMR is applied to obtain information regarding the chemical microstructure of the oil. The obtained results for the ^{13}C and ^{1}H liquid-state NMR are collected in Figure 3.20.

Attending to the results presented in Figure 3.20, similar spectra are obtained in the ^{13}C and ^{1}H liquid-state NMR for the pristine and 1500 hours tested oil. These results confirm the conclusions extracted from FTIR and Raman spectroscopies allowing to ensure that no corrosion/degradation mechanism nor contamination of the *Delcoterm Solar E15* oil occur when operating in direct contact with the *Magnetite ore* at 310 °C, at least during 1500 hours.

3.6. Conclusions

In this chapter the compatibility of the previously selected TES materials, three EAFS samples and *Magnetite ore*, operating in direct contact with air, a molten nitrate salt and a thermal oil has been addressed.

The analysis performed under air guarantee the stability of the four investigated material at temperatures up to 1000 °C with some restrictions. Regarding the EAFS samples, the oxidation of the Wustite (FeO) present in the pristine materials, to form Magnetite (Fe_3O_4) and Hematite (Fe_2O_3) occurs at temperatures above 500 °C. On the other hand, in the *Magnetite ore* a slight oxidation was also observed up to reach an equilibrium of 60%$_w$ Hematite and 40%$_w$ Magnetite in the sample, together with the decomposition of carbonate traces present in the material. Nevertheless, once these transformations have occurred, no further modifications happen in the materials. As a consequence of the mentioned oxidation processes, the thermo-physical properties of the four materials vary. In this regard, the new properties of the obtained oxidized-materials have also been characterized in this chapter.

Overall, the presented results allow concluding the suitability of using air as heat transfer fluid in direct contact with the four analysed materials. Nonetheless, the observed transformation involves, that in order to perform an accurate design of the TES system, when the operation temperature is established above 500 °C, the thermo-physical properties of the transformed materials should be considered.

The study of the compatibility between the three investigated EAFS samples with the *Solar salt*, at 565 °C revealed a degradation mechanism in the salt promoted by the EAFS. The analysis of the crystallographic structure of the EAFS samples did not show a corrosion layer between the EAFS samples and the salt. The only transformation observed in the EAFS is, as in the case of using air as heat carrier, the oxidation of the Wustite to form Magnetite and Hematite. However, the detailed analysis of the thermal properties of the salt revealed a modification on its melting/solidification temperatures as well as on the phase change enthalpies. After applying different characterization techniques, this modification was found to occur by the formation of nitrites in the salt, and to the migration of some cations, at ppm level, from the EAFS to the salt. In addition, the formation of nitrites was found to be not only caused by the experimental conditions, but also intensified by the presence of the EAFS (Wustite phase).

From the obtained results a further investigation is needed to demonstrate the viability of these two materials to operate in direct contact. In these terms, the potential saturation of the mentioned cation exchange and nitrite formation needs to be assessed in order to ensure reproducible thermal properties of the salt. On the other hand, the continuation of the observed transformation with time would lead to an unacceptable degradation of the salt.

Finally, the compatibility investigation of the possibility of using the *Magnetite ore* in direct contact with a commercial thermal oil used in CSP plants, *Delcoterm Solar E15*, was investigated at the maximum operation temperature of the latter, 310 °C. The solid material characterization shown that no corrosion layer was formed in the interface in contact with the oil. In addition, the crystallographic analysis of the *Magnetite ore* showed a slight modification associated to the decomposition of the carbonates present in the pristine material as it occurs when operating with air as heat transfer fluid. On the hand, the analysis of the chemical structure of the *Delcoterm Solar E15* oil did not reveal any degradation/contamination mechanism. Overall, the obtained results guarantee the suitability of these two materials to operate in direct contact at temperatures up to 310 °C.

3.7. References

[1] SQM [Online]: http://www.sqm.com/en-us/productos/quimicosindustriales/salestermo-solares/productostermo-solares.aspx

[2] DELCO, Delcoterm Solar E15 Data sheet.

[3] L.B. Railsback, "Density of minerals III: Oxides and stoichiometry," in *Some Fundamentals of Mineralogy and Geochemistry*., 2016.

[4] Y. Grosu, A. Faik, I. Ortega-Fernández, and B. D'Aguanno, "Natural magnetite for thermal energy storage: excellent thermophysical properties, reversible latent heat transition and controlled thermal conductivity," *Solar Energy Materials & Solar Cells*, vol. 161, pp. 170-176, 2017.

[5] M. Takeda, T. Onishi, S. Nakakubo, and S. Fujimoto, "Physical properties of iron-oxide scales on Si-containing steels at high temperature," *Materials Transactions*, vol. 50, no. 9, pp. 2242-2246, 2009.

[6] J.K. Nimmo and B.W. Lucas, "The crystal structures of γ- and β-KNO3 and the α←γ←β phase transformations," *Acta Cryst.*, vol. B32, pp. 1968-1971, 1976.

[7] A. Lomonaco, D. Haillot, E. Pernot, E. Franquet, and J.-P. Bédécarrats, "Sodium nitrate thermal behavior in latent heat thermal energy storage: A study of the impact of sodium nitrite on melting temperature and enthalpy," *Solar Energy Materials & Solar Cells*, vol. 149, pp. 81-87, 2016.

[8] R.W. Berg, D.H. Kerridge, and P.H. Larsen, "NaNO2 + NaNO3 Phase Diagram: New Data from DSC and Raman Spectroscopy," *Journal of Chemical & Engineering Data*, vol. 51, pp. 34-39, 2006.

[9] T. Bauer, D. Laing, and R. Tamme, "Recent Progress in Alkali Nitrate/Nitrite Developments for Solar Thermal Power Applications," in *Molten Salts Chemistry and Technology, MS9*, Trondheim, Norway, 5 - 9 June 2011.

[10] D. Kearney et al., "Assessment of a molten salt heat transfer fluid in a parabolic trough solar field," *Journal of Solar Energy Engineering*, vol. 125, pp. 170-176, 2003.

[11] T. Bauer, N. Breidenbach, N. Pfleger, D. Laing, and M. Eck, "Overview of molten salt storage systems and materials development for solar thermal power plants," in *World Renewable Energy Forum*, Denver, Colorado, EEUU, 2012.

[12] K.S. Goto, "Solid state electrochemistry and its applications to sensors and electronic devices," in *Materials Science Monographs*., 1988, vol. 45, pp. 1-454.

[13] C. Feilmayr, A. Thurnhofer, F. Winter, H. Mail, and J. Schenk, "Reduction behavior of hematite to magnetite under fluidized bed conditions," *ISIJ International*, vol. 44, no. 7, pp. 1125-1133, 2004.

[14] D.M. Burt, "The system Fe-Si-C-O-H: a model for metamorphosed iron formations," in *Carnegie Institute Washington Yearbook*., 1971–1972, pp. 435-443.

[15] T. Miyano, "Diagenetic to low-grade metamorphic conditions of Precambrian ironformations," in *Precambrian Iron Formations*, P.W.U., LaBerge, G.L. (Eds.) Appel, Ed. Athens, Greece, 1987, pp. 155-186.

[16] B.M. French, "Stability of siderite (FeCO3) in the system of Fe-C-O," *American Journal of Science*, vol. 271, no. 1, pp. 37-78, 1971.

[17] Y. Yu and C. Qi, "Magnetizing roasting mechanism and effective ore dressing process for oolitic hematite ore," *Journal of Wuhan University of Technology Materials Science*, vol. 26, no. 2, pp. 176-181, 2011.

[18] T. Fasquelle, Q. Falcoz, P. Neveu, G. Flamant, and J. Walker, "Compatibility tests between Jarytherm DBT synthetic il and solid materials from wastes," *AIP Conference Proceedings*, vol. 1734, p. 040004, 2016.

Chapter 4:

Model description and validation

4 Model description and validation

This chapter aims at presenting the complete physical model developed in this thesis able to predict the thermal behaviour of packed bed thermal energy storage systems. The model constructed includes all the relevant heat transfer and fluid dynamic mechanisms involved in the studied system. Its accuracy and computational economy are also carefully assessed. In addition, when compared to the standard modelling strategies of similar systems, the developed model includes a serie of innovative contributions and capabilities beyond the state-of-the-art. Overall, the developed physical model demonstrates a full flexibility, accuracy and improved competencies able to simulate different operation conditions, cycling behaviour and the description of the proposed TES concept in novel implementation environments with the corresponding boundaries and requirements.

4.1. Thermal storage description

In this research, as mentioned in the introductory section, the proposed concept to achieve an effective heat storage solution is the solid packed bed arrangement. The particular benefits derived from this dual media storage concept are very attractive in terms of technological exploitation, thermal performance and economic effectiveness.

A general overview of the packed bed storage concept, exploitation and implementation is given in section 1.3. In this configuration, the discrete pieces of the TES material are placed inside a cylindrical tank in a random packing distribution. The interstitial fluid flow, introduced from the top or from the bottom of the tank during the charge or discharge operations respectively, is responsible of the heat exchange to/from the solid packing. Even if the real operation of such system implies different challenges, which clearly affect to the thermal performance of the packed bed TES concept, in the described system only the thermo-fluidic behaviour in the solid packing is analysed, including a lateral thermal insulation. In this system, homogeneous fluid flow distribution is assumed in the tank inlet, both in the charge and discharge processes. A schematic view of the modelled system domain is shown in Figure 4.1, including the boundary conditions considered in the model construction.

a)

b)

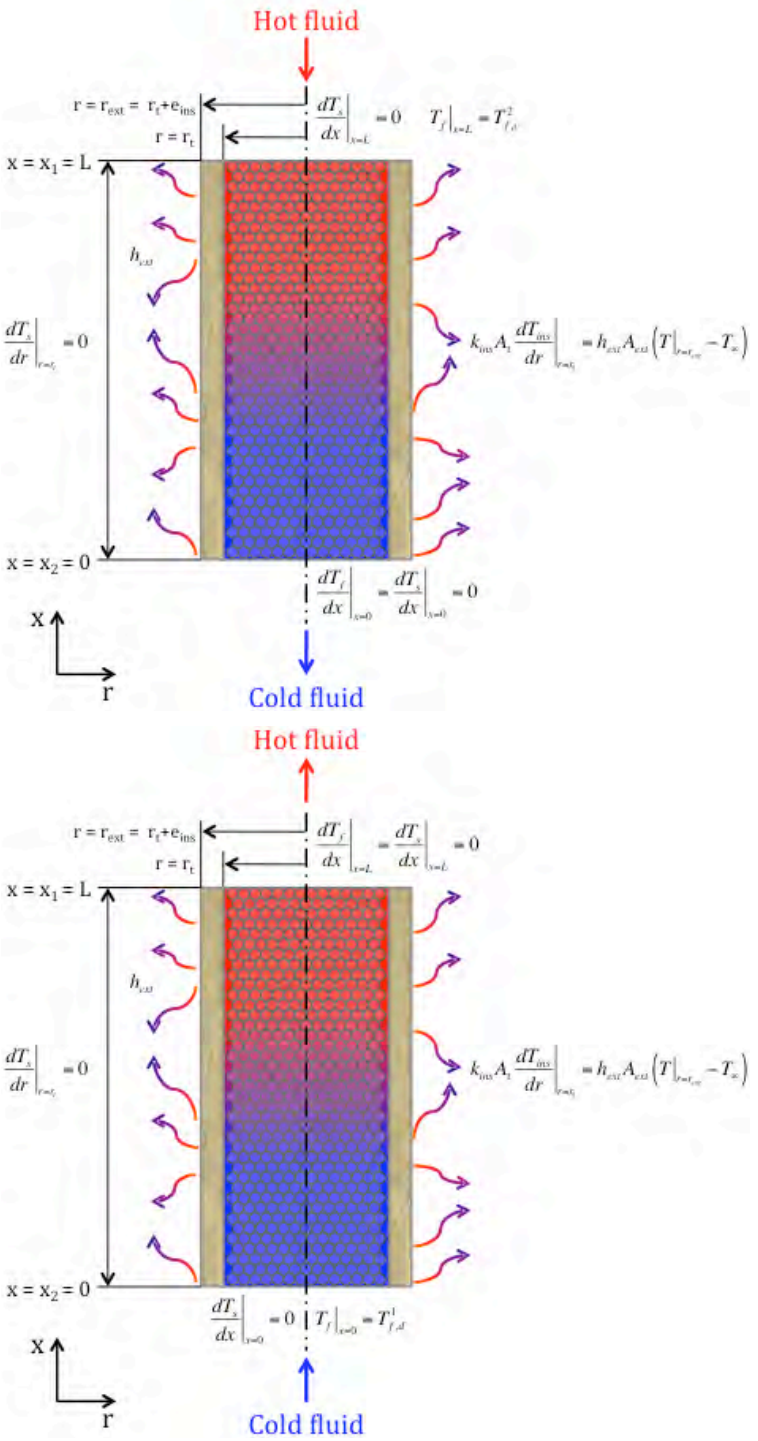

Figure 4.1. Schematic view of the studied system domain together with the assumed boundary conditions in the a) charge and b) discharge operations.

In addition, in all the modelled systems, the following initial conditions are assumed:

$$T_s(x,r,t=0) = T_f(x,r,t=0) = T_{amb} = 20\,^{\circ}C;$$

$$v_f(x,r,t=0) = 0;$$

$$p(x,r,t=0) = p_{inital}.$$

4.2. Model description

The main conservation equations used for the construction of the heat transfer and fluid dynamic model, which describes the simulated systems are established in this section: the mass or continuity, the momentum and the energy equations. These governing equations are numerically solved in a simultaneous coupled scheme described in the following sections. In addition to these partial differential equations solved by using the boundary and initial conditions shown in Figure 4.1, different closing equations need to be included in the model. These equations comprise the complex heat transfer mechanisms involved in the packed bed, including conductive, convective and radiative thermal transport principles. The complete set of equations is explained below.

4.2.1. Mass or continuity equation

In its general form, the mass conservation or continuity equation can be described as follows:

$$\frac{d\rho_f}{dt} + \nabla \cdot \left(\rho_f \cdot \vec{v}\right) = 0; \tag{4.1}$$

where first term accounts for the mass evolution with time and the second for the mass entering or leaving the domain. It has to be noted that even if in all the modelled cases in this thesis, the fluid flow is considered as incompressible, this equation is valid for both compressible and incompressible flows.

4.2.2. Momentum equation

The interstitial fluid movement through the packed bed is modelled using the porous media formulation included in many commercial computational fluid

dynamics (CFD) packages. The porous model considers the domain as a continuous medium adding a source term ($\vec{S}_i$) to the standard momentum equation for describing the interference of the packed bed on the fluid flow, as shown in eq. (4.2):

$$\frac{d}{dt}\left(\rho_f \cdot \vec{v}\right) + \nabla \cdot \left(\rho_f \cdot \vec{v} \cdot \vec{v}\right) = -\nabla p + \nabla \cdot (\bar{\bar{\tau}}) + \rho_f \cdot \vec{g} + \vec{S}_i; \tag{4.2}$$

where ρ_f is the fluid density, $\vec{v}$ the fluid velocity, p the static pressure, $\bar{\bar{\tau}}$ the stress tensor and $\vec{g}$ the gravity constant.

The source term, $\vec{S}_i$, added to the momentum equation according to the porous continuous media approach generates a pressure gradient in the three spatial directions, proportional to the fluid velocity given by the following equation:

$$S_i = -\left(\sum_{j=1}^{3} F_{ij} \cdot \mu \cdot v_j + \sum_{j=1}^{3} C_{ij} \cdot \frac{1}{2} \cdot \rho_f \cdot |v| \cdot v_j\right). \tag{4.3}$$

F_{ij} and C_{ij} correspond to the permeability and inertial loss tensors respectively.

If the porous medium can be considered homogeneous in all the spatial directions, the non-diagonal components of the mentioned F_{ij} and C_{ij} tensors vanish. Considering the random nature of the solid packing studied in this thesis work, this assumption can be applied, leading to a simplified version of eq. (4.3):

$$S_i = -\left(\frac{\mu}{\sigma} \cdot v_i + C_2 \cdot \frac{1}{2} \cdot \rho_f \cdot |v| \cdot v_i\right); \tag{4.4}$$

where σ is the permeability of the porous medium and C_2 the inertial resistance factor. In this approach, $1/\sigma$ and C_2 correspond to the diagonal elements of tensors F_{ij} and C_{ij} respectively.

4.2.2.1. Evaluation of the pressure drop

The pressure drop associated to the fluid flow through the solid packing can be calculated by using different approaches. The calculation of this magnitude is always a complex issue, which usually involves a wide variety of physical mechanisms depending on the nature of the fluid, the laminar or turbulent flow conditions and the structure of the packing. As a consequence, different empirical correlations can be found in order to determine the pressure drop in a porous

medium, such as Darcy´s law and its different implementation versions depending on the particular flow conditions. One of the most used approaches is the Ergun's semi-empirical correlation [1], shown in eq. (4.5). This correlation is selected for the calculations performed in this work.

$$\frac{\Delta p}{L} = \frac{150 \cdot \mu}{{d_p}^2} \cdot \frac{(1-\varepsilon)^2}{\varepsilon^3} \cdot v_\infty + \frac{1.75 \cdot \rho_f}{d_p} \cdot \frac{(1-\varepsilon)}{\varepsilon^3} \cdot {v_\infty}^2; \tag{4.5}$$

where L is the tank length, d_p the solid particle diameter, ε the packed bed void fraction and v_∞ the superficial velocity.

This approach is chosen due to its demonstrated accuracy in a wide range of Reynolds number and different porous medium natures in terms of particle packing configurations.

Once established the approach selected for the pressure drop evaluation, its direct relation with the source term added in the standard momentum equation, leads to the identification of the F_{ij} and C_{ij} tensor components. In this frame, the permeability and the inertial loss coefficients can be calculated as:

$$\sigma = \frac{{d_p}^2}{150} \cdot \frac{\varepsilon^3}{(1-\varepsilon)^2}; \tag{4.6}$$

$$C_2 = \frac{3.5}{d_p} \cdot \frac{(1-\varepsilon)}{\varepsilon^3}. \tag{4.7}$$

As shown in eq. (4.6) and (4.7), the explicit functional form of the F_{ij} and C_{ij} tensor components only depend on the solid packing configuration, i.e. d_p and ε. Whereas d_p is fixed according to the modelled system, ε can present important physical implications as a function of the bed length, diameter of the tank, and other factors, which lead to a non-constant value of the void fraction. As shown in the following section, in this model, the dependency of σ and C_2 coefficients with the void fraction in the bed is explicitly considered.

4.2.2.2. Evaluation of the packed bed void fraction

The modelling of solid particles packing is a complex mathematical issue. The description of different packing configurations trying to determine the efficiency of filling the available volume has been an active research field since years. The high complexity of this phenomenology can be addressed under different

approximations degrees. As a starting point, regular sphere packing can be assumed in order to obtain a clear view of the different packing configurations.

In this frame, the highest efficiency for filling the available volume using spherical particles is the hexagonal close packing (HCP), where a single sphere presents 12 surrounding contacting spheres. In this configuration, as demonstrated by Gauss [2], a 74% of the total volume is filled. This packing strategy is the most efficient one, leading to a void fraction of 0.26. The face centred cubic packing (FCC) also shows a similar space filling behaviour.

When dealing with random distribution of spheres, the packing efficiency drastically changes. Whereas the packing value and void fraction in the mentioned HCP configuration can be easily mathematically addressed, the random packing configurations can only be investigated by means of sophisticated numerical, empirical and statistical procedures. In this regard, different investigations have shown the particular behaviour of the void fraction in various sphere random packing arrangements. A summary of the obtained void fraction values for several random sphere-packing distributions is shown in Table 4.1.

Table 4.1. Space filling efficiency and void fraction values of different sphere random packing configurations.

Packing model	ε
Thinnest regular packing	0.4764
Very loose random packing	0.44
Loose random packing	0.4 to 0.41
Poured random packing	0.375 to 0.391
Close random packing	0.359 to 0.375
Densest regular packing	0.2595

Considering the aforementioned random packing arrangements, in this work, the close random packing strategy is identified as the more realistic one. The spherical geometry of the solid particles is also an idealized view of the modelled system. However, the implications of both mentioned statements can also be considered within the developed model by means of the appropriate change of the void fraction value, empirically obtained. Overall, the void fraction value is fixed on 0.37 in this thesis work.

Even if this constant value is an appropriate selection able to describe the modelled TES system with a successful accuracy, a more sophisticated approach is applied in this model. Namely, depending on the TES tank size, the packing void fraction can show a noticeable dependence with the bed length or diameter values. As a consequence, the void fraction is considered as a functional distribution depending on the spatial directions, radial [3] and axial [4], rather than constant.

In the axial direction, the effect of large bed lengths on the packing efficiency is included in the model through a quadratic function, ranging from 0.37 on the top to 0.345 on the bottom, according to Zanganeh et al. [4]. It must be noted that this variable behaviour is only considered on real scale packed bed TES systems.

In the radial direction, the variation of the void fraction value is associated to the ratio between the tank and solid particle diameters (d_t/d_p). Values of this coefficient lower than 40 lead to the generation of preferential paths of the flow in the regions close to the wall, so-called channelling [3]. In order to perform an adequate description of the fluid flow in this region, a variable radial void fraction is also considered when d_t/d_p < 40. Different semi-empirical models are available in the literature for describing this phenomenon [5-8] that shows a decaying-cosine porosity profile (Figure 4.2). The bulk value of the void fraction is reached by an oscillating function starting at the wall with ε = 1, corresponding to an empty packing region.

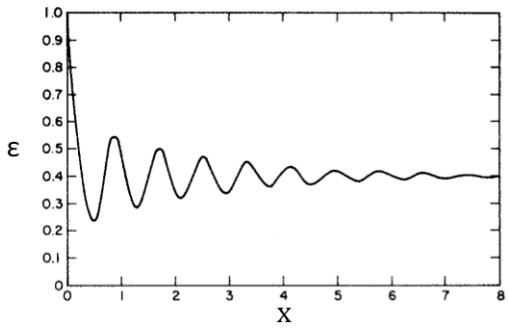

Figure 4.2. Voidage variations near the wall of a cylindrical column randomly packed with spheres of uniform size [5].

In this work, a minimum saturation void fraction value of $\varepsilon = \varepsilon_\infty = 0.37$ is fixed for the bulk random bed packing. For describing this variation, the expression used by Hunt and Tien [**6**] is considered:

$$\varepsilon = \varepsilon_{\infty}\left(1 + A \cdot e^{-B\cdot\frac{r}{d_p}}\right); \tag{4.8}$$

where B is a constant coefficient equal to 8, as established in [6], due to the irregular shape of the solid particles, and A is adjusted for each particular case in such a way ε is equal to 1, when r is equal to d_t (wall).

4.2.3. Energy equation

The heat transfer modelling in packed bed systems can be addressed by means of different simulation strategies [9]. Among them, the continuous medium approach implemented in this work offers a good compromise between the calculation accuracy and computational effort. This approach considers a cooperative and averaged quantification of the governing heat transport phenomena in a macroscopic continuous medium approach, without entering on the detailed description of the local effects derived from the individual particle packing. In this scheme, the energy conservation equations for the fluid and solid phases can be expressed as:

$$\frac{d}{dt}\left(\varepsilon \cdot \rho_f \cdot H_f\right) + \nabla \cdot \left(\vec{v} \cdot \left(\rho_f \cdot H_f + p\right)\right) = \nabla \cdot \left(\varepsilon \cdot k_f \cdot \nabla T_f\right) + h_{fs} \cdot A_{fs} \cdot \left(T_s - T_f\right) + S_f^H; \tag{4.9}$$

$$\frac{d}{dt}\left((1-\varepsilon) \cdot \rho_s \cdot H_s\right) = \nabla \cdot \left((1-\varepsilon) \cdot k_s \cdot \nabla T_s\right) + h_{fs} \cdot A_{fs} \cdot \left(T_f - T_s\right) + S_s^H. \tag{4.10}$$

The terms on the left-hand side of eq. (4.9) stand for the time enthalpy change and advective energy contribution associated to the fluid forced movement respectively. The first term on the right-hand side corresponds to the heat transport in the fluid phase. The second term is associated to the heat exchange between the solid and fluid phases. The last term accounts for an eventual enthalpy source to the fluid energy equation, among them thermal losses.

Following a similar description than in eq. (4.9), the term on the left-hand side of eq. (4.10) accounts for the enthalpy change in the solid medium; the first term on the right-hand side stands for the conduction heat transfer in the solid; the second one for the heat exchange between solid and fluid zones; and the third one for an eventual enthalpy source to the solid energy equation, among them thermal losses.

4.2.3.1. Local thermal equilibrium approximation

The local thermal equilibrium (LTE) assumption is a useful simplification of the energy equations presented above. This approach supposes an immediate local heat transfer between the solid and the fluid or, equivalently, null heat transfer resistance between both. Even if this approximation could seem far from its realistic implementation, the application of the LTE formulation is very useful under certain conditions. One of the main implementation frames, which guarantee the validity of this statement, is a large solid thermal conductivity value compared with the one of the fluid [10,11]. As a consequence, the two energy conservation equations presented in section 4.2.3 can be reduced [12] to the following single expression:

$$\frac{d}{dt}\left(\varepsilon \cdot \rho_f \cdot H_f + (1-\varepsilon) \cdot \rho_s \cdot H_s\right) + \nabla \cdot \left(\vec{v} \cdot \left(\rho_f \cdot H_f + p\right)\right) = \nabla \cdot \left(k_{eff} \cdot \nabla T\right) + S^H. \qquad (4.11)$$

The obtained equation accounts on the left-hand side for the time fluid and solid enthalpy change (first term) and for the advective energy associated to the fluid forced movement. The terms on the right-hand side correspond to the heat transport in the packed bed and to an eventual enthalpy source, i.e. thermal losses.

In this thesis work both, local or non-local equilibrium energy formulations are used depending on the particular operation conditions and materials properties on each proposed TES system. The implementation of one or other modelling alternatives is fully justified, and the main objectives of a high calculation accuracy together with an effective computational economy preserved.

4.2.3.2. Evaluation of the effective thermal transport properties

The modelling of the heat transfer phenomena at high temperatures in packed beds involves complicated mechanisms and contributions of different natures, conductive, convective and radiative [13]. According to these authors, the physical manifestation of these heat transport phenomena lead to complex contributions to the overall heat transfer, summarized below:

1. Thermal conductivity through the solid;
2. Thermal conduction through the contact surfaces of two packings;
3. Radiant heat transfer between surfaces of two packings;

4. Radiant heat transfer between neighbouring voids;
5. Thermal conduction through the fluid film near the contact surface of two packings;
6. Heat transfer by convection solid-fluid-solid;
7. Heat transfer by advective mixing.

It has to be noted that radiant mechanisms only occur when a gaseous fluid is considered as heat transfer fluid. In this regard, when the considered heat transfer fluid is a liquid, the third and fourth mechanisms can be neglected.

The inclusion of the mentioned heat transfer mechanisms in the energy conservation equation (eq. (4.9) and (4.10) or eq. (4.11)) becomes, according to the mentioned physical mechanisms, a highly complex issue. In order to include all of them in a simplified and effective manner, a modified effective thermal conductivity (k_{eff}) is applied. In this work, the calculation of the effective thermal conductivities of the solid and fluid phases of the modelled system are performed according to the semi-empirical model developed by Wakao & Kaguei [14], and established by eq. (4.12):

$$k_{eff} = k_e^0 + 0.5 \cdot Pr \cdot Re_p \cdot k_f; \tag{4.12}$$

which is valid for a wide range of particle Reynolds number (eq. (4.13)). In this equation, k_e^0 accounts for all the heat transfer phenomena that occur under motionless fluid conditions, so-called stagnation term. The second term on the right-hand side includes the energy transport associated to the fluid flow motion.

$$Re_p = \frac{v_\infty \cdot \rho_f \cdot d_p}{\mu}. \tag{4.13}$$

$$Pr = \frac{c_p}{\mu \cdot k_f}. \tag{4.14}$$

For the estimation of the stagnation term (k_e^0) two different semi-empirical models are considered within this thesis. On one hand, the one developed by Yagi & Kunii [13] and Kunii & Smith [15] which includes radiative effects. And, on the other hand, the one developed by Krupiczka [16] that neglects radiation. In this line, the first model will be implemented in those systems operating with gases at high temperature, above 150 °C as indicated in ref. [4] in which radiation mechanisms cannot be neglected. Consequently, the second model is applied when

liquids are considered as heat transfer fluids, or complementarily, in any fluid/solid combination at low temperatures, below the mentioned threshold.

In the following subsections, both models are described in detail.

4.1.3.2.1.Stagnation term evaluation including radiative heat transfer mechanisms

For those systems on which radiative heat transfer mechanisms inside the packed bed cannot be neglected, Kunii & Smith [15] proposed the use of the following equation for the evaluation of stagnated effective thermal conductivity:

$$k_e^0 = \frac{\beta\cdot(1-\varepsilon)\cdot k_f}{\zeta\cdot\left(\frac{k_f}{k_s}\right)+\frac{1}{(1/\psi)+\left(d_p\cdot h_{rs}/k_f\right)}} + \varepsilon\cdot\left(k_f + \beta\cdot d_p\cdot h_{rv}\right); \tag{4.15}$$

where β is the ratio of the average length between the centres of two neighbouring particles. This parameter ranges between 1, for loose packing arrangements, and 0.82 for close packing configurations. Due to the random packing in all the considered systems in this thesis, a value of 0.9 is used. The value of ζ is 2/3 and corresponds to the ratio between the solid length affected by the thermal conductivity and the average particle diameter. The h_{rs} and h_{rv} factors correspond to the heat transfer coefficients for radiation between solid-solid surfaces and between void-void respectively. These two heat transfer coefficients can be calculated from the equations given by Yagi & Kunii [13]:

$$h_{rs} = 0.227\cdot\left(\frac{\varepsilon_s}{2-\varepsilon_s}\right)\cdot\left(\frac{T_s}{100}\right)^3; \tag{4.16}$$

$$h_{rv} = \frac{0.227}{1+\frac{\varepsilon}{2\cdot(1-\varepsilon)}\cdot\frac{1-\varepsilon_s}{\varepsilon_s}}\cdot\left(\frac{T_f}{100}\right)^3. \tag{4.17}$$

Finally, the parameter ψ shown in eq. (4.15) corresponds to the effective thickness of the fluid film adjacent to the contact surface of two particles. Following Kunii & Smith [15] indications, it can be calculated from the equation:

$$\psi = \psi_2 + (\psi_1 - \psi_2)\cdot\frac{\varepsilon-\varepsilon_2}{\varepsilon_1-\varepsilon_2}; \tag{4.18}$$

where ψ_1 and ψ_2 correspond to the ψ_i coefficient when the void fraction is 0.26 (close packing) and 0.476 (open packing) respectively. ψ_i is calculated with the following expression:

$$\psi_i = \frac{1}{2} \cdot \frac{\left(\frac{\kappa-1}{\kappa}\right)^2 \cdot \sin^2\theta_i}{\ln(\kappa-(\kappa-1)\cdot\cos\theta_i)-\frac{\kappa-1}{\kappa}(1-\cos\theta_i)} - \frac{2}{3}\cdot\frac{1}{\kappa}; \quad (4.19)$$

where κ is the coefficient between the solid and fluid thermal conductivities (k_s/k_f) and $\sin^2\theta_i = 1/n_i$. n is the equivalent number of contact points for the semispherical surface of a particle and has as values $4\sqrt{3}$ and 1.5 for the close and open packing cases respectively.

4.1.3.2.2.Stagnation term evaluation neglecting radiative heat transfer mechanisms

In those cases on which radiative heat transfer mechanisms can be neglected, the semi-empirical model developed by Krupiczka [16] is considered. In this frame, k_e^0 might be calculated as:

$$k_e^0 = k_f \cdot \left(\frac{k_s}{k_f}\right)^m; \quad (4.20)$$

where m corresponds to the following expression:

$$m = 0.280 - 0.757 \cdot \log_{10}\varepsilon - 0.057 \cdot \log_{10}\left(\frac{k_s}{k_f}\right). \quad (4.21)$$

The dependency of k_{eff} in both models on the material properties and the packed bed void fraction is introduced in the CFD model through the compilation of specific code routines. These self-developed code modifications permit to include in the model temperature dependent material properties together with the inclusion of customized void fraction distributions depending on the particular modelled TES system.

4.2.3.3. Evaluation of the fluid-solid heat transfer coefficient (h_p)

When dealing with the non-local thermal equilibrium energy modelling strategy, the quantification of a finite heat transfer coefficient between the solid and fluid phases needs to be carried out. Many fluid-solid heat transfer correlations have been published under different operational parameters such as fluid Reynolds number values. Even if the comparative analysis of the particular heat transfer coefficient values obtained with different correlations can differ in a noticeable range, the assessment of their implementation has shown negligible differences [17-19] in the predicted thermal behaviour. From these expressions,

the ones of Peffer [20] and Wakao et al. [21] are selected in this work for low and high Re_p respectively. Taking this into account, the following expression is implemented when Re_p is lower than 15:

$$h_{fs} = \frac{k_f}{d_p} \cdot 1.26 \cdot \left[\frac{1-(1-\varepsilon)^{5/3}}{W}\right]^{1/3} \cdot \left(Re_p \cdot Pr\right)^{1/3}; \quad (4.22)$$

where W corresponds to:

$$W = 2 - 3 \cdot (1-\varepsilon)^{1/3} + 3 \cdot (1-\varepsilon)^{5/3} - 2 \cdot (1-\varepsilon)^2. \quad (4.23)$$

On the other hand, for Re_p higher than 15 the following expression is considered:

$$h_{fs} = \frac{k_f}{d_p} \cdot \left(2 + 1.1 \cdot {Re_p}^{0.6} \cdot Pr^{1/3}\right). \quad (4.24)$$

It has to be noted that eq. (4.22) is applicable when $Pe = Re_p \cdot Pr >> 1$, and eq. (4.24) to Re_p up to 8500. In all the modelled cases in this thesis, both dimensionless numbers are within the applicability range.

The inclusion of the dependency of h_{fs} with local fluid flow characteristics such as temperature, velocity or material properties, is carried out through the development of customized code routines, able to modify accordingly the overall developed CFD model.

4.2.3.4. Evaluation of the thermal losses

The evaluation of the thermal losses of the TES tank is another complex issue. The evaluation of all the contributions to the overall thermal losses include complicated calculations to quantify different mechanisms such as geometrical, solar radiation effects due to the open location of the TES unit, very sophisticated insulation strategies and others.

Even if this complicated evaluation could provide very accurate results, the insulation alternatives deployed in real systems are very advanced, which leads to a quasi-adiabatic TES tank insulation. As a consequence, in this work, a simplified TES insulation strategy is modelled, which allows a satisfactory energetic calculation with an easy model implementation. In this frame, in order to evaluate the thermal losses from the packed bed to the exterior, only the lateral wall is

considered. The particular insulation configuration considers three different regions, i) the packed bed, ii) the insulation layer and iii) the exterior, as depicted in Figure 4.3.

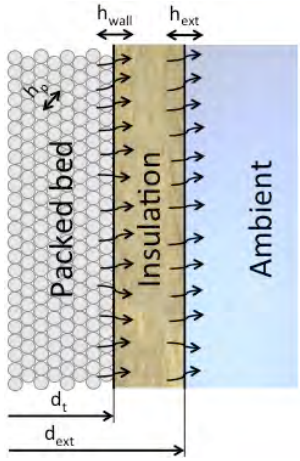

Figure 4.3. Schematic description of the thermal losses.

The evaluation of the thermal losses from the bed is determined considering the heat evacuated from the packed bed to the insulation, and the convective heat transfer established in the domain external boundary. The first one is quantified in this thesis work by means of the approximation of Beek [22]. In this frame, the corresponding heat transfer coefficient, h_w, is evaluated as a multiplication by a factor of 0.8 of the fluid-solid heat transfer coefficient (h_{fs}). Taking this into account, the following source term is added to the energy equation (eq. (4.9) and eq. (4.11)):

$$S_f^H = S^H = h_w \cdot A_t(T_f - T_w). \tag{4.25}$$

In the second region, insulation material, only conductive mechanisms are accounted for. Free convection between the external layer of insulation and the external atmosphere, assuming a free stream temperature of 20 °C, is fixed. The corresponding convective heat transfer coefficient (h_{ext}) is obtained from the expression:

$$h_{ext} = \frac{k_f}{d_t} \cdot \left[0.825 + \frac{0.387 \cdot {Ra_L}^{1/6}}{\left(1+\left(\frac{0.492}{Pr}\right)^{9/16}\right)^{8/27}} \right]^2; \tag{4.26}$$

which describes a free convection process in a vertical plate [23]. In this equation Ra_L corresponds to the tank Rayleigh number calculated as:

$$Ra_L = \frac{g \cdot \rho_f \cdot \omega \cdot (T_{ext} - T_{amb}) \cdot L^3}{\mu \cdot \alpha}; \quad (4.27)$$

where, g is the gravity constant and equal to 9.8 m·s^{-2}, ω and α are the air thermal expansion coefficient and thermal diffusivity respectively, and L is the tank length. It has to be noted that eq. (4.27) is also applicable for vertical cylindrical walls when the following condition is satisfied:

$$\frac{d_{ext}}{L} \geq \frac{35}{Gr_L^{0.25}}; \quad (4.28)$$

where Gr_L is the tank Grashof number, and can be calculated according to the following expression:

$$Gr_L = \frac{g \cdot {\rho_f}^2 \cdot \omega \cdot (T_{ext} - T_{amb}) \cdot L^3}{\mu^2}. \quad (4.29)$$

For the calculation of the overall thermal losses coefficient in this work, a stationary insulation temperature distribution is assumed. The obtained heat transfer coefficient shows a very good agreement with the ones calculated through different correlations [9], which guarantee the validity of this approach.

Overall, and considering a single insulation layer, the global heat transfer coefficient (h_{loss}) for evaluating the thermal losses from the packed bed to the exterior can be expressed as:

$$h_{loss} = \frac{1}{\frac{1}{h_w} + \frac{d_t}{2 \cdot k_{ins}} \cdot \ln\left(\frac{d_{ext}}{d_t}\right) + \frac{d_t}{d_{ext}} \cdot \frac{1}{h_{ext}}}. \quad (4.30)$$

4.3. Numerical methods

Once the governing and closing equations of the developed model are established, a successful solving strategy is needed in order to reach a satisfactory resolution. In these terms, the numerical scheme used to solve the complete set of differential equations is as important as the selection of the equations itself. In this section a complete overview of the numerical methods used in the performed calculations is given, including mathematical methods, domain discretization and calculation schemes.

In the definition of the computational domain, when possible, the axial symmetry of the cylindrical and conical geometries is exploited and, hence, a two-dimensional axisymmetric spatial discretization is considered. In all the performed calculations, the included domain is exclusively limited to the packed bed region and homogeneous fluid flow distribution is considered in the inlet of the tank.

Prior to the calculations, a mesh optimization analysis is performed to determine the best calculation economy together with a maximization of the accuracy. As a result of this assessment, the optimum spatial discretization is obtained for each modelled system.

In the description of the fluid flow regime, the Re_σ criterion is used [24]:

$$Re_\sigma = \frac{v_\infty \cdot \sigma^{0.5} \cdot \rho_f}{\mu}. \tag{4.31}$$

Following this criterion, the transition from laminar to turbulent regimen occurs when Re_σ shows a value above 100. Depending on the modelled conditions, laminar or turbulent regimen is applied.

The absence of local big pressure variation in the computational domain, together with the relatively low velocities of the fluid throughout the modelled packed beds, allows the consideration of the fluid flow as incompressible (Ma < 0.3).

$$Ma = \frac{v}{v_{sound}}. \tag{4.32}$$

The treatment of the pressure in the calculation is also of paramount importance since it is one of the governing parameters on the investigated TES systems. For this reason, the accuracy of the pressure calculation has to be guaranteed. With this objective, the numerical solution of the above-mentioned equations is accomplished using the "pressure based" solver implemented in the CFD model. In this approach, the pressure is derived from the continuity and the momentum equations so that, the velocity field, corrected by the pressure, satisfies the continuity. For the coupling of the pressure and velocity equations, the Pressure-Implicit with Splitting of Operators (PISO) algorithm is selected. This algorithm is a bit more expensive in computational effort but offers a better convergence.

The Green-Gauss node-based algorithm is used for the spatial discretization due to its higher accuracy in comparison to cell-based models. Even though, it requires higher computational resources. In addition, the PRESTO! algorithm is applied for the pressure spatial discretization and the momentum and energy equations are solved with the second order accurate numerical scheme (Second Order Upwind).

The calculation convergence criteria are strengthened in order to ensure the good quality of the calculation. Namely, for the continuity, radial and axial velocities residuals an accuracy of 10^{-5} is fixed while, in the case of the energy equation, the residual is set to 10^{-8}.

The time discretization criterion varies depending on the modelled system. Its selection is made in such a way the maximum number of iterations per time step is kept below 20 [25].

All calculations are performed with ANSYS Fluent 16.2 in a Linux based Workstation equipped with 32 cores Intel® Xeon™ and 64 Gb of DDR4 RAM

4.4. Data treatment

In addition to the velocity, temperature and pressure field results obtained directly by solving the CFD model equations reported in section 4.2, the energies, entropies and exergies associated to the storage tank operation are also evaluated.

It has to be noted that, for the charge and discharge operations of the TES system, the quantitative evaluation of the energy, entropy and exergy is exclusively limited to the thermal implications. In this line, the evaluation is restricted to the heat introduced or released to/from the TES during the charge/discharge operations. In this frame, all the output fluid obtained during the charge operation is useless, whereas the one obtained in the discharge is considered useful.

Quantitatively, the expressions used in this thesis work to evaluate energy, entropy and exergy are reported in the following.

4.4.1. First Law efficiency evaluation

In order to evaluate the performance of the TES unit in terms of the First Law of the Thermodynamics, only thermal energy is considered. In these terms, the

total enthalpies charged or discharged can be calculated by means of the following expressions:

$$\Delta H_c = \int_0^{t_c} \left(\dot{m}_c \cdot c_{p,f} \cdot \left(T_{1,c} - T_{amb} \right) \right) dt; \tag{4.33}$$

$$\Delta H_d = \int_0^{t_d} \left(\dot{m}_d \cdot c_{p,f} \cdot \left(T_{1,d} - T_{2,d} \right) \right) dt; \tag{4.34}$$

where, $T_{1,c}$ corresponds to the hot fluid temperature; $T_{1,d}$ to the temperature of the released fluid from the TES tank during the discharge stage, and $T_{2,d}$ to the inlet fluid temperature (bottom part) in the discharge stage. The integration limits t_c and t_d correspond to the charge and discharge times respectively. Finally, $\dot{m}$ is the heat transfer fluid mass flow rate.

It has to be mentioned that thermal losses through the lateral wall and due to thermocline (temperature stratification) region formation inside the solid medium are implicitly included in ΔH balances.

Therefore, the thermal efficiency of a complete cycle (charge + discharge) can be calculated from:

$$\eta_I = \frac{\Delta H_d}{\Delta H_c}. \tag{4.35}$$

4.4.2. Second Law efficiency evaluation

According to the Second Law of Thermodynamics, the fluid entropy in the charge and discharge operations is evaluated from the following equations:

$$\Delta S_c = \int_0^{t_c} \dot{m}_c \cdot \left(c_{p,f} \cdot \ln \frac{T_{1,c}}{T_{amb}} - R \cdot \ln \frac{p_{1,c}}{p_{2,c}} \right) dt; \tag{4.36}$$

$$\Delta S_d = \int_0^{t_d} \dot{m}_d \cdot \left(c_{p,f} \cdot \ln \frac{T_{1,d}}{T_{2,d}} - R \cdot \ln \frac{p_{1,d}}{p_{2,d}} \right) dt; \tag{4.37}$$

where, p_1 and p_2 correspond to the pressure in the upper and lower parts of the tank respectively, and R to de ideal gas constant.

4.4.3. Exergetic evaluation

In addition to the energetic and entropic evaluation, the analysis of the quality and usability of the stored heat needs to be addressed. In these terms, the exergy

involved in the charge and discharge processes (ΔB) has also been quantified in this work according to the following equation:

$$\Delta B = \Delta H - T_{amb} \cdot \Delta S. \tag{4.38}$$

Considering a complete charge and discharge cycle, the process exergy efficiency can be calculated from:

$$\eta_B = \frac{\Delta B_d}{\Delta B_c}. \tag{4.39}$$

4.4.4. Pumping energy

To evaluate the energy required for pumping the heat transfer fluid through the packed bed, the following expressions are used for the charge and discharge respectively:

$$H_{pump,c} = \int_0^{t_c} \frac{\dot{m}_c}{\rho_f} \cdot \Delta p \, dt; \tag{4.40}$$

$$H_{pump,d} = \int_0^{t_d} \frac{\dot{m}_d}{\rho_f} \cdot \Delta p \, dt. \tag{4.41}$$

In both equations, the Δp value corresponds to the pressure drop associated to the packed bed interstitial fluid flow obtained from eq. (4.5).

4.4.5. Thermal losses

From the thermal losses overall heat transfer coefficient (h_{loss}), calculated following eq. (4.30), the energy lost through the external wall of the storage tank is evaluated as:

$$H_{loss,c} = \int_0^{t_c} h_{loss,c} \cdot A_{ext} \cdot (T_f - T_{amb}) \, dt; \tag{4.42}$$

$$H_{loss,d} = \int_0^{t_d} h_{loss,d} \cdot A_{ext} \cdot (T_f - T_{amb}) \, dt. \tag{4.43}$$

4.5. Model validation

Different packed bed units have been reported in the literature showing the associated behaviour in a wide range of length scale, storage materials, operational parameters, etc. After an appropriate bibliographic search, the most representative

case studies have been selected in order to perform a literature-based experimental validation of the model described in section 4.2. The main goal of this validation is to guarantee the accuracy of the developed model, and as a consequence, ensure that the obtained results are fully extensible to real systems. Four works are used for the mentioned validation: two of them using air as heat transfer fluid, one operated with thermal oil and one with molten nitrate salt. In what follows, the obtained results are presented and the corresponding model accuracy and precision is carefully assessed.

4.5.1. Air as heat transfer fluid

For the validation of the model using air as heat transfer fluid two different systems are considered from ref. [4] and [26] respectively. The first one is an experiment carried out at the company *Airlight Energy* in Switzerland. The experimental facility consists in a 30 m^3 conical tank filled with local natural rocks using electrically heated air at 500 °C as heat transfer fluid [4] for the charging process. The second benchmark system is a smaller facility (0.078 m^3) constructed at *CSIR* (*Council for Scientific and Industrial Research*) in Pretoria [26]. In this case, a gas burner is used to heat air to 900 °C and a commercial ceramic material typically used in catalyst support applications, Denstone 2000, is applied as TES material.

4.5.1.1. Airlight Energy experiment

A schematic view of the setup used in ref. [4] is shown in Figure 4.4. In this figure it can be observed how the fluid flow is distributed in the upper part of the tank and collected through a metallic grid on its lower part. The tank is located underground and constructed in two types of concrete. Between the tank shell and ground a layer of insulating material is placed to minimize the thermal losses.

The reported experiment consists in a single 110 h charge operation starting from ambient temperature. During the experiment, the temperature is monitored at 5 positions distributed in the tank length and close to the external wall (Figure 4.4). The main operational parameters used in such experiment are collected in Table 4.2.

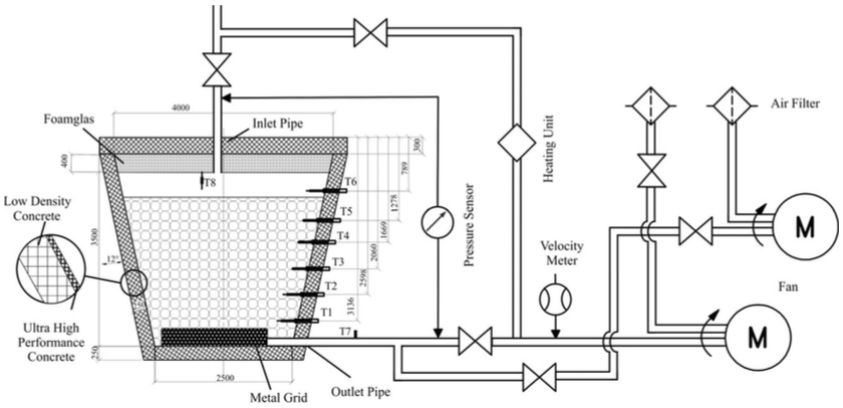

Figure 4.4. Scheme of the experimental setup used in ref. [4].

The comparison of the results obtained in the performed experiment (dots) and the model-calculated data (continuous lines) are shown in Figure 4.5. In this plot the temperature time evolution in the five measurement positions (T1 to T5 from bottom to top) is presented.

Table 4.2. Operational parameters of the experiments in ref. [4].

Storage capacity (MWh_{th})	6.5
Average tank void fraction (-)	0.342
Average spherical particle diameter (cm)	2.5
Heat transfer fluid temperature (°C)	500
Average heat transfer fluid mass flow rate ($kg \cdot s^{-1}$)	0.06
Charging time (h)	110

A good agreement is observed between the experimental and model-calculated temperature data in Figure 4.5. For the four upper thermocouples (T2 to T5), the model predicts slightly lower temperatures than the real ones, showing a similar trend during the complete system heating process. The deviation observed in the case of the T1 temperature measurement is related to the particular experimental conditions of the reported facility. In this terms, interferences caused by the proximity of this thermocouple to the lower tank fluid collector lead to a noticeable temperature difference when compared with the model obtained one. However, this phenomenon is strictly an experimental basis, which does not affect to the accuracy of the developed model, since the particular experimental details associated to this collector are not considered on the modelled domain.

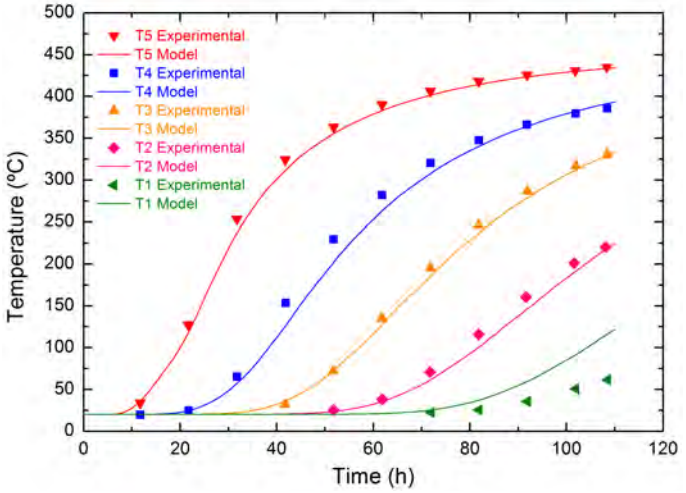

Figure 4.5. Model validation with the experiments from ref. [4].

In order to perform a numerical assessment of the fitting between the experimental and modelled temperatures, the root mean square deviation (RMSD) together with the mean absolute error (MAE) are presented in Table 4.3. It has to be noted that for the upper thermocouples, the absolute error is kept between 3-6% and the standard deviation does not exceed 15 °C. As expected from the mentioned experimental based difference, these errors are higher for the lowest measurement point (T1).

Table 4.3. RMSD and MAE between the experimental and modelled temperatures.

Position	RMSD (°C)	MAE (%)
T1	22.1	26.8
T2	8.0	5.1
T3	5.5	2.8
T4	14.1	5.5
T5	8.2	3.0

4.5.1.2. CSIR experiment

With the motivation of providing a full validation of the developed model in different tank sizes, in this section a laboratory scale TES unit is used as benchmark, in contrast with the previous pilot scale experiment. A schematic view of the selected *CSIR* facility is shown in Figure 4.6.

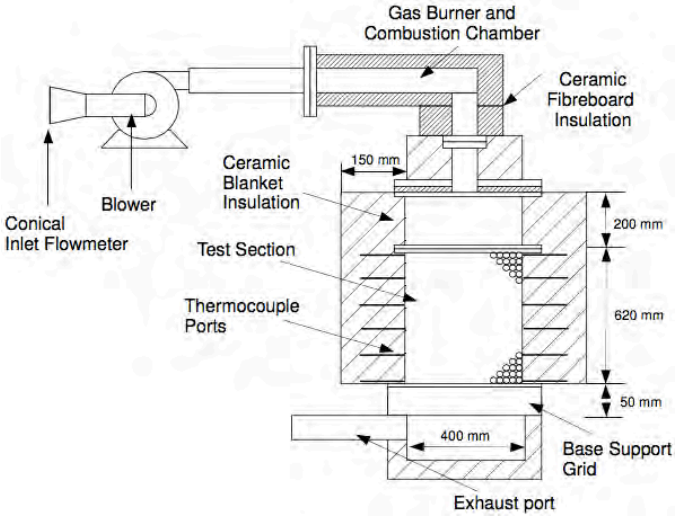

Figure 4.6. Scheme of the experimental setup at CSIR [26].

The reported experiment in ref. [26] consists in a pre-charge of the system starting from room temperature up to 350 °C. Then, a complete charge to 900 °C is performed, followed by a discharge operation introducing air at 350 °C. For the validation of the model carried out, as an example, the charge period from 350 °C to 900 °C is considered. The main operational parameters of the unit for the mentioned experiment are collected in Table 4.4.

Table 4.4. Operational parameters of the experiments in ref. [26].

Packed bed volume (m^3)	0.078
Packed bed void fraction (-)	0.39
Average spherical particle diameter (cm)	1.9
Heat transfer fluid temperature (°C)	900
Average heat transfer fluid mass flow rate ($kg \cdot s^{-1}$)	0.023
Charging time (h)	1.5

The comparison between the experimental data from [26] (dots) and the results obtained from the model (continuous lines) is presented in Figure 4.7. In this figure, the temperature in the tank axial direction is presented each 15 min.

As it can be observed, at the beginning of the experiment (0.25 h) the temperature prediction in the thermocline region shows slightly lower temperature values compared with the experimental ones. However, after half an

hour of experiment the model predicts very accurate temperatures. This trend is kept until 1.25 hours when the model shows slightly higher temperatures. On the other hand, attending to the thermocouple in the lowest part of the tank (x =1) a temperature over-prediction is obtained likely associated to higher thermal losses in this region of the experimental setup than the ones considered in the model. Nevertheless, attending to the errors between the measured and modelled temperatures, included in Table 4.5, it can be observed that the MAE is kept below 3% during the complete experiment, which implies a very good accuracy of the calculation results.

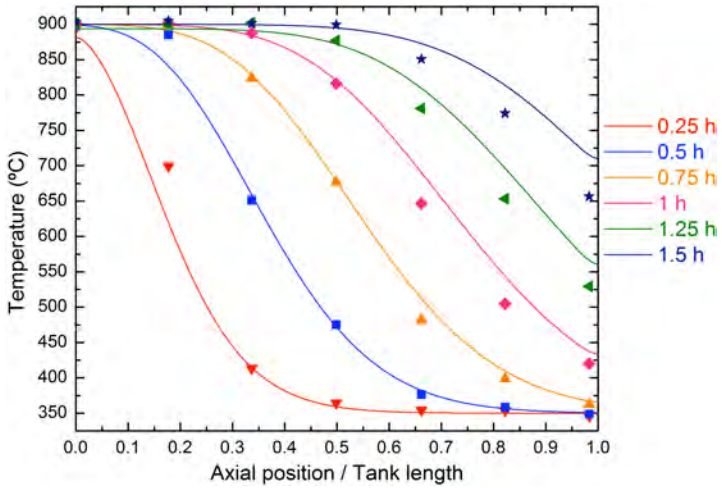

Figure 4.7. Model validation with the experiments from ref. [26].

Table 4.5. RMSD and MAE between the experimental and modelled temperatures.

Time (h)	RMSD (°C)	MAE (%)
0.25	30.5	2.8
0.5	16.7	1.4
0.75	12.4	1.7
1	22.3	2.8
1.25	24.4	2.9
1.5	27.5	2.4

The obtained results with the detailed air operated packed bed TES systems show the accuracy of the theoretical model at different length scales and temperatures.

4.5.2. Thermal oil as heat transfer fluid

Once the model is validated using air as heat transfer fluid, in this section, the experimental validation operating with a liquid fluid (thermal oil) is presented. In this regard, the experiment carried out at *PROMES-CNRS* laboratory in France and reported in ref. [27] is considered as benchmark. The experimental setup (Figure 4.8) consists in a 1.8 meters length tank filled with quartzite rock operated with *Rapeseed oil* as heat transfer fluid.

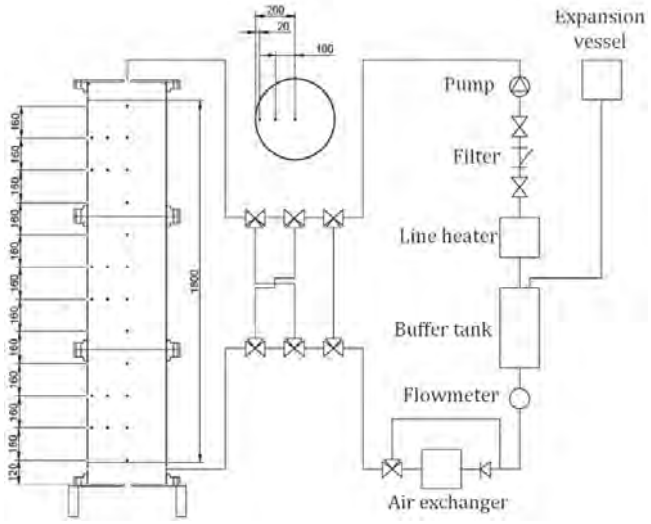

Figure 4.8. Scheme of the experimental setup at PROMES-CNRS [27].

The published experiment consists in a discharge process of three hours performed after a complete charge of the packed bed up to 210 °C. The particular parameters of the mentioned experiment and TES facility are collected in Table 4.6.

Table 4.6. Operational parameters of the experiments in ref. [27].

Storage capacity (kWh_{th})	8.3
Average spherical particle diameter (cm)	4
Packed bed void fraction (-)	0.22
Heat transfer fluid temperature (°C)	160
Average heat transfer fluid mass flow rate ($kg \cdot s^{-1}$)	0.0191
Discharging time (h)	3.5

In order to demonstrate the accuracy of the model in reproducing the obtained experimental temperature profiles from ref. [27], the temperature in the axial direction of the tank is represented at eight different times in Figure 4.9. The continuous lines correspond to the model obtained profiles while dots reproduce the experimental measured values.

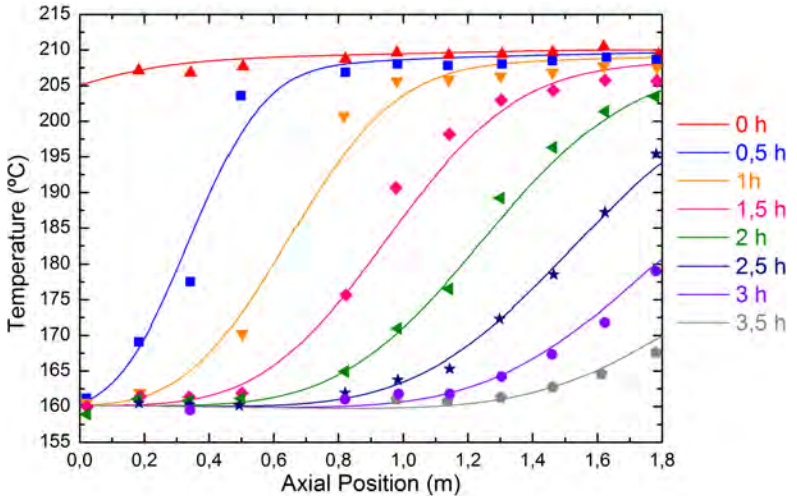

Figure 4.9. Model validation with the experiments from ref. [27].

As it can be observed in Figure 4.9, the matching between the experimental and calculated temperatures is very good. Small differences around 5 °C are found in the temperature profiles after 0.5 and 1 hour charge in the thermocline region. In order to numerically evaluate the accuracy of the model, in Table 4.7 the RMSD and MAE between the experimental and modelled temperatures for each time are summarized. In all cases, the MAE is kept below 1% and RMSD below 3 °C.

Table 4.7. RMSD and MAE between the experimental and modelled temperatures.

Time (h)	RMSD (°C)	MAE (%)
0.5	2.6	0.9
1	2.2	0.9
1.5	2.3	0.9
2	1.4	0.6
2.5	0.9	0.4
3	0.9	0.4
3.5	0.1	0.3

These results permit to extend the suitability of the developed model not only to gaseous fluids but also to liquid fluids. The obtained results demonstrate the reliability of the calculation of packed bed TES systems thermal behaviour when using oil as heat transfer fluid.

4.5.3. Molten nitrate salt as heat transfer fluid

Finally, in order to analyse the validity of the developed code in modelling a packed bed operated with molten salt as heat transfer fluid, the experimental results published in ref. [28] are considered. The experimental setup (Figure 4.10) consists in a tank constructed by *Sandia National Laboratory*, which operates with a mixture of sodium and potassium nitrates (1:1) as heat carrier and is partially filled with a mixture of quartzite rock and silica sand. Many authors have used these results, depicted in Figure 4.11, to assess the accuracy of different developed packed bed thermo-fluidic models [17,27,29-31].

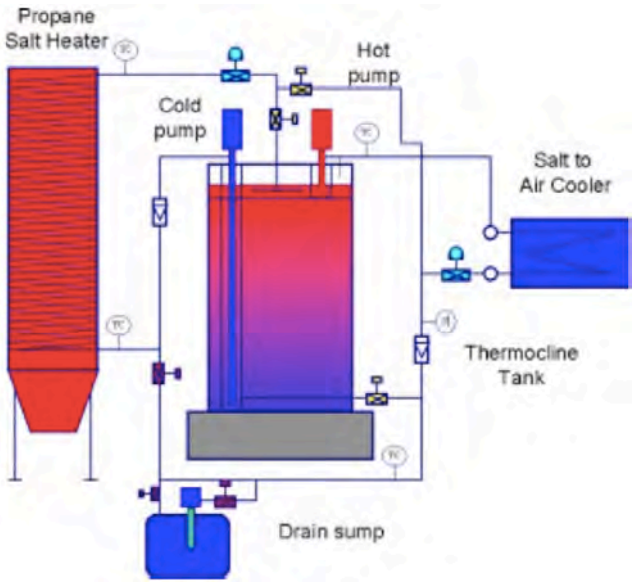

Figure 4.10. Scheme of the experimental setup used in ref. [28].

Starting from a partially charged TES unit, the results reported in ref. [28] correspond to the discharge run performed in the storage unit shown in Figure 4.10. The temperature profile inside the tank at the beginning of discharge is depicted in Figure 4.11 (t = 0h). The main operational parameters of the published experiment are collected in Table 4.8.

Table 4.8. Operational parameters of the experiments in ref. [28].

Storage capacity (MWh_{th})	2.44
Tank length (m)	6.1
Tank diameter (m)	3.0
Average tank void fraction (-)	0.22
Average spherical particle diameter (cm)	1
Heat transfer fluid temperature (°C)	289
Average heat transfer fluid mass flow rate ($kg \cdot s^{-1}$)	5.46
Discharging time (h)	2

The time evolution of the axial temperature profiles inside the storage tank is shown Figure 4.11. Dots represent the experimentally measured temperature at different axial positions of the storage tank at four different discharging times. The continuous lines represent the numerically calculated temperature values obtained from the developed model for the same tank positions at the same discharging times.

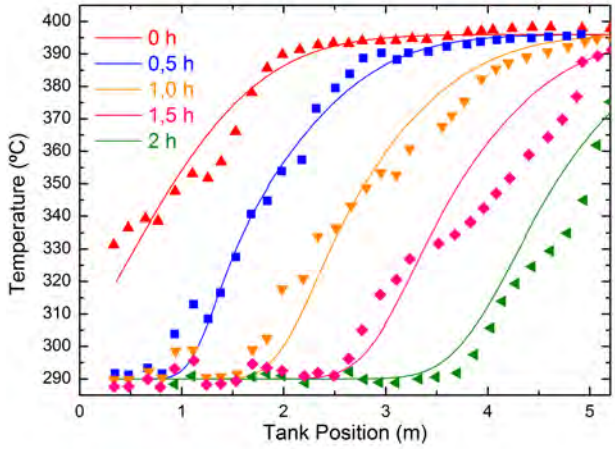

Figure 4.11. Model validation with the experiments from ref. [28].

The experimental reported results, depicted in Figure 4.11, show a noticeable dispersion, which leads to a more difficult assessment of the calculated results. However, the numerical results describe correctly the average temperature profiles with a maximum local temperature deviation of around 20 °C. In average for each compared time, the assessment leads to an experimental-numerical error within 4-10 °C, which represents around 0-2% of mean absolute error (Table 4.9).

Table 4.9. RMSD and MAE between the experimental and modelled temperatures.

Time (h)	RMSD (°C)	MAE (%)
0.5	4.5	0.8
1	6.7	1.5
1.5	9.4	2.0
2	8.2	1.8

The obtained results also permit to rely on the theoretical model developed in this thesis for the modelling of packed bed TES systems running with molten salts as heat transfer fluid.

4.6. Conclusions

In this chapter a complete computational fluid dynamics model has been presented. This theoretical model includes all the governing energy and fluid flow mechanisms that occur in packed bed TES systems. In particular, the porous continuous medium formulation is selected for describing the fluid flow in the packed bed. Even if complex phenomena are involved on the description of the thermo-fluidic system behaviour, the developed model includes all the main heat transport mechanisms such as conduction, convection, radiation, dispersion, and boundary layer behaviour, among others. In the developed model, the mentioned sophisticated heat transport phenomena are included through the semi-empirical calculation of an effective solid and fluid thermal conductivity value. Together with the main governing differential conservation equations, a complete set of closing equations is also determined, leading to the successful resolution of the complete problem. It has to be noted that the model detailed in this chapter represents a successful and innovative modelling strategy since it permits an accurate treatment of radiative transport mechanisms together with the possibility of modelling variable packing void fraction values. In addition, the formulation associated to the pressure treatment in the overall calculation results of particular interest. This modelling strategy opens new possibilities on the description of high temperature and high pressure packed bed systems with different approximation degrees, according to the unified or separate treatment of the energy equation in the fluid and solid phases.

Furthermore, the numerical solution strategy selected for the above-mentioned equation is also explained in detail. Particular care is paid to the spatial discretization strategy, guaranteeing a satisfactory compromise between the meshing and the calculation accuracy and economy.

Finally, four experiments reported in the literature are used as benchmark for the validation of the developed model. The obtained results show an accurate agreement of the proposed modelling strategy to simulate the real performance of packed bed TES systems operating at different temperature ranges, filler materials, heat transfer fluids and tank length scales. The performed validation allows performing precise calculations to determine a general optimization process of packed bed storage units as a function of a wide variety of design parameters as it is shown in further chapters of this thesis.

4.7. References

[1] S. Ergun, "Fluid flow through packed bed columns," *Chemical Engineering Progress*, vol. 48, pp. 89-94, 1952.

[2] C.F. Gauss, "Discussion of L.A. Seeber's book: Studies on the characteristics of positive ternary quadratic forms etc," 1981.

[3] A. Meier, C. Winkler, and D. Wuillemin, "Experiment for modeling high temperature rock bed storage," *Solar Energy materials*, vol. 24, pp. 255-264, 1991.

[4] G. Zanganeh, A. Pedretti, S. Zavattoni, M. Barbato, and A. Steinfeld, "Packed-bed thermal storage for concentrated solar power - Pilot-scale demonstration and industrial-scale design," *Solar Energy*, vol. 86, pp. 3084-3098, 2012.

[5] Y. Cohen and A.B. Metzner, "Wall effects in laminar flow of fluids through packed beds," *AiChe Journal*, vol. 27, pp. 705-715, 1981.

[6] M.L. Hunt and C.L. Tien, "Non-Darcian convection in cylindrical packed beds," *Journal of heat transfer*, vol. 110, pp. 378-384, 1988.

[7] K. Vafai, "Convective flow and heat transfer in variable-porosity media," *Journal of Fluid Mechanics*, vol. 147, pp. 233-259, 1984.

[8] D. Vortmeyer and J. Schuster, "Evaluation of steady flow profiles in rectangular and circular packed beds by a variational method," *Chemical Engineering Science*, vol. 38, pp. 1691-1699, 1983.

[9] K.A.R. Ismail and R. Stugrinsky Jr., "A parametric study on possible fixed bed models for pcm and sensible heat storage," *Applied Thermal Engineering*, vol. 19, pp. 757-788, 1999.

[10] M. Kaviani, *Principles of heat transfer in porous media*.: Springer US, 1991.

[11] R.G. Carbonell and S. Whitaker, *Fundamentals of transport phenomena in porous media*.: Springer Netherlands, 1984.

[12] D. Vortmeyer and R.J. Schaefer, "Equivalence of one- and two-phase models for heat transfer processes in packed beds: one dimensional theory," *Chemical Engineering Science*, vol. 29, pp. 486-491, 1974.

[13] S. Yagi and D. Kunii, "Studies on effective thermal conductivities in packed beds," *AIChE Journal*, vol. 3 (3), pp. 373-381, 1957.

[14] N. Wakao and S. Kaguei, *Heat and mass transfer in packed beds*.: Gordon and breach science publishers, 1982.

[15] D. Kunii and J.M. Smith, "Heat transfer characteristics of porous rocks," *AIChE Journal*, vol. 6 (1), pp. 71-78, 1960.

[16] R. Krupiczka, "Analysis of thermal conductivity in granular materials," *International Chemical Engineering*, vol. 7, p. 122, 1967.

[17] C. Xu, Z. Wang, Y. He, X. Li, and F. Bai, "Sensitivity analysis of the numerical study on the thermal performance of a packed-bed molten salt thermocline thermal storage system," *Applied Energy*, vol. 92, pp. 65-75, 2012.

[18] B. Alazmi and K. Vafai, "Analysis of variants within the porous media transport models," *Journal of Heat Transfer*, vol. 122, pp. 303-326, 2000.

[19] A.R. Balakrishnan and D.C.T. Pei, "Heat transfer in gas-solid packed bed systems. 1. A critical review," *Industrial & Engineering Chemistry Process Design and Development*, vol. 18, pp. 30-40, 1979.

[20] R. Pfeffer, "Heat and mass transport in multiparticle systems," *Industrial & Engineering Chemistry Fundamentals*, vol. 3 (4), pp. 380-383, 1964.

[21] N. Wakao, S. Kaguei, and R. Funazkri, "Effect of fluid dispersion coefficients on particle-to-fluid heat transfer coefficients in packed beds," *Chemical Engineering Science*, vol. 34, pp. 325-336, 1979.

[22] J. Beek, "Design of packed catalytic reactors," *Advances in Chemical Engineering*, vol. 3, pp. 203-271, 1962.

[23] T.L. Bergman, A.S. Lavine, F.P. Incropera, and D.P. DeWitt, *Fundamentals of heat and mass transfer*.: John Wiley & Sons, 1999.

[24] D.A. Nield and A. Bejan, *Convection in porous media*.: Springer-Verlag New York, 2013.

[25] ANSYS, Inc, *ANSYS Fluent User's Guide*, 162nd ed., 2015.

[26] P. Klein, T.H. Roos, and T.J. Sheer, "Experimental investigation into a packed bed thermal storage solution for solar gas turbine systems," *Energy Procedia*, vol. 49, pp. 840-849, 2014.

[27] J.-F. Hoffmann, T. Fasquelle, V. Goetz, and X. Py, "A thermocline thermal energy storage system with filler materials for concentrated solar power plants: Experimental data and numerical model sensitivity to different experimental tank scales," *Applied Thermal Engineering*, vol. 100, pp. 753-761, 2016.

[28] J.E. Pacheco, S.K. Showalter, and W.J. Kolb, "Development of a molten-salt thermocline thermal storage system for parabolic trough plants," *Journal of Solar Energy Engineering*, vol. 124, pp. 152-159, 2002.

[29] A.M. Bonanos and E.V. Votyakov, "Sensitivity analysis for thermocline thermal storage tank design," *Renewable Energy*, vol. 99, pp. 764-771, 2016.

[30] J.T. van Lew, P. Li, C.L. Chan, W. Karaki, and J. Stephens, "Analysis of heat storage and delivery of a thermocline tank having solid filler material," *Journal of Solar Energy Engineering*, vol. 133, p. 021003, 2011.

[31] Z. Yang and S.V. Garimella, "Thermal analysis of solar thermal energy storage in a molten-salt thermocline," *Solar Energy*, vol. 84, pp. 974–985, 2010.

Chapter 5:

Conceptual design and parametric analysis

5 Conceptual design and parametric analysis

In the previous chapter, a complete theoretical physical model for describing the thermo-fluid performance of a packed bed thermal energy storage system was presented and validated. In this chapter, this model is extensively implemented in order to obtain a detailed optimization guideline of the main design and operational parameters governing the thermal performance of packed bed TES systems. In this regard, the impact of the geometry, heat transfer fluid flow rate, or solid particle diameter, among other design parameters on the thermal performance of the storage unit is discussed. In addition, different operational and thermal management strategies of the TES system are also investigated in order to demonstrate the flexibility and suitability of the packed bed storage concept to different exploitation environments. Of particular importance is the thermal stability analysis, presented in this chapter. Overall, the real implementation under industrial environments of this storage technology requires a deep understanding of the long term charge/discharge cycling behaviour of the packed bed TES, carefully addressed in this work.

5.1. System description and management

In order to establish a common reference framework, which allows the comparison and the outcome of fair conclusions about the design optimization guideline, in this chapter, a benchmark case study is pre-selected. Using this reference system, different parametric and optimization analyses are performed by means of the implementation of the developed physical model. The design parameters selected for the benchmark TES system are collected in Table 5.1.

Even if these design parameters of the reference TES system can be arbitrarily fixed, the mentioned benchmark parametric selection is made according to generic criteria following the maximization of the utility of the obtained results. With this goal, the volume of the reference TES unit is fixed to 3 m^3, corresponding to a pilot/demonstration scale. This tank size allows a good compromise between computational cost and representativeness of the obtained results. The operational temperature range for the modelled TES units is selected between 20 and 700 °C. This selection covers two possible applications, usually targeted by TES systems: heat recovery in industrial processes and concentrated solar power plants.

Table 5.1. Fixed TES tank parameters.

Parameter	Value
Tank volume (m^3)	3
Storage material	*EAF Slag 1*
Heat transfer fluid	Air
Hot fluid temperature (°C)	700
Cold fluid temperature (°C)	20
Storage pressure (bar)	1
Insulation material	*Mullite fibre*
Insulation thickness (m)	0.25

Considering the selected temperature range and the demonstrated stability, thermal behaviour and chemical compatibility (see chapters 2 and 3), *EAF Slag 1* and air are proposed as heat storage material and heat transfer fluid respectively.

The selected material combination and TES design parameters, in terms of volume and temperature range, lead to a maximum storage capacity of around 1 MWh_{th} considering the total storage material deployment in the 20-700 °C temperature range.

Taking into account that the physical model developed in this work allows the description of the thermal losses from the storage domain, a realistic insulation strategy is proposed for the reference TES system. In particular, a 25 cm layer of *Mullite fibre* is considered as insulation material, according to its appropriate properties at high temperature (see Annex 1 for its properties).

5.2. Analysis of different operational strategies

Following the optimization of the TES system performance, several aspects need to be addressed. In this line, the detailed customization of the heat management strategy to an optimum exploitation frame, addressed in this section, is found to be as important as the optimization of the TES system design parameters, discussed in the following sections.

In order to obtain a full exploitation of the proposed packed bed system, a detailed analysis of the different operation and management strategies must be

assessed. This strategy typically depends on the application of the TES, as a function of its installation, coupling to the particular thermal process and diverse implementation criteria. In general, the deployment of the packed bed TES system is limited by the heat source (solar concentrators, industrial process, etc.) and/or the final application of the heat (power production, plant component pre-heating, etc.). Regarding the heat source, two main scenarios can be distinguished:

1. Fixed heat source operation time: this deployment mode is applicable when the availability of the heat source is time-limited, and, eventually, it is not enough to reach a complete charge of the TES. Under these conditions, the system is only partially charged in a fixed time period. An example of this scenario is the CSP plants where the heat source depends on the solar irradiation hours.
2. Unlimited heat source: the TES implementation associated to this strategy is suitable when a continuous primary thermal energy supply, without any time limitation, is available. As an example, a continuous industrial thermally driven process involving the release of heat is an example of this operation mode.

Attending to the final application of the stored heat, different constrains can be found, being the following the most representatives ones:

1. Temperature level of the discharged fluid: when the temperature boundaries derived from a particular TES application environment are a limiting factor in the storage management, a temperature criterion has to be considered for the fluid discharged from the storage. In these terms, the system is assumed discharged when a pre-selected temperature criterion is reached in the output fluid from the storage according to the heat demanding application coupled to the TES. This operation mode is usual when the final application of the heat is power production by means of a turbine. It has to be noted that the more flexibility on the allowed output fluid temperature variation, the more storage capacity will be obtained since larger amount of fluid will be useful. In an extreme implementation case, a complete TES discharge could be also considered if no temperature limitations are introduced from the heat demanding application. Potential

examples of this deployment mode are the heating of particular industrial plant components or the pre-heating of different raw material feedstock.

2. Thermal reproducibility of the TES: Usually, most of the heat demanding applications such as turbine operations, thermodynamic cycles or heating/cooling processes, require a reproducible primary heat input. In this frame, an invariant thermal cycling behaviour of the TES is an important added value in order to fully determine the nature and performance of the associated thermal process. However, the thermal operation and heat management of different TES alternatives not always show a reproducible behaviour when a subsequent charge/discharge cycles are performed. In these terms, the analysis of the stability of the heat supply from any storage solution becomes of great importance.

Considering all the aforementioned TES implementation scenarios, in this thesis three different packed bed deployment modes are proposed as a function of the particular operation conditions. These conceptual deployment modes are idealized exploitation scenarios that allow a detailed analysis of the implications derived from each one. Of course, usually, under real operation conditions, a mixed thermal management based on the proposed conceptual modes will be found. The three studied modes are:

1. Complete TES charge and discharge: unlimited heat source is assumed in the charge of the system. The charge process is considered finished once the complete TES material reaches the hot fluid temperature. On the other hand, no boundaries are assumed in the temperature level of the discharged fluid. Hence, in this process, the TES material changes its temperature from the hot to the cold fluid one.

2. Fixed charge and discharge times: both, charge and discharge operations occur in a limited time, without reaching a complete TES material heating/cooling up to the hot/cold fluid temperature in the charge/discharge process respectively. Consequently, the heat management under this deployment conditions needs to deal with the implications derived from the presence of a temperature stratification (thermocline) in the initial charged and discharged TES states after the first thermal cycle.

3. Fixed temperature tolerance in the charge and discharge: a maximum output fluid temperature variation is fixed during the charge and discharge operations. Once the established temperature threshold is reached in the fluid output, the charge/discharge operation is considered finished.

In order to study the thermal performance of the TES unit under the mentioned operational conditions, the reference case defined in Table 5.1 is selected. In addition to the aforementioned tank parameters, some others are fixed for the calculations performed in this section. Among them, the particle diameter, air mass flow rate and, the tank geometry and aspect ratio are fixed to the values reported in Table 5.2.

Table 5.2. TES tank parameters used for the different operational strategies analyses.

Parameter	Value
Particle diameter (cm)	1
Mass flow rate ($kg \cdot m^{-3}$)	0.3
Tank geometry	Cylindrical
Tank aspect ratio (L/d_t)	2

5.2.1. Complete charge and discharge operation

In this section the analysis of the thermal performance of a TES unit when operated in a complete charge/discharge mode is addressed. In order to carry out such analysis, the output fluid temperatures obtained in the storage tank outlet during the charge and discharge operations are presented in Figure 5.1. Attending to the curve obtained in the charge, it is observed that during the first 3 hours, the introduced heat is effectively transferred to the solid storage material, since the fluid temperature does not exceed the cold fluid one (20 °C). However, a continuous output fluid temperature raise is observed for the following 3 hours of charge operation up to values close to the hot fluid temperature (700 °C). From this time, as the overall temperature of the solid storage material is near to the maximum system temperature a poor thermal transport governs the storage system, leading to negligible energy storage. Even if an approximated calculation frame could consider the TES unit charged after the mentioned 6.5 hours, a more precise calculation also needs to consider the slight asymptotic output

temperature trend between 6.5 and 8 charging hours. After this time, the TES system is considered completely charged.

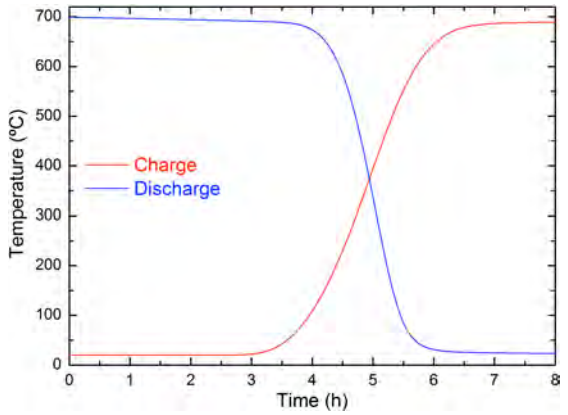

Figure 5.1. Output air temperature during the charge and discharge operations.

In the discharge operation, slight differences are found if compared to the charge one. The most relevant one is the extension of the constant output fluid temperature at 700 °C in the first 3.75 hours. The different time extension compared with the charge process is associated to a double phenomenology. First, the considered thermal insulation is initialized at the cold system temperature (20 °C) in the first charge operation. Consequently, this operation is affected by larger thermal losses due the heating of the insulation material. However, in the subsequent thermal cycling, the insulation provides a more efficient control of the thermal losses. Second, the large operation temperature range implies a noticeable change on the thermal properties of the involved materials (introduced in the model as indicated in Annex 1), which directly affects to the energetic balance of the system.

After these 3.75 hours of constant temperature, the thermocline is extracted from the TES between the 3.75 and 5.5 discharge hours. From this time to the eighth discharge hour, the output fluid temperature asymptotically reaches the cold fluid one with a minimum thermal variation.

Aiming at understanding the thermocline region formation inside the tank during the charge and discharge operations, the hourly temperature profile in the central axis of the TES is presented in Figure 5.2. In these plots, the extremes 0 and 1 x-coordinates correspond to the upper and lower parts of the tank respectively.

The analysis of the axial temperature profiles during the charge (Figure 5.2a) shows that the thermocline region is kept inside the tank around three hours. It is also seen that the temperature slope in the temperature stratification region continuously decreases during the complete process. This is caused due to the heat transport mechanisms between the hot and cold fluid zones governing the spreading/formation of the thermocline region.

It has to be noted that, between the sixth and seventh hour, the temperature of the packed bed only increases around 50 °C in a 10% of the tank, what indicates a large waste of energy, due to the inefficient heating of the system, already close to the hot fluid temperature, as explained above. This phenomenon is reinforced in the case of the last modelled hour, when almost no variation in the packed bed temperature is obtained.

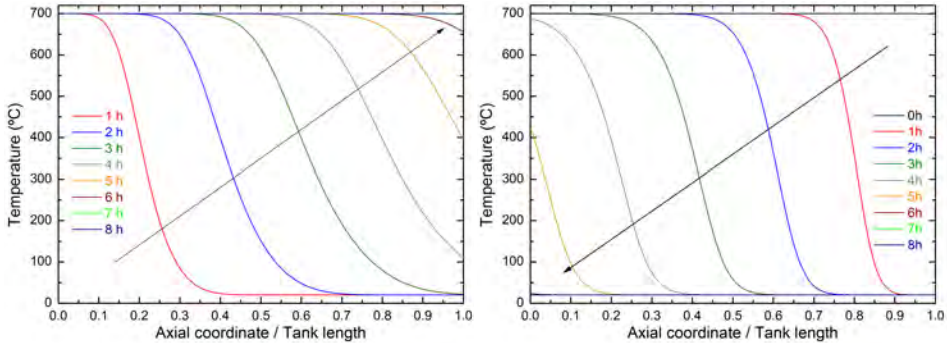

(a) (b)

Figure 5.2. Hourly axial temperature profiles in the centre of the tank. a) charge and b) discharge operations.

According to the axial temperature profiles obtained for the discharge operation (Figure 5.2b), it is observed that the slope of the thermocline region is more pronounced than in the case of the charge curves. This behaviour, as explained above, is associated to the non-symmetric charge/discharge performance due to the thermal losses and the variable material properties. On the other hand, as observed in Figure 5.1, there is no extraction of the thermocline region during the first four hours. This removal is performed between the forth and sixth hour. From this point, no more energy is available inside the TES unit.

In order to analyse these results in terms of energy and cycle efficiency, the hourly-involved stored/released energies are presented in Figure 5.3a, and the

associated efficiencies in Figure 5.3b. In the former, the red line corresponds to the energy introduced in the system each hour (henceforth "charged"); the green one to the energy transferred during the charge operation to the TES material, i.e. stored energy, and the blue one to the energy released during the discharge stage. Focusing on the energy stored during the charge operation, an important decrease on this value is observed after four hours, associated to the energy disposed (not stored) from the TES unit. Referring to the discharged energy curve, a similar behaviour is obtained. In this case, most of the stored energy is released during the first four discharge hours.

Overall, attending to the total energy introduced in the charge operation and the one released in the discharge run, an overall cycle efficiency (eq. (4.35)) of 59.5% is obtained. This value is noticeably affected by the energy disposed during the charge stage. On the other hand, looking at the exploitation of the TES material (total discharged energy divided by the maximum storage capacity of the system) a 98.8% is obtained.

Even if this operational strategy maximizes the use of the storage material, the obtained cyclic efficiency is quite low. This last constrain may make the complete charge/discharge mode not attractive or useful for real applications. It has to be mentioned that this charging strategy results in a very inefficient procedure, since a large amount of heat is lost. As a consequence, in the absence of an eventual application for this non-captured energy, the overall TES cycle efficiency is noticeably decreased. This is identified as one of the main drawbacks of this operation strategy.

In order to evaluate the separate charge and discharge performances, in Figure 5.3b two additional efficiency criteria are presented. In particular for the charge operation, depicted in the red line, the ratio between the stored energy (green line in Figure 5.3a) and the charged energy (red line in Figure 5.3a) is defined. The results show that this parameter maintains a high efficiency value above 90% for the first four charge hours, whereas after this time suffers a drastic decrease. On the other hand, for the discharge operation, depicted in the blue line, the ratio between the hourly-discharged energy (blue line in Figure 5.3a), and the total energy discharged from the system in the 8 hours operation is defined. From these

results, an 80% of the total discharged energy is released during the first four hours. Meanwhile, for the extraction of the remaining 20% another four hours are necessary.

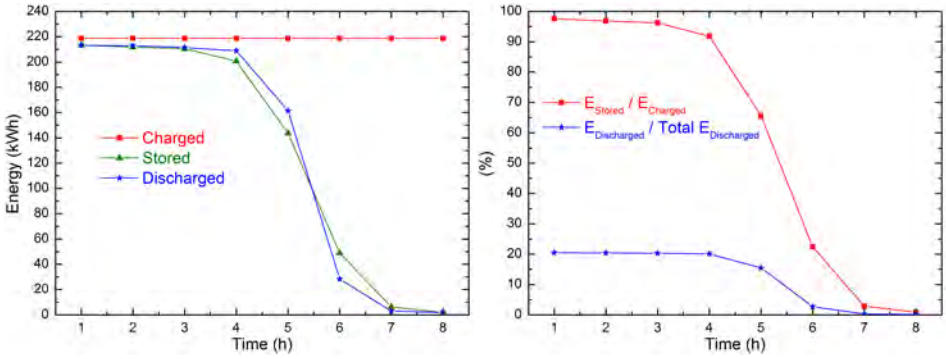

(a) (b)

Figure 5.3. a) Involve energies and, b) efficiencies, at each hour of the charge and discharge operations.

5.2.2. Fixed time operation

Taking into account the low efficiency attained due to the large energy disposal in the complete charge operation described above, in this section, the operation of the same unit is analysed considering a pre-determined fixed time for the charge and discharge runs. In order to show the impact of this operation mode in contrast to the complete charge/discharge methodology, in this case, the operation time is selected to attain a partial charge/discharge state of the TES.

With the objective of maintaining the representativeness of the calculated results, the same TES unit parameters described in Table 5.2 are considered, fixing additionally an arbitrary charge/discharge time of 4 hours. The partial charge/discharge of the packed bed TES unit presents strong differences when compared with the complete charge/discharge operation. The most representative one is the effect of the thermocline evolution in consecutive charge/discharge cycles. The thermal transport mechanisms, responsible for the thermocline formation, became in this operational mode as a capital governing phenomenon, since they lead to a continuous widening of the thermocline. The null or eventually partial extraction of this thermal gradient region from the tank during its cyclic operation leads to different initial conditions for consecutive charge or discharge

processes. Consequently, a non-reproducible transient behaviour can be expected. For this reason, in order to analyse the thermal evolution of the thermocline, the transient behaviour of the TES and the overall system performance up to ten consecutive charge/discharge cycles are modelled in this section.

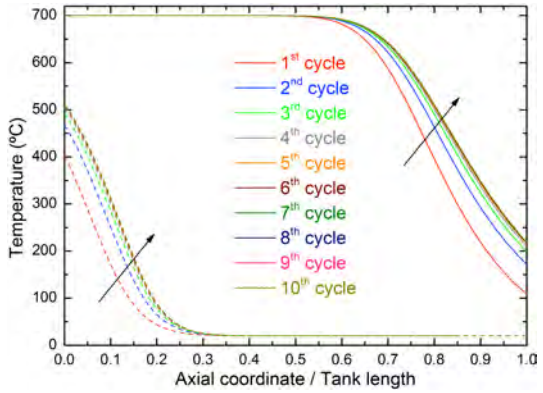

Figure 5.4. Axial temperature distribution in the packed bed after 4 hours of charge (upper continuous lines)/discharge (lower dashed lines) cyclic operation.

The results of the performed continuous cycling calculations under the mentioned partial charge/discharge conditions are shown in Figure 5.4. In this plot the temperature in the central axial coordinate of the tank, once the charge (upper curves) and the discharge (lower curves) processes are finished, is presented. The calculations show a monotonously increasing energy not extracted from the packed bed TES unit with the continuous cycling in the discharge operation. After 5-6 cycles, the obtained temperature distribution in the TES becomes reproducible, which implies a similar energetic and thermal performance. A direct consequence is that, after a certain number of cycles, the system attains a stationary behaviour with reproducible thermal performance. This stationary condition of the packed bed is satisfied once the partial extraction of the thermocline region in a thermal cycle equals the thermocline spreading during the charge and discharge operations. Under the particular selected operation parameters in the performed calculations, shown in Table 5.1 and Table 5.2, the transient period is extended to 5-6 cycles.

In order to discuss the quality of the released heat during the charge (disposed thermal energy) and discharge operations, the obtained output fluid temperature for the ten-modelled cycles is presented in Figure 5.5.

Going through the charge curves (Figure 5.5a), during the first run the output fluid temperature is kept in 20 °C during the first three hours. From this threshold time, the output fluid temperature starts increasing continuously up to 110 °C at the end of the charge (4 hours). After 5-6 cycles, when the stationary thermal performance of the storage is reached, the fluid is released at 20 °C during 1.5-2 hours, to start increasing up to 220 °C at the end of the four charging hours.

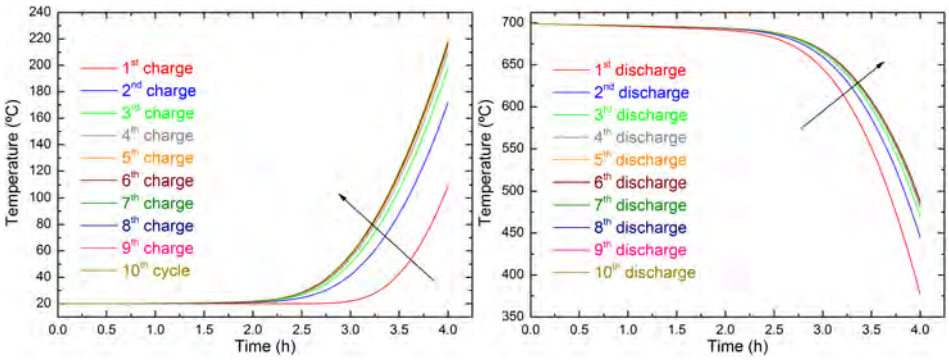

(a) (b)

Figure 5.5. Tank output fluid temperatures in the a) charge and b) discharge operations.

On the other hand, during the TES discharge operation an opposite trend is observed. As shown in Figure 5.5b, in the first run, the released fluid temperature is kept around 700 °C during 2 hours, only decreased by the lateral thermal losses. After this time, it shows a continuous decrease up to 375 °C at the end of the discharge. In this operation, the output fluid temperature shows longer times at temperatures close to 700 °C with subsequent thermal cycling. Once the transient behaviour is finished, this temperature remains almost constant during 2.5 hours, before decreasing up to 480 °C at the end of the discharge process.

The overall thermal behaviour during a continuous cycling of the packed bed TES system is associated to the thermal evolution of the thermocline during the charge/discharge processes, and to its displacement through the storage tank. In these terms, the fixed time operation leads to a continuous displacement of the thermocline to the bottom part of the storage tank during the cycling. As a consequence, an increasing amount of thermal energy is disposed during consecutive charge processes, whereas larger hot output fluid temperatures are obtained in subsequent discharge runs.

Aiming at discussing the quality of the released heat in terms of charged/discharged energies and cycle efficiencies, these magnitudes are presented in Figure 5.6. In particular, in Figure 5.6a the charged (red line) and discharged (blue line) energies in each cycle are collected. On the other hand, in Figure 5.6b the efficiency according to eq. (4.35) in red line, and the ratio of the TES material exploited (blue line) in each cycle are presented.

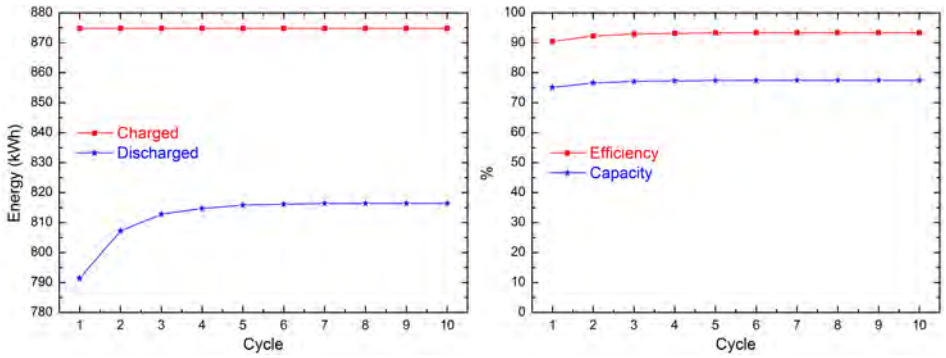

(a) (b)

Figure 5.6. a) Energies and b) efficiencies involved in each thermal cycle.

Considering the discharged energy and efficiency, a continuous increasing trend is observed, showing a maximum value when the stationary thermal performance condition is satisfied. This behaviour is caused by two main reasons: on one hand, to the energy associated to the temperature stratification, or thermocline formation, during the first cycles, and, on the other hand, to the increasing discharged energy (higher temperature level).

Quantitatively, the obtained cycle efficiency ranges from values slightly above 90% in the first cycle to 93% when the stationary condition is reached. On the other hand, the ratio of the exploited solid storage material also presents high values, ranging from 75% in the first cycle up to 77.5% in the stationary.

5.2.3. Temperature tolerance operation

To complete the analysis of the three proposed operation methodologies, in this section, a pre-determined output fluid temperature criterion is selected to stop the charge and discharge operations. In the following, this maximum allowed output fluid temperature variation during the charge/discharge process is denoted

as “temperature tolerance”. For the sake of clarity, if a temperature tolerance of T_{tol} is selected for both, the charge and discharge operations, the system is considered charged or discharged once the output fluid temperature is $T_{cold}+T_{tol}$ or $T_{hot}-T_{tol}$ respectively.

Considering the deep implications of this operation method, the main goal of this section is double: to present a detailed analysis of the long-term thermal stability and to study the impact of the temperature tolerance in the global thermal performance. Aiming at fulfilling both mentioned objectives, a specific methodology adapted to each phenomenon is proposed. For the first one (long-term stability) a complete transient analysis is performed under continuous charge and discharge cyclic operation. In these terms, an exhaustive analysis of the temperature stratification evolution in the packed bed is presented. In addition, the developed methodology also includes a discussion about the possibility of attaining a reproducible thermal behaviour with continuous thermal cycling.

Second, a sensitivity analysis of the temperature tolerance is performed. In these regards, the influence of this parameter on the storage capacity, overall efficiency and thermal performance is presented. In order to make the obtained results extensible to a more general framework, a quantitative analysis of the relation between the temperature tolerance and the storage capacity of the TES unit is also included.

Finally, the eventual influence of the operation temperature range is also addressed. To investigate this behaviour, two temperature ranges are studied. The first one corresponds to the conventional molten salt storage technology, whereas the second one is associated to the use of thermal oil as heat transfer fluid.

5.2.4.1. Reference case: thermal stability analysis

In this first part, in addition to the TES system parameters defined in Table 5.1 and Table 5.2, an arbitrary value of 20 °C for the temperature tolerance is fixed as reference. As a consequence, under these conditions, following the aforementioned charge/discharge stopping criterion, the system is assumed charged when the output fluid temperature is 40 °C, whereas is considered discharged when this temperature reaches 680 °C.

In Figure 5.7a the evolution of the tank axial temperature distribution in consecutive cycles once the system is considered charged (continuous lines) and discharged (dashed lines) is presented. In this figure, x-coordinates 0 and 1 correspond to the upper and lower parts of the tank respectively. The obtained results show a clear evolution of the thermal performance of the packed bed TES system with cycling. This behaviour, also obtained for the fixed time operation derives in a transient stage, prior to satisfy a stationary operation condition. The thermal transport mechanisms responsible for the thermocline formation and evolution are associated to this transient thermal performance, leading to different initial conditions for consecutive charge/discharge cycles. Considering the axial temperature profiles of the charged system, it can be observed that the width of the thermocline region grows with increasing the number of thermal cycles. The same phenomenon is observed in the discharge curves. Thereby, the evolution of the thermocline ranges from a temperature stratification of around half of the tank in the first charge to the total tank length in the last one.

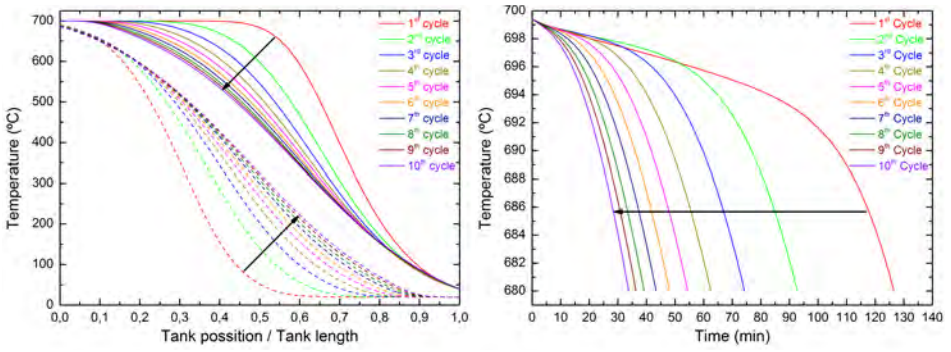

(a) (b)

Figure 5.7. a) Axial temperature distribution in the packed bed at the end of the charge (continuous lines) and discharge (discontinuous lines) operations for ten cycles; (b) Output fluid temperature during ten discharge operations.

On the contrary to the effect observed in the fixed time operation mode, the calculated axial temperature profiles in the charged and discharged states under the fixed temperature tolerance criterion show a continuous reduction of the storage capacity with thermal cycling. However, the observed difference between consecutive cycles is gradually reduced during the transient period. As a consequence, this indicates the possibility of reaching a reproducible stationary

performance after certain number of cycles. The underlying reason of this phenomenon, as mentioned in the previous section, is the equilibrium between the energy released from the TES within the selected temperature tolerance and the growth of the thermocline between two consecutive cycles. As a result coming out from this analysis, the temperature tolerance becomes of paramount importance to determine the transient performance of the packed bed. Due to the narrow temperature tolerance value selected for this reference analysis, 20 °C, the lack of a stationary behaviour is observed (Figure 5.7a) after a reasonable number of cycles for the real implementation of the system.

Figure 5.7b shows the output fluid temperature during the consecutive discharge operations. As expected from the thermocline results discussed above, the total time releasing air at a temperature within the tolerance value is noticeably shortened with cycling. In this particular case, comparing the first and the tenth cycles, a time reduction around a 70% is obtained.

Figure 5.8 presents a complete energetic and efficiency balance during the mentioned transient performance analysis. Red dots correspond to the values of the charged energy, the vertical blue triangles to the discharged or useful energy, the green squares to the lateral thermal losses, the horizontal magenta triangles to the pumping energy and the orange stars to the system efficiency as described in eq. (4.35).

Aligned with the results observed in Figure 5.7b, Figure 5.8 shows an equivalent thermal storage capacity reduction with cycling. In these terms, the energies discharged in the first and tenth cycles are 450 and 120 kWh_{th} respectively. Based on the maximum capacity of the storage material (1.05 MWh_{th}), these energies represent respectively around a 42% and 11% of the TES material usage. According to this criterion, a poor efficiency in the exploitation of the storage material is found. Therefore, a complete optimization of the proposed packed bed design must also consider the maximization of this parameter.

Finally, the reference study is completed with the quantification of the thermal losses through the lateral storage wall and with the required pumping mechanical energy. These calculations are performed according to eq. (4.40) – (4.43) including a complete charge/discharge run. It can be noted that the correct design of the

storage permits to obtain satisfactory values for both magnitudes, around 1.5% of the energy introduced in the system.

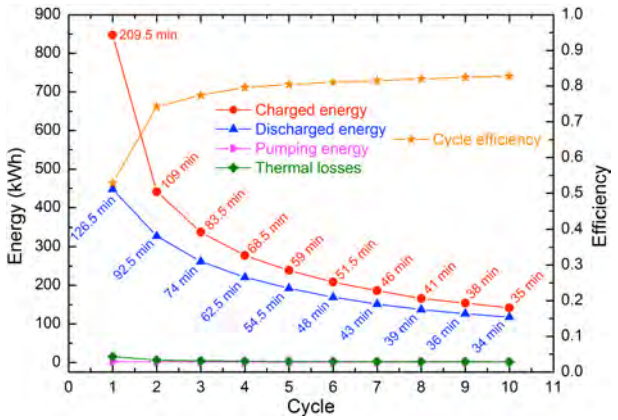

Figure 5.8. Involved energies and efficiency balances for each of the ten-modelled cycles in the reference case.

Regarding the cycle efficiency of this reference tolerance case, an increasing behaviour is observed during the transient period. Starting from a poor performance value of around 53%, after four cycles, the resulting efficiency is enhanced up to around 80% and maintained in subsequent cycles with a slightly increasing trend. The underlying reason for the low efficiency in the first cycles is the energy required in the development of the thermocline region. As a consequence, the resulting temperature distribution leads to the degradation of the input energy, showing a thermal level out of the required tolerance, which penalizes the cycle efficiency.

5.2.4.2. Sensitivity analysis of the temperature tolerance

In the previous section, a temperature tolerance of 20 °C has been considered for reference. Based on the obtained low thermal performance, larger temperature tolerance values are proposed in the following aiming at maximizing the storage capacity, the exploitation of the storage medium and hence, the process efficiency. The particular selected values for the temperature tolerance are 100 and 150 °C, aiming at the obtainment of representative conclusions. The sensitivity analysis obtained results will determine the influence of this operational parameter in the TES thermal performance.

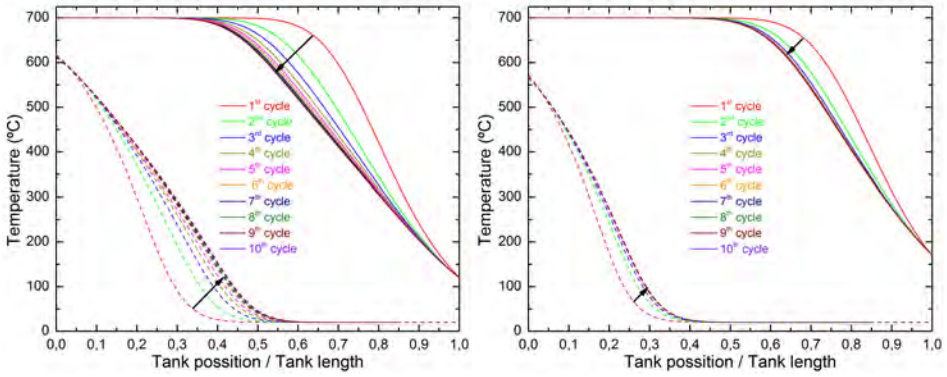

(a) (b)

Figure 5.9. Temperature distribution in the axial coordinate of the packed bed at the end of the ten performed charge (continuous lines)/discharge (dashed lines) operations with a tolerance of a) 100 °C and, b) 150 °C.

The results included in Figure 5.9 show the axial temperature distribution of the packed bed once the charge and discharge operations are finished according to the selected temperature tolerance criterion. As a result, a noticeable difference on the transient thermal behaviour is found. When compared with Figure 5.7a, a clear shortening of the number of cycles necessary for reaching a reproducible stationary state is observed. Quantitatively, the transient performance associated to the 100 and 150 °C temperature tolerances takes 6-7 and 4-5 cycles respectively. This is a very important improvement with respect to the lower temperature tolerance reference case, where a stationary behaviour is not attained in a reasonable number of cycles for the real deployment of this TES alternative.

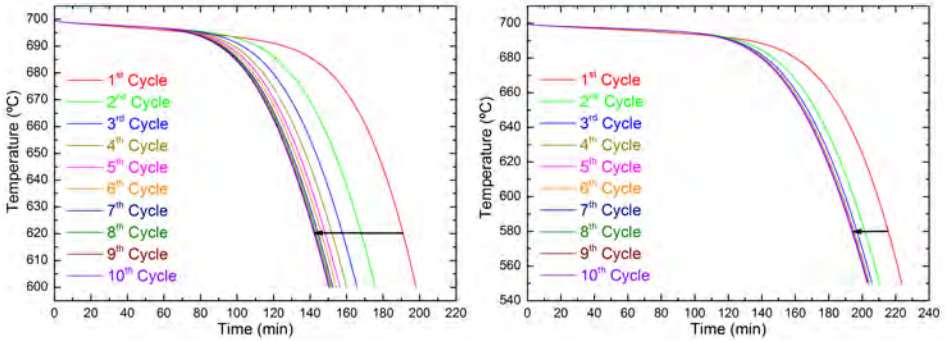

(a) (b)

Figure 5.10. Output fluid temperature during the discharge processes. a) 100 °C and b) 150 °C of temperature tolerance.

Figure 5.10 presents the output fluid temperature in the discharge operations corresponding to both analysed tolerance values. The obtained results confirm the shortening of the transient TES performance with increasing temperature tolerance values. Furthermore, a clear enhanced thermal behaviour is promoted by larger tolerance values, enlarging the discharge times providing useful heat. Quantitatively, selecting the tenth cycle for the three studied cases, 35, 150 and 200 min are obtained for the 20, 100 and 150 °C tolerances respectively. This increase leads to an enhancement of around 430% and 575% when compared to the lowest proposed tolerance value.

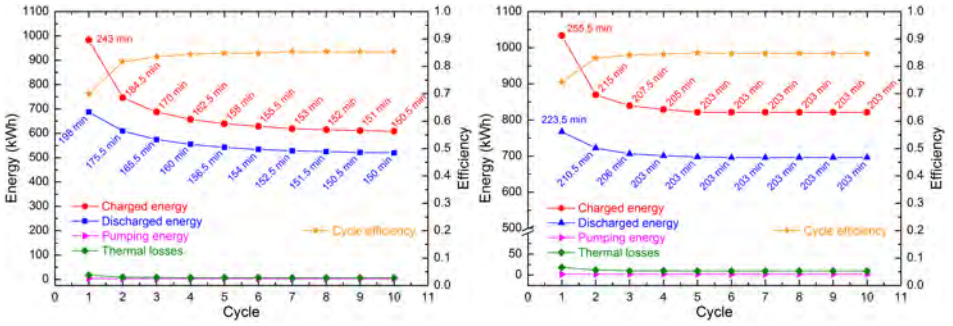

(a) (b)

Figure 5.11. Involved energies and efficiency balances for the ten performed cycles: a) 100 °C and b) 150 °C of temperature tolerance.

Figure 5.11 summarizes the values of the involved energies together with the overall efficiency. The values refer to the transient states shown in Figure 5.9 and Figure 5.10. In both cases, the total stored/released energy is much larger than in the reference case. Attending to the last modelled cycle, the discharged energies are around 520 and 700 kWh_{th} for the systems with 100 and 150 °C of temperature tolerance respectively. Comparing any of these values with the stored energy in the reference case, around 120 kWh_{th}, a noticeable increase on the exploitation of the storage material is observed.

The cycle efficiency presented in the right vertical axis in Figure 5.11, shows that in both systems the obtained values are around 85% once the stationary performance of the TES unit is attained. These values are slightly higher to those obtained in the reference case (82%) demonstrating that the use of higher temperature tolerances also improves the thermal performance of the TES unit.

However, it has to be pointed out that the increase of the tolerance, despite of the mentioned benefits, also presents some shortcomings. The main one is the increasing amount of heat wasted with the output fluid during the charge, associated to larger tolerance values. In the efficiency definition used in this thesis (eq. (4.35)) this energy is considered as useless. In the studied cases, this energy, in the stationary performance of the TES, accounts for 50 and 75 kWh_{th} for the 100 °C and 150 °C of temperature tolerance respectively. In case of finding an appropriate application for this heat, a noticeable increase on the cycle efficiency would be achieved.

To fully assess how the proposed TES unit is being exploited, the evaluation of the efficient usage of the storage material must be studied. In this regard, the ratio between the released energy in the discharge operation and the maximum capacity based on the storage material (1.05 MWh_{th}) is considered as a satisfactory measurement. In order to discuss this parameter, Figure 5.12 collects this ratio for the two temperature tolerances analysed in this section together with the reference case. The evaluation of this magnitude shows values around 50 and 65% in the stationary performance for the 100 and 150 °C tolerances respectively. The obtained values represent a substantial improvement in the material usage in comparison to the reference case.

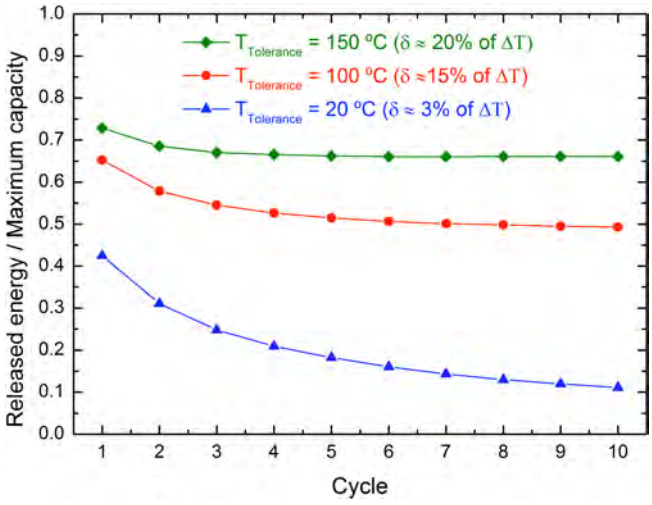

Figure 5.12. Ratio between the cycle released energy and the maximum thermal capacity of the storage material.

With the objective of establishing a minimum acceptable threshold, which permits a successful deployment of the proposed TES technology, in this thesis, a value $\gtrsim 50\%$ of material usage is proposed. As a consequence, attending to the obtained results, a minimum temperature tolerance value of 100 °C should be considered. In the same line, it must be noted that the selected case also promotes the shortening of the transient TES performance, which becomes of great interest on the real exploitation of this concept.

Aiming at a full extrapolation of the obtained results to a more general framework, a dimensionless parameter, the specific tolerance, δ, is introduced. The specific tolerance is defined as:

$$\delta = \frac{Temperature\ tolerance}{\Delta T} \cdot 100. \quad (5.1)$$

In this regard, the considered 20, 100 and 150 °C tolerance values correspond to a δ = 4, 15 and 22% respectively. Introducing the technological threshold defined in the previous paragraph, a value $\gtrsim 15\%$ is recommended for a satisfactory operation of the TES packed bed.

5.2.4.3. Sensitivity analysis of the operational temperature range

In order to extend the conclusion extracted in the previous section, a similar sensitivity analysis adapted to different temperature ranges is presented. First, the current ΔT exploited in conventional CSP plants with the standard molten salt storage technology (290-565 °C, ΔT=275 °C), named Case 2 in this work, is analysed. Second, the temperature range associated to the operation of an organic Rankine cycle (ORC) turbine (180 and 300 °C, ΔT=120 °C), named Case 3, is investigated. In order to maintain a similar tolerance criterion considered in the reference case (sections 5.2.4.1 and 5.2.4.2), specific tolerance values of δ = 4, 15 and 20%, for each ΔT, are considered. Table 5.3 summarizes all the relevant operational parameters such as the maximum storage capacity, temperature tolerances and selected charge/discharge stopping criteria.

Table 5.3. Operational temperature ranges, stopping criteria temperatures and maximum storage capacities for all the modelled cases.

			Reference Case	Case 2	Case 3
		$T_{f,hot}$ (°C)	700	565	300
		$T_{f,cold}$ (°C)	20	290	180
		ΔT (°C)	680	275	120
		Storage max. (kWh_{th})	1054	445	178
$T_{tolerance}$		δ = 4%	20	10	5
		δ = 15%	100	40	20
		δ = 20%	150	60	25
Stopping criteria (°C)	Charge	δ = 4%	40	300	125
		δ = 15%	120	330	140
		δ = 20%	170	350	145
	Discharge	δ = 4%	680	555	295
		δ = 15%	600	525	280
		δ = 20%	550	505	275

In Figure 5.13 all the cycle-involved energies together with the efficiency balances evaluated according to eq. (4.35) for all the analysed systems are presented. The results obtained for δ = 4% still show a clear evolution of the thermal behaviour in Cases 2 and 3 after the ten modelled cycles. These results are in agreement with those obtained in section 5.2.4.1 for the reference case. On the other hand, for δ = 15% and δ = 20%, Cases 2 and 3 present a limited transient performance attaining a reproducible behaviour after a reasonable number of cycles (6-7 and 4-5 respectively). These results are also in agreement with the obtained ones for the similar δ values studied in the reference temperature range (section 5.2.4.2). As a consequence, these results show the independence of the transient thermal performance of the TES with the selected operational temperature range, which represents a very important conclusion.

The efficiency analysis of the obtained cyclic transient performance is also included in Figure 5.13 (right-hand side axis). As found for the reference case, the tenth cycle efficiency value is increased above 80% in all the modelled systems. It

can be noticed that the efficiency difference found in the first cycle when compared to the reference case depends on the initial considered temperature of the TES (ambient temperature, 20 °C).

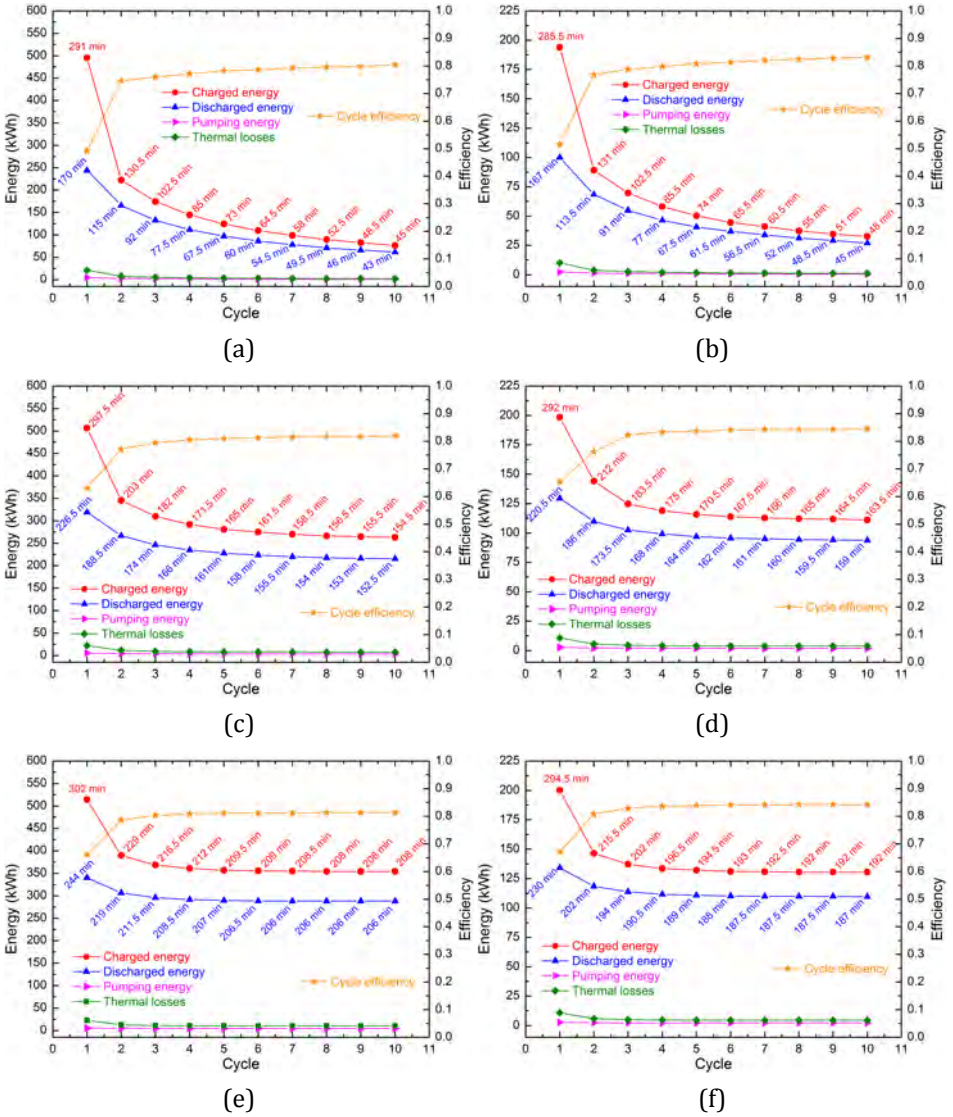

Figure 5.13. Involved energies and cycle efficiency balances for: Case 2 in left-hand side graphs and Case 3 in right-hand side graphs. From top to bottom δ = 4, 15 and 20% respectively.

Following the same results analysis scheme than in the reference case, Figure 5.14 shows the efficiency on the usage of the storage material. The results confirm the full extrapolation of the analysis carried out, where the independence of the

system thermal performance and material usage efficiency with the operational temperature range is demonstrated, once the δ parameter value is selected. Figure 5.14 supports this conclusion since similar material usage efficiency values are obtained in comparison to the reference case (Figure 5.12).

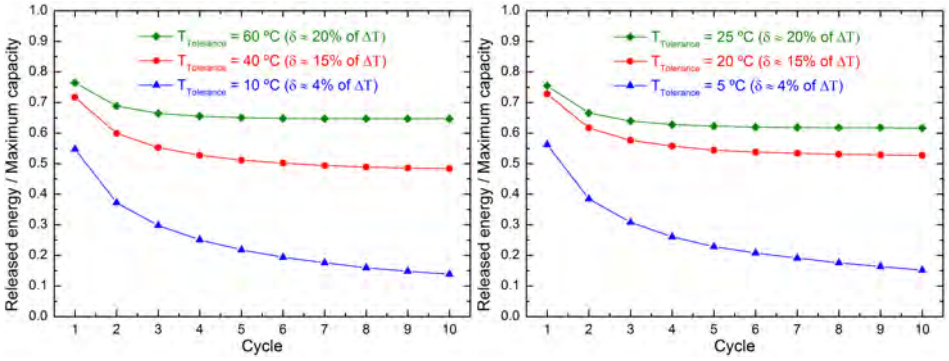

(a) (b)

Figure 5.14. Ratio between the cycle released energy and the maximum thermal capacity of the storage medium: a) ΔT = 275 °C and b) ΔT = 120 °C.

5.3. Analysis of the main TES tank design components

After investigating the different proposed operational strategies, in this section the impact on the thermal performance of the main TES tank design parameters is addressed. In this regard, parametric analyses of the tank geometry and aspect ratio, solid material particle size and fluid flow rate are presented.

For these analyses, in order to maintain a general comparative frame, the reference case described in section 5.1 is selected (see Table 5.1) to perform the aforementioned calculations. In addition, according to the operational strategy analysis carried out in the previous section, the temperature tolerance strategy (section 5.2.3) is selected as a benchmark. In this regard, considering an optimum deployment of the packed bed storage technology, a temperature tolerance of 100 °C (δ=15%) is fixed for both, the charge and discharge operations. In agreement with the thermal transient/stationary performance of the selected reference case, up to ten cycles are modelled in each investigated system to study the complete transient stage up to a reproducible thermal behaviour.

5.3.1. Parametric analysis of the tank geometry

In this first section a parametric analysis for the selection of an optimized TES tank geometry is presented. In order to explore an innovative approach to the standard packed bed storage solution, in addition to the conventional cylindrical tank geometry, a conical one is also investigated. The first mentioned tank geometry has extensively been used in the TES field, as well as in many other industrial applications. On the other hand, the conical tank has been recently introduced (see section 1.3) aiming at the reduction of the mechanical stresses generated between the TES solid medium and the container. The treatment of the conical geometry has also some additional implications, such as the lack of spatial symmetry in the axial direction. As a consequence, both conical orientations are analysed: the first one with the larger tank side in the top of the tank, (henceforth "regular"), and the second one with the larger tank side in the bottom, (henceforth "inverse"). A layout of the two studied geometries, cylindrical and conical, and the different orientations of the latter option are included in Figure 5.15.

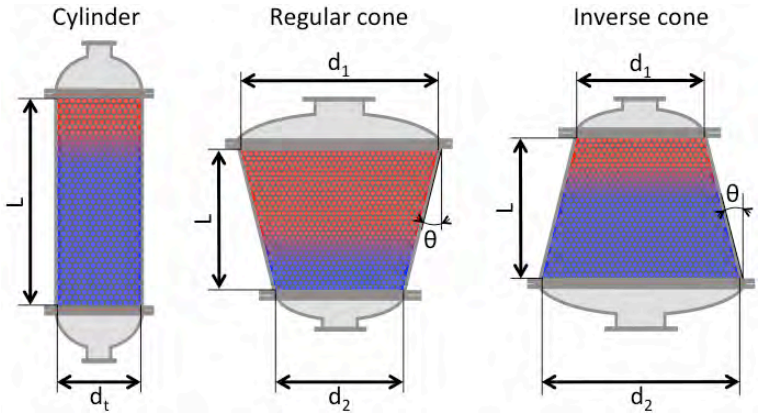

Figure 5.15. Tank geometries and orientations investigated in the storage tank geometry parametric analysis.

A second consequence of the non-symmetric conical geometry is the complex definition of the aspect ratio of the TES tank. In the case of the cylindrical tank, the definition of the aspect ratio is straightforward as the tank length (L) divided by the tank diameter (d_t). Meanwhile, in the conical shape, an additional degree of freedom is introduced since the diameter of the storage tank depends on the height. For comparative reasons, the tank volume and the conicity angle (θ) are

fixed in this study to the values included in Table 5.1 and Table 5.4 respectively. As a consequence, the height of the tank remains like the only free parameter.

The quantitative ranges, in which the cylindrical tank aspect ratio and the conical tank height are varied in the parametric analysis reported in this section, are collected in the lower part of Table 5.4.

Table 5.4. Magnitudes fixed and varied in tank geometry parametric analysis.

Parameter	Value
Particle diameter (cm)	1
Mass flow rate ($kg \cdot m^{-3}$)	0.3
Tank geometry	Cylindrical/Conical
Conicity angle (°)	10
Cylindrical tank aspect ratio (L/d_t)	0.5 / 1 / 2 / 3
Conical tank height (m)	1 / 1.2 / 1.4 / 1.6 / 1.8 / 2 / 2.4 / 2.6 / 3

The obtained stored energies in the stationary performance for the regular and inverse conical geometries together with the ones associated to the cylindrical geometry are collected in Figure 5.16. In order to compare the influence of the aspect ratio in both geometries, the stored energy is presented for different tank length values in this graph.

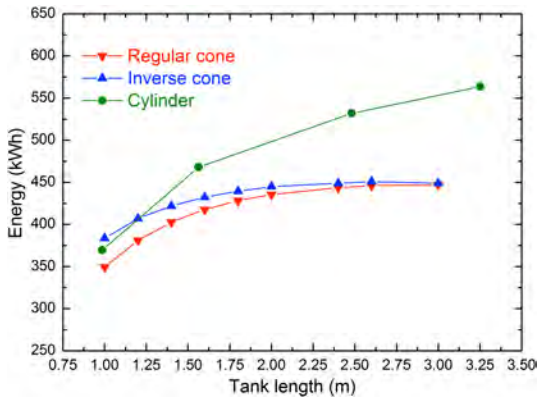

Figure 5.16. Stored energy in the stationary thermal performance of the two investigated geometries and two conical orientations.

Attending to the results obtained for both conical orientations, for all the modelled tanks, larger stored energies are obtained for the inverse conical

orientation. This difference is more pronounced for low tank lengths, and it is found to be almost negligible in the highest ones.

Comparing the energy stored in both conical orientations to the ones in the cylindrical tank, considerably higher values are attained in the latter, exception made for the shortest cylinder and inverse cone. Consequently, the cylindrical geometry promotes better storage capacities than the conical one.

Overall, from the obtained results, in terms of thermal energy storage capacity maximization, cylindrical tank geometries should be selected. However, considering the benefits of the conical geometry on the management of thermal stresses, mechanical implications and ratcheting phenomena associated to the packed bed, the deployment of this tank geometry could be addressed, even if the storage capacity is reduced.

5.3.2. Parametric analysis of the cylindrical geometry

Considering the demonstrated benefit on the maximization of the storage capacity derived from the cylindrical tank, in the following, this geometry is selected. As a consequence, in this section, a deep analysis of the design of the cylindrical tank geometry is presented. In this regard, the influence of the implemented fluid flow rate, the selected TES material particle size or the tank aspect ratio is deeply analysed in the following.

In addition to the reference case parameters shown in Table 5.1, a summary of the free studied parameters together with their associated variability ranges is included in Table 5.5. The selection of the ranges in which each parameter is varied, far from an arbitrary selection, is performed according to the following criteria:

1. Mass flow rate: the velocity of the heat transfer fluid (air) through the packed bed is ranged from laminar to turbulent conditions.
2. Particle size: it is selected considering the most usual size fractions reported in the literature for packed bed TES systems.
3. Aspect ratio: it is selected considering the limits of the mechanical stability and construction issues of the storage tank.

Table 5.5. Magnitudes varied in the cylindrical tank parametric analysis.

Parameter	Value
Mass flow rate (kg·s^{-1})	0.01 / 0.1 / 0.3 / 1
Particle diameter (cm)	0.5 / 1 / 2 / 3 / 4 / 5
Tank aspect ratio (L/d_t)	0.5 / 1 / 2 / 3

It has to be noted that, in the following, a complete parametric analysis is carried out including all the possible combinations of the investigated parameters summarized in Table 5.5. This leads to the complete understanding of the packed bed system behaviour under all the potential design selection criteria.

5.3.2.1. Influence of the fluid flow rate

In this first section of the cylindrical geometry parametric analysis, the impact on the TES thermal performance of the fluid flow rate is discussed. A summary of the obtained results is presented in Figure 5.17, where six plots are included corresponding to the six particle diameters investigated. The presented stored energy results are addressed to the tenth cycle, since the stationary and thermally reproducible conditions are needed for a fair comparison. Considering the transient behaviour obtained in the previous section, the continuous charge/discharge process guarantees the stationary thermal behaviour after ten cycles, in the particular studied system. As a consequence, the reproducible stored energy on each case is presented as a function of the mass flow rate. In each plot, four curves are shown associated to the investigated cylindrical tank aspect ratios.

The results of the parametric analysis shown in Figure 5.17 reveal a strong impact of the fluid mass flow rate on the thermal performance of the TES unit. The energy storage is drastically decreased for low mass flow rates. On the other hand, the energy storage is maximized for mass flow rates between 0.1 and 0.3 kg·s^{-1} depending on the particle size and tank aspect ratio. Values above 0.3 kg·s^{-1} again show a slight decrease in the storage capacity in all the modelled systems.

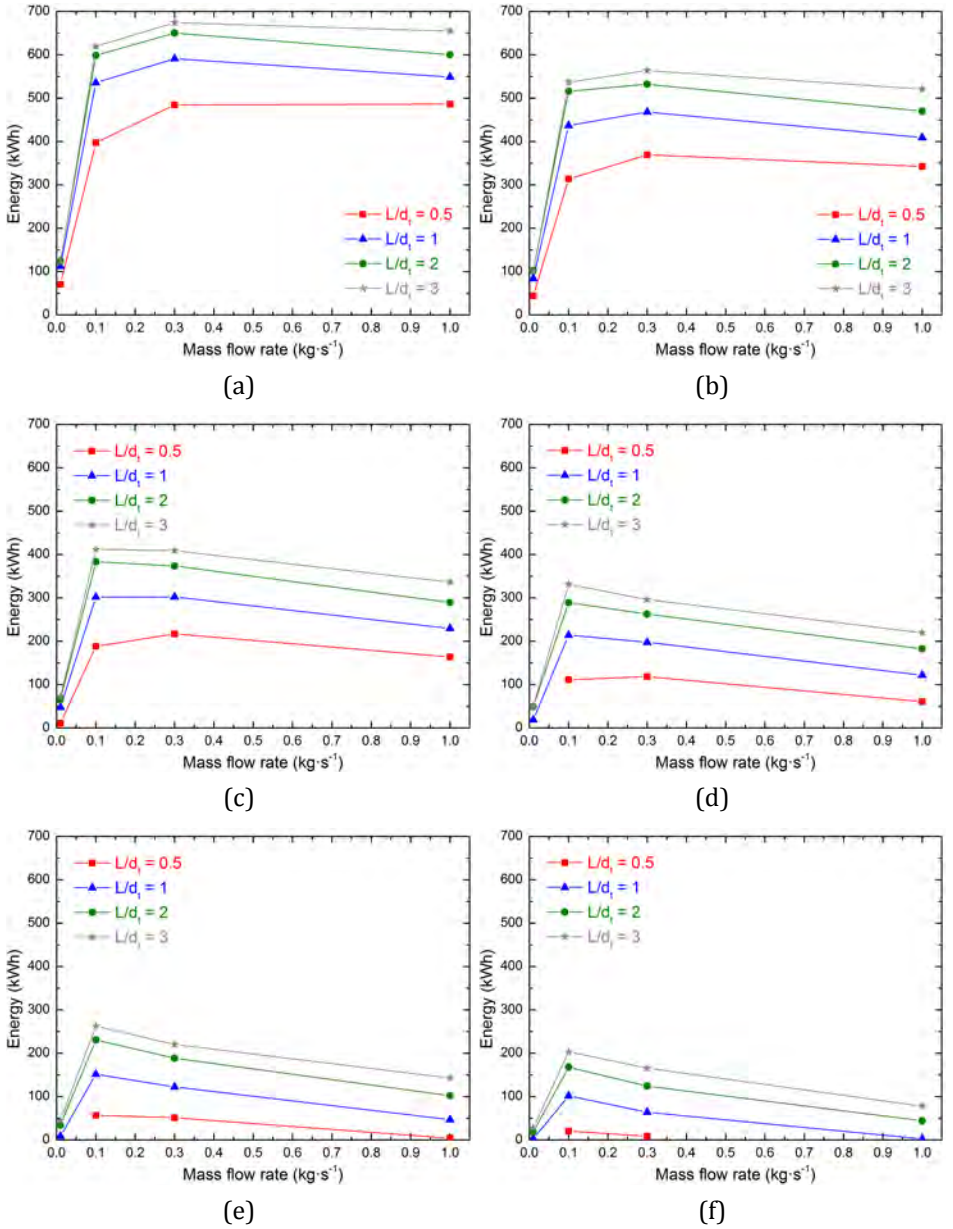

Figure 5.17. Stored energy for different tank aspect ratios and air mass flow rates after ten cycles, when using particles of: a) 0.5; b) 1; c) 2; d) 3; e) 4 and f) 5 cm.

The reasons for this behaviour are related to the heat transfer mechanisms governing the thermal transport in the packed bed. In the case of very low fluid velocities, the conduction and radiation between particles control the formation of the thermocline region. Under these conditions, the thermocline formation is

mainly affected by the thermal conductivity of the solid material in the axial direction. On the other hand, high fluid velocities favour convective mechanisms because of higher turbulence in the fluid. Depending, among others, on the particle size and the thermo-physical properties of the TES material, the solid medium is not able to absorb/release all the heat content from/to the HTF, leading to the formation of a larger thermocline region in the fluid. Both behaviours have a direct non-desirable effect on the heat transfer, which lead to a higher spreading of the thermocline, associated to a storage capacity loss. In this regard, average velocities, in this case, associated to mass flow rates between 0.1 and 0.3 $kg \cdot s^{-1}$, balance the convective and conductive/radiative mechanisms. Consequently, an optimized thermocline is generated. These results show the great importance of a detailed fluid flow rate optimization on the particular deployed packed TES system.

5.3.2.2. Influence of the solid particle diameter

This section is devoted to the analysis of the influence of the particle size on the TES unit thermal performance. For this purpose, in Figure 5.18 the results obtained in the parametric analysis for the stationary thermal performance are presented in four graphs. Each one corresponds to a different fluid flow rate and, in each plot four curves are included associated to the different cylindrical tank aspect ratio values modelled.

In Figure 5.18, it can be observed that for the four fluid flow rates, the higher is the particle diameter, the smaller is the stored energy. In this figure, it is also seen that the stored energy is considerably decreased for particle diameters above 1 cm. However, the selection of small particle diameters may have a strong impact on the pressure drop induced in the packed bed, and consequently, in the energy required for the pumping of the heat transfer fluid. This phenomenon is depicted in Figure 5.19. As it is observed in these plots, the required mechanical energy for the pumping in a complete charge/discharge cycle is considerably enlarged with increasing the fluid flow rate value. The calculated pressure drop behaviour and the subsequent associated mechanical pumping energy show an exponential increase with decreasing particle sizes. This increment is very relevant for particles below 1 cm.

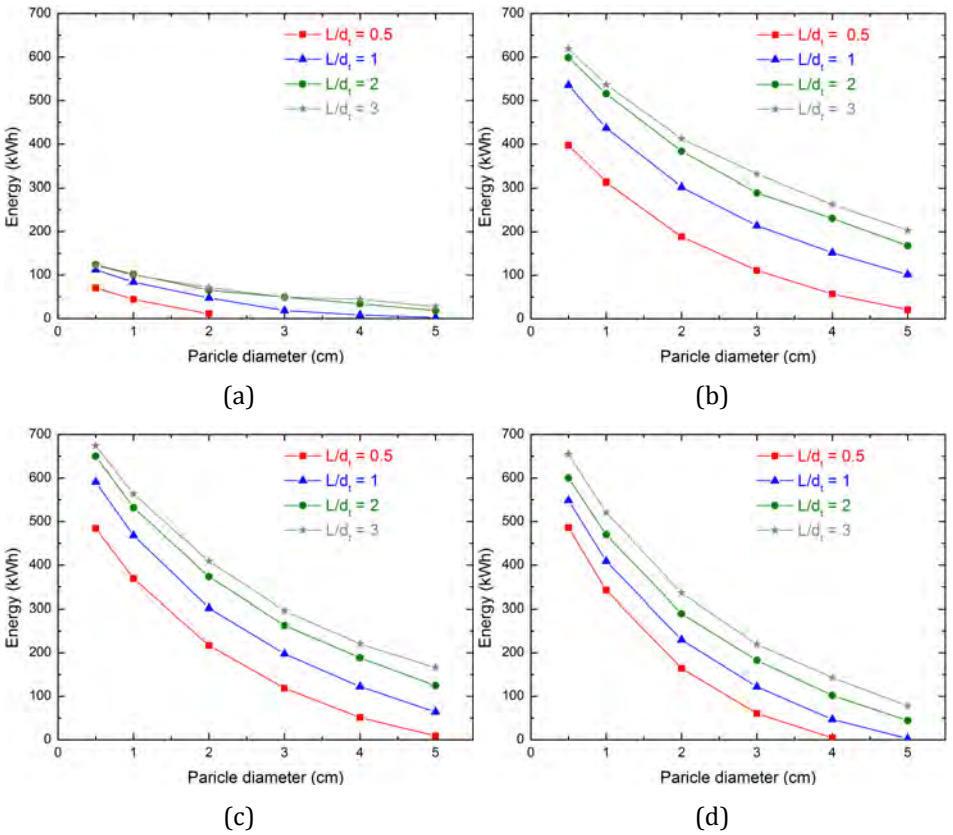

Figure 5.18. Stored energy for different tank aspect ratios and particle diameters in the stationary TES performance, when using mass flow rates of: a) 0.01; b) 0.1; c) 0.3 and d) 1 kg·s^{-1}.

Overall, the results obtained in this section show the importance of the selection of an appropriate particle diameter size in order to optimize the TES unit storage capacity. Furthermore, the performed calculations demonstrate that smaller particles promote larger storage capacities. However, the analysis of the required mechanical energy to pump the fluid through the packed bed shows a strong increase of this magnitude for decreasing solid particle diameter values. In the studied TES configurations, particles below 1 cm show an exponential pumping energy increase.

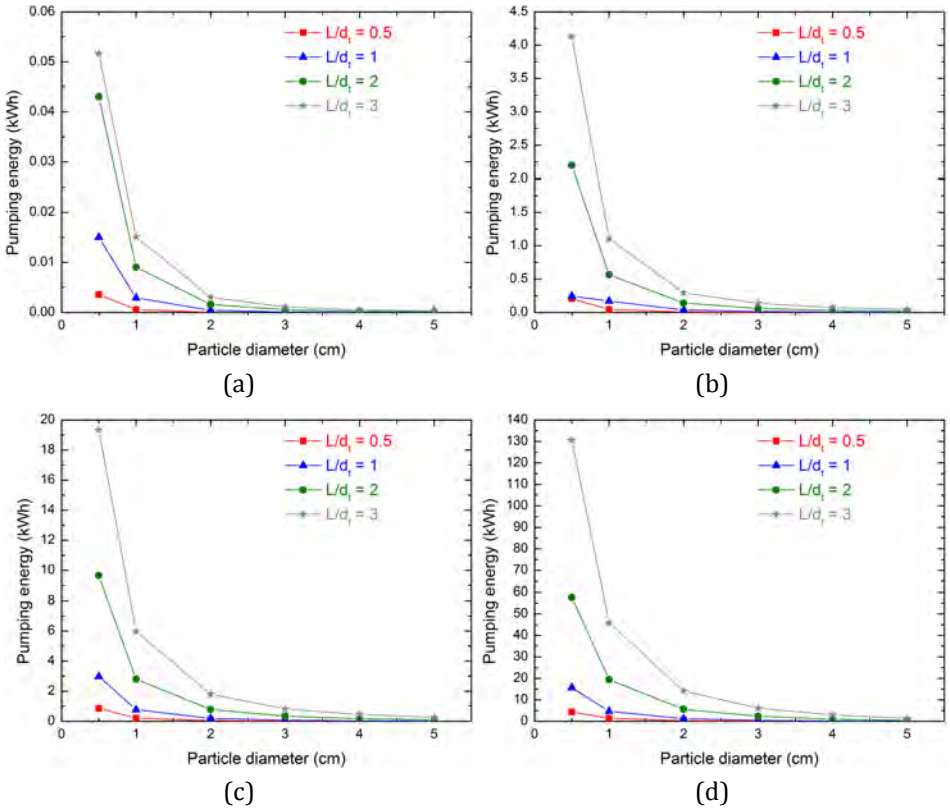

Figure 5.19. Pumping energy required for different tank aspect ratios and particle diameters after ten cycles, when using mass flow rates of: a) 0.01; b) 0.1; c) 0.3 and d) 1 kg·s^{-1}.

5.3.2.3. Influence of the cylindrical tank aspect ratio

In previous sections, two of the main design parameters, the heat transfer fluid flow rate and the particle diameter have been found of paramount importance in the maximization of the storage capacity of the TES unit. To continue with the parametric analysis, the impact of a third parameter, the cylindrical tank aspect ratio is addressed in this section.

The results obtained from this analysis are included in Figure 5.20. In the four plots it can be observed that higher tank aspect ratio values promote larger storage capacities. Quantitatively, as an example, changing the TES aspect ratio value from 0.5 to 4, keeping constant the particle diameter and the fluid flow rate, a thermal capacity enhancement of around 50% is achieved. However, the obtained results show a non-linear increase of the storage capacity with the aspect

ratio, as shown in Figure 5.20. In these terms, an asymptotic behaviour is obtained with increasing aspect ratio values.

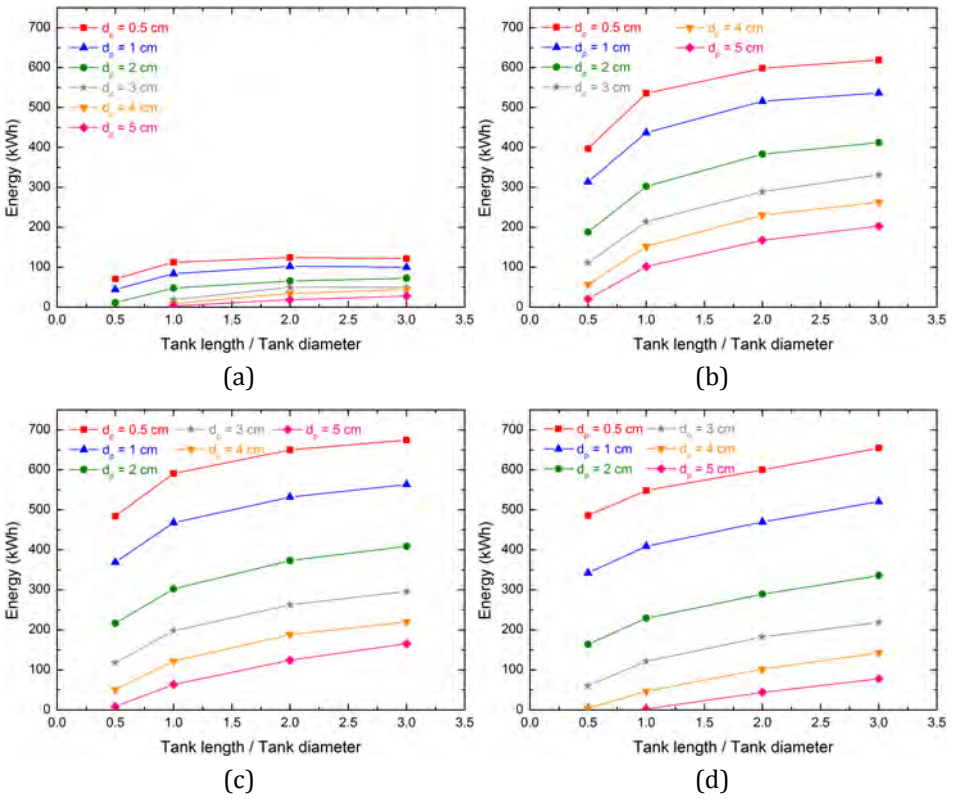

Figure 5.20. Stored energy for different tank aspect ratios and particle diameters in the stationary TES performance, when using mass flow rates of: a) 0.01; b) 0.1; c) 0.3 and d) 1 kg·s^{-1}.

However, in the selection of the optimized tank aspect ratio, some additional considerations have to be taken into account. Firstly, as depicted in Figure 5.19, higher tank aspect ratio values lead to higher pressure drop values and hence, larger required mechanical pumping energies. Secondly, the selection of a high tank aspect ratio, also involve higher packed bed heights and hence, stronger mechanical stresses on the material in the lower part of the tank. Finally, larger aspect ratio values also lead to larger TES tank lateral wall areas, which imply also larger thermal losses. This last behaviour can be observed in Figure 5.21, where the tank lateral area as a function of the cylindrical tank aspect ratio is presented for the reference modelled case. Consequently, an optimized packed bed TES tank

design implies a good balance between all the mentioned parameters. Overall, in the modelled reference case, a cylindrical tank aspect ratio value around two is identified as a successful selection in order to balance an enhanced thermal performance with an accessible mechanical construction, equilibrated pressure drop values and thermal losses.

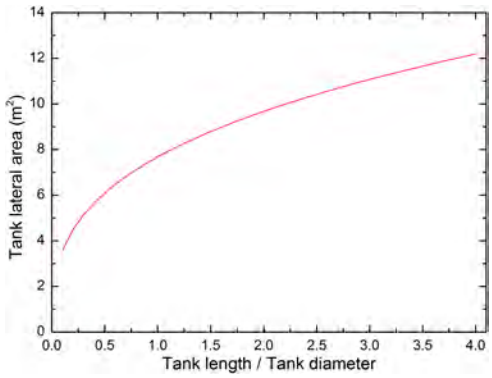

Figure 5.21. Tank lateral area as a function of the cylindrical aspect ratio.

As a final result coming out from the analysis performed in this section, the cylindrical tank aspect ratio is also identified as one of the main design parameters for an optimized system design.

5.3.3. Validity of the local thermal equilibrium approach

The detailed analysis of the thermal performance of the packed bed TES system performed in this chapter has revealed the governing mechanisms of this storage solution. On the variety of the system design alternatives shown, the obtained thermal performance is drastically affected by the different analysed parameters such as the fluid flow rate, particle diameter or tank aspect ratio. These magnitudes determine the overall heat transfer on the packing, ranging from close to thermal equilibrium transfer to large thermal imbalance between the fluid and the solid phases, depending on the heat transfer capacity and conditions between both materials.

As described in section 4.1, the nature of the heat transport between the solid and the fluid determines the appropriate modelling strategy in order to correctly describe the thermal performance of the packed bed TES system in terms of the local thermal equilibrium (LTE) or non-local thermal equilibrium conditions.

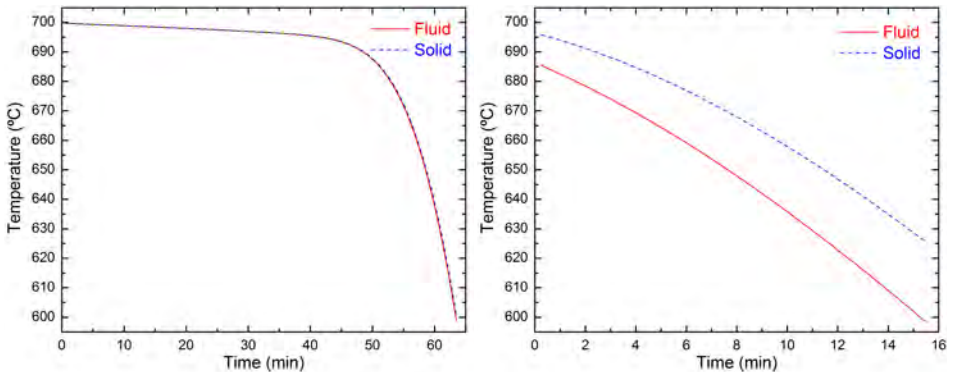

(a) (b)

Figure 5.22. Solid and fluid temperatures in the top of the tank during the first discharge operation, when a tank aspect ratio of 2, a mass flow rate of 1 kg·s^{-1} and particle diameters of a) 0.5 and b) 5 cm are applied.

In this section, the quantitative difference between both heat transfer scenarios, close and far from the thermal equilibrium, is explicitly analysed. With this objective, the results presented in section 5.3.2 are selected for this analysis. These results show an important reduction in the storage capacity of the proposed system when using large particle diameters, or when considering very high fluid flow rates. This effect is based on the effectiveness of the heat transport between the fluid and the solid materials. In order to study the underlying reason of these large differences in the energetic performance, in Figure 5.22 the fluid and solid temperatures in the outlet region (upper part) of the storage during the first discharge is included for two of the already modelled systems. As representative examples, both cases correspond to a mass flow rate of 1 kg·s^{-1} and a cylindrical tank aspect ratio of 2. In the figure on the left-hand side, Figure 5.22a, the TES unit with a particle diameter of 0.5 cm is presented, whereas in the right-hand side (Figure 5.22b) the one of 5 cm.

It can be noted that, in Figure 5.22a, a similar temperature in the fluid and the solid is obtained. However, in Figure 5.22b a difference around 10 °C is found during all the discharge process between both materials. In this system, the solid temperature is higher than the fluid one. A similar behaviour is found in the charge operation (not shown in the plot). In this case, the temperature of the fluid is equivalently higher than the one on the solid.

Even if in both presented cases in Figure 5.22 the heat transfer fluid velocity is the same, the obtained thermal performance differs considerably between them. In the case of the smallest particle, the system is able to provide up to 830 and 470 kWh_{th} within the allowed temperature tolerance in the first and tenth cycle respectively. Meanwhile, in the system with the largest particle it is only possible to release up to 167 and 44 kWh_{th} in the first and tenth cycles respectively. These differences indicate a reduction of around a 500% in the storage capacity.

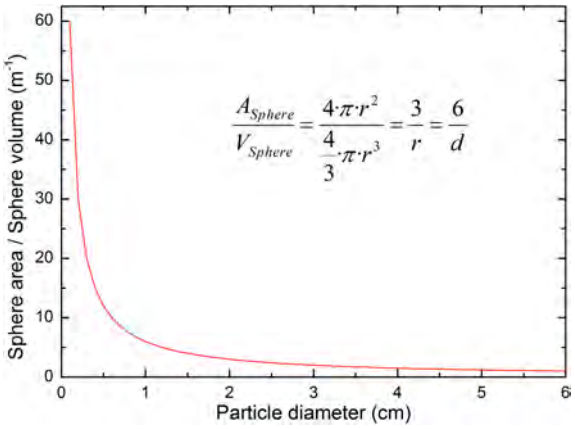

Figure 5.23. Volumetric superficial area as a function of the particle diameter.

One of the reasons of such behaviour is the available heat exchange area in the particle. This area is considerably reduced while increasing the size of the sphere, as it is depicted in Figure 5.23. It has to be noted that the higher the available area for heat exchange, the better is the heat transfer between the particle and the fluid. This fact becomes of paramount importance when implementing high fluid flow rates/velocities, as in the systems presented in Figure 5.22.

According to the results presented in Figure 5.22, when the temperature between the fluid and the solid is negligible, the system can be considered as optimized, since a good balance is satisfied regarding the heat transfer capacity to/from the fluid/solid phases, close to the thermal equilibrium condition. Conversely, when relevant differences are found between the solid and fluid temperatures, the system is far from a thermal equilibrium condition and it is susceptible for a better eventual performance and hence, to an optimization process.

Consequently, the LTE approach is only valid for systems such as the one presented in Figure 5.22a, otherwise, an important error would be attained with such approximation. This conclusion is of paramount importance in order to obtain a successful modelling and design of the packed bed TES system, since the thermal transport nature plays a capital role on the associated thermal equilibrium or non-equilibrium treatment.

5.4. Conclusions

In this chapter the most usual operational strategies of packed bed TES systems have been addressed together with a complete parametric analysis of the most relevant design boundaries of this type of TES solution.

In the analysis of the packed bed operational strategy, three different modes have been identified. The main conclusions extracted from the obtained results are summarized in the following:

1- The complete charge and discharge strategy allows operating the TES unit under reproducible stationary conditions from the first cycle. Attending to the storage material exploitation, values around 99% are found. However, the cycle efficiency shows a much lower value, around 60%. This low efficiency is associated to the large amount of energy released during the charge operation with the tank output fluid before reaching the complete charge condition.

2- The fixed time operation in the charge and discharge results in a transient performance of the packed bed before attaining reproducible conditions. The underlying reason of this performance is the energy left inside the tank after each cycle. This operational mode has a strong implication on the thermal performance of the packed bed TES, since it involves a transient thermal period before the thermocline stabilization. In the modelled system this transient performance is extended during 5-6 charge/discharge cycles. Attending to the cycle efficiency, under this operational mode it is kept above 90% from the first cycle. On the other hand, the exploitation of the storage medium results in values around 75%.

3- The temperature tolerance mode also reveals a transient performance of the storage before attaining reproducible thermal conditions. The sensitivity analysis of the temperature tolerance value shows the capital importance of this parameter in shortening the transient period and in enhancing the storage capacity and cycle efficiency. In a subsequent analysis of other temperature ranges to generalize the results obtained in the reference case, a clear dependency of the thermal performance on the ratio between the temperature tolerance and the temperature range (δ) is found. In this regard, a minimum value around a δ=15% is identified as satisfactory threshold to shorten the transient behaviour to a reasonable number of cycles and to enhance the thermal performance. Under these conditions, values in the exploitation of the TES medium slightly higher to 50% and cycles efficiencies around 90% are obtained. In addition, it is observed that the implementation of higher δ lead to higher values in the exploitation of the storage material maintaining the cycle efficiency in the same range.

As a consequence of the obtained results, the selection of the operation strategy becomes of paramount importance in the management of this type of TES systems. Even if in most industrial applications the operation of the TES unit will depend on the boundaries imposed by the particular heat demanding application, the performed analysis aimed at presenting a general guideline for the successful selection of the most relevant design parameters leading to an optimized operation of the packed bed TES solution.

The subsequent parametric analysis performed over the main variables in the design of the storage tank resulted in the following conclusions:

1- The storage tank geometrical analysis shows that the cylindrical tank promotes better thermal performance and hence, higher storage capacities than the conical one. Comparing between both conical orientations, the one denoted as inverse allows storing slightly higher amounts of energy. As a consequence, based on the thermal capacity, the cylindrical geometry should be selected for TES applications. However, based on implications of different natures, such as the mechanical, constructive and ratcheting management, the conical geometry could present a better performance.

Taking this into account, even with a decreased storage capacity, the conical geometry could be appropriate.

2. The analysis of the heat transfer fluid mass flow rate, together with the particle diameter shows the necessity of a detailed optimization process of these two parameters in order to have a satisfactory heat transfer in the packed bed. A direct consequence of the obtained successful heat transfer is the maximization of the energy stored in the TES unit.

3- In the fluid flow rate optimization, the implementation of very low values results in a poor thermal performance since, the conduction/radiation in the solid material governs the heat transfer in the axial direction of the tank. On the other hand, the implementation of very high fluid flow rates also penalises the heat transfer if the exchange area is not enough to absorb/release the amount of heat involved in an effective manner. Both performances are not desirable for the packed bed as they promote the enlargement of the thermocline region and consequently the decrease of the storage capacity. As a consequence, a satisfactory balance needs to be determined between all the heat transfer mechanisms. In the modelled reference case, values between 0.1-0.3 $kg \cdot s^{-1}$ are found to be the most appropriate ones.

4- The use of small particle diameters always promotes larger storage capacities. However, the pressure drop associated to the interstitial fluid flow through the packed bed shows an exponential increase with decreasing particle diameter values. In the modelled reference case, the pressure drop considerably increases when using particles below 1 cm.

5- The analysis of the cylindrical tank aspect ratio (L/d_t) shown that higher values of this parameter enhance the storage capacity of the packed bed. However, it was observed that higher tank aspect ratio values also induce a higher pressure drop and a larger lateral area. Both issues lead to higher energy losses. From the presented analysis, cylindrical tank aspect ratio values around 2 are found as optimal.

Overall, the operation and design guideline presented in this chapter could open new objectives and applications for the packed bed TES technology as it

represents a cost-effective and highly performing storage alternative. In order to demonstrate its suitability and deployment in diverse environments, in the next chapter, a packed bed storage is analysed and adapted for three different industrial applications: the waste heat recovery from the exhaust gases of an EAF, the heat recovery and supply in an adiabatic compressed air energy storage process, and in a concentrated solar power plant equipped with an organic Rankine cycle turbine.

Chapter 6:

Industrial scale-up, customization and deployment

6 Industrial scale-up, customization and deployment

In the previous chapter the behaviour of the proposed packed bed TES system has been investigated in detail through a parametric and sensitivity analysis of the main storage design parameters. In this section, the scale-up, customization and deployment of this type of TES technology in three different real applications is exhaustively analysed. In particular, the waste heat recovery in the steel industry, the compressed air energy storage (CAES) and the concentrated solar power (CSP) generation are the selected industrial applications. Each of these three applications include very different boundaries such as mass flow rates, heat transfer fluid temperatures, fixed times in the charge or the discharge, etc. which require a customized design and optimization of the packed bed TES unit. In this section, a careful performance and suitability analysis is performed on each TES implementation frame, addressing a complete study of the thermal behaviour of TES unit.

6.1. Waste heat recovery in the steel industry

One of the main energy demanding activities of advanced societies is the heavy industrial sector (see section 1.4.2), where a huge amount of input energy is required involving a variety of sources, with mainly fossil origin. The associated temperature level of heavy industrial processes covers a wide range, from low temperatures up to very high ones depending on the particular industrial process (see Table 1.4). Even if the search of a maximum thermal efficiency is a priority of any industrial activity, the relevance of the heat losses becomes of particular importance when the involved temperature increases. In these terms, industrial processes such as glass, cement or iron/steel production suffer a critical thermal loss, which represents a vast opportunity for the implementation of innovative TES solutions adapted to each deployment environment.

Considering its large worldwide activity, the steelmaking industry is selected as a representative scenario for the introduction of a high temperature heat storage solution. In particular, the thermal energy recovery from the off-gasses of the electric arc furnace (EAF) is proposed in this section. Figure 6.1 shows a detailed view of the EAF operation process together with the associated temperatures of the off-gas and storage strategy.

In addition to the large benefits derived from the waste heat recovery itself, an added benefit is also addressed in this work. In particular, the continuous heat supply from a batch process such as the EAF operation is targeted. The uninterrupted heat availability gives an important added value to the TES, since opens new possibilities for the stored heat, covering the requirements of a wide variety of heat demanding applications, such as power generation turbines, or continuous heating processes among others.

In the following, the main implications of the proposed design together with the required boundaries are detailed.

6.1.1. Boundary conditions and TES characteristics

For the proposed continuous heat supply operation from the batch EAF operation, the implementation of a double storage tank solution is necessary. Both packed bed units operate simultaneously and synchronically according to the working times of the EAF. Thus, while one of the tanks is in charge mode storing the heat coming out from the exhaust gases of the EAF, the other tank, previously charged, is in discharge mode. When both tanks attain the charged and discharged state respectively, the operation is inverted, and the discharged tank is used to store the EAF waste heat, whereas the charged tank starts its discharge operation. A schematic view of this configuration is included in Figure 6.1.

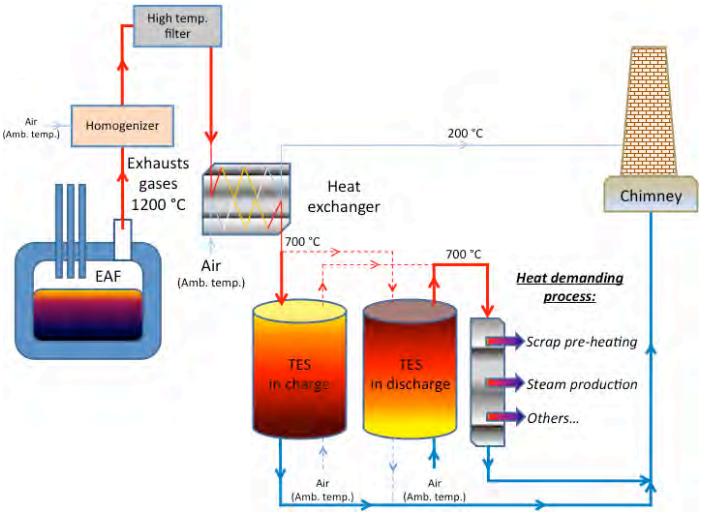

Figure 6.1. Schematic view of the proposed TES system in the EAF process.

It is important to note that this concept corresponds to the pilot plant that is currently being constructed in the framework of the *RESLAG European research project (H2020, Ref. 642067)*. The complete facility, to be coupled in a real steelmaking plant, presents a very sophisticated layout including different components to capture, homogenize the temperature and clean the EAF off-gas, such as a static mixer, a high-temperature dust filter and an off-gas/air heat exchanger, prior to the TES. One of the main reasons motivating the introduction of the mentioned components is the high dust content of the off-gas, which cannot be inserted directly in the packed bed TES tank. As a consequence, a heat exchange to a clean fluid, air, is proposed. This air is used as heat transfer fluid in the storage unit.

6.1.1.1. TES tank geometry and properties

Considering the TES concept demonstration scale addressed in the mentioned *RESLAG project*, the TES unit volume is fixed to 3 m^3 as a representative pre-industrial system. Taking into account the results obtained in the parametric analysis presented in the previous chapter, a cylindrical geometry is selected. On the other hand, the tank aspect ratio and the pebble size are selected by means of a parametric analysis, presented in section 6.1.2.1. The ranges where these two parameters are varied, together with a summary of other TES tank design characteristics are collected in Table 6.1.

Table 6.1. Summary of the main TES unit characteristics.

Storage tank volume (m^3)	3
Storage tank geometry	Cylindrical
Tank aspect ratio (L/d_t)	0.5/1/2/4
TES material	*EAF Slag 1*
TES particle diameter (cm)	0.5/1/2
Void fraction	0.37
Insulation material	*Mullite fibre*
Insulation thickness (cm)	25

As shown in Table 6.1 the selected TES material corresponds to a steel slag (*EAF Slag 1*). This represents a very important added value of the proposed system

as it permits the valorisation of a by-product generated in the same steelmaking process. As a consequence, a double benefit is obtained for the steel production, heat recovery and by-product valorisation, helping to a greener activity in terms of produced waste, required input energy and environmental impact.

6.1.1.2. Operational parameters

The thermal management of the TES unit is directly conditioned by the batch operation of the EAF. In this regard, an approximated scheme of the real EAF operation is presented in Figure 6.2. It can be noted that the complete casting lasts about 60 minutes, in which the EAF is active around 45 min expelling gases above 1200 °C. Considering the pilot plant design presented in Figure 6.1, after the off-gas cleaning and exchanging processes introduced, the expected temperature of the air used for the charge operation of the TES tank is around 700 °C. After these 45 min, the EAF is stopped for 15 min, interrupting the off-gas supply. This time corresponds to the aperture of the furnace lid for the steel pouring and scrap charge. Under regular operational conditions, the daily steelwork operation is 24 hours hence, 24 castings are assumed each day.

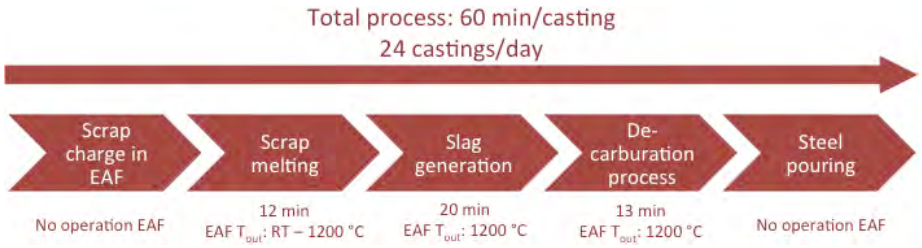

Figure 6.2. Stages and times of the electric arc furnace operation.

As a consequence, for the operation of the TES unit modelled in this section, the charge is assumed to take 45 min, during the EAF operation, followed by 15 min of idle conditions (no fluid circulation through the packed bed). On the other hand, the discharge operation must take 60 min (whole casting process) to ensure the targeted continuous heat supply. These operational times imply the adjustment of the air mass flow rate inserted in the charge/discharge operations in order to satisfy a possible stopping criterion. It must be highlighted that this flow rate value determination is a complex issue as it depends on the particular thermal behaviour of the designed TES tank as presented in chapter 5.

In order to obtain preliminary fluid flow rate values, the ideal condition in which no thermal stratification occurs in the packed bed is considered as an initial approximated frame. This initial estimation of the fluid flow rate indicates very large values, compared to the optimum ones for this system obtained in the parametric analysis performed in the previous chapter. Considering that these values are required by the EAF waste heat recovery availability during its operation, the mentioned parametric analysis shows the successful path to palliate the considerable deviation from the optimum flow rate values. Accordingly, values for the tank aspect ratio of 1 and solid particle diameters of 1 cm are pre-selected. Starting from these preliminary values, in order to obtain a better adjustment of the fluid flow rates, numerical simulations are performed. As a result, the approximated thermocline width is calculated, showing a length of around 30% of the storage tank. In a second iteration considering these results, precise fluid flow rate values are calculated considering the obtained thermal stratification behaviour. The results of these calculations are included in Table 6.2.

Regarding the operational method selected for the TES, the synchronic behaviour of the storage with the EAF results of capital importance. In this case, the reproducibility and predictability of the TES unit becomes a critical issue in order to maintain the targeted continuous heat supply. As a consequence, aiming at obtaining a stationary behaviour from the first charge/discharge cycle, according to the operational analysis performed in section 5.2, a complete TES charge strategy is selected. As established in section 5.2.1, the associated heat disposal during the charge reduces considerably the thermal efficiency of the TES unit. However, this drawback can be considered as a minor issue since the availability of waste heat from the EAF is much larger than the storage capacity of the demonstration pilot of 3 m^3, representing a pre-industrial scale concept. Of course, the operation method should be discussed in detail when the up scaling of the proposed TES is addressed.

For the discharge operation, a specific procedure is proposed. Considering the continuous heat supply objective, one of the most common deployments of the stored energy is the power production. This application is very restrictive with the TES discharge conditions, since the output fluid must fulfil strict temperature and

flow criteria. One of the most important ones is the supply of a very stable and low temperature fluctuating fluid for the turbine operation. Consequently, a 40 °C of output fluid temperature tolerance is selected.

Aiming at providing more generality and scalability to the basic design obtained in this section, in addition to the straight charge/discharge of the TES tank in a single casting process, multiple casting processes are also investigated. As an example, the cases in which the TES unit is charged/discharged during two and three consecutive steel castings are also analysed. The obtained times for each strategy, together with the associated fluid flow rates are shown in Table 6.2.

Table 6.2. Number of castings and associated operational times and fluid flow rates.

Number of castings	Process	Time (min)	Mass flow ($kg \cdot s^{-1}$)
1	charge	45 + 15 idle	2.88
	discharge	60	1.12
2	charge	45 + 15 idle + 45 + 15 idle	1.40
	discharge	120	0.58
3	charge	45 + 15 idle + 45 + 15 idle + 45 + 15 idle	0.94
	discharge	180	0.39

Finally, a summary of the parameters fixed for the system proposed for the EAF steelmaking waste heat recovery is collected in Table 6.3. It has to be noted that, given the mentioned operational parameters and TES tank size, the maximum energy that could be stored in the proposed prototype, if all the TES material varies its temperature from 20 to 700 °C, is 1.05 MWh_{th}.

Table 6.3. Main operational parameters of the TES unit.

Heat transfer fluid	Air
Mass flow rate ($kg \cdot s^{-1}$)	Variable
Hot fluid temperature (°C)	700
Cold fluid temperature (°C)	20
Charge stopping criterion	Complete charge
Discharge stopping criterion	T_{hot} – 40 °C

6.1.2. Results

In order to design an optimized TES unit according to the aforementioned operational conditions, a parametric analysis considering the most relevant variables affecting to the thermal performance of the storage (see chapter 5) is carried out. As a result coming out from this analysis, an optimized TES tank is selected for each of the charge/discharge strategies, one, two and three castings.

6.1.2.1. Pressure drop and parametric analysis

Taking as a reference the fluid flow rate values listed in Table 6.2, the system pressure drop is calculated by eq. (4.5) for the different TES tank configurations considered in the parametric study (see Table 6.1). The obtained pressure drop values are collected in Figure 6.3 for the systems charged/discharged in one (Figure 6.3a), two (Figure 6.3b) or three (Figure 6.3c) castings. In each figure, continuous lines correspond to the pressure drop in the charge operation while, dashed lines to the ones in the discharge.

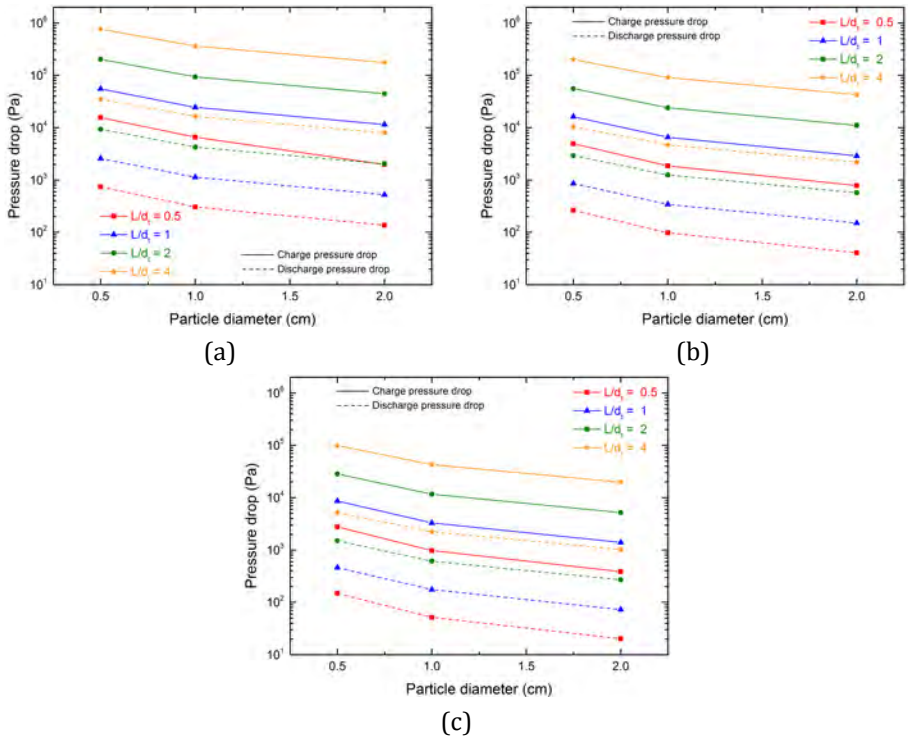

Figure 6.3. Pressure drop in the proposed tanks, when operated in: a) 1 casting; b) 2 castings and c) 3 castings.

As previously obtained in section 5.3.2.2, the system pressure drop increases substantially when the particle diameter is reduced or the tank aspect ratio increased. The obtained trend is similar for all the analysed cases. However, the influence of each parameter is considerably different. As an example, an increment of the tank aspect ratio in eight times (from 0.5 to 4) implies an increment in the pressure drop of around 50 times. Nevertheless, for the particle diameter, an increment of 4 times (from 0.5 to 2 cm) leads to a similar increment of the pressure drop. Regarding the influence of the number of steel castings to charge/discharge the TES system, a direct impact on the pressure drop is observed. In these terms, the use of three castings involves an almost proportional reduction of the mass flow rate, around 3 times, what results in a 8 times lower pressure drop.

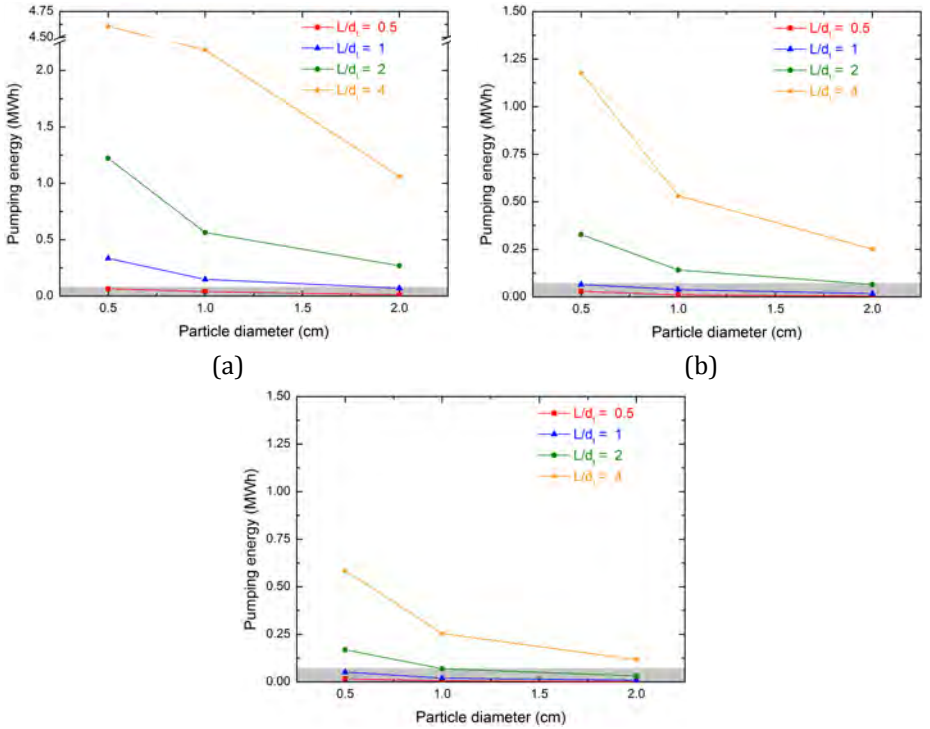

Figure 6.4. Pumping energy in the proposed tanks when operated in: a) one; b) two and c) three castings.

In order to consider the proposed TES system feasible from an operational point of view, a maximum assumable pressure drop limit is fixed. This criterion is

based on a maximum pumping energy around 5% of the maximum thermal energy capacity of the TES system. This operational requirement derives on a very restrictive condition to be satisfied by the TES tank design in order to reach a satisfactory overall energetic efficiency. In these terms, the total mechanical energy required in the pumping is calculated from eq. (4.40) and (4.41). The obtained pumping energy values (charge + discharge) are collected in Figure 6.4 where, from a) to c), the required pumping energy in one, two or three castings strategy are presented respectively. Additionally, the region in which the mentioned pumping energy condition is fulfilled is also shown, grey shadow in the three plots included in Figure 6.4.

Attending to the obtained results, and to the design guideline performed in chapter 5, the following considerations can be made for the three investigated TES charge/discharge strategies:

1. For the one casting strategy, only a tank aspect ratio of 0.5 might fulfil the established pumping energy requirement. Considering that this condition is satisfied for the three investigated particle diameters, a tank with an aspect ratio of 0.5 and a particle diameter of 0.5 cm is selected for further analysis.
2. For the two casting strategy, tank aspect ratios of 0.5 and 1 satisfy the mentioned pressure constrain for the three analysed particle diameters. Considering the results observed in section 5.3, which established that larger aspect ratio values and smaller particle diameters promote better thermal performance, a tank aspect ratio of 1 and a particle diameter of 0.5 are selected.
3. For the three casting strategy, the obtained results lead to a similar parametric selection than in the two casting strategy: a tank aspect ratio of 1 and a particle diameter of 0.5.

6.1.2.2. Refinement of the fluid flow rate values

Considering the three selected preferential designs, a refinement of the fluid flow is performed to obtain a precise coupling and synchronization of the TES unit with the EAF. As established in section 6.1.1.2, the determination of this fluid flow rate value satisfying the synchronic performance for a continuous heat supply is

not straightforward. The particular design criteria in terms of tank aspect ratio, particle diameter, operation temperature range and others present a noticeable effect on the thermal stratification behaviour of the TES unit. As a consequence, the definition of this magnitude requires detailed numerical calculations in order to obtain the satisfactory flow rate values.

The simulations performed for the particular selected cases, detailed in the previous section, have permitted to identify the accurate fluid flow rate values, appropriate for the successful synchronic behaviour. The obtained results are shown in Table 6.2 for the charge and discharge operations.

Table 6.4. Fluid flow rates associated to the selected tank configurations.

Number of castings	Tank configuration		Process	Refined mass flow rate (kg·s^{-1})
	L/d_t	d_p (cm)		
1	0.5	0.5	charge	2.65
			discharge	1.25
2	1	0.5	charge	1.29
			discharge	0.65
3	1	0.5	charge	0.90
			discharge	0.43

It can be observed that the obtained air flow rates are slightly lower than the ones considered in the parametric analysis (section 6.1.2.1), which indicates that the pressure drop induced in the packed bed would also be lower, improving the overall efficiency of the system.

6.1.2.3. Idle period performance

As mentioned in section 6.1.1, the EAF process is a batch operation, which is active for 45 minutes, and is in stand-by for 15 minutes. As a consequence, in addition to the charge/discharge TES behaviour explained in the previous sections, the analysis of the 15 minutes stand-by period is required. This period implies the unavailability of waste heat from the EAF, and as a consequence, no fluid flow can be circulated through the packed bed TES.

This stand-by process, so-called idle period, needs to be independently investigated since potential undesired thermal phenomena could occur in terms of

thermal stratification effects or the associated losses on the storage capacity. In this section, the possible thermal evolution under idle condition is studied.

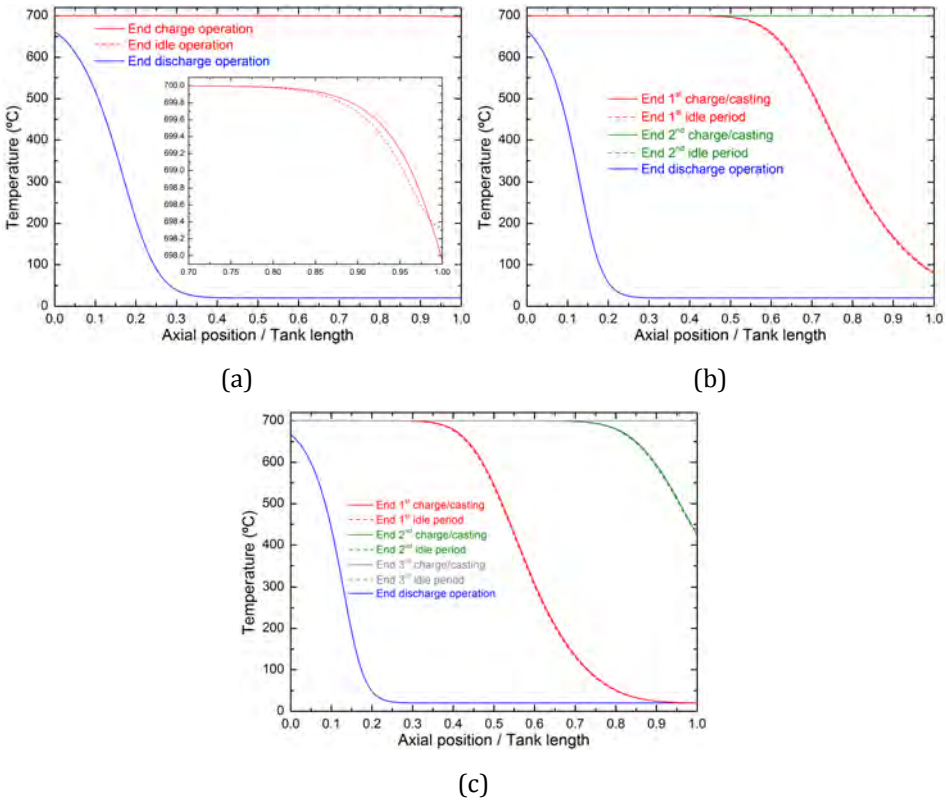

Figure 6.5. Axial temperature profiles in the idle periods on: a) one; b) two and c) three castings strategy.

In this regard, in Figure 6.5 the temperature distribution in the axial coordinate of the TES tank at the beginning and at the end of all the idle periods is presented for the three investigated charge/discharge strategies (1, 2 and 3 steel castings). In these terms, in Figure 6.5a it is presented the system charged in one casting and hence, only one idle period is included, the one after the 45 min of charge and before starting the discharge. In a similar way, Figure 6.5b and c include the axial temperature profiles of the systems operated in two and three castings respectively. In Figure 6.5b, two idle periods are shown, between the first and second casting operation charges, and between the second charge and before the discharge, whereas Figure 6.5c shows the corresponding three idle periods. In all the cases, the continuous lines correspond to the thermocline status once the

charge run is finished, and the dashed line to the profile just before the begging of the subsequent charge or discharge operation.

The obtained results clearly show that the analysed idle periods of 15 min do not have a relevant influence on the thermal stratification of the TES. In all cases the spreading of the thermocline region in the axial direction is below 1% and the local temperature difference below 2 °C. It has to be pointed out that, the idle periods modelled in this section are quite short, and that longer ones could have stronger effects in the system performance.

6.1.2.4. Outlet temperature in the charge and discharge operations

The air output temperature during the charge process for the three investigated strategies is represented in Figure 6.6. Additionally, dashed circles are included in each curve corresponding to the times in which an idle period occurs.

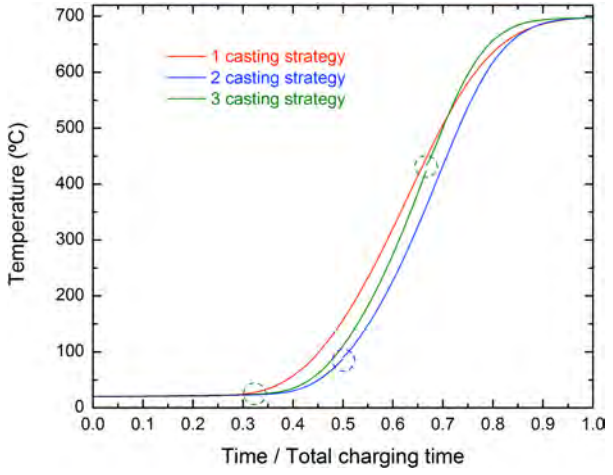

Figure 6.6. Output air temperature during the charge operation.

The obtained results confirm that the idle periods do not have relevant impact on the average output fluid temperature. Only between the second and third charge runs, in the three castings strategy, a slight difference of 10 °C is obtained. In addition, comparing the obtained temperatures for the three charge/discharge strategies, the highest temperature is obtained for the one casting strategy, while the lowest one for the two casting strategy. It has to be noted that high temperatures in the outlet of the TES tank during the charge operation promote a large dispose of energy, and hence, low thermal cyclic efficiency.

On the other hand, the output fluid temperature during the discharge operation is presented in Figure 6.7. A similar performance between the two and three casting strategies is observed. Both of them are slightly better than the associated temperature to the one casting strategy. From this figure, a heat supply at constant temperature (700 °C) during the 80-85% of the TES discharge time can be also observed in all the modelled scenarios. Additionally, the higher temperatures obtained for the two and three castings strategies reveal that higher energies are also extracted from the TES tank within the selected temperature tolerance criterion.

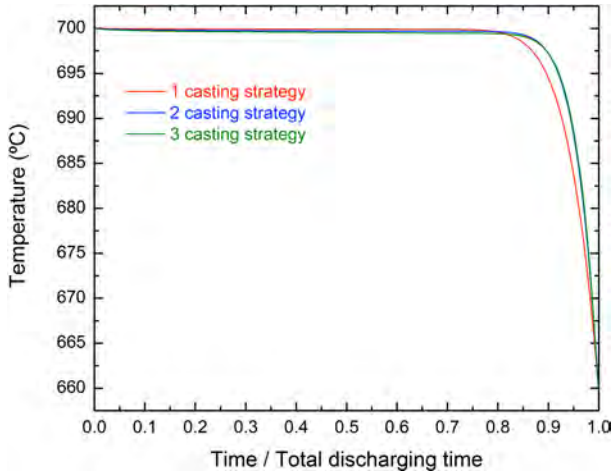

Figure 6.7. Output air temperature during the discharge operation.

6.1.2.5. Energetic analysis of the selected cases

The detailed energetic analysis of the three considered studied systems is shown in Table 6.5. From the obtained results, one of the already mentioned shortcomings of the proposed operation method can be observed, the large amount of energy disposed in the charge process. As a palliative method, the use of this energy for another heat demanding application is recommended. For example, in the steelmaking process numerous heat-demanding processes are present such as the pre-heating of the scrap before being introduced in the EAF.

Comparing the obtained charged energies, the values introduced in the storage are almost similar in all the cases. Regarding the energy released from the tank in the discharge process, when operating the TES system in higher number of

castings, slightly higher released energies are obtained. On the other hand, attending to how the TES material is exploited, considering a maximum capacity of 1.05 MWh_{th}, efficiencies of around 85% are obtained for the three-modelled charge/discharge strategies.

Table 6.5. Energy and efficiency balances.

Number of castings	Energy (kWh_{th})			Efficiency (%)
	Charged	Discharged	Pumping	
1	1419	893	46	62.9
2	1382	928	29	67.1
3	1445	930	17	64.4

Finally, attending to the system overall cycle efficiency, values around 65% are obtained. These values show the great recovery potential of the investigated TES system after an appropriate optimization and parametric analysis. Even if the obtained values could be increased by the implementation of a different charge mode, the presented analysis shows the potential of the packed bed TES solution in the steelmaking waste heat recovery environment.

6.2. Integration in a compressed air energy storage plant

As described in section 1.4.3, compressed air energy storage (CAES) is a valid alternative to grid storage. The underlying fundamental mechanism, which governs this storage method, consists in the use of energy excess periods, i.e. electric energy from the grid, to compress air. Then, the compressed air is stored in high-pressure vessels or natural caverns. When the demand of electric energy increases, the compressed air is expanded in a turbine to generate, again, electricity.

In the CAES process a large amount of heat is involved in the compression/expansion cycle. In these terms, the compression stage produces a large amount of heat, which is usually released to the ambient. On the other hand, the expansion stage requires a noticeable heat supply in order to promote an effective expansion and useful work production for the turbine operation. This

thermal energy is usually supplied by external fossil fuels. A promising alternative to improve CAES cycle efficiency, avoiding the disposal of large amounts of heat and the consumption of fossil fuels, is represented by adiabatic-CAES (henceforth A-CAES). This solution is based on the direct storage of the heat produced on the compression stage, and its later use on the air expansion.

In this section, the integration of a packed bed TES system in a regular CAES plant is analysed with the objective of promoting an A-CAES scheme. In this regard, with the goal of maximizing the round efficiency, a detailed study of a steel slag (*EAF Slag 1)* based packed bed TES unit is presented. It has to be noted that the particular boundaries of the CAES process in terms of operational temperatures, pressures and storage capacity are considered.

6.2.1. CAES plant description and TES characteristics

6.2.1.1. CAES plant operational parameters

The *Huntorf* CAES plant is used as reference in this section. This plant is designed for a peak power generation of 2 hours at full load of the turbines while, the compressors are dimensioned to charge the air reservoirs in 8 hours. Taking this into account, the selected operation mode for the packed bed is the fixed time one, according to section 5.2.2. The reservoirs, compressors and turbines are designed to operate at a minimum and a maximum pressure of 22 and 76 bars respectively. However, the maximum performance of the plant is reached when it is operated between 46 and 66 bars. On the other hand, the compressors are able of supplying 108 $kg \cdot s^{-1}$ to the reservoirs (charge operation) while, during discharge, the nominal mass flow rate of the turbines is 417 $kg \cdot s^{-1}$. In order to maximize the storage capacity of the reservoirs, and to avoid environmental issues, compressed air is stored at a maximum temperature of 50 °C. According to the particular compressors characteristics of the plant, the temperature of the released air to the reservoirs is around 500 °C. The production of this high-temperature fluid opens a very attractive heat recovery opportunity, which is currently not addressed in the plant. The technology implemented in the *Huntorf* CAES plant includes a direct cooling stage through an intercooler leading to a noticeable heat waste. The recovery of this amount of thermal energy is proposed

in this section. As a summary, in Table 6.6 the main operational parameters of the *Huntorf* plant considered in this work are collected.

Table 6.6. Operational parameters for the TES unit.

	Units	Charge		Discharge	
		Inlet	Outlet	Inlet	Outlet
Temperature	°C	500	-	20	-
Pressure	bar	From 46 to 66		From 46 to 66	
Mass flow rate	$kg \cdot s^{-1}$	108		417	
Time	h	8		2	

6.2.1.2. Proposed TES system configuration

The proposed TES solution is a single-tank packed bed configuration in which *EAF Slag 1* is exploited as heat storage material. In particular, a particle diameter of 1 cm is considered. As heat transfer fluid, the compressed air coming from the compressors (charge operation) or from the reservoir (discharge operation) is implemented.

A preliminary calculation of the heat storage tank operational and design parameters adapted to the selected reference plant heat production/demand requirements (Table 6.6) is carried out. As a result, the heat storage capacity of the TES tank is fixed to 450 MWh_{th} in order to couple the system performance to a "one-day" operation strategy, namely, to eight charging hours. A secure design up scaling factor of 1.5 is introduced in order to account any potential performance losses, connected to thermal losses, temperature stratification losses and other undesired contributions, in principle, difficult to consider in a conceptual design. Overall, introducing the influence of the pebble packing, a total storage tank volume of around 2750 m^3 is obtained.

On the TES tank geometric selection, according to the criteria studied in section 5.3, the large size of the obtained storage tank must be explicitly considered. The potential mechanical implications of large beds can derive on the accumulation of noticeable thermal stresses or ratcheting phenomena. As a consequence, a conical geometry (Figure 6.8) is selected as a successful solution able to minimize the impact of these mechanical issues. The main benefits of this

design are associated to the wall inclination of this geometry, which favours the movement of the bed particles inside the tank. This effect promotes a better structural force distribution, decreasing both, particle-particle and particle-tank thermo-mechanical stresses.

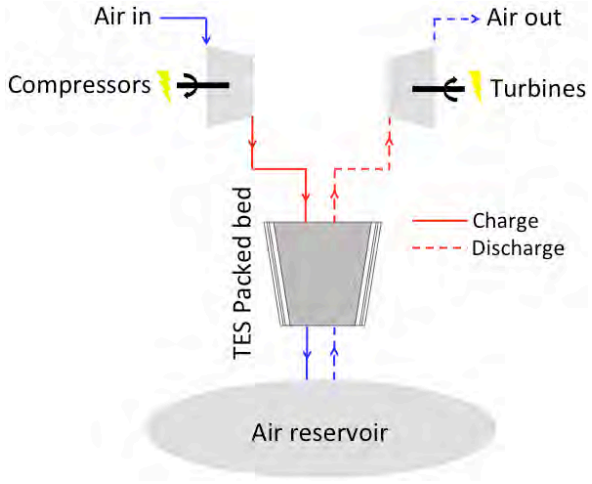

Figure 6.8. Scheme of the CAES plant with a packed bed TES tank integrated.

Considering the large volume of the proposed TES solution, the division of the total storage volume in different tanks operating in parallel is also proposed. In this regards, as an example, three different arrangements are suggested, a single (1-tank), double (2-tanks) and quadruple (4-tanks) storage tank solutions. Table 6.7 collects the particular dimensions together with the fluid flow rates associated to each tank configuration.

Table 6.7. Tank dimensions and mass flow rate.

System	Volume (m^3)	d_1 (m)	d_2 (m)	L (m)	$\dot{m}_c$ ($kg \cdot s^{-1}$)	$\dot{m}_d$ ($kg \cdot s^{-1}$)
1-tank	2759	16.5	9.0	21.0	108	417
2-tanks	1358	13.0	7.2	16.5	54	208.5
4-tanks	675	10.3	5.75	13	27	104.25

In the modelling of the systems, the TES tanks constructive criteria are also considered in the performed calculations. In these regards, a low density concrete with a wall thickness of 0.8 m is assumed. To minimize thermal losses, a "sandwich" of two insulating materials is exploited. The first layer of 0.24 m

thickness corresponds to a commercial micro-porous insulating material (*Microtherm*®) and, the external layer, is a 0.4 m thickness of *Foamglas*®, a rigid and lightweight insulation material for temperatures up to 480 °C. The thermo-physical properties of these materials are reported in Annex 1.

6.2.2. Results

6.2.2.1. Reference case: single packed bed storage tank

In this section the thermal performance of a 1-tank solution in a continuous charge/discharge cyclic operation (a total of 20) is discussed. In Figure 6.9 the output fluid temperature during the mentioned charge (Figure 6.9a) and discharge (Figure 6.9b) runs is presented. The former clearly shows that in the first charge, the output fluid temperature remains constant at 20 °C during the 8 hours. However, from the second cycle, this temperature starts increasing gradually up to an almost steady reproducible behaviour after 16-17 cycles. Under these conditions, the output air temperature starts to increase after 6 hours reaching 180 °C at the end of the process. As aforementioned, one of the operational requirements of the CAES plant is that the compressed air has to be stored at temperatures not higher than 50 °C. Consequently, the obtained results show the necessity of introducing an extra component to cool down the air released from the packed bed prior to its storage in the reservoir.

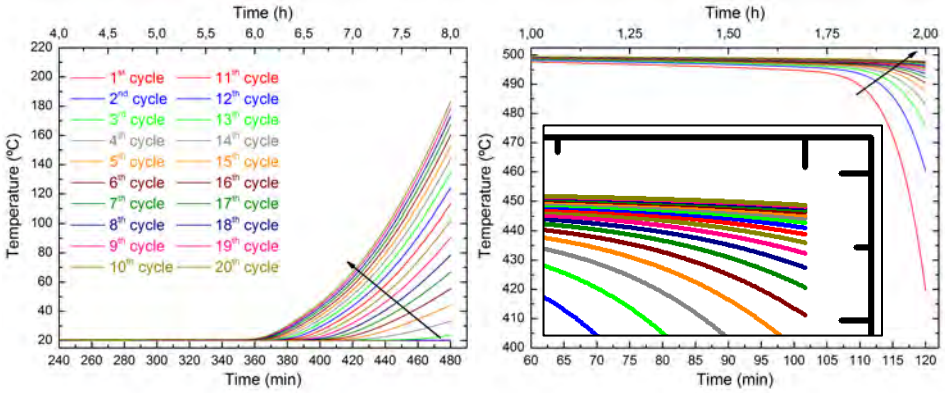

(a) (b)

Figure 6.9. Air output temperature for the 1-tank system: a) during the charge process and b) during the discharge process.

Regarding the behaviour in the discharge, Figure 6.9b shows that during the first run, the temperature of the released fluid drops down to 420 °C. This result reveals that the obtained fluid temperature does not fulfil the operational requirements of the power block (fluid temperature above 480 °C) during the complete discharge time (2 hours). However, this performance is gradually improved with the cycling leading to a successful operation after three cycles, in which the fluid output temperature satisfies these power block requirements.

The physical cycling behaviour observed in the proposed TES system is related to two different phenomena, which are characteristic of packed bed arrangements. On one hand, the thermal performance is essentially driven by the natural temperature stratification due to the temperature difference between the hot and cold fluid regions. On the other hand, it is associated to the different initial conditions obtained for each charge/discharge run. The non-reproducibility occurs due to the different amount of energy left inside the packed bed storage unit. As a result of these phenomena, the thermal stratification (thermocline) region is gradually moved from the top to the bottom part of the storage tank leading to a partial extraction of the temperature gradient from the TES. In any case, after an enough number of charge/discharge cycles, the widening of the thermocline region during a single charge/discharge cycle balances the partial extraction of the thermocline zone. When this condition is satisfied, a reproducible steady behaviour of the TES tank is attained.

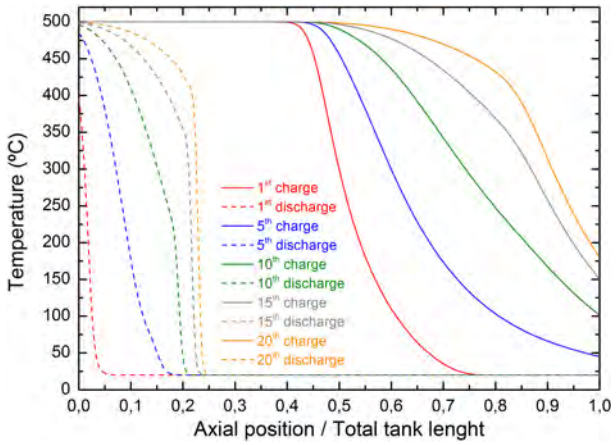

Figure 6.10. Axial temperature profile at the end of the charge and discharge for the 1-tank system.

Figure 6.10 shows the axial temperature profile once the 1st, 5th, 10th, 15th and 20th charge (continuous lines) and discharge (dashed lines) runs are completed. In this figure, in the x-axis, values of 0 and 1 correspond to the upper and lower parts of the tank respectively. The continuous lines depict that the temperature stratification region moves to the bottom part of the tank with the cycling. In the discharge process a similar behaviour is attained.

From Figure 6.10 the shape of the thermocline region can also be determined. Comparing the temperature profiles of the same cycle once the system is charged and discharged, a noticeably different slope of the temperature gradient is observed. This slope is much higher in the discharge profiles than in the charge ones, which indicates a stepper thermocline, hence, a better thermal stratification on the discharge than on the charge. These differences between the charge and discharge runs are directly related to the conical geometry of the investigated TES tank, non-symmetric, and to the difference between the air flow rate in the charge and discharge.

6.2.2.2. Multi-tank TES configuration

In this section, the splitting of the 1-tank TES solution presented in the previous section is introduced. The main motivation of the implementation of a multi-tank TES comes from the large volume of the obtained 1-tank. In this section, the already presented 1-tank TES system is compared to a multi-tank TES solution. In order to obtain a fair comparative frame, the total storage capacity is maintained. As an example, in this study the alternative of using 2 or 4 tanks is investigated to determine the viability and the technical impact of the proposed splitting. In all the presented multi-tank cases, the TES tanks are operated in parallel (see Figure 6.11). Table 6.7 compiles the associated TES tank dimensions.

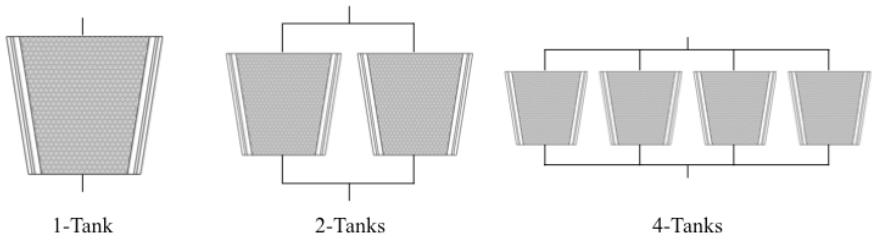

Figure 6.11. Layout of the investigated single and multi-tank TES solutions.

In Figure 6.12 the output fluid temperature during the charge (Figure 6.12a) and discharge (Figure 6.12b) operations for the three analysed systems (1-tank, 2-tanks and 4-tanks) is presented. For the sake of clarity, only the output fluid temperature as a function of time corresponding to the 1st, 5th, 10th, 15th and 20th cycle are included. In both figures, the dashed-dotted lines correspond to the 1-tank system, the dashed curves to the 2-tanks system and the continuous lines to the 4-tanks system.

As it can be observed in both figures, overall, the performance of the 2-tanks and 4-tanks configurations are very similar to the 1-tank system. Although the output fluid temperature is maintained below 50 °C in the first five charge processes, a gradual increase is observed with further cycling. A maximum temperature of 200 °C is obtained after the reproducible stationary state is reached. On the other hand, during the discharge runs, it is observed that in the first cycles the output air temperature drops down to 410 °C, and only after almost five cycles the fluid matches the requirements of the power block during the complete discharge time.

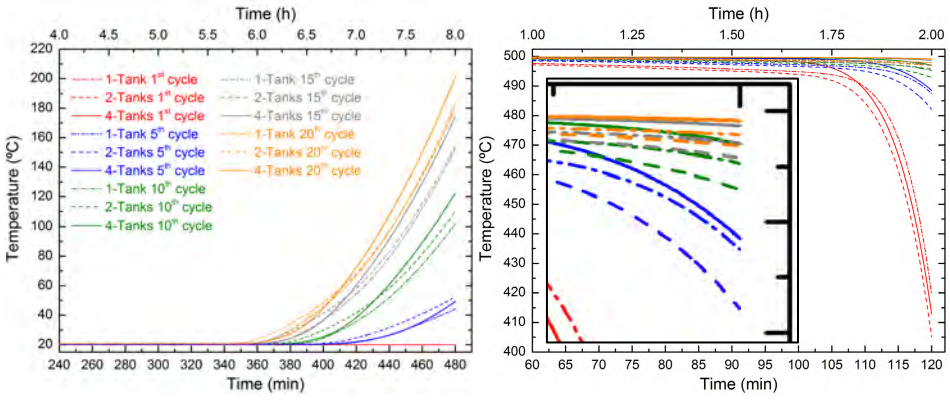

(a) (b)

Figure 6.12. Output air temperature for the 1-tank, 2-tanks and 4-tanks configurations: a) charge and b) discharge.

In addition to the output air temperature, in Figure 6.13 the energy (Figure 6.13a) and exergy (Figure 6.13b) efficiencies for the 20 performed cycles over the three analysed systems are presented. The obtained efficiency values increase gradually with the cycling up to the stationary performance, where a maximum efficiency of around 96.5% is reached. The lower values obtained in the first cycles

are explained by the energy required for the thermocline formation and for the heating of the tank materials, i.e. concrete and insulation.

The small difference observed between the absolute values of the energy and exergy efficiencies is indicative of the low exergy destruction in the operation of the tank. However, this small difference is also related to the fact that in the modelled TES systems, the energy balance is exclusively limited to the energy introduced/stored in the TES tanks. This excludes any other energy consuming system needed for further implementation of the proposed technology, such as fluid distributors, piping or any other additional system components, not addressed in this work.

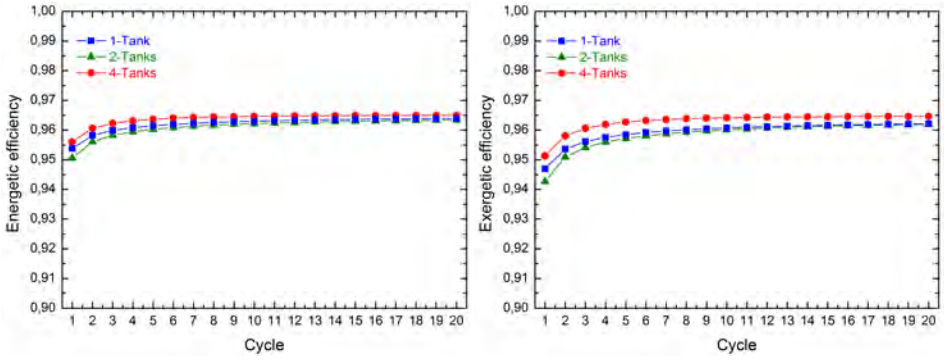

Figure 6.13. Cycle efficiency for the 1-tank, 2-tanks and 4-tanks systems: a) energy and b) exergy.

Even if the 4-tanks configuration shows a slightly better behaviour in comparison to the 1-tank and 2-tanks arrangements (see Figure 6.12 and Figure 6.13), the obtained differences are very small to discard any of the proposed systems only due to its energetic or thermal performance. Therefore, construction or mechanical implications should be determinant for a successful design selection. Taking this into account, the simplification of the storage design could be one of the driving parameters in order to achieve a satisfactory implementation of the proposed technology. In these terms, the reduction of the tank size could present important benefits on the minimization of usual construction/mechanical problems. Taking this into account, the 4-tanks configuration is selected for further analysis.

6.2.2.3. Effect of an initial pre-charge operation

Once the implications of the storage tank volume have been analysed in terms of the overall thermal efficiency and complementary engineering criteria, the enhancement of the thermal behaviour during the transient stage of the TES is addressed in this section. With this purpose, the quality of the released heat during the discharge operation of the 4-tanks configuration is analysed in detail under continuous thermal cycling.

A possible solution to boost the thermal performance from the first TES operation cycle is to perform a preliminary partial charge of the system before the regular charge of 8 hours. This procedure is referred as pre-charge in this work. During the pre-charge operation of the system, the output fluid is released to the atmosphere instead of being stored into the reservoir. The reason for this operation is that the subsequent regular charge of the system must be below the maximum pressure of the reservoir (66 bar). As an example, in this section, the impact of a pre-charge operation of 6 hours using pressurized air at 46 bars and 500 °C is analysed in detail.

In Figure 6.14 the output air temperature corresponding to the successive charge operations of the complete cycling are presented for both, pre-charged (Figure 6.14a) and non pre-charged (Figure 6.14b) systems. Attending to Figure 6.14a it can be observed that during the pre-charge operation no high-temperature fluid is extracted from the TES unit. However, during the first charge of the system, the air output temperature starts increasing after three hours, reaching 500 °C at the end of the process. This temperature attained at the end of the first charge indicates that all the TES material is at the maximum temperature (500 °C) before the first discharge starts. On the other hand, attending to the evolution of this parameter with the consecutive thermal cycles, a gradual decrease of the output fluid temperature up to a reproducible value around 215 °C after 8-9 cycles is observed.

Comparing this behaviour with the one of the non pre-charged system (Figure 6.14b), an opposite trend is observed. In this case, the output air temperature during the first charge does not experience a noticeable increment. With the continuous thermal cycling this behaviour shows a non-desirable trend with

increasing output temperatures during the transient operation of the storage. In the subsequent reproducible performance (after 17-18 cycles), the fluid temperature increases up to 215 °C. However, once the stationary condition is satisfied both, the pre-charged and the non pre-charged systems, show similar output fluid temperature behaviour as a function of the charge time.

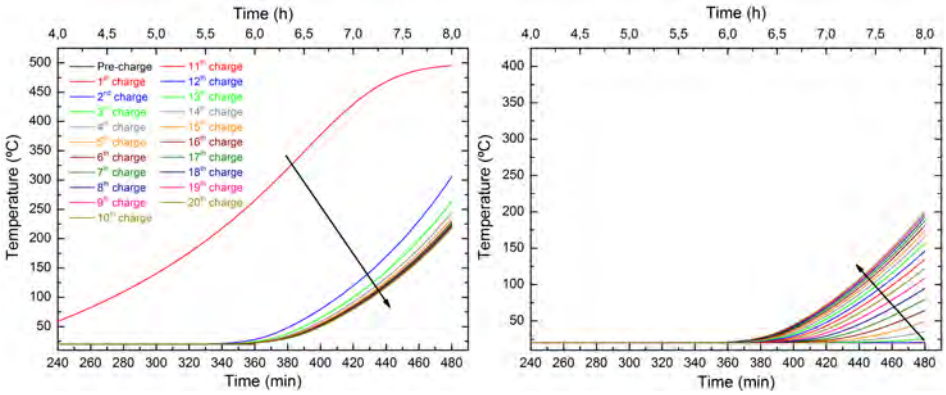

(a) (b)

Figure 6.14. Output air temperature during the charge process in the: a) pre-charged and b) non pre-charged systems.

Figure 6.15 contains the output fluid temperature as a function of time during the TES discharge operation. Both, the pre-charged (Figure 6.15a) and the non pre-charged (Figure 6.15b) systems are shown. Attending to Figure 6.15a, almost a flat temperature behaviour is obtained during all the modelled runs. The noticed slight temperature decrease from the beginning of the discharge is caused by the thermal losses through the lateral wall, and it is not related to the thermocline region extraction from the storage. It can be noted that, during the two discharge hours, the output fluid temperature does not drop more than 2 °C, accomplishing the requirements of the power block.

On the other hand, the non pre-charged system shows a different thermal behaviour (Figure 6.15b). In this case, during the first discharge run, the output air temperature decreases up to 90 °C at the end of the process. This behaviour improves with cycling, reaching a stationary state after 9-10 cycles. In this condition, the maximum temperature decrease is also around 2 °C.

Comparing the released fluid temperature in both analysed operational approaches, it can be concluded that performing a pre-charge operation has a

strong impact on the quality of the released heat during the first cycles. A very important consequence of the pre-charge is the possibility of a direct use of the stored energy in the power block (temperature higher than 480 °C) from the beginning of the TES thermal cycling. Without a pre-charge, the released air only accomplish the power block requirements after four cycles.

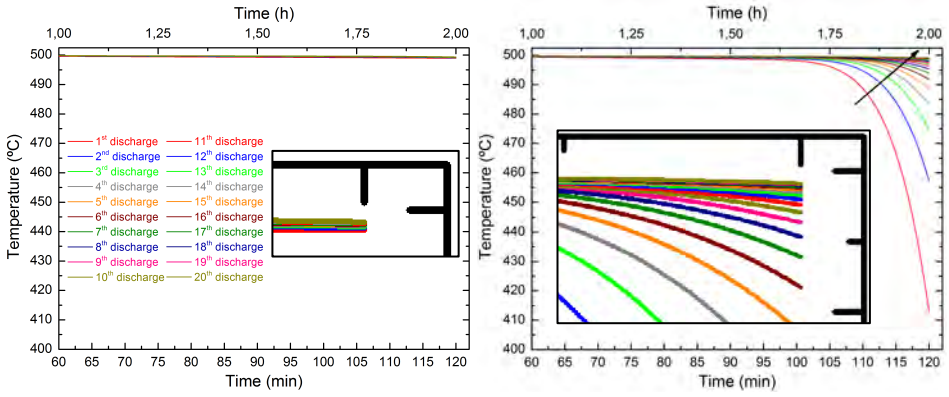

(a) (b)

Figure 6.15. Output air temperature during the discharge process in the: a) pre-charged and b) non pre-charge systems.

In addition to the air output temperature variation, the impact of the pre-charge on the energetic and exergetic efficiencies is determined. With this objective, Figure 6.16 shows the obtained efficiency values with and without the initial pre-charge. It has to be pointed out that for this quantification, the energy (Figure 6.16a) and exergy (Figure 6.16b) associated to the pre-charge process has not been considered. The evaluation represents exclusively the efficiency of the cyclic charge/discharge behaviour. As a consequence, the impact of the pre-charge on the subsequent cycling performance is monitored. It must also be noted that even if the absolute energy involved on the pre-charge operation could be noticeable, this value remains negligible compared to the total energy introduced/released to/from the TES in the subsequent operation. This is sustained by the fact that the enhanced thermal performance of the storage, once pre-charged, is maintained in further cycling, which avoids the need of extra pre-charge operations.

As shown in Figure 6.16, this system leads to a reproducible efficiency after 2-3 cycles. Under stationary conditions, a maximum efficiency of 96.5% is obtained.

On the contrary, in the non pre-charged tank, the transient efficiency shows a lower value than the pre-charged case. This trend is asymptotically extended with the cycling up to the stationary performance. In these conditions, a similar maximum efficiency value of around 96.5% is obtained in both cases.

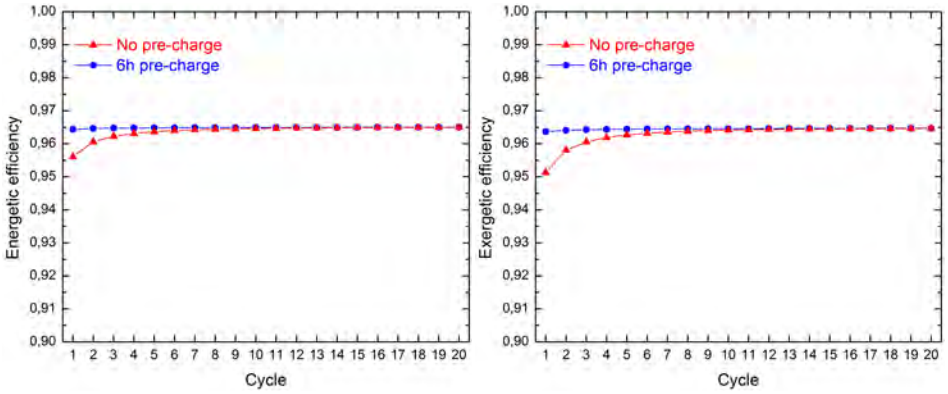

(a) (b)

Figure 6.16. Cycle efficiency for the systems with and without pre-charge: a) energy and b) exergy.

Attending to these results, it can be concluded that performing a pre-charge operation during the start-up operation of the TES is highly recommended. In particular, this operation presents two clear benefits: (i) the output air temperature obtained during the complete discharge fits the requirements of the power block from the first cycle; (ii) the transient behaviour of the TES tank is noticeably shortened.

6.2.2.4. Effect of daily cycling in the TES performance

So far, in this case study, in order to obtain a clear understanding of the proposed storage system, a continuous complete charge/discharge operation has been assumed according to Table 6.6. However, in a real CAES plant, the operation conditions are often far from this ideal behaviour. With the aim of performing a realistic analysis, in this section the charge of the plant is programmed during the hours with lower electricity price (valley hours). The discharge is matched to the main energy consumption peaks (morning, mid-day and evening), corresponding also to the higher electricity price periods. This particular exploitation strategy is depicted in Figure 6.17. Starting from a complete charged initial condition at the

beginning of the day (6:00), two partial charge (7:30 – 12:30 and 13:50 – 20:00) and discharge (6:00 – 7:30 and 12:30 – 13:50) operations are programmed. Then, the stored energy is released in a complete discharge run (20:00 – 22:00), followed by a complete charge process from (22:00) until next morning (6:00). It must be noted that exception made for the charge/discharge duration, the rest of the operational parameters are unchanged (see Table 6.6).

In order to exploit the benefits of the pre-charge of the TES system, found in the previous section, the same conditions are followed in this analysis. With this objective, as an example, a similar 6 hours pre-charge operation is assumed prior to the first TES regular charge (22.00 – 6.00).

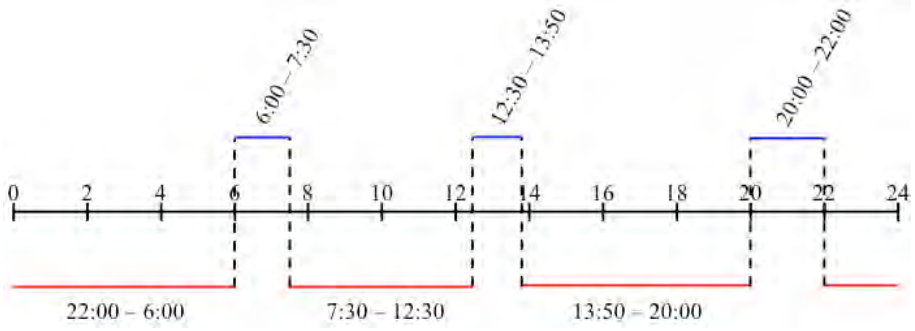

Figure 6.17. Scheme for a daily TES operational cycling. Red and blue lines correspond to charge and discharge periods respectively.

With the goal of obtaining a representative conclusion of the long-term cyclic behaviour of the storage under the mentioned strategy, a complete month is modelled.

The obtained output fluid temperatures as a function of time are presented in Figure 6.18. The three left-hand side figures (Figure 6.18a, Figure 6.18c and Figure 6.18e) correspond to the charge periods, whereas Figure 6.18b, Figure 6.18d and Figure 6.18f, on the right-hand side, are associated to the three-programmed discharge operations. Attending to the curves corresponding to the night charge (8 hours) operation (Figure 6.18a), it can be observed that in the first day the temperature in the outlet increases up to 500 °C. This undesirable temperature increase is a side effect of the pre-charge, which is gradually improved in consecutive days. In particular, after 3-4 days a reproducible stationary state is attained with a maximum output fluid temperature that does not exceed 270 °C.

On the other hand, in the two partial charge periods of 5 (Figure 6.18c) and 6.2 (Figure 6.18e) hours lower output fluid temperatures are obtained.

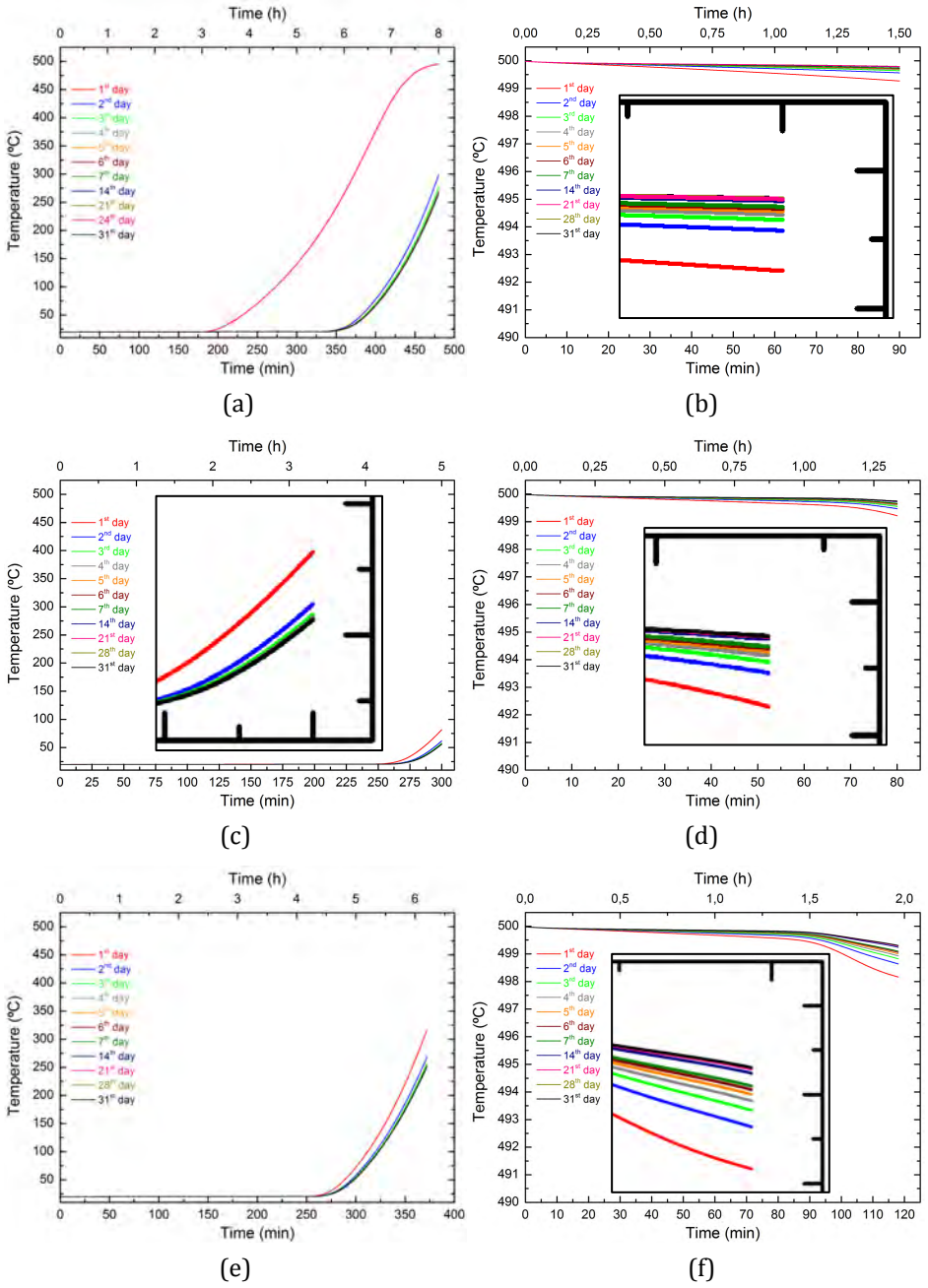

Figure 6.18. Output air temperature from: a) 22.00 to 6.00; b) 6.00 to 7.30; c) 7.30 to 12.30; d) 12.30 to 13.50; e) 13.50 to 20.00; f) 20.00 to 22.00.

Focusing on the output fluid temperature during the three discharge stages, the benefit of the pre-charge can clearly be observed. In all these cases, the released fluid temperature is above 480 °C, matching the requirements of the power block from the first discharge run. A detailed analysis of the two partial discharge periods (Figure 6.18b and Figure 6.18d) reveals that almost no output fluid temperature decrease occurs (less than 1 °C).

The obtained thermal behaviour in both, the charge and discharge periods, allow to conclude that the proposed TES tank is valid not only for a continuous complete charge and discharge operation, but also for a partial charge and discharge cycling condition. Furthermore, the performed analysis demonstrates that the TES behaviour in the charge and in the discharge is only slightly dependent on the particular operation strategy.

Finally, the energy and exergy efficiencies for the modelled daily cycling operation are presented in Figure 6.19. For their quantitative evaluation, the addition of the separate energies and exergies introduced/extracted in the TES during the three daily charge/discharge periods is considered.

The obtained results show nearly constant efficiency behaviour around 96.5%, from the first day. This value is similar to the obtained in the case of a continuous complete charge/discharge operation, described in the previous sections.

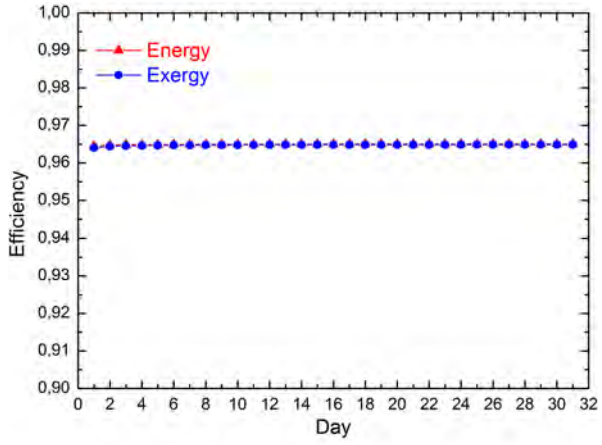

Figure 6.19. Long-term (one month) daily energy and exergy efficiencies.

Overall, this section demonstrates the viability of introducing a packed bed TES solution in the CAES process. The flexibility shown by the proposed TES under

different operation conditions could open a new technological frame for the implementation of CAES processes with improved efficiencies. The obtained high efficiency values guarantee a successful management of the thermal energy involved on the CAES process, leading to a clear step forward in this storage alternative. Finally, the implementation of realistic daily cycling conditions clearly demonstrate the importance of the optimized thermal operation of the proposed storage, able to provide a round-trip efficiency close to 100% and fulfilling all the boundaries and requirements of the CAES application.

6.3. Integration in a CSP plant with an ORC turbine

In addition to the two aforementioned potential implementations of a TES system, where a clear technological gap is found on the application of storage technologies, concentrated solar power (CSP) generation is the most extended application for TES solutions. Even if in this frame, TES is a mature technology based on the molten salt double-tank concept, the international techno-scientific community is very active on the search of new and improved heat storage alternatives. As stated in section 1.4.1, the decrease of the total cost associated to the TES, which presents a direct impact on the cost of the produced electricity, together with the overcoming of the shortcomings of the molten salt technology are a priority for boosting the CSP sector.

For all these reasons, the third industrial application proposed for the packed bed TES system in this thesis work corresponds to the CSP production. In particular, for the concept demonstration, a linear Fresnel collector solar field coupled to an organic Rankine cycle (ORC) turbine for power production is selected. It can be mentioned that this implementation scenario is the core of the *ORC-plus project (Horizon 2020, Ref. 657690)*. The main target of this action is the demonstration of the possibility of extending the full load operation of the ORC turbine up to 4 hours, matching the electricity production with demand peaks in the evening period. It is also very important to note that the work presented in this section will be the basis for the real design and construction of the addressed packed bed TES system in the *ORC-plus project* piloting activities.

6.3.1. CSP plant description

As reference scenario, a 1 MW_{el} concentrated solar power plant using linear Fresnel collectors that is being constructed in Ben Guerir (Morocco) is considered in this section. This plant is equipped with two solar fields with a total aperture of 16,400 m^2. The primary solar field (SF1) accounts for the 70% of the concentrators and is used to feed the power block (ORC turbine) during radiation periods. On the other hand, the secondary solar field (SF2), which accounts for the 30% of the total aperture, is implemented to charge the TES unit.

Considering the dimensions of the CSP plant, a 20 MWh_{th} TES unit is proposed. The charge and discharge operations of the TES unit are performed by two independent loops. In the charge process, the fluid input is obtained directly from the SF2, whereas for the discharge operation, the primary fluid piping line is used. This primary loop is connected to the power block.

For the sake of clarity, a layout of the mentioned CSP plant and TES unit is included in Figure 6.20.

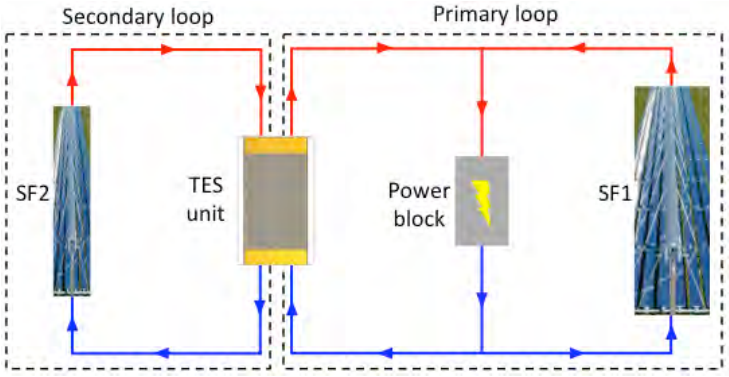

Figure 6.20. CSP plant layout with the thermal energy storage.

Regarding the involved materials, in the solar field and also matching the ORC turbine requirements, a thermal oil, *Delcoterm Solar E15*, is used as heat transfer fluid. On the TES side, taking into account the good compatibility between this oil and the *Magnetite ore* to operate in direct contact (see section 3.5), this is the proposed TES material for the packed bed arrangement.

According to the ORC power block specifications, the operational temperature range of the CSP plant is fixed between 180 and 300 °C. On the other hand, the

targeted parameter for the TES is a supply, on the discharging stage, of 20 MWh_{th} in four hours. In addition, according to the fixed oil circulating capacity of the already selected pumps in the facility, mass flow rates of 6.74 and 15.72 $kg \cdot s^{-1}$ are obtained in the charge and discharge operations respectively.

As a summary, in Table 6.8 the main operational parameters of the CSP plant and the TES unit considered in the analysis performed in this section are presented.

Table 6.8. CSP plant and TES unit operational parameters.

TES capacity (MWh_{th})	20
Heat transfer fluid	*Delcoterm Solar E15*
TES medium	*Magnetite ore*
Hot HTF temperature (°C)	300
Cold HTF temperature (°C)	180
Charge mass flow rate ($kg \cdot s^{-1}$)	6.74
Discharge mass flow rate ($kg \cdot s^{-1}$)	15.72
Discharge time (h)	4

6.3.2. TES unit thermal management

As already mentioned throughout this thesis work, the thermal operation and management of the storage system plays a capital role on the obtained storage capacity and overall performance. In this particular case, the design parameters of the proposed TES unit are conditioned by different boundaries associated to the CSP environment, mainly introduced by the ORC operation and the solar field. These boundaries are detailed in the following:

1. The minimum fluid inlet temperature for the ORC turbine is 260 °C. This implies that the discharge procedure of the storage unit must be stopped when the output fluid temperature reaches this threshold limit.
2. The maximum output fluid temperature from the TES unit during the charge process is also limited to 260 °C as the hot oil coming from the storage is re-inserted in the solar field. The design and control of the solar field makes unfeasible the management of oil temperatures close to the maximum target temperature (300 °C) in the circuit input. This limitation is associated to the

automation and control of the Fresnel mirrors, being very difficult to achieve a satisfactory focusing/defocusing procedure at temperatures close to the maximum operation one.

6.3.3. Results

6.3.3.1. TES tank macroscopic design

A preliminary macroscopic design of the TES tank is performed to identify its main design parameters. Considering that the heat stored in the fluid phase cannot be neglected due to the high energetic density of the mineral oil (density and specific heat), the approximated required masses of the TES material, *Magnetite ore*, and *Delcoterm Solar E15* oil can be obtained from the following equations:

$$E_{stored} = 20\ MWh_{th} = \left(m_s \cdot c_{p,s} + m_f \cdot c_{p,f}\right) \cdot \Delta T; \tag{6.1}$$

$$\frac{V_f}{V_s} = \frac{\varepsilon}{1-\varepsilon} = \frac{m_f/\rho_f}{m_s/\rho_s}. \tag{6.2}$$

Given the small ΔT exploited in the packed bed, 120 °C, no strong thermo-mechanical stresses are expected between the *Magnetite ore* and the container material. Consequently, a cylindrical geometry is considered for the storage tank.

The main characteristics of the considered TES tank together with the required masses of *Magnetite ore* and oil are shown in Table 6.9.

Table 6.9. TES tank characteristics.

Storage tank geometry	Cylindrical
Storage tank volume (m^3)	171.2
Delcoterm Solar E15 mass (t)	40.6
Magnetite ore mass (t)	576.9
Insulation material	*Mullite fibre*
Insulation thickness (cm)	30

6.3.3.2. Parametric analysis

A parametric analysis is performed in order to optimize the thermal performance of the TES unit for the particular addressed application. In this regard, three design variables are investigated: the TES tank aspect ratio, the solid

particle diameter and the stopping criterion in the charge operation. A summary of the considered variability range for these three parameters is presented in Table 6.10.

Table 6.10. Parametric analysis variables and their range of study.

Aspect ratio (L/d_t)	0.5/1/2/3/4
TES medium particle size	0.5/1/2/4
Charge stopping criterion (°C)	180/210/240/260

6.3.3.2.1. *Tank aspect ratio and particle diameter*

In the study of the tank aspect ratio and particle diameter impact in the released energy within the established discharge temperature tolerance, above 260 °C, a single charge and discharge operations are studied. In order to perform such analysis, the maximum accepted output fluid temperature, 260 °C, is selected as reference for the calculations, according to the system boundaries established in section 6.3.2.

The obtained discharged energies for the different analysed tank aspect ratio and particle diameter values are shown in Figure 6.21.

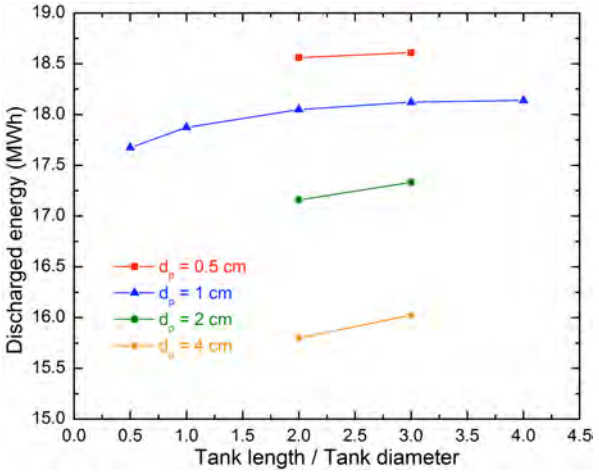

Figure 6.21. Stored energy as a function of the tank aspect ratio and particle diameter.

According to the presented results, small particle diameters promote larger storage capacities and, for a fixed particle diameter, larger tank aspect ratio values also promote larger storage capacities. Taking this into account, small particle

diameters should be considered together with a large tank aspect ratio. However, in the final design selection, not only thermal considerations need to be done, but also additional engineering and constructive implications need to be pondered (already presented in section 5.3):

1. The tank mechanical stability is much difficult to manage with high tanks;
2. No strong benefit in the storage capacity is observed from aspect ratios larger than 2;
3. The lateral wall surface of the tank increases with the aspect ratio, and hence, the management of thermal losses is also more complex.

Consequently, an aspect ratio of 2 is identified as a successful TES tank design criterion. In addition, in Figure 6.22, the pressure drop values associated to the interstitial oil flow through the packed bed are presented for the configurations with this selected aspect ratio value. As it can be clearly observed, this parameter is not an issue in any of the considered cases, since it is under 500 Pa in all of them. This permits to reduce the particle diameter value without penalizing the overall TES performance due to large pumping energies. According to the obtained results, a particle diameter between 0.5 - 1 cm is identified as the satisfactory range. For operative reasons, considering that, as explained in section 2.1.4, one of the particle sizes in which the *Magnetite ore* is commercially provided is around 1 cm, this value is selected as a best candidate.

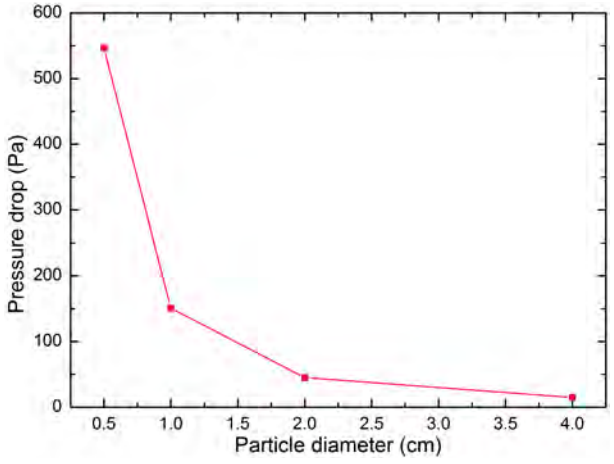

Figure 6.22. Pressure drop in a packed bed with an aspect ratio of 2.

6.3.3.2.2. *Stopping criterion*

Once the macroscopic design parameters of the TES tank are identified, the impact of the charge strategy is analysed in this section. As presented in Table 6.10, four different charge stopping criteria are considered as a function of the output fluid temperature: 180, 210, 240 and 260 °C.

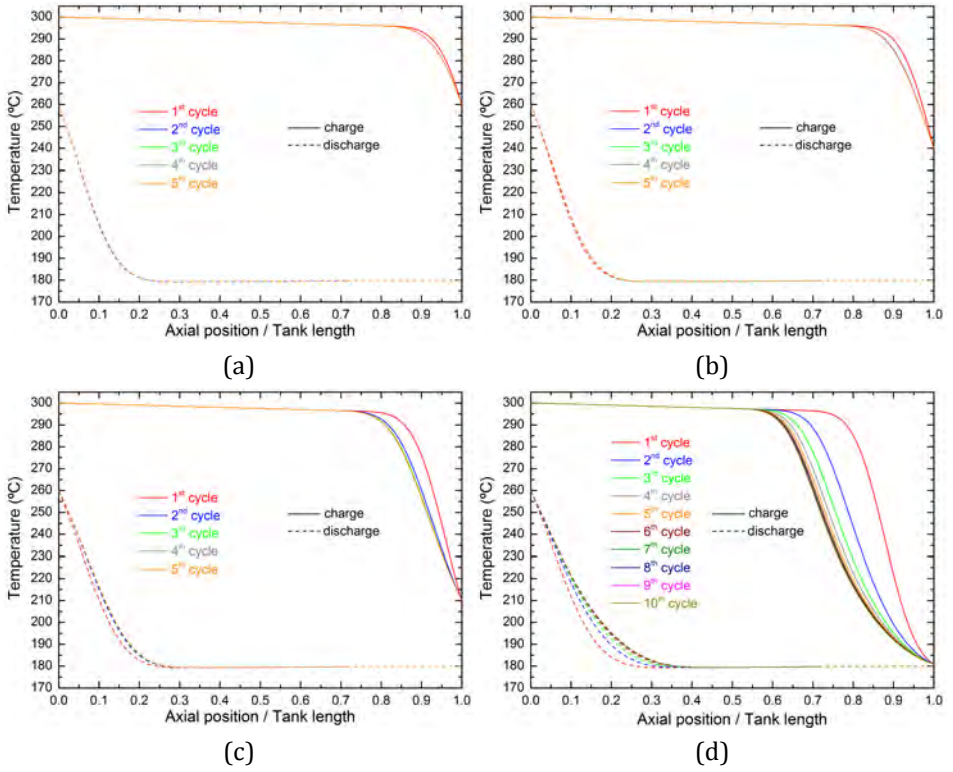

Figure 6.23. Axial temperature distribution at the end of the charge and discharge operations once the stopping criterion is reached: a) 260 °C; b) 240 °C; c) 210 °C and 180 °C in the charge, and 260 °C in the discharge.

Figure 6.23 shows the axial temperature distribution in the storage once the TES unit is considered charged (continuous lines) and discharged (dashed lines) according to the mentioned four charging criteria. In all cases the discharge stopping criterion is fixed to the minimum ORC turbine oil temperature requirement, 260 °C. In agreement with the charge/discharge scenario with fixed temperature criteria depicted in section 5.2.3, the operational method selected for this TES case implies a transient stage before attaining a reproducible stationary thermal behaviour. As a consequence, Figure 6.23 shows the complete transient

cycling behaviour in all the investigated cases. From these results two main conclusions can be obtained:

1. The stored energy is proportional to the area between the charge and discharge temperature distributions. Taking this into account, when larger is the allowed output fluid temperature larger is also the released energy in the discharge operation.
2. The number of cycles required to reach a stationary performance increase with lower output fluid temperature criteria for the charge operation. It has to be noted that, for an easier management of the TES unit, low number of cycles to reach reproducible conditions are preferred.

In addition to the axial temperature profiles presented in Figure 6.23, in Table 6.11 the required number of cycles for attaining reproducible conditions in the TES unit, the useful energy for the power block and the cycle efficiencies are included. Additionally, for each scenario, the stored energy and efficiency in the first cycle is included between brackets. Taking into account that, during the charge operation, the output fluid from the TES unit is re-inserted in the solar field, the calculation of the cycle efficiency is not penalized, as all the disposed heat can be considered useful.

Table 6.11. Results summary.

Stopping criterion in the charge (°C)	Cycles to stationary state	Stored energy (MWh_{th})	Efficiency (%)
180	8	13.1 (15.8)	66 (79)
210	4	16.6 (17.2)	83 (86)
240	3	17.6 (17.8)	88 (89)
260	2	17.9 (18.0)	90 (90)

As observed in Figure 6.23, from Table 6.11 it is also seen that when larger is the temperature allowed in the output fluid during the charge operation, the

energy released in the discharge increases considerably. In addition, the larger this temperature is, the less number of cycles are required before attaining reproducible conditions in the TES unit.

From the results presented in Table 6.11 it can also be noted that in the case of implementing a temperature criterion in the charge operation of 260 °C, the reproducible performance of the unit is almost achieved from the first cycle. Considering this operational advantage together with the maximization of the storage capacity when higher output temperatures are allowed during the TES charge, the 260 °C stopping criterion is selected as an optimum value.

6.3.3.3. Storage tank size refinement

The analysis presented up to now is associated to the preliminary macroscopic design parameters. As can be seen from the results presented in section 6.3.3.2, even if close, in any of the analysed systems the energy extracted from the TES tank, and useful for the power block, reaches the targeted 20 MWh_{th}. The obtained difference is related to the stratification phenomenon undergone in the TES unit, which leads to an axial temperature gradient profile. This phenomenon implies a decrease of the total storage capacity, difficult to predict on a macroscopic preliminary estimation without performing numerical calculations. As a consequence, in order to obtain an accurate design, a refined TES tank dimensioning is necessary.

Table 6.12. Summary of the TES unit final design and operational parameters.

Storage tank volume (m^3)	190
Aspect ratio (L/d_t)	2
Delcoterm Solar E15 mass (t)	45.1
Magnetite ore mass (t)	640.8
TES particle size (cm)	1
Stopping criterion in charge (°C)	260
Stopping criterion in discharge (°C)	260

Considering the storage tank parameters obtained from the parametric analysis, aspect ratio = 2, particle diameter = 1 cm and charge/discharge temperature stopping criteria of 260 °C, the extracted energy is around 18 MWh_{th}.

This represents a 90% of the targeted storage capacity. Therefore, the final TES tank has to be oversized in order to compensate these thermal losses due to the thermocline formation. The obtained final tank dimensions are summarized in Table 6.12.

Additionally, in Figure 6.24 the output fluid temperature during the discharge operation for the obtained final design is presented. Considering the energy released from the TES unit within the temperature criterion, above 260 °C, a total of 20 MWh_{th} are extracted in 4.1 hours. These two values agree with the targets established for the TES system (see Table 6.8).

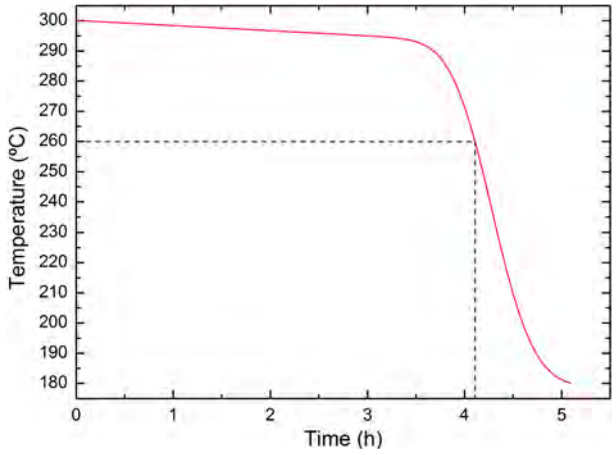

Figure 6.24. Output fluid temperature in the discharge operation.

Finally, the obtained thermal efficiency according to the unit management proposed in this section indicates values around 90%, which makes this solution very suitable for the CSP plant exploitation.

6.3.3.3.1. *TES performance in idle conditions*

In the analysed particular CSP application, the main objective of the TES is to extend the electricity production during 4 hours after the sunset. This is one of the most power demanding daily periods, and, as a consequence, one of the critical issues to solve in CSP through the implementation of an effective TES solution, such as the packed bed proposed in this section.

Following the thermal boundaries of the studied system, after the TES is discharged for the extended ORC turbine operation, a noticeable amount of heat is

still left inside the TES system. Considering that this partially charged TES state would be maintained during the complete night, a detailed analysis of the thermal evolution of the remaining energy is needed. From this investigation, the initial TES state for the next day charging process would be determined.

According to the particular targeted time exploitation of the TES, around 8.5 hours of night idle period are expected. In order to investigate the evolution of the thermocline region during this static condition, in Figure 6.25 the temperature profile in the axial direction of the tank is presented. In this figure, the red curve corresponds to the status of the TES tank once the regular discharge, associated to the ORC turbine operation, is finished. The blue curve corresponds to the temperature profile in the TES tank after the idle period. From this figure, it is observed that the temperature in the packed bed remains almost unchanged. Consequently, the energetic status of the TES in terms of temperature stratification and thermal quality, can be considered to be unaffected by the idle period.

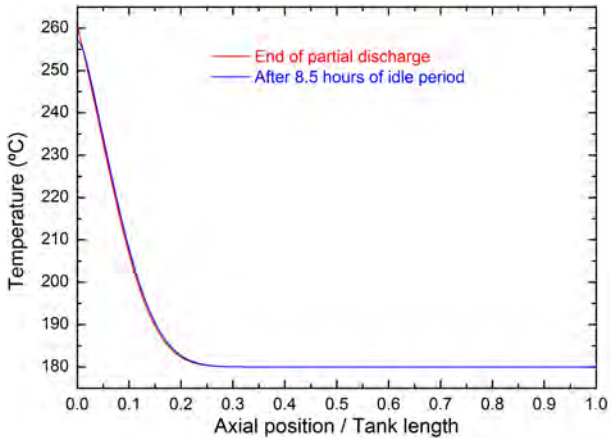

Figure 6.25. Axial temperature profiles in the TES unit before and after 8.5 hours of idle conditions.

Considering this result, two main conclusions can be extracted. On one hand, the stagnation heat transfer mechanisms which govern the heat transfer performance under idle condition do not lead to a significant degradation of the thermocline region in the modelled time. On the other hand, the thermal losses through the tank wall, modelled as convective natural convection transfer, do not show a strong impact on the quality of the stored heat during the idle conditions.

6.3.3.3.2. *Deployment of the remaining heat beyond ORC operation*

The aforementioned results show that the selected tank design and operation strategy result in a short thermal transient stage limited to 1-2 cycles. In addition, based on the results shown in Figure 6.24, up to 1.1 MWh_{th} are found in the TES tank after the heat suitable for the ORC turbine operation has been extracted. Considering this large amount of thermal energy with temperatures below 260 °C, this subsection is devoted to the analysis of the applicability of this remaining heat within the power plant, without affecting the regular operation of the proposed TES unit.

From the different possible heat demanding applications inside the CSP plant, its implementation in the warm-up operation of the ORC turbine components is identified as one of the most attracting options. The main motivation of this approach is the large turbine optimization potential. A correct pre-heating of these components show a great influence on the reduction of the plant start-up time, and also on the efficiency of the thermal-electrical conversion.

To perform this study under realistic conditions, considering that the deployment of the remaining stored energy is made during the CSP plant start-up process, the status of the TES unit after the 8.5 hours of idle period is used as initial condition for the calculations. Additionally, taking into account that during the plant start-up there is not available enough solar radiation for a direct oil heating, the temperature of the oil from the solar field is assumed to be at the minimum operational temperature, namely 180 °C. Considering this, several simulations are performed varying the oil mass flow rate between 6-18 $kg \cdot s^{-1}$, which are the upper and lower limits of the plant oil circuit pump.

The average output oil temperature during the discharge operation is shown in Figure 6.26. As expected, when implementing low oil mass flow rates, the temperature drops down slower than when high velocities are used. Thus, for an oil mass flow rate of 18 $kg \cdot s^{-1}$ the output fluid temperature drops at an average of 2 $°C \cdot min^{-1}$. Meanwhile, for a mass flow rate of 6 $kg \cdot s^{-1}$ an average of 0.5 $°C \cdot min^{-1}$ is observed. In this frame, for the highest mass flow rate (18 $kg \cdot s^{-1}$) the total energy content inside the tank is discharged in about one hour, whereas this time can be extended up to three hours as the mass flow rate decreases up to 6 $kg \cdot s^{-1}$.

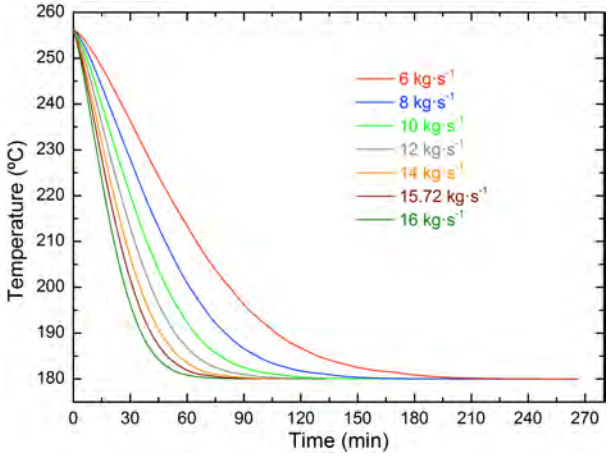

Figure 6.26. Output oil temperature as a function of the mass flow rate.

These results show the great potential of the remaining heat in the TES unit for its implementation beyond the ORC operation. This strategy could result a very appropriate alternative in order to maximize the plant efficiency based on a sustainable exploitation.

6.4. Conclusions

So far, based on the storage materials proposed in this thesis work, in this chapter the design and deployment of a packed bed TES system in three different industrial applications has been presented. Overall, the obtained results have demonstrated the high potential and flexibility of the packed bed thermal energy storage concept in these real implementation scenarios.

In the first industrial deployment study, a packed bed TES system has been proposed for heat recovery in a steel production plant from the exhaust gases of an electric arc furnace. The main objective of this system is to achieve a continuous heat supply from the inherent batch operation of the steel furnace. This implementation strategy presents great advantages, since the added value of a continuous heat source opens a wide number of applications, not accessible for discontinuous sources. The continuous heat availability from the TES unit is a very restrictive boundary, leading to an accurate synchronization of the TES charge/discharge procedure with the electric arc furnace operation. As a consequence, in this particular case, large pressure drop values have been

obtained associated to the large amount of energy lost from the furnace and the short available times for its capture and storage. These phenomena clearly lead to strict design conditions, in order to minimize the associated fluid pumping energy without reducing the thermal performance of the TES.

In this analysis, the influence of the idle period associated to the batch operation of the furnace is also investigated. The short time of static operation together with the thermal stratification behaviour in the proposed TES unit, have demonstrated the negligible impact of the idle period in the TES operation.

The obtained results revealed that, after an appropriate optimization and parametric analysis, efficiency values around 65% could be achieved considering the power production as final application of the heat. These values show the great recovery potential of the investigated TES system. Even if the obtained values could be increased by the implementation of a different charge strategy, the presented analysis shows the potential of the packed bed TES solution in the steelmaking waste heat recovery environment.

In the second deployment analysis, the suitability of including a packed bed TES unit in a CAES plant to recover the heat associated to the air compression operation, and its further utilization on the expansion process in the power block has been addressed. Considering the boundaries of this implementation frame, mainly the high operation pressure and large involved energies, a careful basic design is proposed. As a result, in order to obtain a successful thermo-mechanical management of the derived large TES unit, a conical geometry has been identified as an appropriate geometrical selection for the TES tank.

The reliability, high efficiency and stability of the proposed TES system have also been pointed out. After a limited thermal transient stage, the reproducibility of the system is guaranteed, performing at very high efficiency level. The presented work has not only explored the straightforward implementation of a packed bed storage but, enhancement and improvement alternatives have also been demonstrated, including a sizing, cycling and long-term performance analysis. In this line, the thermal management of the TES unit under the CAES deployment conditions has been found of great importance. Even if the direct heat storage and exploitation alternative shows a great potential, the implementation of particular

heat management strategies, such as performing a pre-charge of the TES system, have demonstrated a large benefit on the thermal performance. The main effect of the pre-charge is the shortening of the transient stage together with the supply of a larger energy with a better thermal level in the TES discharge operation.

Overall, the obtained results have revealed the thermal viability of the proposed TES system for the heat recovery and its reuse, leading to a substantial efficiency increase of the complete CAES process.

Finally, the industrial deployment analysis was completed with the study of the integration of a packed bed TES unit in a concentrated solar power plant. As a benchmark scenario, a linear Fresnel-type plant implementing thermal oil as heat transfer fluid, and coupled to an organic Rankine cycle (ORC) turbine for power production has been considered. The obtained results have revealed the high flexibility of the proposed solution even though the restrictive boundaries imposed by the solar field and the ORC turbine. The presented parametric analysis of the main design and operational boundaries has permitted the obtainment of an optimized TES system able to accomplish the storage requirements of the considered CSP plant with thermal cyclic efficiencies above 90%. In addition, the selected operation strategy shortens the transient performance to 1-2 cycles, which results of great importance for the practical implementation and management of the TES.

In addition to the direct usage of the stored heat on the ORC turbine operation, the exploitation of the stored heat not useful for the power production ($T < 260$ °C) is also proposed. This TES deployment mode results of particular interest since it is able to extend between 1-3 hours, depending on the selected mode, the discharge of the storage system, supplying up to 1 MWh_{th} of additional energy. It has to be noted that the exploitation of this extra energy can only be done after a long idle period, associated to the night time. In the presented work, the detailed analysis of this idle stage has also been addressed, demonstrating that no substantial thermal evolution is produced. As a consequence, the quality of the stored heat is not decreased during this period. This opens new opportunities for enhancing the efficiency of the considered plant as this heat can be used in the ORC turbine component pre-heating in the morning plant start-up procedure.

Chapter 7:

General conclusions and future perspectives

7 General conclusions and future perspectives

This thesis has aimed at studying cost effective and high performance concepts for thermal energy storage applications. In essence, without entering into its implementation, a successful heat storage solution must provide a satisfactory balance between the two basic aspects of any TES alternative, the storage material and the implemented technology. Both aspects have been addressed in this thesis work achieving an optimal compromise between the variables governing the cost, efficiency and thermal performance of the heat storage solution.

First, on the storage material side, the implementation of low cost solid materials has been proposed. A double approach has been followed in the selection of appropriate material candidates. On one hand, different by-products from the iron and steel manufacturing, slags, have been identified as suitable TES materials. The valorisation of these by-products in the thermal storage frame could represent a win-win approach. It permits an important reduction of waste generation from the steelmaking process and provides a competitive alternative for TES. On the other hand, a natural material, magnetite ore, has been selected as an appropriate storage material based on its abundance, low ecologic impact and satisfactory thermo-mechanical properties. Both proposed materials families have been extensively characterized in terms of their main thermal, structural, mechanical and durability properties, demonstrating their potential for high temperature packed bed thermal energy storage systems.

Second, regarding the technological solution able to extract the maximum performance from the identified heat storage materials, a packed bed TES alternative has been proposed in this work. This solution represents a flexible, cost effective and highly performing technology. Even if this TES concept has already been proposed, its industrial deployment still requires a deep understanding of the associated thermal transport and optimization phenomena. This issue has been addressed in detail within this thesis work. In this regard, the great importance of a deep customized parametric analysis and optimization associated to the

particular implementation frame has been found to be critical to obtain the maximum benefits of the proposed packed bed TES solution.

Overall, this thesis work has covered the main aspects to fully develop an innovative approach for solid packed bed TES technology, from the basics related to material science, through the development of customized modelling and design strategies up to the up-scaling of the packed bed TES on different realistic industrial environments. Based on the initially established thesis objectives, summarized on the introductory section, the main conclusions of each step of the addressed techno-scientific value chain are highlighted in the following:

1. Seven materials have been identified as potential candidates for thermal energy storage: six by-products from the iron and steel production (one blast furnace slag, two basic oxygen furnace slags and three electric arc furnace slags) and a natural material, magnetite ore. Among them, the careful study of their main properties affecting to the behaviour of a thermal energy storage material in packed bed arrangements allowed the selection of the most promising ones. In this regard, according to their energetic density, thermal transport and mechanical properties, together with their wide availability, electric arc furnace slag and magnetite ore were selected for further analysis in this thesis. In these cases, the performed thermo-physical characterization showed very appropriated values of the heat capacity, thermal conductivity and density, ranging within the values usually found for ceramic materials.

2. A complete chemical compatibility analysis has been carried out between the selected TES materials and a wide variety of heat transfer fluids: air, thermal oil and nitrate molten salts. The stability analysis of the selected materials under air atmosphere up to 1000 °C revealed that a full compatibility is guaranteed, with some minor restrictions. In both solid materials, the presence of FeO or Fe_3O_4 activates an oxidation process at temperatures above 500 °C. However, once oxidations have occurred, the materials do not suffer any further evolution.

   On the other hand, the study of the compatibility between the electric arc furnace slag and the *Solar salt* at the maximum operating temperature of the

latter, 565 °C, showed a limited stability. The underlying reasons of such incompatibility are the formation of nitrites in the salt promoted by the iron oxides present in the slag, and the migration of cations, at ppm level, from the slag to the salt. As a consequence, the complete demonstration of the suitability of this materials combination to operate in direct contact requires of further analysis. In these terms, the mentioned migration mechanisms need to be analysed in order to determine an eventual saturation limit, or, on the contrary, the full degradation of the salt.

Finally, the stability analysis has been completed with the study of the compatibility between magnetite ore and a thermal oil, *Delcoterm Solar E15*, at the maximum operation temperature of the latter, 310 °C. The obtained results guarantee the stability of both materials when operating in direct contact, at the mentioned temperature, without any found restrictions.

3. In order to investigate the performance of the selected thermal energy storage materials under a packed bed TES deployment frame, a complete physical model has been developed. This modelling tool accounts for the governing energy, thermal transport (conduction, convection, radiation, or dispersion among others) and fluid flow mechanisms, which occur in the packed bed TES arrangement. The presented model represents a successful and innovative modelling strategy since it permits an accurate treatment of radiative transport mechanisms together with the possibility of modelling variable packing void fraction values. In addition, the formulation associated to the pressure treatment in the overall calculation results is a relevant contribution. This modelling strategy opens new possibilities on the description of high temperature and high pressure packed bed systems. In addition, in order to determine the accuracy of the performed calculations, four different experiments reported in the literature have been used as benchmark for the model validation. The calculations carried out showed a very precise agreement between the results obtained from the developed model and the selected experimental results. It has to be highlighted that the extensive validation addressed in this thesis work results of particular importance since satisfactory results have been obtained in a wide range of

length scales, operational parameters (temperatures, flow rates etc.) and characteristics of the investigated materials (liquids and gaseous heat transfer fluids).

4. The developed and validated physical model has been used to deeply understand the thermo-fluidic behaviour of the packed bed storage system. In this regard, a double exploitation level has been investigated by means of computational calculations. First, a detailed technology implementation analysis has been performed in terms of thermal management of the packed bed TES unit. This study has led to the identification of three main operational modes: complete charge and discharge, time-limited partial charge and discharge and output fluid temperature limited partial charge and discharge (temperature tolerance). As a main conclusion from this analysis, the former mentioned operation mode allows reproducible conditions of the storage from the first cycle, maximizing the exploitation of the material storage capacity in the complete temperature range. However, it has to be noted that this operational mode results in a large energy disposal before reaching the complete charge status, what considerably penalises the cycle efficiency. On the other hand, the fixed-time and temperature tolerance operation modes lead to a transient operation stage before attaining a reproducible stationary thermal behaviour. The obtained modelling results have also revealed that the underlying reason of the thermal stationary performance is associated to the temperature stratification mechanisms (thermocline formation), and their balance with the fluid extracted during charge or discharge operation. As a consequence, even if the energetic exploitation of the storage material is decreased when compared with the complete charge/discharge method, the obtained efficiency is clearly improved since the energy disposal in the charging process is noticeably reduced.

   On the other hand, the performed conceptual parametric analysis has been completed with the impact analysis of the main packed bed design criteria. In particular, the influence of the tank aspect ratio and geometry, the solid particle diameter and the heat transfer fluid mass flow rate on the overall

thermal performance has been carefully studied. The obtained results have shown the importance of finding a good balance among them, in order to maximize the performance of the storage unit. The particular optimized behaviour parametric ranges are also quantitatively determined for the analysed benchmark case. These parameters are of paramount importance in order to obtain an adequate heat transfer between the solid particles of the storage material and the heat transfer fluid, together with controlled energy losses associated to the required mechanical pumping energy or lateral thermal losses. Summarizing, this conceptual basic investigation of the packed bed system has allowed addressing a full optimization and customization of the TES unit, also including eventual engineering, constructive and mechanical design criteria. The control of the temperature stratification phenomena through an optimized tank design is the main obtained result, leading to a customized and improved scenario for the packed bed storage technology deployment.

5. The obtained conceptual design and operation guideline have been applied together with the physical model to investigate the deployment of packed bed TES units, based on the previously selected materials, in three different industrial applications:

   i. Waste heat recovery from the exhaust gases of an electric arc furnace in a steelmaking plant: the possibility of a continuous heat supply from a batch process implementing a synchronic operation of the TES with the furnace has been demonstrated. In the analysis, the most restrictive boundary has been found to be the pressure drop derived from the large operation power. Finally, after an appropriate optimization and parametric analysis, efficiency values around 65% could be achieved considering the electricity production as final application of the heat.

   ii. Compressed air energy storage plant: the obtained results have shown the feasibility of the recovery of the heat involved in the air compression stage to be used in the later expansion process. This implementation is a novel and effective solution allowing the migration from a standard CAES to an Adiabatic-CAES scheme. Even if the large operation pressures could

represent a restrictive criticality, the obtained results have revealed a round-trip thermal efficiency above 90%. The obtained results have shown a satisfactory control of the thermocline thermal stabilization under different implementation conditions, including a start-up pre-charging stage. This finding opens new cyclic operation exploitation possibilities.

iii. Concentrated solar power plant with an ORC turbine: the obtained results have demonstrated the suitability of the packed bed TES concept in the CSP industry leading to an important cost-reduction in this plant component. The parametric analysis of the operation strategy, considering the boundaries imposed by the solar field and the power block, and the tank design resulted in an optimized storage unit able to accomplish the requirements of the selected CSP plant. Furthermore, the proposed TES system allows the deployment of the useless heat for power production, for example, in the plant component pre-heating in the morning, without affecting the regular operation of the unit.

Overall, the performed analyses under realistic conditions guarantee the suitability of the packed bed TES concept in a wide range of operation environments and conditions. As a consequence, new opportunities can be accessed by the proposed TES solutions.

It must to be highlighted that, leaving apart the demonstrated technical feasibility of the mentioned materials and technologies, the overall economical effectiveness of the developed full concept has been one of the core proposals of this thesis work. The implementation of the packed bed storage based on the investigated low cost materials represents a very important step forward in the search of a viable high temperature heat storage solution, able to open new market possibilities at industrial scale.

However, even if the activities carried out in this thesis work have permitted the development and scale-up of a cost effective TES concept with customization capabilities, the full deployment of this technology must address some additional considerations. Aligned with the idea of obtaining a mature packed bed TES technology in the near future, in the following, a list of future actions is presented:

1. Experimental testing of the proposed TES solutions at pilot or pre-industrial demonstration scale: in order to validate the obtained thermal performance of the materials and developed storage concepts, their direct experimental testing in real implementation environments is of paramount importance. It has to be noted that the complete set of results obtained in this thesis work will go beyond the conceptual stage. The developed material and system investigation will represent the basis for a real detailed design and construction of three different packed bed demonstration scale units, summarized below:
   i. A pre-industrial 1 MWh_{th} storage capacity packed bed unit based on slag, available at the end of 2017 in the facilities of ArcelorMittal steelwork in Sestao (Spain). This system will be devoted to the practical demonstration of the feasibility of waste heat recovery from the exhaust gases of the electric arc furnace during the steel production. Such plant is being constructed in the framework of the *RESLAG European project*.
   ii. A laboratory scale packed bed TES unit, also based on slag, that will be operated at CIC Energigune facilities reproducing conditions of a concentrated solar power plant by means of an "air loop" able to supply air in the 25 - 800 °C temperature range. This is the core activity of the *Slagstock European project*.
   iii. The third facility also corresponds to a pilot scale plant, already constructed at CIC Energigune, in the framework of the *ORC-Plus European project*. Regarding the involved materials, a magnetite ore based packed bed thermal energy storage unit is going to be tested using thermal oil as heat transfer fluid. The conditions of a linear Fresnel-type concentrated solar power plant will be reproduced by means of an experimental oil-testing loop. In addition, based on the pilot scale experience and the obtained basic design in this thesis work, the industrial scale-up of the proposed packed bed TES system in the concentrated solar power plant constructed in Ben Guerir (Morocco) will also be carried out.

Overall, these experimental plants will permit the demonstration of the real potential of packed bed thermal energy storage systems in different industrial sectors. Their operational flexibility in terms of boundary conditions, temperature ranges, fluid flow nature and other specifications will made the mentioned experiments of capital importance to demonstrate the packed bed technology in the real scale.

2. Development of a model including mechanical implications: as indicated through this thesis work, one of the main concerns in the design of packed bed thermal energy storage systems are the mechanical issues of the solid storage material. In the worst scenario, an inappropriate mechanical behaviour could cause a failure of the system (storage material and container) upon thermal cycling. The addition of mechanical considerations to the physical model developed in this thesis allowing the description of the mechanical-thermal interactions in the storage system, could imply an important step forward in obtaining a powerful tool to design this type of thermal energy storage systems. In this line, the use of Discrete Element Method (DEM) modelling techniques, or the more sophisticated X-DEM methods integrating thermal properties of the modelled elements coupled to the standard computational fluid dynamic (CFD) code could lead to a complete description of the packed bed system.
3. Durability analyses: this thesis has addressed the compatibility/stability of the slag and magnetite ore with air, *Solar salt* and *Delcoterm Solar E15* thermal oil. As mentioned in this work, the direct contact of the slag with the *Solar salt* has been found to be not fully compatible. However, additional studies should be addressed in order to investigate whether this incompatibility can be controlled. Furthermore, the compatibility of the investigated materials with other usual heat transfer fluids such as salt mixtures as *HITEC XL* or thermal oils as *Therminol VP1* or *Syltherm 800* could be addressed in order to extend the possible thermal energy storage material-heat transfer fluid combinations. This analysis could permit a wider expansion of the materials/storage concept proposed in this thesis to different industrial applications.

Annexes

A Annex

A.1. Materials properties

This appendix contains the thermo-physical properties of the materials used as heat transfer fluid or insulation in all the systems modelled in this thesis work. In the following, the density, viscosity, specific heat and thermal conductivity of such materials are presented. It has to be noted that, thermo-physical properties of the solid materials used as TES medium are compiled from the performed experimental measurements in chapters 2 and 3.

It must be highlighted that the thermal properties of the investigated heat transfer fluids or insulation materials are obtained from different literature resources, mentioned throughout this annex. In order to introduce the effect of temperature dependent material properties, polynomials fittings are performed with a satisfactory compromise between the obtained accuracy and polynomial order. These functions are obtained in the appropriate range, avoiding any mismatch between the operation and fitting temperatures. Finally, the polynomial function for each thermal property has been included in the CFD model.

A.1.1. Heat transfer fluids

Two different heat transfer fluids are studied in the packed bed devices modelled in chapters 5 and 6, air and *Delcoterm Solar E15* thermal oil. In the following the thermal properties of these two fluids are detailed.

A.1.1.1. Air

Thermo-physical properties of air are estimated using the Peng-Robinson equation of state [1], and fitted to a polynomial function for its insertion in the CFD model. Table A.1 contains the obtained coefficients according to the following polynomial structure:

$$Property = A + B \cdot T + C \cdot T^2 + D \cdot T^3 + E \cdot T^4 + F \cdot T^5; \qquad \text{(A.1)}$$

where, T is the temperature in Kelvin. The values presented in Table A.1 correspond to the air properties at atmospheric pressure.

Table A.1. Air polynomials coefficients at ambient pressure.

	ρ (kg·m^{-3})	c_p (J·K^{-1}·kg^{-1})	k (W·m^{-1}·K^{-1})	μ (Pa·s)
A	3.46597	1107.78152	0.00141	2.03696E-7
B	-0.0133	-0.82272	9.72368E-5	7.90211E-8
C	2.55967E-5	0.00209	-6.28035E-8	-7.521E-11
D	-2.62097E-8	-1.90843E-6	5.18469E-11	5.95958E-14
E	1.36159E-11	8.01706E-10	-2.45236E-14	-2.69603E-17
F	-2.8197E-15	-1.28725E-13	4.82049E-18	5.12096E-21

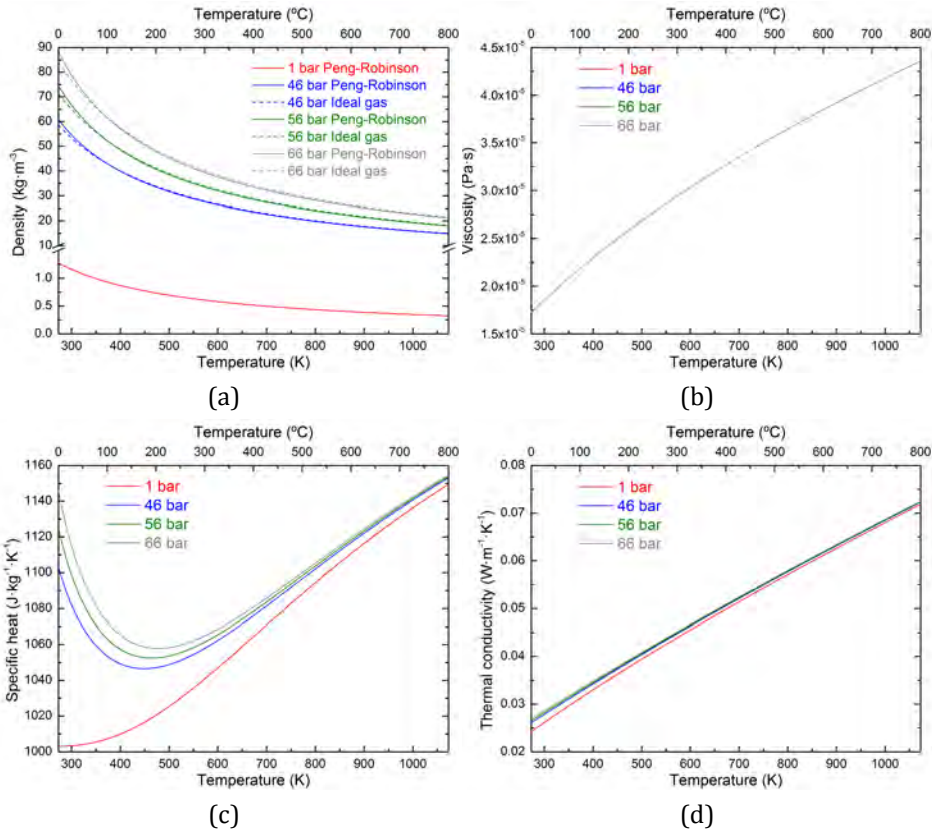

Figure A.1. Thermal properties of air at 1, 46, 56 and 66 bars: (a) density; (b) viscosity; (c) specific heat; and (d) thermal conductivity.

Taking into account that, in the systems modelled in section 6.2, the heat transfer fluid is compressed air between 46 and 66 bar, in Figure A.1 the same thermal properties are also plotted for 46, 56 and 66 bar. These values correspond

to the maximum, average and minimum pressures modelled in such section respectively.

Table A.2. Air polynomials coefficients corresponding to air at 56 bar.

	c_p ($J \cdot K^{-1} \cdot kg^{-1}$)	k ($W \cdot m^{-1} \cdot K^{-1}$)
A	1983.58434	0.00795
B	-6.58365	7.11292E-5
C	0.01803	-1.28523E-8
D	-2.43134E-5	2.33006E-12
E	1.65627E-8	-
F	4.53876E-12	-

As shown in Figure A.1b, the viscosity does not show any pressure dependence in the complete investigated range, from 1 to 66 bar. As a consequence, in all the modelled systems the same viscosity polynomial is implemented (Table A.1). The thermal conductivity shows a negligible dependence with the pressure in the 46-66 bar range, but slight differences are found when compared with the values at 1 bar. Consequently, in section 6.2 the thermal conductivity polynomial at the average pressure, 56 bar, included in Table A.2, is used. The specific heat shows a noticeable difference as a function of the pressure at temperatures below 200 °C. However, at high temperatures this difference can be disregarded. In order to simplify the modelling strategy, without losing the required accuracy, in section 6.2 a specific heat value, evaluated at the average operation pressure (56 bar), is considered. The associated coefficients of the polynomial fitting are also included in Table A.2. Finally, a noticeable pressure and temperature dependence is found for the density. As a consequence, both dependencies are accounted for in the performed calculations. For comparison, the density of an Ideal gas at different pressure values has also been included in Figure A.1a. Comparing the obtained densities with both equations of state, almost negligible differences are found between them. Taking this into account, and the simplicity of implementing the Ideal gas law in comparison to the Peng-Robinson equation of state, the density is introduced using the former strategy. As a consequence, in section 6.2 density is calculated by using the following equation:

$$\rho_{air} = \frac{p \cdot M}{R \cdot T}. \quad \text{(A.2)}$$

A.1.1.2. Delcoterm Solar E15

The thermo-physical properties of the *Delcoterm Solar E15* thermal oil are taken from the data sheet provided by the supplier [2]. Following a similar approach than in the one of the previous section, the density, thermal conductivity and specific heat are introduced in the CFD model via polynomials fittings. In Table A.3 the coefficients of these polynomials according to eq. (A.1) are included. Additionally, the four obtained thermo-physical temperature dependent properties are plotted in Figure A.2.

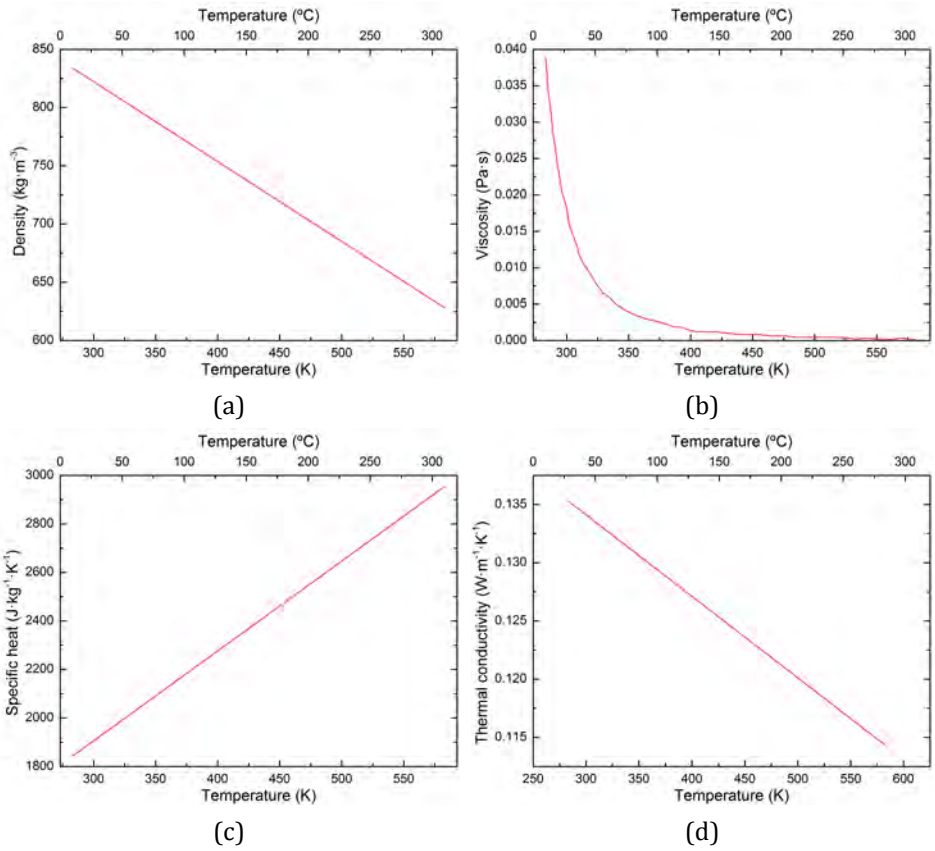

Figure A.2. Thermal properties of *Delcoterm Solar E15* thermal oil: (a) density; (b) viscosity; (c) specific heat and (d) thermal conductivity.

In the case of the viscosity, the polynomial fitting does not offer a successful matching with the experimental data from ref. [2]. Consequently, this thermal

behaviour is introduced through a multiple step function by means of a *Piecewise-linear* formulation.

Table A.3. *Delcoterm Solar E15* polynomials coefficients.

	ρ (kg·m^{-3})	c_p (J·K^{-1}·kg^{-1})	k (W·m^{-1}·K^{-1})
A	1028.21594	794.5171	0.15512
B	-0.68632	3.70498	-7.00067E-5

A.1.2. Insulation and construction materials

Different insulating and construction materials are considered in the systems modelled in chapters 5 and 6. These materials are: *Mullite*, *Foamglas*, *Microtherm* and *Concrete*. In the following their specific heat, thermal conductivity and density values are presented.

Regarding the insulation materials, first, the properties of *Mullite*, obtained from ref. [3], are presented in Table A.4. The specific heat and density values are introduced as constant magnitudes, not temperature dependent. On he other hand, the thermal conductivity is implemented as a temperature dependent polynomial.

Table A.4. *Mullite* thermo-physical properties [3].

	c_p (J·K^{-1}·kg^{-1})	k (W·m^{-1}·K^{-1})	ρ (kg·m^{-3})
A	1250	0.05354	128
B	-	2.17107E-5	-
C	-	-3.27813E-8	-
D	-	1.01975E-10	-

Second, the density and thermal conductivity values of *Microtherm* and *Foamglas* are included in Table A.5. These two properties are assumed to be constant values in the complete temperature range. The specific heat of *Foamglas* is also introduced as a temperature independent constant. In the case of the *Microtherm,* a multiple step function via *Piecewise-linear* formulation is used for the specific heat (see Figure A.3).

Table A.5. Specific heat, thermal conductivity and density of *Microtherm*, *Foamglas* and *Concrete.*

	c_p (J·K^{-1}·kg^{-1})	k (W·m^{-1}·K^{-1})	ρ (kg·m^{-3})
Microtherm	-	0.02	250
Foamglas	840	0.045	140
Concrete	701	0.4	900

Finally, a construction material, *Concrete* is also used in the TES systems modelled in section 6.2. Its thermal properties are considered constant in the CFD model. The corresponding values are shown in Table A.5. As a summary, in Figure A.3 the temperature dependent specific heat and the thermal conductivity of all the considered insulation and construction materials are shown.

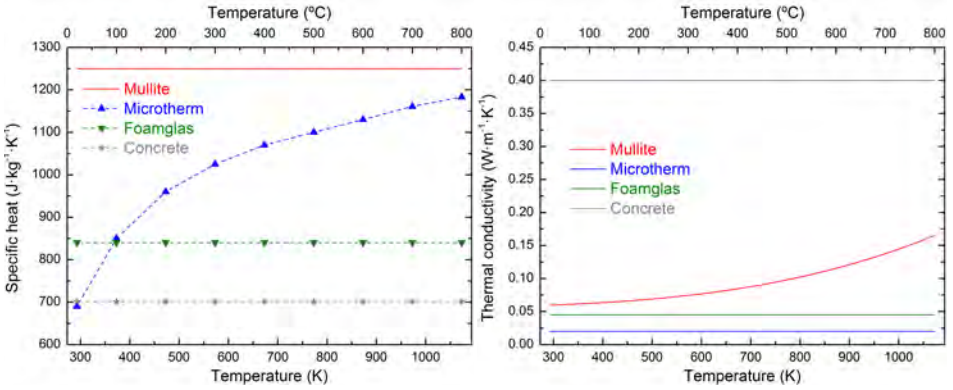

(a) (b)

Figure A.3. (a) Specific heat and (b) thermal conductivity of: *Mullite, Microtherm, Foamglas* and *Concrete*.

A.1.3. References

[1] D.Y. Peng and D.B. Robinson, "A new two-constant equation of state," *Industrial and Engineering Chemistry: Fundamentals*, vol. 15, pp. 59-74, 1976.

[2] DELCO, "DelcoTerm Solar E15," Datasheet.

[3] Morgan Thermal Ceramics, "MAFTEC Blanquet,".

A.2. List of publications

A.2.1. Papers

1. **I. Ortega-Fernández**, I. Uriz, I. Loroño, A. Ortuondo, P.L. Arias, B. D'Aguanno and J. Rodríguez-Aseguinolaza, "Thermal management and cycling behaviour of a packed bed thermal energy storage system," Under review in *Applied Thermal Engineering* (Submitted 13th May 2017).
2. **I. Ortega-Fernández**, Y. Grosu, A. Ocio, P.L. Arias, J. Rodríguez-Aseguinolaza and A. Faik, "New insights into the corrosion mechanism between molten nitrate salts and ceramic materials for packed bed thermocline systems. A case study for steel slag and solar salt," Under review in *Solar Energy* (Submitted 25th January 2017).
3. **I. Ortega-Fernández**, S.A. Zavattoni, J. Rodríguez-Aseguinolaza, M.C. Barbato and B. D'Aguanno, "Analysis of an integrated packed bed solution for heat recovery in compressed air energy storage application," Under review in *Applied Energy* (Submitted 24th December 2016).
4. **I. Ortega-Fernández**, I. Loroño, A. Faik, I. Uriz, J. Rodríguez-Aseguinolaza and B. D'Aguanno, "Parametric analysis of a packed bed thermal energy storage system," Accepted for publication in *AIP Conference Proceedings*, 2017.
5. Y. Grosu, A. Faik, **I. Ortega-Fernández** and B. D'Aguanno, "Natural magnetite for thermal energy storage: excellent thermophysical properties, reversible latent heat transition and controlled thermal conductivity," *Solar Energy Materials & Solar Cells*, vol. 161, pp. 170-176, 2017.
6. **I. Ortega-Fernández**, A. Faik, K. Mani, J. Rodríguez-Aseguinolaza and B. D'Aguanno, "Experimental investigation of solid by-product as sensible heat storage material: characterization and corrosion study," *AIP Conference Proceedings*, vol. 1734, pp. 050036, 2016.
7. **I. Ortega-Fernández**, N. Calvet, A. Gil, J. Rodríguez-Aseguinolaza, A. Faik and B. D'Aguanno, "Thermophysical characterization of a by-product from the steel industry to be used as a sustainable and low-cost thermal energy storage material," *Energy*, vol. 89, pp. 601-609, 2015.

8. **I. Ortega-Fernández**, A. Faik, A. Gil, J. Rodríguez-Aseguinolaza and B. D'Aguanno, "Thermophysical properties of a steel-making by-product to be used as thermal energy storage material in a packed-bed system," *Energy Procedia*, vol. 69, pp. 968-977, 2015.
9. **I. Ortega-Fernández**, J. Rodríguez-Aseguinolaza, A. Gil, A. Faik and B. D'Aguanno, "New thermal energy storage materials from industrial waste: compatibility of steel slags with the most common heat transfer fluids," *Journal of Solar Energy Engineering*, vol. 137, pp. 041005, 2015.

A.2.2. Contributions to conferences

1. **I. Ortega-Fernández**, S.A. Zavattoni, J. Rodríguez-Aseguinolaza, M. Barbato and B. D'Aguanno, "Analysis and optimization of the heat management in compressed air energy storage," *ASME Power&Energy 2017*. Charlotte, North Caroline, United States of America, 26th-30th June 2017. Accepted for oral presentation.
2. **I. Ortega-Fernández**, I. Uriz, A. Ortuondo, A.B. Hernández, A. Faik, I. Loroño, J. Rodríguez-Aseguinolaza and B. D'Aguanno, "Guidelines for an optimized design and management of packed-bed sensible thermal energy storage systems," *ASME Power&Energy 2017*. Charlotte, North Caroline, United States of America, 26th-30th June 2017. Accepted for oral presentation.
3. Y. Grosu, **I. Ortega-Fernández** and A. Faik, "How smart can a natural material get? Magnetite for thermal energy storage: excellent thermophysical properties, reversible latent heat transition and controlled thermal conductivity," *ASME Power&Energy 2017*. Charlotte, North Caroline, United States of America, 26th-30th June 2017. Accepted for oral presentation.
4. **I. Ortega-Fernández**, I. Loroño, A. Faik, I. Uriz, J. Rodríguez-Aseguinolaza and B. D'Aguanno, "Parametric and optimization analysis of a packed bed thermal energy storage system," *SolarPACES 2016 – Solar Power&Chemical Energy systems*. Abu Dhabi, United Arab Emirates, October 11th-14th 2016. Oral presentation.
5. Y. Grosu, **I. Ortega-Fernández**, A. Faik, K. Mani and B. D'Aguanno, "Corrosion study for different sensible heat storage materials and heat transfer fluids,"

SolarPACES 2016 – Solar Power & Chemical Energy systems. Abu Dhabi, United Arab Emirates, October 11th-14th 2016. Poster.

6. **I. Ortega-Fernández**, Y. Grosu, K. Mani, A. Faik and B. D'Aguanno, "Thermophysical characterization of potential ceramic materials for sensible thermal energy storage," *SolarPACES 2016 – Solar Power & Chemical Energy systems*. Abu Dhabi, United Arab Emirates, October 11th-14th 2016. Poster.
7. **I. Ortega-Fernández**, A. Faik, K. Mani, J. Rodríguez-Aseguinolaza and B. D'Aguanno, "Experimental investigation of solid by-product as sensible heat storage material: characterization and corrosion study," *SolarPACES 2015 – Solar Power & Chemical Energy systems*. Cape Town, South Africa, October 13th-16th 2015. Oral presentation.
8. **I. Ortega-Fernández**, A. Pérez, J. Rodríguez-Aseguinolaza, A. Faik and B. D'Aguanno, "Valorisation of steel slag as thermal energy storage material for industrial heat storage applications," *8th European Slag Conference*. Linz, Austria, October 21st-23rd 2015. Oral presentation.
9. **I. Ortega-Fernández**, A. Gil, A. Faik, J. Rodríguez-Aseguinolaza and B. D'Aguanno, "Parametric and Thermal Management Optimization of a Steel Slag Based Packed Bed Heat Storage," *ASME Power&Energy 2015*. San Diego, California, United States of America, 28th June - 2nd July 2015. Oral presentation.
10. **I. Ortega-Fernández**, A. Faik, A. Gil, J. Rodríguez-Aseguinolaza and B. D'Aguanno, "Thermophysical properties of a steel-making by-product to be used as thermal energy storage material in a packed-bed system," *SolarPACES 2014 – Solar Power & Chemical Energy systems*. Beijing, China, September 16th-19th 2014. Oral presentation.
11. **I. Ortega-Fernández**, A. Gil, J. Rodríguez-Aseguinolaza, A. Faik and B D'Aguanno, "Valorisation of a waste material resulting from iron and steel production: use of slag as thermal energy storage material," *European Steel Environment & Energy Congress*. Teesside University, United Kingdom, September 15th-17th 2014. Oral presentation.
12. **I. Ortega-Fernández**, J. Rodríguez-Aseguinolaza, A. Gil, A. Faik and B. D'Aguanno, "New thermal energy storage materials from industrial waste: compatibility of steel slags with the most common heat transfer fluids," *8th*

ASME International Conference on Energy Sustainability. Boston, Massachusetts, United States of America, 30th June – 2nd July 2014. Oral presentation.

13. A. Gil, N. Calvet, **I. Ortega-Fernández**, E. Risueño, A. Faik, P. Blanco and J. Rodriguez-Aseguinolaza, "Characterization of a by-product from steel industry applied to thermal energy storage in concentrated solar power," *Eurotherm Seminar 99 – Advances in Thermal Energy Storage*. Lleida, Spain, 28th-30th May 2014. Oral presentation.

eman ta zabal zazu
Universidad del País Vasco
Euskal Herriko Unibertsitatea
CIC energiGUNE
energy cooperative research centre

This thesis aims at studying cost effective and high performance concepts for thermal energy storage applications. Without entering on its implementation, a successful thermal energy storage solution must provide a satisfactory balance between two basic aspects, the storage material and the implemented technology. Both aspects are addressed in this thesis achieving an optimal compromise between the variables governing the cost, the efficiency and the thermal performance of the heat storage solution.